


Spring 2-1-2018

Systematic Size Control in the Synthesis of Zero-Valent Iron Nanoparticles

Grant C. Bleier

Follow this and additional works at: https://digitalrepository.unm.edu/chem_etds

 Part of the [Inorganic Chemistry Commons](#), [Materials Chemistry Commons](#), and the [Organic Chemistry Commons](#)

Recommended Citation

Bleier, Grant C.. "Systematic Size Control in the Synthesis of Zero-Valent Iron Nanoparticles." (2018).
https://digitalrepository.unm.edu/chem_etds/89

This Dissertation is brought to you for free and open access by the Electronic Theses and Dissertations at UNM Digital Repository. It has been accepted for inclusion in Chemistry ETDs by an authorized administrator of UNM Digital Repository. For more information, please contact disc@unm.edu.

Grant C. Bleier

Candidate

Chemistry and Chemical Biology

Department

This dissertation is approved, and it is acceptable in quality and form for publication:

Approved by the Dissertation Committee:

Richard A. Kemp

, Chairperson

Dale L. Huber

Martin L. Kirk

Fernando H. Garzon

**Systematic Size Control in the Synthesis of Zero-Valent Iron
Nanoparticles**

By

Grant C. Bleier

B.A., Chemistry, University of New Mexico 2011

DISSERTATION

Submitted in Partial Fulfillment of the

Requirements for the Degree of

Doctor of Philosophy

Chemistry

The University of New Mexico

Albuquerque, New Mexico

May, 2018

© 2017, Grant Christopher Bleier

Dedication

I dedicate this dissertation to my mom, who is the strongest single mom I know. I am who I am today because of her strength and dedication. She is someone who inspires me to be the best person I could possibly be, and whose constant love and support I could not live without. I also dedicate this to my loving dog Kaiser who is like my only child; I don't know how I could live without his constant joyful attitude and companionship.

Acknowledgements

I would like to express the deepest appreciation and gratitude to my extremely intelligent, supportive, and understanding research advisor, Dr. Dale L. Huber. Your technical guidance, scholarly advice, and patience has been invaluable to me. Aside from being a perfect advisor, you have truly acted as a father figure to me and inspire me to be the best scientist possible. Your constant, witty humor and easygoing demeanor is a perfect model for how I aspire to be. I look up to you more than you will ever know.

I owe a deep sense of gratitude to my UNM advisor, Dr. Richard A. Kemp. As my undergraduate professor, you highly influenced my decision to pursue a graduate degree in chemistry and have provided the wisdom, enthusiasm, and encouragement necessary for me to achieve this goal. You are one of the most influential people in my academic and personal life. I look up to you with the utmost respect and I cannot think of a better person to mold me into the scientist I am today.

To my committee member and former professor Dr. Martin L. Kirk, whose absolute genius has continuously acted as a source of inspiration to me. I can honestly say you are one of the best professors I have ever had. Your uncanny ability to translate the most complex forms of chemistry into simplified, comprehensible material continues to astonish me. I will never forget how you continuously made our class ease up and laugh with your “there’s no crying in chemistry!” quotes, when difficult concepts were introduced in class.

I am extremely grateful for my final committee member, Dr. Fernando Garzon. Although our interactions together have been limited, I deeply appreciate the time and

effort you have dedicated to making sure my ultimate goal is accomplished. A professor who is willing to sacrifice time in their busy schedule to accommodate a student in need is someone who deserves special recognition in this dissertation.

To my colleague, Dr. John Watt, who continuously acts as a model scientist that is hard-working, highly intelligent, and accomplishes nearly everything he sets out to achieve. Your commendable diligence and ethic is a huge inspiration not only to me, but also to our undergraduates and many others around you. Thank you for your continuous support and advice both in and out of the laboratory.

I am extremely grateful for our technologist Bradley Hance. The skills you have taught me over the years have been invaluable, and will continue to help me in many years to come. I am still convinced you deserve a Ph.D. in engineering, physics, and computer science. Thank you for constantly making me laugh and being someone I can talk to regularly about anything.

To Dr. Erika Vreeland, who served as a model graduate student when I first began my studies. You have maintained incredible balance between caring for a newly born child, your graduate studies, and personal life, which has been incredibly inspiring to me. Dropping anything you had on your plate to assist with my persistent questions made me look up to you, and showed me what a model colleague should be.

To Dr. Chester K. Simocko, who helped provide me with a rich sense of organic chemistry knowledge throughout my time in the laboratory. I will never forget our

interesting and intelligent conversations that got me through long days. I still think that the best Star Wars episodes goes in this order: IV > V > VI > III > II > I.

I also want to thank Dr. Sergei Ivanov, Dr. Todd Monson, and CJ Pierce, for your mentorship and sharing your knowledge of characterization techniques and data interpretation with me. To our undergraduates in the laboratory, Mariah Austin, Jolie Lucero, and Zachary Romero for constantly supporting me and assisting me when needed. I know you all will go on to do absolute amazing research and work in your lives, and will be successful at whatever you do.

The body of research described in this dissertation was supported by the U.S. Department of Energy, Office of Basic Energy Sciences, Division of Materials Science and Engineering. HRTEM imaging and XRD/SAXS measurements were performed courtesy of the Center for Integrated Nanotechnologies, a U.S. Department of Energy, Office of Basic Energy Sciences user facility. Sandia National Laboratories is a multi-mission laboratory managed and operated by National Technology and Engineering Solutions of Sandia, LLC., a wholly owned subsidiary of Honeywell International, Inc., for the U.S. Department of Energy's National Nuclear Security Administration under contract DE-NA-0003525.

Systematic Size Control in the Synthesis of Zero-Valent Iron Nanoparticles

By

Grant C. Bleier

B.A., Chemistry, University of New Mexico, 2011

Ph.D., Chemistry, University of New Mexico, 2017

Abstract

A novel synthetic method for the production of highly magnetic, low size-dispersity nanoparticles through reversible magnetic agglomeration is introduced and studied in detail. Initially, a weakly coordinating surfactant (3-octadecyl-2,4-pentanedione) is employed to produce a wide range of nanoparticle sizes ranging from 8 to 20 nm in diameter. The kinetics faced in these reactions by cheap and widely available iron complex precursors can be avoided in this method with the introduction of thermodynamic control, which occurs in the form of a magnetic precipitation event that essentially halts nanoparticle growth. Utilizing this synthetic method, the length of the alkyl chain on the surfactant can be modified to shorter lengths to ultimately control the size to which the particles can grow by varying the degree of steric stabilization. Surfactants increasing in alkyl chain length from the bare surfactant (2,4-pentanedione) to 4 and 10 carbons long (3-

butyl-2,4-pentanedione and 3-decyl-2,4-pentanedione, respectively) were used to further provide fundamental insight into the surfactant nanoparticle relationship. Through this relationship our research could also elaborate on the factors that influence and control nanoparticle nucleation, growth, and stabilization.

Post-processing techniques on the as-synthesized nanoparticles are also introduced, opening numerous opportunities for further customization of nanoparticle properties for a given system. The magnetization saturation can be drastically enhanced and the collective blocking temperature altered through simple hydrogenation procedures. It was discovered through these techniques that the nanoparticles can also behave as active catalysts for the hydrogenation of alkenes with a high prospect for many other substrates.

The magnetic properties of the nanoparticles were studied using a superconducting quantum interference device (SQUID) magnetometer and the physical characteristics were analyzed using transmission electron microscopy (TEM), small angle X-ray scattering (SAXS), and X-ray diffraction (XRD). Nuclear magnetic resonance (NMR) assisted in the identification of the custom-synthesized surfactants as well as the substrate conversion progress in the alkene hydrogenation reactions.

| | |
|---|--------|
| Systematic Size Control in the Synthesis of Zero-Valent Iron Nanoparticles..... | ii |
| Dedication..... | iv |
| Acknowledgements..... | v |
| Abstract..... | ix |
| List of Figures..... | xiv |
| List of Tables..... | xxxiii |
| List of Abbreviations and Acronyms..... | xxxv |
| Chapter 1. Introduction..... | 1 |
| 1.1. Research Objectives..... | 2 |
| 1.2. Outline..... | 3 |
| 1.3. Chapter Summary..... | 4 |
| Chapter 2. Fundamentals..... | 5 |
| 2.1. Magnetic Nanomaterials..... | 5 |
| 2.2. Magnetism Overview..... | 5 |
| 2.2.1. Diamagnetism..... | 6 |
| 2.2.2. Paramagnetism..... | 7 |
| 2.2.3. Ferromagnetism..... | 8 |
| 2.2.4. Ferrimagnetism..... | 11 |
| 2.2.5. Antiferromagnetism..... | 11 |
| 2.3. Magnetic Domains and Hysteresis..... | 12 |
| 2.4. Magnetic Nanoparticles and Superparamagnetism..... | 14 |
| 2.4.1. Blocking Temperature..... | 16 |
| Chapter 3. Iron Nanoparticle Synthetic Approaches and Literature Review..... | 19 |
| 3.1. Top Down Approaches to Nanoparticle Synthesis..... | 22 |
| 3.1.1. Laser Techniques..... | 22 |
| 3.2. Bottom-Up Approaches to Nanoparticle Synthesis..... | 26 |
| 3.2.1. Introduction..... | 26 |
| 3.2.2. Reduction of Iron Salts..... | 26 |
| 3.2.3. Reduction of Iron Oxides..... | 28 |
| 3.2.4. Sonochemical Decomposition (Sonolysis)..... | 29 |
| 3.2.5. Thermal Decomposition..... | 31 |
| 3.2.5.1. Introduction..... | 31 |

| | |
|--|----|
| 3.2.5.2. Literature Review | 33 |
| 3.3. Surfactant Stabilization and Passivation | 37 |
| 3.3.1. Introduction | 37 |
| 3.3.2. Literature Review | 38 |
| 3.4. Mechanisms of Nanoparticle Formation | 40 |
| Chapter 4. Characterization | 44 |
| 4.1. Transmission Electron Microscopy (TEM) | 44 |
| 4.2. SQUID Magnetometry | 45 |
| 4.3. X-ray Diffraction (XRD)..... | 47 |
| 4.4. Small Angle X-ray Scattering (SAXS) | 50 |
| 4.5. UV-Visible Spectroscopy (UV-Vis) | 51 |
| 4.6. Nuclear Magnetic Resonance (NMR) | 54 |
| Chapter 5. Nanoparticle Size Control Through Reversible Magnetic Agglomeration. 57 | |
| 5.1. Introduction | 57 |
| 5.2. Experimental | 60 |
| 5.2.1. Surfactant Synthesis | 62 |
| 5.2.2. Surfactant Characterization | 63 |
| 5.2.3. Synthesis of Nanoparticles | 65 |
| 5.3. Results and Discussion..... | 65 |
| 5.3.1. Transmission Electron Microscopy..... | 66 |
| 5.3.2. Small Angle X-ray Scattering | 74 |
| 5.3.3. SQUID Magnetometry | 79 |
| 5.3.4. Effects of Ligand Concentration | 80 |
| 5.3.5. Post Processing Techniques | 86 |
| 5.3.5.1. Results and Discussion..... | 88 |
| 5.4. Conclusions | 94 |
| Chapter 6. Size Control through Modification of the Stabilizing Surfactant | 95 |
| 6.1. Introduction | 95 |
| 6.2. Experimental | 97 |
| 6.2.1. Materials..... | 97 |
| 6.2.2. Synthesis of Stabilizing Surfactants | 97 |
| 6.2.3. Surfactant Characterization | 98 |

| | | |
|--|--|-----|
| 6.2.4. | Synthesis of Nanoparticles | 100 |
| 6.3. | Results and Discussion..... | 102 |
| 6.3.1. | 2,4-Pentanedione Surfactant..... | 102 |
| 6.3.2. | 3-Butyl-2,4-Pentanedione Surfactant | 110 |
| 6.3.3. | 3-Decyl-2,4-Pentanedione Surfactant | 116 |
| 6.3.4. | Further Characterization..... | 124 |
| 6.3.5. | Summary of All Surfactants | 129 |
| 6.3.6. | Scale-Up Synthesis..... | 139 |
| 6.3.6.1. | Scale-Up Nanoparticle Synthesis Using Decylamine | 140 |
| 6.4. | Conclusions | 142 |
| Chapter 7. Size Dependent Catalytic Activity of Magnetically Recoverable Heterogeneous Zero-Valent Iron Nanoparticle Catalysts | | 143 |
| 7.1. | Introduction | 143 |
| 7.2. | Experimental | 144 |
| 7.2.1. | Synthesis of Stabilizing Surfactants | 144 |
| 7.2.2. | Nanoparticle Stock (Catalyst) Preparation | 144 |
| 7.2.3. | Materials..... | 151 |
| 7.2.4. | Characterization Techniques | 155 |
| 7.3. | Results and Discussion..... | 161 |
| 7.3.1. | Nanoparticle Catalytic Activity..... | 161 |
| 7.3.1.1. | 18.4 (d.nm) Nanoparticle Catalyst | 161 |
| 7.3.1.2. | 18.4 (d.nm) Nanoparticle Catalyst Reaction Kinetics..... | 167 |
| 7.3.1.3. | 14.6 (d.nm) Nanoparticle Catalyst | 174 |
| 7.3.1.4. | 14.6 (d.nm) Nanoparticle Catalyst Reaction Kinetics..... | 177 |
| 7.3.1.5. | 9.2 (d.nm) Nanoparticle Catalyst | 178 |
| 7.3.2. | Conclusions | 186 |
| Chapter 8. Conclusions and Outlook..... | | 188 |
| Appendix A. Publications | | 190 |
| References..... | | 191 |

List of Figures

- Figure 2.1 (a) Magnetic moment M versus an external applied magnetic field H for a diamagnetic material. (b) Susceptibility versus temperature graph which displays the temperature independent susceptibility observed in diamagnetic materials. (c) Applying an external magnetic field creates an induced magnetic field in the opposite direction. 6
- Figure 2.2 (a) Magnetic moment M versus an externally applied magnetic field H for a paramagnetic material. (b) Susceptibility versus temperature graph which displays the temperature dependent susceptibility known as the Curie Law. (c) In the absence of a field magnetic moments are randomized. When a field is applied, the magnetic moment of a paramagnetic material displays partial alignment in the direction of the field. 7
- Figure 2.3 Shown above is a common curve called a hysteresis loop. A hysteresis loop is obtained by measuring the magnetic moment of a ferromagnetic material in the presence of a positive and negative externally applied saturating magnetic field (M , $-M$)..... 9
- Figure 2.4 Susceptibility versus temperature plot, displaying the temperature dependent susceptibility for a ferromagnetic material. 10
- Figure 2.5 Susceptibility versus temperature for an antiferromagnetic material. Below the Néel temperature (T_N), magnetic ordering dominates, resulting in antiferromagnetism. Above T_N , the susceptibility of these materials follow the Curie-Weiss law for paramagnets. 12
- Figure 2.6 (left) The multi-color block shown here represents a ferromagnetic material consisting of multiple domains. If you were to take a small section (uniform in color) out

of this multiple domain structure, it would be considered a single domain. As this small piece grows, domain wall formation occurs to lower the overall energy of the system... 13

Figure 2.7 This figure shows overall magnetic energy with respect to angle. The “easy axis” is an energetically favorable direction of spontaneous magnetization. 15

Figure 2.8 The status of a nanoparticle either being in the blocked or superparamagnetic state depends on the operational temperature of the system and the blocking temperature of the nanoparticles. 17

Figure 3.1 Synthetic approaches to iron nanoparticle synthesis. Bottom up techniques synthesize nanoparticles from atomic or molecular species. Top down approaches achieve nanoparticles by breaking bulk materials into smaller pieces using mechanical, chemical, or other forms of energy. 20

Figure 3.2 Nanoparticles synthesized with various solvents using laser ablation techniques. (Top to bottom) The solvents implemented were ethanol (EtOH), tetrahydrofuran (THF), acetonitrile (AN), dimethylformamide (DMF), dimethylsulfoxide (DMSO) and toluene (TOL). (Left to right) TEM micrographs obtained, histograms displaying size distribution, and X-ray diffraction data for some samples. Reproduced with permission from Ref²⁶.. 24

Figure 3.3 (a,b) TEM images and their corresponding electron diffraction patterns of the amorphous Fe nanoparticles annealed at (a) 200°C and (b) 400°C. (c) XRD patterns of the amorphous Fe nanoparticles annealed at temperatures of 200 and 400°C. (d) Magnetic property comparison between the amorphous iron nanopowder and pure iron. Reproduced with permission from Ref²⁷ 25

Figure 3.4 (a) and (b) TEM micrographs of aggregates of iron particles. Nanoparticles formed through the reduction of iron salts with sodium borohydride. (c) Particle size distribution (PSD) of nanoparticle product. Median diameter is located at 60.2 nm. Reproduced with permission from Ref⁴³. 27

Figure 3.5 (a) TEM showing amorphous iron nanoparticles stabilized by oleic acid as surfactant, produced through the sonochemical decomposition of iron carbonyl. Scale bar represents 20 nm. (b) TEM showing as-synthesized amorphous iron nanoparticles stabilized by PVP. (c) Electron diffraction pattern of the as-synthesized iron nanoparticles showing its amorphous nature (left), and heating from the beam induces crystallization in situ (right), forming a weak FeO phase. Reproduced with permission from Ref⁵⁴. 30

Figure 3.6 Pathways showing the early stages of decomposition for iron pentacarbonyl. This is an exceptional visual representation which displays the complexity involved in decomposition, and why reaction kinetics are difficult to control. Structures shown are drawn for well-known, metastable, isolable compounds. Reproduced with permission from Ref³. 32

Figure 3.7 (a) Dispersion of ~6 nm particles prepared in poly(4-vinylpyridine-styrene)/dichlorobenzene. Diffraction patterns below of the (b) as prepared particles and (c) after standing for 1 year. (d) Dispersion of ~16 nm particles prepared in poly(4-vinylpyridine-styrene)/dichlorobenzene which spontaneously form magnetic chains and (e) the diffraction pattern inset. Reproduced with permission from Ref⁶⁴. 34

Figure 3.8 (a) TEM micrographs of iron nanoparticles at low magnification, showing their formation of chain-like aggregates form in the absence of an external applied field. The

scale bar represents 600 nm. (b) Higher magnification images show that these aggregates are made up of individual nanoparticles in the range of 6 nm in diameter. The scale bar represents 60 nm. Inset diffraction pattern verifies that this sample is pure bcc Fe with diffraction rings at 0.8, 0.9, 2.0, 1.2, 1.4 and 2.0 Å. (c) Magnetization vs field for the same nanoparticle sample at 150K. The sample is below the blocking temperature and therefore shows a weak, but detectible coercivity (5.6 mT). Saturation magnetization is determined by extrapolating to infinite field, and is 178 Am²/kg. Reproduced with permission from Ref⁶⁷ 36

Figure 3.9 The classic LaMer mechanism to nanoparticle synthesis. In stage I, the concentration of monomer increases until it reaches a critical supersaturated state (C_{MIN}). In stage II, burst nucleation partially relieves this supersaturation and the monomer concentration drops below the critical nucleation concentration. In stage III, growth of nuclei occurs by diffusion of the monomer to the particle surface, and the monomer concentration slowly approaches the lower solubility limit (C_S). Being a closed system, additional growth of the nanoparticles occurs through ripening due to the change in nanoparticle solubility as a function of size. This ripening leads to increased particle dispersity, thus affecting particle properties. 40

Figure 3.10 The extended LaMer mechanism for nanoparticle formation. The beginning stages mirror the classic LaMer mechanism. However, the continuous addition of monomer in the extended LaMer introduces a new stage, stage IV. With the continuous addition of precursor to solution, there is no observable ripening effects that occur. This method leads to a slow but steady particle growth and low size dispersity..... 42

Figure 4.1 Schematic of an X-ray diffractometer. X-rays are generated by striking a pure anode of a particular metal with high energy electrons in a sealed vacuum tube and are directed toward the sample. The sample diffracts the X-ray beam differently, depending on its orientation and structure. An area detector then collects the diffracted X-rays. The crystal structure is then determined from the diffraction pattern which consists of reflections of various intensities. 48

Figure 4.2 Simplified schematic of how a SAXS spectrum is obtained. A sample is illuminated by a collimated monochromatic X-ray beam, and the intensity of the scattered X-rays is recorded by an X-ray detector. The resulting scattering pattern is related to the overall shape and size of the particles in the sample. 50

Figure 4.3 Schematic of UV-Vis excitation and emission. When the light energy the sample is exposed to matches the energy difference between an electronic ground and excited state, the sample will absorb a fraction of that light of frequency (ν) and promote electrons to the higher energy state orbital. 52

Figure 4.4 NMR analyzes the response of multiple atomic nuclei's spin within a compound to an applied external magnetic field. Applying a weak external magnetic field causes the atomic nuclei's spin to orient with the applied field (α , $I = +1/2$, lower energy) or against the applied field (β , $I = -1/2$, higher energy). When irradiating the nucleus with electromagnetic radiation of the correct energy (ΔE), a nucleus in a low energetic orientation α , can be excited to the higher energetic state, β 55

Figure 5.1 (a) The reversible magnetic agglomeration mechanism can be explained through the following stages: Stage I, monomer concentration increases to a critical

supersaturated level (C_{MIN}) which is then partially relieved by a nucleation event (Stage II). In Stage III, monomer concentration drops below the level required for nucleation and particle growth occurs. Then, due to a continuous addition of monomer, the reaction enters steady state growth conditions. In Stage IV, particles grow to a critical size before their magnetic dipole interactions become strong enough to overcome steric stabilization leading to a magnetic agglomeration event. Once particles agglomerate and precipitate out of solution, their reactivity is drastically decreased. Monomer concentration again begins to increase to a critical supersaturated level (I b), and a second nucleation event takes place (II b). These newly formed nanoparticles then grow until magnetic agglomeration occurs, and the cycle repeats (III b – IV b). (b) A visual representation of reversible magnetic agglomeration taken from an experiment using unsubstituted 2,4-pentanedione as surfactant..... 58

Figure 5.2 (a) Processed 1H NMR spectra (90 MHz, $CDCl_3$) of the 3-octadecyl-2,4-pentanedione product after purification (normalizing 3.4 ppm triplet to 1.0 H): δ 3.61 (t, 1.00H), 2.17 (s, 6.44H), 1.81 (m, 3.65H), 1.26 (s, 39.34H), 0.89 (t, 4.66H). (b) Predicted 1H NMR spectra of 3-octadecyl-2,4-pentanedione: δ 3.12 (t, 1H), 2.31 (s, 6H), 1.56 (m, 2H), 1.40 (m, 2H), 1.26 (s, 30H), 0.89 (t, 3H)..... 63

Figure 5.3 (a) Processed ^{13}C NMR spectra (90 MHz, $CDCl_3$) of the 3-octadecyl-2,4-pentanedione product after purification (excluding 3 $CDCl_3$ peaks at 75.0, 76.0 and 78.0): δ 204.2, 68.7, 31.5, 29.2, 28.9, 28.6, 27.9, 27.1, 22.3, 13.7. (b) Predicted ^{13}C NMR spectra of 3-octadecyl-2,4-pentanedione: δ 207.0, 68.9, 31.9, 29.8, 29.6, 29.3, 25.4, 25.1, 22.7, 14.1..... 64

Figure 5.4 (a-h) Transmission electron microscopy (TEM) images and their corresponding histograms produced from size analysis of iron nanoparticles synthesized using 3-octadecyl-2,4-pentanedione as the stabilizing surfactant. All scale bars are equal to 20 nm. Average nanoparticle sizes are 9.2 ± 0.7 nm, 12.0 ± 1.0 nm, 15.2 ± 0.7 nm, 17.1 ± 0.8 nm, 16.4 ± 2.6 nm, 18.8 ± 1.7 nm, 16.8 ± 2.7 nm, and 18.6 ± 1.5 nm for images (a-h), respectively. 69

Figure 5.5. Transmission electron micrographs of iron nanoparticles synthesized using 3-octadecyl-2,4-pentanedione as the stabilizing surfactant before and after a renucleation event. All scale bars are equal to 100 nm. (a) Iron nanoparticles before the renucleation event, synthesized with 9.1 mmol iron addition. Average nanoparticle size is 17.1 ± 0.8 nm (4.5% dispersity). (b) Iron nanoparticles after the renucleation event, synthesized with 10.9 mmol iron addition. Average nanoparticle size is 16.4 ± 0.8 nm (15.7% dispersity)..... 71

Figure 5.6 Histogram produced from size analysis of TEM images from 10.9 mmol iron addition. The bimodal distribution shows a distinct renucleation event that has occurred. Analysis can be broken into a high and low distribution of sizes. The low distribution shows a mean size of 13.0 ± 1.2 nm (9.6% dispersity). The high distribution shows a mean size of 18.4 ± 0.8 nm (4.5% dispersity). 73

Figure 5.7 Summary of nanoparticle size analysis through TEM. The mean bimodal high and low are included to show where the maximum particle size is achieved before agglomeration. 74

Figure 5.8 A typical SAXS measurement of as-synthesized nanoparticles showing the experimental raw data, the simulated fit (red), and the simulation residuals. 75

Figure 5.9 (a) Nanoparticle sizes obtained with small angle X-ray scattering (SAXS) experiments. Renucleation events can be observed in SAXS by a decrease in particle size accompanied by an increase in size dispersity, a characteristic of a bimodal size distribution. Average nanoparticle sizes are 9.2 ± 0.7 nm, 12.0 ± 1.0 nm, 15.2 ± 0.7 nm, 17.1 ± 0.8 nm, 16.4 ± 2.6 nm, 18.8 ± 1.7 nm, 16.8 ± 2.7 nm, and 18.6 ± 1.5 . (b) Comparison of mean particle sizes obtained through SAXS and TEM analytical techniques. 76

Figure 5.10 All raw experimental SAXS measurements of as-synthesized nanoparticles with 3-octadecyl-2,4-pentanedione surfactant. Intensity has been normalized to allow for comparison..... 77

Figure 5.11 Experimental raw data, the simulated fit (red), and the simulation residuals for nanoparticles samples composed of 1.8, 3.6, 7.3, 9.1, 10.9, 14.6, 18.2, and 25.5 mmol Fe for samples (a-h), respectively..... 78

Figure 5.12 Plot displaying saturation magnetization values obtained for all samples synthesized with 3-octadecyl-2,4-pentanedione surfactant. 80

Figure 5.13 (1-5) Stages of iron precursor addition. When the iron precursor is added through the syringe the initial solution is a light-yellow color. As iron carbonyl heats up and slowly decomposes, this solution progresses to a light orange and reddish orange color. Nucleation occurs during the transition from a reddish-brown solution to a brown-black solution..... 82

Figure 5.14 Transmission electron micrographs of iron nanoparticles synthesized using 3-octadecyl-2,4-pentanedione as the stabilizing surfactant with varying concentrations. All

scale bars are equal to 20 nm. Particles synthesized with (a) 5 mg, (b) 10 mg, (c) 20 mg, and (d) 40 mg 3-octadecyl-2,4-pentanedione surfactant in starting flask..... 84

Figure 5.15 (a) Average nanoparticle sizes for reactions synthesized with 3-octadecyl-2,4-pentanedione. Amounts shown are from 10 mg, 20 mg, and 40 mg. Due to nanoparticle coalescence observed in the 5 mg reaction, it is excluded from this data. (b) Nucleation time (seconds) as a function of 3-octadecyl-2,4-pentanedione amounts. The nucleation timer is started once the first drip of the iron precursor solution is added to the solvent and surfactant..... 85

Figure 5.16 Schematic of the Parr reactor reduction set up. This set up involves a hot plate with a bored-out aluminum block which heats the reactor, producing even heating with improved heat transfer. 88

Figure 5.17 All temperature sweeps (MvT) were performed with the same sequence. For zero-field cooled measurements, sample moments were measured 5K to 250K with no applied field. For field-cooled measurements, a weak 10 Oe field was applied and sample moments were measured from 250K down to 5K. Temperature sweeps are shown for (a) stock nanoparticle solution, $T_B = 125K$, and (b) Parr reduction product, $T_B = 150K$. (c) Comparison of blocking temperatures before and after Parr reduction method. 89

Figure 5.18 Field sweeps were performed on both samples from -5 to 5 T at 5K and 250K. Field sweeps are shown for (a) stock nanoparticle solution, $M_{Sat} = 184.5 \text{ Am}^2/\text{kg}$, and (b) Parr reduction product, $M_{Sat} = 208.0 \text{ Am}^2/\text{kg}$ 91

Figure 5.19 Transmission electron micrographs of (a) the stock nanoparticle sample before undergoing reduction, and (b) reduced nanoparticles using the Parr reactor technique. All scale bars represent 20 nm. 93

Figure 6.1 Substitution was carried out at the 3-position of 2,4-pentanedione with alkyl chains composed of 4 (butyl), 10 (decyl), and 18 (octadecyl) carbons to yield several different length surfactants. 96

Figure 6.2 Schematic showing the proposed agglomeration mechanism with varying surfactants. The larger steric bulk provided by the surfactant allows for larger nanoparticles to be synthesized before magnetic agglomeration occurs..... 96

Figure 6.3 (a) Processed ^1H NMR spectra (90 MHz, CDCl_3) of the 3-decyl-2,4-pentanedione product after purification: δ 3.40 (t, 1H), 2.05 (s, 6H), 1.86 (m, 2H), 1.26 (s, 14H), 0.89 (t, 3H) (b) Predicted ^1H NMR spectra of 3-decyl-2,4-pentanedione: δ 3.12 (t, 1H), 2.31 (s, 6H), 1.56 (m, 1H), 1.40 (m, 1H), 1.26 (s, 14H), 0.89 (t, 3H). 99

Figure 6.4 (a) Processed ^{13}C NMR spectra (90 MHz, CDCl_3) of the 3-decyl-2,4-pentanedione product after purification: δ 204.7, 191.1 69.3, 34.9, 31.8, 31.0, 29.8, 29.7, 29.6, 29.2, 27.8, 22.8, 14.2. (b) Predicted ^{13}C NMR spectra of 3-decyl-2,4-pentanedione: δ 207.0, 68.9, 31.9, 29.8, 29.6, 29.3, 25.4, 25.1, 22.7, 14.1..... 99

Figure 6.5 Transmission electron micrographs and their corresponding histograms produced from size analysis of iron nanoparticles synthesized using 2,4-pentanedione as the stabilizing surfactant. All scale bars are equal to 20 nm. Average nanoparticle sizes are 4.9 ± 0.8 , 5.4 ± 0.6 , 5.7 ± 0.8 , 6.4 ± 0.7 , and 5.9 ± 1.2 nm for images (a-e), respectively. 104

Figure 6.6 Combined histograms obtained from size analysis of transmission electron micrographs for all samples synthesized with 2,4-pentanedione surfactant..... 105

Figure 6.7 Graph of mean particle diameter (nm) vs Fe mmol addition for iron nanoparticles synthesized using 2,4-pentanedione as the stabilizing surfactant. Particle sizes for the 0.067, 0.135, 0.202, 0.269, and 0.337 Fe mmol additions were 4.9 ± 0.8 , 5.4 ± 0.6 , 5.7 ± 0.8 , 6.4 ± 0.7 , and 5.9 ± 1.2 nm, respectively. The mean maximum size obtained with this surfactant was determined to be 6.4 nm, as renucleation can be observed in the 0.337 mmol Fe addition, leading to a lower average particle size with increased size dispersity..... 106

Figure 6.8 Transmission electron micrographs of iron nanoparticles synthesized using 2,4-pentanedione as the stabilizing surfactant before and after a renucleation event. All scale bars are equal to 20 nm. (a) Iron nanoparticles before the renucleation event, synthesized with 0.269 mmol iron addition. Average nanoparticle size is 6.4 ± 0.7 nm (11.5% dispersity). (b) Iron nanoparticles after the renucleation event, synthesized with 0.337 mmol iron addition. Average nanoparticle size is 5.9 ± 1.2 nm (19.8% dispersity). A near bimodal distribution can be observed visually within magnetic agglomerates, where small and large particles had the tendency to agglomerate with similar sizes. 108

Figure 6.9 Transmission electron micrographs and their corresponding histograms produced from size analysis of iron nanoparticles synthesized using 3-butyl-2,4-pentanedione as the stabilizing surfactant. Average nanoparticle sizes are 4.4 ± 0.6 , 5.0 ± 0.8 , 5.6 ± 0.7 , 6.4 ± 1.1 , 7.1 ± 1.0 , 8.3 ± 0.7 , 10.0 ± 1.1 , and 8.8 ± 2.7 nm for images (a-h), respectively. All scale bars are equal to 20 nm..... 113

Figure 6.10 (a) Mean particle diameter (nm) vs Fe mmol addition for iron nanoparticles synthesized using 3-butyl-2,4-pentanedione as the stabilizing surfactant. Particle sizes for the 0.151, 0.226, 0.301, 0.452, 0.602, 0.753, 0.903, and 1.05 mmol Fe additions were 4.4 ± 0.6 , 5.0 ± 0.8 , 5.6 ± 0.7 , 6.4 ± 1.1 , 7.1 ± 1.0 , 8.3 ± 0.7 , 10.0 ± 1.1 , and 8.8 ± 2.7 nm, respectively. (b) Graph including the average high and low sizes from the bimodal distribution for the 1.05 Fe mmol reaction. The mean size for the low and high segments are 5.7 ± 1.1 nm (19.4% dispersity), and 10.7 ± 1.0 nm (9.2% dispersity), respectively. 113

Figure 6.11 Histogram size analysis for the 1.05 Fe mmol addition which shows renucleation has occurred through a bimodal size distribution. 114

Figure 6.12 Combined histograms obtained from size analysis of transmission electron micrographs for all samples synthesized with 3-butyl-2,4-pentanedione surfactant..... 115

Figure 6.13 Transmission electron micrographs and their corresponding histograms produced from size analysis of iron nanoparticles synthesized using 3-decyl-2,4-pentanedione as the stabilizing surfactant. Average nanoparticle sizes are 5.3 ± 0.7 , 6.9 ± 1.0 , 9.0 ± 0.5 , 11.1 ± 1.1 , 12.9 ± 1.1 , 13.7 ± 1.2 , and 12.1 ± 3.0 nm for images (a-g), respectively. All scale bars are equal to 20 nm..... 118

Figure 6.14 (a) Mean particle diameter (nm) vs Fe mmol addition for iron nanoparticles synthesized using 3-decyl-2,4-pentanedione as the stabilizing surfactant. Particle sizes obtained were 5.3 ± 0.7 , 6.9 ± 1.0 , 9.0 ± 0.5 , 11.1 ± 1.1 , 12.9 ± 1.1 , 13.7 ± 1.2 , and 12.1 ± 3.0 nm for the 0.336, 0.671, 1.34, 2.01, 2.68, 3.36, and 5.37 mmol Fe additions, respectively. (b) Graph including the average low and high sizes from the bimodal

distribution for the 5.37 Fe mmol reaction. The mean size for the low and high segments are 9.1 ± 1.4 nm (14.9% dispersity) and 14.5 ± 1.1 nm (7.7% dispersity), respectively. 119

Figure 6.15 Histogram size analysis for the 5.37 Fe mmol addition which shows renucleation has occurred through a bimodal size distribution. 120

Figure 6.16 (a) Nanoparticle sizes obtained with small angle X-ray scattering (SAXS) experiments. Average nanoparticle sizes are 4.9 ± 0.7 nm, 6.3 ± 0.9 nm, 8.5 ± 0.8 nm, 10.2 ± 1.4 nm, 11.6 ± 1.7 nm, 13.1 ± 1.7 nm, and 12.7 ± 2.2 for the samples synthesized with 0.336, 0.671, 1.34, 2.01, 2.68, 3.36 and 5.37 mmol Fe additions, respectively. (b) Comparison of mean particle sizes obtained through SAXS and TEM analytical techniques. 122

Figure 6.17 All raw experimental SAXS measurements of as-synthesized nanoparticles with 3-decyl-2,4-pentanedione surfactant. Intensity has been normalized to allow for comparison. 123

Figure 6.18 (a) Assembled air-free holder purchased from Rigaku (Part #2392B101). (b) Disassembled air-free holder, showing the sample enclosure (1), the venting plug with an O-ring seal (2), and the sample stage (3). 124

Figure 6.19 X-ray diffraction spectra obtained for the as-synthesized iron nanoparticles with 2,4-pentanedione surfactant. The red lines correspond to bcc Fe peak positions (ICSD #01-085-1410). 125

Figure 6.20 High resolution TEM image of a cluster of iron nanoparticles. Scale bar represents 50 nm. (Inset) FFT pattern obtained showing the hexagonal close packing of the nanoparticles. 127

| | |
|--|-----|
| Figure 6.21 High resolution TEM of a single zero-valent iron nanoparticle. Scale bar represents 5 nm. (Inset) Selected area electron diffraction (SAED) of particles shown in transmission electron micrograph. | 128 |
| Figure 6.22 Image showing the radius of the nanoparticle core (r_c) and shell (r_s). | 130 |
| Figure 6.23 Hysteresis curve displaying the low magnetic field range utilized in calculations where susceptibility remains constant. | 132 |
| Figure 6.24 3D color map constructed from theoretical calculations for nanoparticle susceptibility with increasing size and surfactant length (nm). | 134 |
| Figure 6.25 (a) Theoretical calculations for the magnetic susceptibility (χ_e) of zero-valent iron nanoparticles synthesized with surfactants varying in length. The magnetic susceptibility for the “domain formation” regime is plotted linearly at $y = 5$. For any given surfactant, nanoparticle sizes in close proximity to this line can provide an expected range for the maximum nanoparticle size obtainable before agglomeration and precipitation occurs. (b) Calculated susceptibilities for the obtained experimental sizes were 6.05, 7.27, 6.44, and 5.80 for nanoparticle diameters of 6.4, 10.7, 14.5, and 18.6 nm, respectively. | 135 |
| Figure 6.26 (a) Graph of mean particle diameters (nm) vs normalized Fe mmol addition for iron nanoparticles synthesized using 3-octadecyl-2,4-pentanedione, 3-decyl-2,4-pentanedione, 3-butyl-2,4-pentanedione and 2,4-pentanedione as the stabilizing surfactants. The amount of Fe is normalized due to the total Fe amount added (mmol) varying slightly between reactions. Because larger nanoparticles require more precursor, growing the particles to larger sizes required more Fe to be added. (b) Same information | |

in 6.22a, except plot is normalized to the first observed agglomeration event. This plot displays the maximum or near-maximum size obtained for each surfactant..... 137

Figure 6.27 Graph of the mean maximum particle diameter (nm) vs the estimated surfactant length (Å) for iron nanoparticles synthesized using 2,4-pentanedione, 3-butyl-2,4-pentanedione, 3-decyl-2,4-pentanedione and 3-octadecyl-2,4-pentanedione. Particle sizes max out at 6.4, 10.7, 14.5, and 18.6 nm for the 0, 4, 10, and 18 carbon chain, respectively. Here it can be visualized how the maximum particle size varies with respect to increasing steric bulk provided by the surfactant. 138

Figure 6.28 TEM images for as-synthesized nanoparticles from the scale-up reaction using the decylamine surfactant. All scale bars represent 20 nm. 140

Figure 6.29 (a) Histogram produced from size analysis of all visible particles in TEM images. (b) Histogram produced from size analysis of particles in the range of the max size observed. The mean size at which particles agglomerate is around 14.1 nm in diameter. 141

Figure 7.1 Actual amount of iron per aliquot (mg) against the aliquot amount (scale weight, mg) for the 18.4 nm stock. The aliquot amount is the weight of the stock particles with organics such as surfactant and solvent. The actual amount of iron is obtained through annealing followed by assessment performed on a UV-Visible spectrometer. 147

Figure 7.2 Actual amount of iron per aliquot (mg) against the aliquot amount (scale weight, mg) for the 14.6 nm stock. The aliquot amount is the weight of the stock particles with organics such as surfactant and solvent. The actual amount of iron is obtained through annealing followed by assessment performed on a UV-Visible spectrometer. 149

Figure 7.3 Picture of the Parr 300 mL non-stirred pressure vessel (model 4760) used in these reactions. This general-purpose pressure vessel has a maximum temperature of 350°C and a maximum pressure of 3000 psi (200 bar)..... 152

Figure 7.4 General steps performed during the hydrogenation reactions. First, nanoparticles are weighed and combined with solvent, substrate, and a Teflon stir bar in the general-purpose reaction vessel under inert atmosphere. The vessel is pressurized with H₂ gas and set at a given temperature for a known period of time. Post reaction, the particles are then magnetically separated from the solvent and substrate. The solvent and substrate mixture is put on a rotary evaporator for product separation, and the dried product is suspended in deuterated chloroform for ¹H NMR analysis. 154

Figure 7.5 Predicted ¹H NMR spectra for E-stilbene (trans-stilbene) and bibenzyl. Spectra were calculated in ChemDraw using a 90 MHz source and deuterated chloroform (CDCl₃) solvent. For products obtained experimentally, the ratio of the integral peak value for the 7-8 ppm peaks over the normalized 2.8 ppm peak helped to determine the amount of substrate that was successfully hydrogenated..... 157

Figure 7.6 Experimental ¹H NMR spectra for the stock solutions containing various mixtures of trans-stilbene and bibenzyl. The forefront red spectrum is that of pure trans-stilbene (substrate), and as the spectra shift upward, the bibenzyl (product) concentration increases. This model displays ¹H NMR spectra progression as the reaction nears full conversion. 159

Figure 7.7 Plot of the actual bibenzyl amount (mol %) against the integrated peak value of the 7-8 ppm peaks on ¹H NMR. The plot uses the (S+B) integrated peak value for the x-

axis for simplicity. When the integrated peak value is obtained after product analysis, it can simply be plugged into the equation above, producing the degree of conversion. .. 160

Figure 7.8 Compiled experimental data for the hydrogenation of trans-stilbene to bibenzyl for the 18.4 nm particles at 100, 140, 155, and 170°C..... 162

Figure 7.9 Conversion and conversion rates (mol %/hr) at (a) 170°C (b) 155°C (c) 140°C and (d) 100°C for the 18.4 nm particles. The rate is equal to the slope of the line (m) in the linear formula $y = mx + b$. Conversion rates were 24.8, 9.0, 3.2, and 0.2 mol %/hr, respectively. 163

Figure 7.10 (Top) Conversion amount (mol %) for the 155°C reaction using 18.4 nm particles. (Middle) Average reaction temperature as a function of reaction time. (Bottom) Average amount of catalyst (mol %) as a function of reaction time. These plots aided in the better understanding of why catalytic activity was higher or lower than expected. . 166

Figure 7.11 Graphs of the conversion of the substrate (trans-stilbene, mol %) as a function of reaction time. (a) A zeroth order reaction is linear with respect to the substrate concentration versus reaction time. A linear regression to our experimental data produces a coefficient of determination (R^2) value of 0.9878, displaying a strong correlation to zeroth order kinetics with respect to the substrate. (b) A first order plot is linear for the natural log of the concentration as a function of reaction time. This model shows significant deviation from our data with an R^2 of 0.7943. (c) A second order plot is linear for the inverse of the concentration as a function of time. Again, this model shows significant deviation from what would be a linear plot, with an R^2 of 0.7867..... 168

Figure 7.12 Conversion rates (mol/m²s) for temperatures at (a) 170°C (b) 155°C (c) 140°C and (d) 100°C for the 18.4 nm particles. The rate is equal to the slope of the line (m) in the linear formula $y = mx + b$. Conversion rates were 7.8E-07, 2.6E-07, 1.0E-07, and 6.3E-09 mol/m²s, respectively. 170

Figure 7.13 (a) Arrhenius plot displaying the logarithm of the reaction rate constants (ln(k)) against inverse temperature (K⁻¹). Arrhenius plots are used to analyze the effect of temperature on the rates of chemical reactions. From the Arrhenius equation, an activation energy and collision frequency for the 18.4 nm reactions were obtained. (b) Reaction rate constants (mol/m²s) for reactions executed at 100 (373.15K), 140 (413.15K), 155 (428.15K), and 170°C (443.15K). 172

Figure 7.14 Graphs showing the conversion and conversion rates (mol %/hr) at (a) 170°C (b) 155°C and (c) 140°C for the 14.6 nm particles. The rate is equal to the slope of the line (m) in the linear formula $y = mx + b$. Conversion rates were 39.5, 13.2, and 4.9 mol %/hr, respectively. 175

Figure 7.15 Compiled experimental data for the hydrogenation of trans-stilbene to bibenzyl for the 14.6 nm particles at 140, 155, and 170°C. 176

Figure 7.16 Conversion rates (mol/m²s) for temperatures of (a) 170°C (b) 155°C and (c) 140°C for the 14.6 nm particles. The rate is equal to the slope of the line (m) in the linear formula $y = mx + b$. Conversion rates were 8.8E-07, 3.1E-07, and 1.1E-07 mol/m²s, respectively. 177

Figure 7.17 (a) Arrhenius plot displaying the logarithm of the reaction rate constants (ln(k)) against inverse temperature (K⁻¹) for the 14.6 nm reactions. (b) Reaction rate

| | |
|---|-----|
| constants (mol/m ² s) for reactions at 140 (413.15K), 155 (428.15K), and 170°C (443.15K). | 178 |
| Figure 7.18 This figure depicts the quantity of nanoparticles of various sizes needed to achieve an equal mass of iron. All three segments contain the same amount of iron (mass = 5.151E-16 grams). To achieve this mass, one would need (1) 50.0 d.nm particle, (21.4) 18.0 d.nm particles, or (171.4) 9.0 d.nm particles. | 179 |
| Figure 7.19 Conversion (mol %) versus time at 155°C for the 9.2 nm particles. For these experiments, catalyst loading and temperature remained constant..... | 181 |
| Figure 7.20 Conversion (mol %) versus temperature for increasing temperatures using the 9.2 nm particles..... | 182 |
| Figure 7.21 Conversion (mol %) as a function of the catalyst loading amount (mol %, iron to stilbene) for the 9.2 nm particles. | 183 |

List of Tables

| | |
|---|-----|
| Table 3.1 Iron nanoparticle pure or core-shell phases obtained through variation in the solvent used during laser ablation synthesis. Reproduced with permission from Ref ²⁶ ... | 22 |
| Table 5.1 Summary of nanoparticle size analysis obtained from transmission electron micrographs..... | 70 |
| Table 5.2 Summary of nanoparticle size analysis obtained from small angle X-ray scattering (SAXS) for particles synthesized with 3-octadecyl-2,4-pentanedione. | 79 |
| Table 5.3 Summary of reactions performed with increasing the amount of 3-octadecyl-2,4-pentanedione surfactant. | 86 |
| Table 5.4 Summary of properties obtained from the reduction techniques performed. The data listed is at the temperature of 5K. | 92 |
| Table 6.1 Summary of nanoparticle size analysis obtained from transmission electron micrographs for 2,4-pentanedione surfactant. | 107 |
| Table 6.2 Summary of nanoparticle size analysis obtained from transmission electron micrographs for 3-butyl-2,4-pentanedione surfactant..... | 115 |
| Table 6.3 Summary of nanoparticle size analysis obtained from transmission electron micrographs for 3-decyl-2,4-pentanedione surfactant. | 121 |
| Table 6.4 Summary of nanoparticle size analysis obtained from small angle X-ray scattering (SAXS) for particles synthesized with 3-decyl-2,4-pentanedione surfactant. | 123 |
| Table 7.1 A summary of the aliquot amounts (scale weight, mg), actual amount of iron per aliquot (assay, mg), the percent difference between the scale weight and assay, and the | |

| | |
|--|-----|
| percent weight, which is the actual amount of iron over the scale weight for the 18.4 nm stock..... | 148 |
| Table 7.2 A summary of the aliquot amounts (scale weight), actual amount of iron per aliquot (assay, mg), the percent difference between the scale weight and assay, and the percent weight, which is the actual amount of iron over the scale weight for the 14.6 nm stock..... | 150 |
| Table 7.3 Stock solutions containing various mixtures (mol %) of starting material (trans-stilbene) and hydrogenated product (bibenzyl). Ten stocks varying from 100 to 6.25 mol % bibenzyl were formulated. These stocks were analyzed using ^1H NMR..... | 158 |
| Table 7.4 Summary of experimental data for the 18.4 nm hydrogenation reactions. Conversion rates are displayed in mol %/hr. | 164 |
| Table 7.5 Summary of experimental data for the 18.4 nm hydrogenation reactions. Conversion rates are displayed in mol/m ² s..... | 171 |
| Table 7.6 Summary of experimental data for the 14.6 nm hydrogenation reactions. Conversion rates are displayed in mol %/hr. | 175 |
| Table 7.7 Summary of experimental data for the 14.6 nm hydrogenation reactions. Conversion rates are displayed in mol/m ² s..... | 178 |

List of Abbreviations and Acronyms

| | |
|------------------|---|
| SPM | Superparamagnetic |
| NP | Nanoparticle |
| TEM | Transmission Electron Microscopy |
| SQUID | Superconducting Quantum Interference Device |
| MPMS | Magnetic Property Management System |
| XRD | X-ray Diffraction |
| UV-Vis | UV-Visible Spectroscopy |
| NMR | Nuclear Magnetic Resonance |
| SAXS | Small Angle X-ray Scattering |
| DI | Deionized |
| HCl | Hydrochloric Acid |
| 1-ODE | 1-Octadecene |
| OLAm | Oleylamine |
| M_{Sat} | Magnetization Saturation |
| d.nm | Diameter (nm) |
| Acac | 2,4-Pentanedione (Acetylacetonate) |
| 3-Butyl | 3-Butyl-2,4-Pentanedione |
| 3-Decyl | 3-Decyl-2,4-Pentanedione |
| 3-Octadecyl | 3-Octadecyl-2,4-Pentanedione |

Chapter 1. Introduction

Nanotechnology and nanoscale materials have attracted widespread recognition for their highly desirable properties which have the power to revolutionize and simplify various aspects of our everyday lives. These materials possess the potential to address challenges on a global scale, from combating the ever-growing threat of climate change to improving underdeveloped health care systems¹⁻². Nanoscience refers to the study of objects and their accompanying phenomena with dimensions ranging from 1 nanometer (10^{-9} meter) to about 100 nm ($0.1 \mu\text{m}$)³. Materials and objects within this size regime attract intense interest due to the unique properties and behavior they exhibit. Their demonstrable change in optical, electronic, and physical behavior is a product of the surface area to volume ratio which increases with decreasing size⁴⁻⁵. However, as new properties emerge within this transition, they have the potential to vary drastically with the most minute changes in size. Although the fundamental interest in these materials and their properties on this scale is captivating and novel in itself, the miniaturization of our everyday devices for numerous applications has accelerated the need for further development within this area⁶. Each application also possess specific criteria that require the particle's properties be tailored, and systematic control has remained elusive⁷. Most the current synthetic routes are kinetically controlled and performed on a small scale, making scale up an arduous task. Therefore, it is essential to introduce systematic size control into synthetic method which is inherently scalable, allowing for the production of highly magnetic nanoparticles with low-size dispersity. This will address present day challenges by allowing a large volume

of nanoparticles to be manufactured with less property variation and thus a higher efficacy for any given application.

1.1. Research Objectives

The research present in this thesis is dedicated to the development of a reproducible and scalable synthetic method to obtain highly magnetic zero-valent iron nanoparticles with low-size dispersity. We want to achieve this by understanding the synthetic factors that affect nanoparticle size, size distribution, and growth. Identifying and understanding the main factors which govern nanoparticle nucleation, growth, and stabilization will allow us to design an improved system and achieve thermodynamic control in solution-based magnetic nanoparticle synthesis.

When highly magnetic nanoparticles reach a certain size, they agglomerate and precipitate out of solution. Since they display greater magnetic capability at larger sizes, stabilization of these larger particles to prevent agglomeration is critical. Our goal is to improve size control through reversible magnetic agglomeration by varying and optimizing the surfactant used in particle stabilization. Through this work, we plan to design a system with precise control and high reproducibility to minimize the variation of magnetic properties from batch to batch. Implementing fine control over particle size will allow us to ultimately control nanoparticle magnetic properties.

We want to also provide further control over nanoparticle properties through post-synthesis processing and modification techniques. This will allow us to provide a greater understanding of how desired properties can eventually be obtained if they are not acquired

directly through synthetic methods. Through these methods, we will show that these nanoparticles can be employed as inexpensive and effective magnetically recoverable hydrogenation catalysts. Because our previous methods allow us to achieve strict size control in these systems, we aim to provide insight showing how catalytic activity changes as a function of nanoparticle size.

1.2. Outline

In the first main section of this dissertation we address the synthesis and characterization of zero-valent iron nanoparticles through a new and novel mechanism. We then take our proposed mechanism for size control to the next level by modifying components within the system. This includes modification or alteration of temperatures, concentrations, and nanoparticle surfactants. This helps introduce tailorability into our system by providing stricter size control, increased regulation over nanoparticle nucleation and growth, and it should allow a greater understanding of how the system functions as a whole. In the later sections, we introduce post synthesis modification of nanoparticles, which paves an alternative route to fine-tuning the nanoparticle properties that are desired by the user. For instance, higher nanoparticle magnetization can be achieved post-synthesis by undergoing reduction reactions in a hydrogenated atmosphere. We also show that depending on the reduction technique used, we can manipulate other magnetic properties or even alter the surface chemistry, allowing the nanoparticles to become catalytically active. Through the combination of our mechanism and these post processing techniques, we provide a multitude of routes to achieving nanoparticles with desired characteristics for any given application.

1.3. Chapter Summary

An outline of this dissertation and contents is as follows:

Chapter 2 begins with a brief introduction to magnetic nanomaterials and an overview of relevant or important magnetic properties that have a role in this research. This is followed by current synthetic approaches, literature review, and mechanisms of growth and stabilization for zero valent iron nanoparticles. Chapter 3 details the methods utilized for nanoparticle characterization such as DC SQUID magnetometry for magnetic measurements and transmission electron microscopy for size, shape, and phase analysis. This chapter also outlines how synthesized nanoparticles were prepared for each characterization method in detail. Chapter 4 introduces the reversible magnetic agglomeration mechanism as the main focus of this research. This entails the particulars of nanoparticle synthesis, stabilization, and characterization of the nanoparticle products formed. In Chapter 5 we introduce surfactant modification and stabilization as a way to ultimately tailor and control size in our reversible magnetic agglomeration mechanism. This includes characterization of as-synthesized nanoparticles formed with a variety of surfactants, and for some chosen surfactants how concentration manipulations affect the underlying mechanism. Chapter 7 introduces the concept of zero valent iron nanoparticles produced through the reversible magnetic agglomeration mechanism as an inexpensive and effective catalyst for the hydrogenation of alkenes. Because we have methods to develop nanoparticles with strict size control, we use that to our advantage to study the nanoparticle catalytic activity as a function of size.

Chapter 2. Fundamentals

2.1. Magnetic Nanomaterials

Over the past few decades, magnetic materials have attracted the curiosity of researchers and general audiences alike and have proven to be a continuously growing area of study from both a technical and fundamental perspective. Recently, thorough investigation and interest surrounding nano-sized magnetic particles has been increasing tremendously due to their high potential for implementation in applications such as magnetic recording media, site-specific drug delivery, biological detection and catalysis⁸⁻¹⁶. This potential is attributed to the change in magnetic, optical, and electrical properties that arise when transitioning from bulk materials into the nano-regime¹⁷. As mentioned before, these properties can vary significantly with the most minor changes in size within this regime, which means the development of methods which systematically control nanoparticle size with low-size dispersity is of great importance.

2.2. Magnetism Overview

The origin of magnetism is derived from the orbital and spin motions of electrons and their interactions. It is well known that all matter is magnetic, however the strength and type of magnetism that matter possesses varies¹⁸. Generally, determining the type of magnetic behavior in a given material is governed by the strength of interactions of atomic magnetic moments within that material. Materials can be classified into one or more of five major groups depending on their magnetic behavior. Materials that display no collective magnetic interactions and lack magnetic order are considered diamagnetic or paramagnetic. Materials that have collective magnetic interactions and order below a certain temperature

fall into the categories of ferromagnetic, antiferromagnetic, or ferrimagnetic depending on the type of order they possess¹⁹.

2.2.1. Diamagnetism

Diamagnetism is a very weak type of magnetism which is a fundamental property of all atoms. In diamagnetic materials, all of the orbital shells are filled with paired electrons, causing the magnetic fields of the electrons to cancel out, leading to no permanent magnetic moment. With the application of an external magnetic field M , the magnetic moment H of the diamagnetic material displays a weak, negative susceptibility which is slightly repelled by the applied field. When the applied field is removed, these materials do not retain their magnetic properties. Another characteristic behavior of these materials is their temperature independent susceptibility as seen in Figure 2.1²⁰.

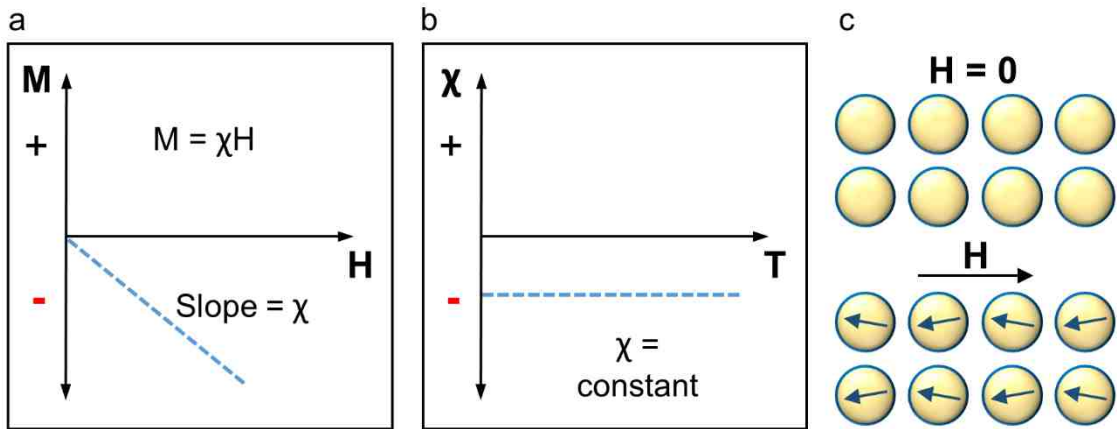


Figure 2.1 (a) Magnetic moment M versus an external applied magnetic field H for a diamagnetic material. (b) Susceptibility versus temperature graph which displays the temperature independent susceptibility observed in diamagnetic materials. (c) Applying an external magnetic field creates an induced magnetic field in the opposite direction.

It is worth noting that we consider atoms to be diamagnetic if they are lacking in a stronger form of magnetism. For example, paramagnetism is orders of magnitude stronger than diamagnetism and if the two are present within the same atom, we only observe the paramagnetism.

2.2.2. Paramagnetism

Paramagnetic materials contain partially filled orbital shells with unpaired electrons, leading to a net magnetic moment present. However, due to the lack of interaction between individual magnetic moments, the magnetization is zero in the absence of an applied field. With the application of an external magnetic field, the magnetic moment of the paramagnetic material exhibits partial alignment of atomic moments in the same direction as the field (Figure 2.2). A net positive magnetization is the result of this alignment, which is directly proportional to the applied field and a net positive susceptibility.

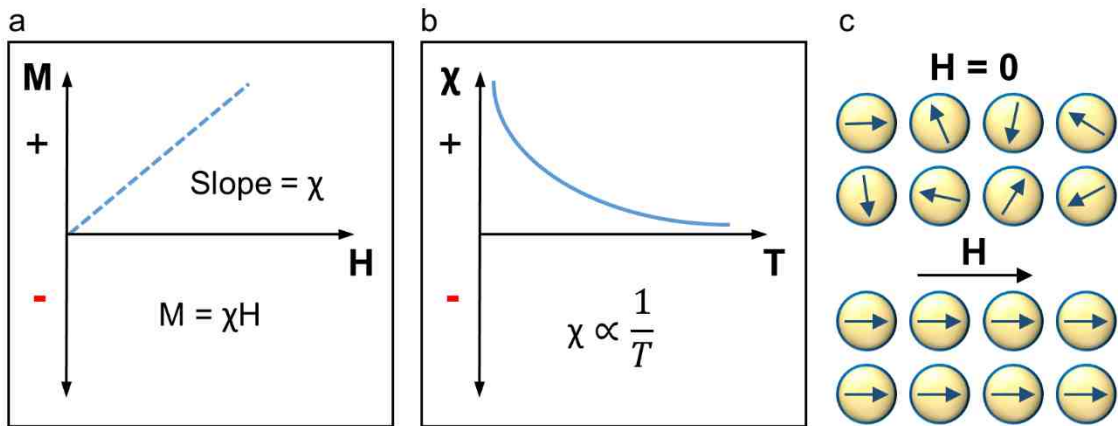


Figure 2.2 (a) Magnetic moment M versus an externally applied magnetic field H for a paramagnetic material. (b) Susceptibility versus temperature graph which displays the temperature

dependent susceptibility known as the Curie Law. (c) In the absence of a field magnetic moments are randomized. When a field is applied, the magnetic moment of a paramagnetic material displays partial alignment in the direction of the field.

However, unlike diamagnetic materials, paramagnetic materials display a temperature dependent susceptibility. This competition between the strength of the applied field and the randomizing effects of temperature can be expressed using Curie's Law (Eq. 2.1).

$$\chi = \frac{C}{T} \quad \mathbf{M} = \chi \mathbf{H} = \frac{C}{T} \mathbf{H} \quad (\text{Eq. 2.1})$$

This law states that the material's susceptibility depends on a material-specific Curie constant C , over the temperature T . When temperature remains constant and low, the magnetization is directly proportional to the applied field. However, because the magnetization is inversely proportional to temperature, at high temperatures magnetization will decrease. Curie's Law applies to low magnetization conditions where it remains linear and becomes inoperable in the case of high-field and low-temperature conditions. It does not account for the magnetization reaching a saturation point at high fields, at which as many magnetic moments as possible have been aligned²¹.

2.2.3. Ferromagnetism

The most common example most people might imagine when thinking about a magnet would be a common household magnet, likely containing iron, cobalt, or nickel. These are all classified as ferromagnetic materials, or materials which have unpaired

electrons and exhibit strong interactions. Electronic exchange forces produce these interactions which result in parallel alignment of atomic moments.

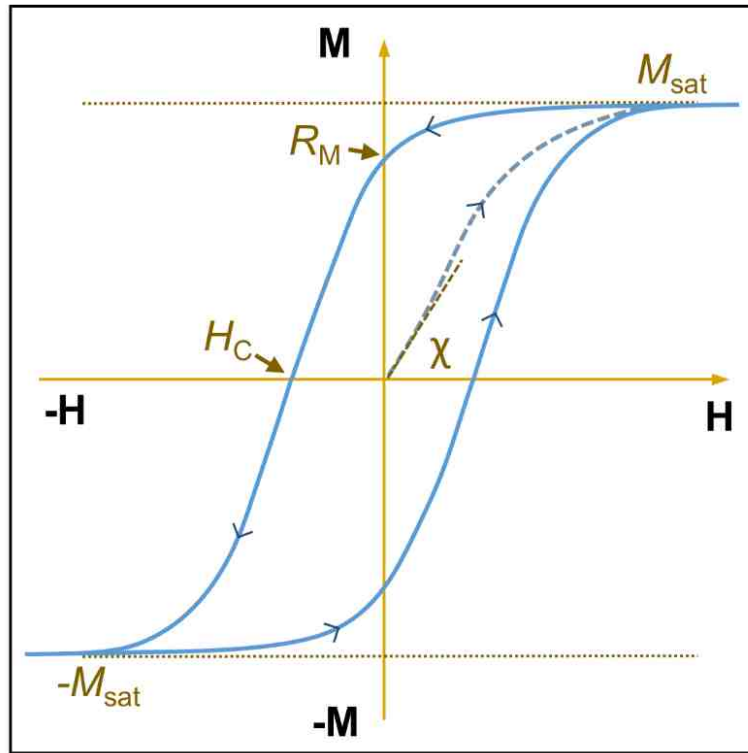


Figure 2.3 Shown above is a common curve called a hysteresis loop. A hysteresis loop is obtained by measuring the magnetic moment of a ferromagnetic material in the presence of a positive and negative externally applied saturating magnetic field (M , $-M$).

A significant amount of information can be learned about the magnetic properties of these materials by examining their hysteresis curves, an example of which is shown above. The most common type of hysteresis curve is a major loop. These are obtained by observing the way a material responds to a positive and negative external magnetic field. When a positive increasing magnetic field is applied to a ferromagnetic sample, the

magnetization of the sample increases with a susceptibility of (χ) until it reaches magnetic saturation M_{sat} . This is where all magnetic moments are aligned and increasing strength of the applied field further prompts no response from the material. When the external field is removed, the amount of residual magnetism that remains in the material is referred to as the remanent magnetization R_M or remanence. The reverse field required to completely remove the residual magnetism in the material back to zero is known as the coercive field H_C . The higher the coercive field, the magnetic sample becomes better at retaining its magnetization when exposed to an external field.

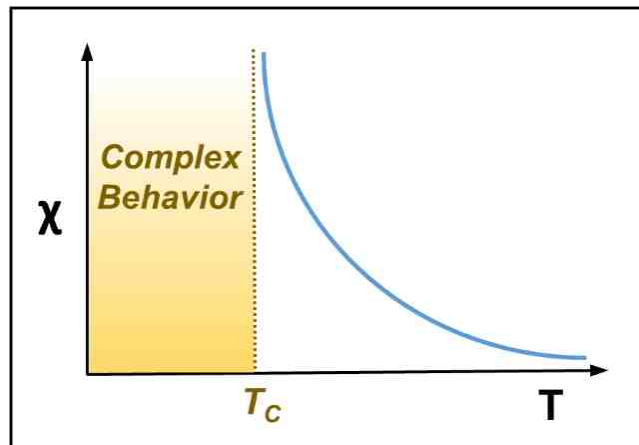


Figure 2.4 Susceptibility versus temperature plot, displaying the temperature dependent susceptibility for a ferromagnetic material.

Similar to paramagnetic materials, ferromagnetic materials also display temperature dependent susceptibility. Below a certain temperature known as the Curie temperature (T_C), ferromagnetism results from atoms which are aligned and parallel. Above T_C these atoms begin to lose their magnetic ordering with increasing thermal energy and the material becomes paramagnetic.

2.2.4. Ferrimagnetism

Ferrimagnetism arises often in ionic compounds such as oxides, where crystal structures can exhibit other complex forms of magnetic ordering. These materials contain two magnetic sublattices, A and B. Interactions within these lattices can lead to an antiparallel alignment of spins between A and B, resulting in unequal magnetic moments and an overall net magnetic moment. It is essentially very similar to ferromagnetism, displaying spontaneous magnetization, Curie temperatures, hysteresis, and remanence, but the main difference being the details of magnetic ordering. A few examples of a ferrimagnetic materials are magnetite (Fe_3O_4), and various metal oxides of cobalt and nickel²².

2.2.5. Antiferromagnetism

Antiferromagnetic materials contain atoms with equal magnetic moments which align in a regular antiparallel fashion, leading to a zero net magnetic moment.

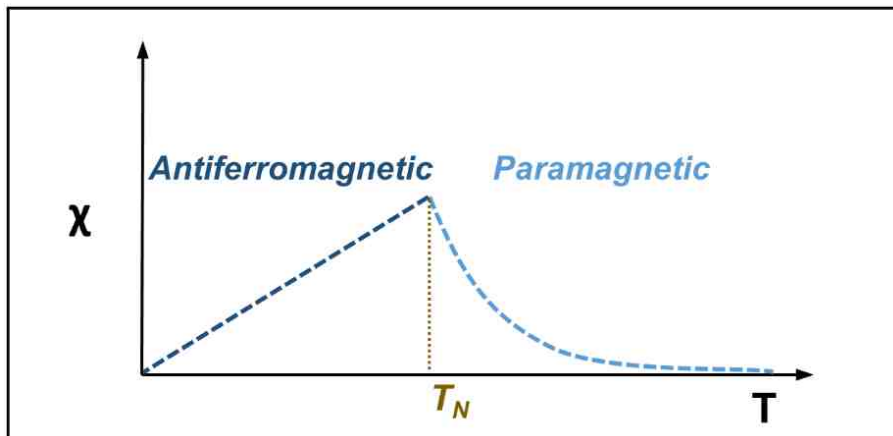


Figure 2.5 Susceptibility versus temperature for an antiferromagnetic material. Below the Néel temperature (T_N), magnetic ordering dominates, resulting in antiferromagnetism. Above T_N , the susceptibility of these materials follow the Curie-Weiss law for paramagnets.

The susceptibility of these materials follows the Curie-Weiss law for paramagnets above the Néel temperature (T_N), which is analogous to the Curie temperature for ferromagnetic materials. Below T_N , magnetic ordering within the material dominates and antiferromagnetism is the result. Above this temperature, thermal energy becomes large enough to overcome magnetic ordering within the material and susceptibility follows the Curie-Weiss law for paramagnets.

2.3. Magnetic Domains and Hysteresis

As mentioned previously, strongly magnetic ferromagnetic materials display hysteresis loops at temperatures below the Curie temperature. In 1907, Pierre Weiss explained this behavior by postulating that these ferromagnetic materials consisted of multiple magnetic domains. These domains illustrated below, are regions of individual magnetic fields of atoms which are grouped together and aligned. The interface which

separates these multiple domains is called the domain wall, which is a transition between the different magnetic moments.

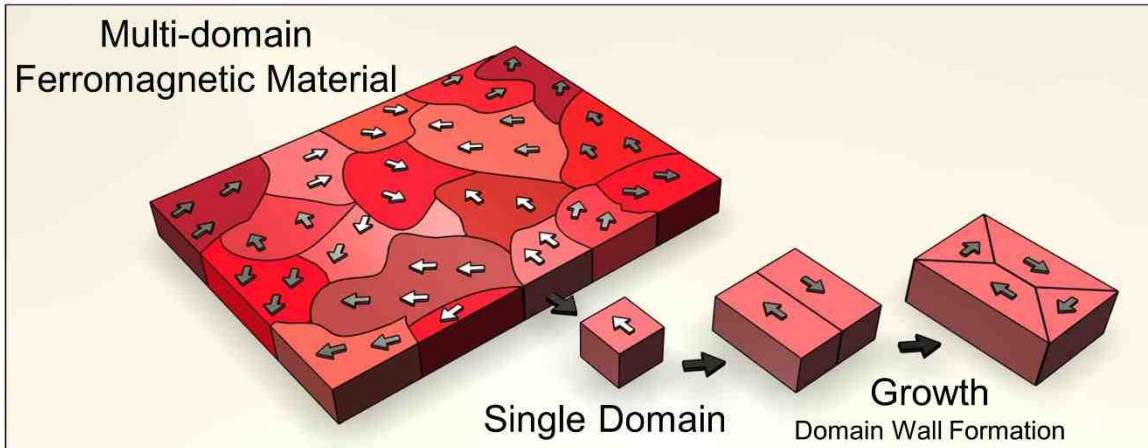


Figure 2.6 (left) The multi-color block shown here represents a ferromagnetic material consisting of multiple domains. If you were to take a small section (uniform in color) out of this multiple domain structure, it would be considered a single domain. As this small piece grows, domain wall formation occurs to lower the overall energy of the system.

To better understand domain walls and their formation, the concept of multiple smaller magnets within a given material is revisited in Figure 2.6 shown above. In this figure, each area or section that is uniform in color represents a separate magnetic domain. If one was to remove a small piece from one of these regions (i.e. smaller than the characteristic domain size), it would be considered a “single domain.” It would be much smaller than the original material, contain uniform magnetization and act as a small permanent magnet. Now imagine this single domain miniature magnet begins to grow in size. As it grows, its magnetostatic energy increases proportionally to the volume of the material and the domain wall energy increases proportionally to the surface area. When the

magnetostatic energy becomes large enough, the material can form two or more domains in order to minimize the overall magnetostatic energy in the system. Therefore, there exists a critical diameter below which it is energetically more favorable for a particle to remain in a single domain state. This occurs when the gain in energy through domain wall formation is less than the energy of the domain walls between domains. For a spherical particle, this critical radius is calculated by

$$R_c \approx \frac{36\sqrt{AK_u}}{\mu_0 M_s^2} \quad (\text{Eq. 2.2})$$

The critical radius R_c of the particle is determined by the exchange constant A , uniaxial anisotropy constant K_u , the constant of permeability μ_0 , and the saturation magnetization M_s . Above this critical radius, domain wall formation is highly favorable. Developing a general understanding of the critical radius size and factors that influence and control it are very important, as it can mean the difference between night and day as far as implementation in a given application.

2.4. Magnetic Nanoparticles and Superparamagnetism

In the previous section, it was mentioned that ferromagnetic particles small enough in size will contain one single domain because the formation of the domain wall is not energetically favorable. These particles tend align parallel to a preferred direction known as an easy axis. This direction is energetically favorable due to the minimization of the particle's magnetic anisotropy energy, or its non-uniform magnetic field. For uniaxial single-domain particles, the activation energy is given by

$$E_a = K_1 V \sin^2(\theta) \quad (\text{Eq. 2.3})$$

Where the magnetic anisotropy energy E_a , is a product of the anisotropy energy density K_1 which is constant for the material, particle volume V ($4/3\pi r^3$ for a spherical particle), and θ which is the angle between the direction of magnetization and the easy axis.

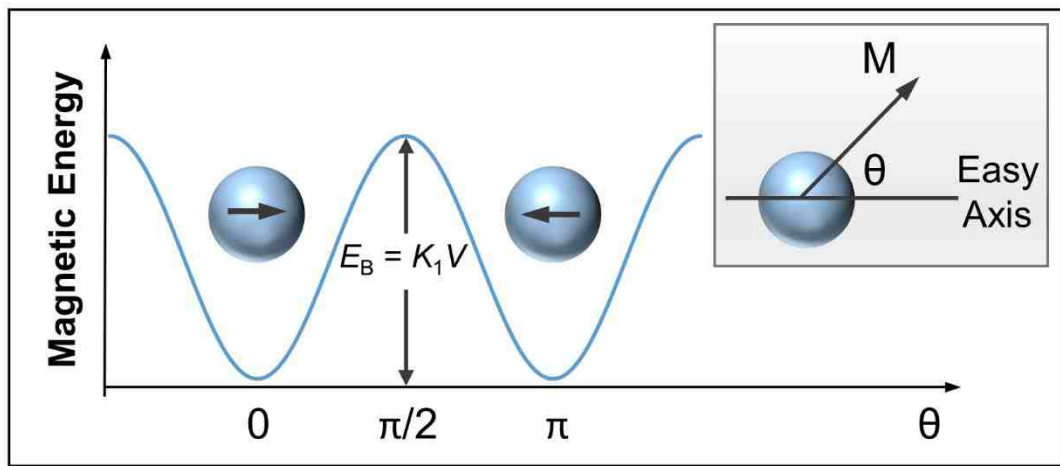


Figure 2.7 This figure shows overall magnetic energy with respect to angle. The “easy axis” is an energetically favorable direction of spontaneous magnetization.

As shown above, the particle fluctuates between parallel and antiparallel and there is an energy barrier it must overcome to do so. This energy barrier which separates the energy minima at $\theta = 0$ and $\theta = \pi$ at is represented by

$$\Delta E = E_B = E_{max} - E_{min} = K_1 V \quad (\text{Eq. 2.4})$$

Néel postulated that if particle size was small enough, the volume would decrease so much that the energy barrier ΔE could be overcome by simple thermal fluctuations. This means that at high temperatures the particle would lose its preferential orientation, leading to random fluctuations between the energetically favorable orientations. This magnetic behavior which arises in very small single-domain particles is known as *superparamagnetism*.

The mean time it takes to flip between these two energetically favorable orientations is known as the Néel relaxation time and is given by the Néel-Arrhenius equation

$$\tau_N = \tau_0 \exp\left(\frac{K_1 V}{k_B T}\right) \quad (\text{Eq. 2.5})$$

Where $K_1 V$ is the energy barrier, k_B is the Boltzmann constant, T is the temperature and τ_0 is the measurement time also known as the attempt frequency (usually between 10^{-9} and 10^{-10} seconds).

2.4.1. Blocking Temperature

When analyzing magnetic and relaxation behavior in these systems, the timescale of the measurement which is known as τ_m , plays an important role. If the measurement time, $\tau_m > \tau_N$, the magnetization will flip several times in the time it takes to collect the measurement, the average magnetization goes to zero and superparamagnetic behavior is

observed. If $\tau_m < \tau_N$, the magnetization will not flip in the time it takes for the measurement and the nanoparticle will appear to be in a frozen or “blocked” state.

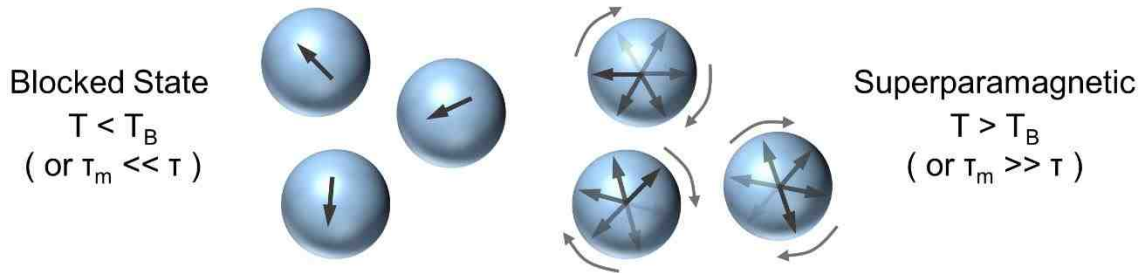


Figure 2.8 The status of a nanoparticle either being in the blocked or superparamagnetic state depends on the operational temperature of the system and the blocking temperature of the nanoparticles.

The exact transition between blocked and superparamagnetic behavior occurs at a temperature where $\tau_m \approx \tau_N$. This is also known as the *blocking temperature* T_B .

To get around this dependence of magnetic behavior with respect to measurement time, the measurement time can be kept constant. Keeping the measurement time constant allows us to manipulate other variables, allowing the transition between superparamagnetism and the blocked state to be observed as a function of temperature. Rearranging the Néel-Arrhenius equation for temperature gives

$$T_B = \frac{K_1 V}{\ln\left(\frac{\tau_m}{\tau_0}\right) k_B} \quad (\text{Eq. 2.6})$$

Also, due to typical laboratory measurements of $\ln(\tau_m/\tau_0)$ being roughly equivalent to 25, this equation can be simplified to

$$T_B = \frac{K_1 V}{25k_B} \quad (\text{Eq. 2.7})$$

This equation holds true for a system with non-interacting particles which are nearly monodisperse and have similar anisotropy values. Any type of volume variance, being an exponential dependence, leads to a much larger distribution of blocking temperatures. That is why it is essential to develop methods with strict size control to minimize fluctuation in blocking temperatures, which in turn leads to minimizing variation and uncertainty within a system.

Chapter 3. Iron Nanoparticle Synthetic Approaches and Literature Review

Over the past few decades there have been numerous studies detailing the synthesis of magnetic iron nanoparticles with a variety of phases and compositions. Iron oxides such as Fe_3O_4 and $\gamma\text{-Fe}_2\text{O}_3$ have recently been attractive for biomedical applications where using zero-valent iron is not practical. Also, compositions involving Fe with Co or Pt have gained attention for their potential to achieve very high saturation magnetizations and systematically vary nanoparticle properties. Because nanoparticle properties tend to vary greatly with small changes in size, the majority of these studies focus on developing synthetic routes that produce stable, shape-controlled nanoparticles with low-size dispersity.

Synthetic methods involve both top-down and bottom-up approaches. To better visualize each approach and how they are used to produce nanoparticles either constructively or destructively, see the figure below.

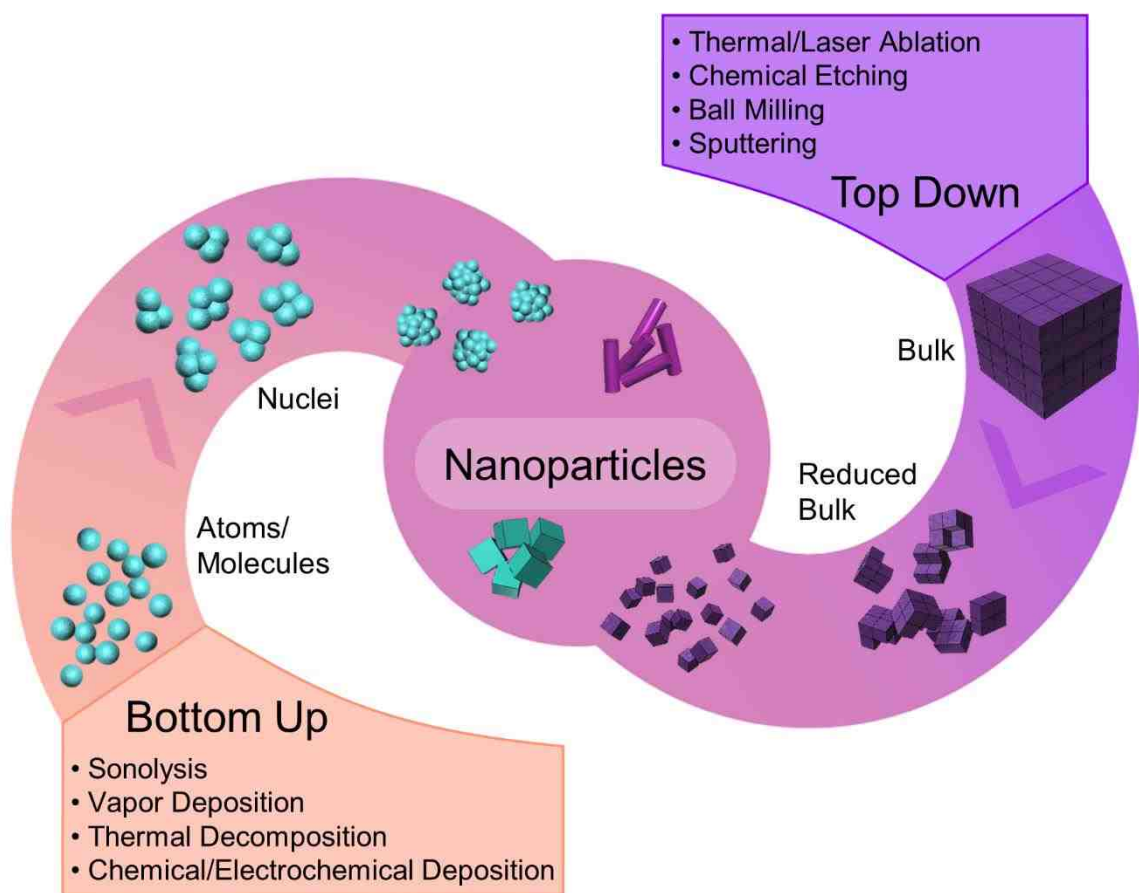


Figure 3.1 Synthetic approaches to iron nanoparticle synthesis. Bottom up techniques synthesize nanoparticles from atomic or molecular species. Top down approaches achieve nanoparticles by breaking bulk materials into smaller pieces using mechanical, chemical, or other forms of energy.

To best describe these approaches fundamentally one can use the example of Lego® toy building bricks. In the bottom-up approach, each Lego piece represents an iron atom. By taking your individual Lego pieces or “atoms” and assembling them to build a larger structure such as a sphere or cube, you are utilizing a bottom-up approach. In chemistry, this can be described as the assembly of atomic or molecular components for the development of nano devices or particles. For the top-down approach, the larger sphere

or cube you just constructed is now defined as a bulk material, such as an iron magnet. If you take a hammer and hit the Lego sphere or cube, the individual Lego pieces begin to break off. After enough time, one is left with many individual pieces. In this case, the pieces now represent a nanoparticle. By destructively creating individual pieces or “nanoparticles” from a much larger Lego structure or “bulk iron magnet”, one can utilize the top-down approach. In chemistry, this can be described as a slicing or cutting of bulk material to get nano-sized particles.

Synthetic methods used to achieve this destruction of a bulk material to form nanoparticles are chemical etching, ball milling, laser ablation and sputtering²³⁻²⁷. Conversely, methods used to achieve a bottom-up approach include spray pyrolysis, thermal decomposition, vapor deposition, and chemical or electrochemical deposition²⁸⁻³². Although the top-down method has its advantages, the majority of researchers utilize the bottom-up approach given that currently the number of advantages outweigh the disadvantages. While the major advantage for the top down method is scalability, its disadvantages include producing particles with high size dispersity, low surface area, and lack of crystalline control³³. On the other hand, the bottom up method has a more commendable reputation for producing nanostructures with less defects, a chemical composition that involves a higher degree of homogeneity, and better short- and long-range ordering³⁴.

3.1. Top Down Approaches to Nanoparticle Synthesis

3.1.1. Laser Techniques

Laser assisted techniques have been utilized by researchers to produce amorphous iron and iron carbide nanoparticles. Amendola *et al.* studied the ablation of bulk materials in a liquid solution by a focused laser pulse²⁶. This method can be considered low-cost and “green” because it does not require expensive chemicals nor does it produce pollutant waste as in wet chemistry methods³⁵. This group shows that iron, iron carbide, and iron oxide nanoparticles can be synthesized, and that by varying the solvent, the nanoparticle phase obtained can be controlled. A summary of the iron nanoparticle phases obtained through solvent variation is shown in Table 3.1.

Table 3.1 Iron nanoparticle pure or core-shell phases obtained through variation in the solvent used during laser ablation synthesis. Reproduced with permission from Ref²⁶.

| Solvent | Bare | Core@Shell |
|--------------------------|----------------|--------------------|
| Tetrahydrofuran (THF) | | metal@oxide |
| Acetonitrile (AN) | oxide | |
| Dimethylfuran (DMF) | oxide | |
| Dimethylsulfoxide (DMSO) | metal | |
| Toluene (TOL) | | amorphous@graphite |
| Ethanol (EtOH) | carbide, oxide | |

Size control with this method can still be considered a challenging task. The only solvent which could produce particles with sizes under 15 nm with a narrower size distribution was DMSO. Figure 3.2 details all of the solvents implemented and their respective products.

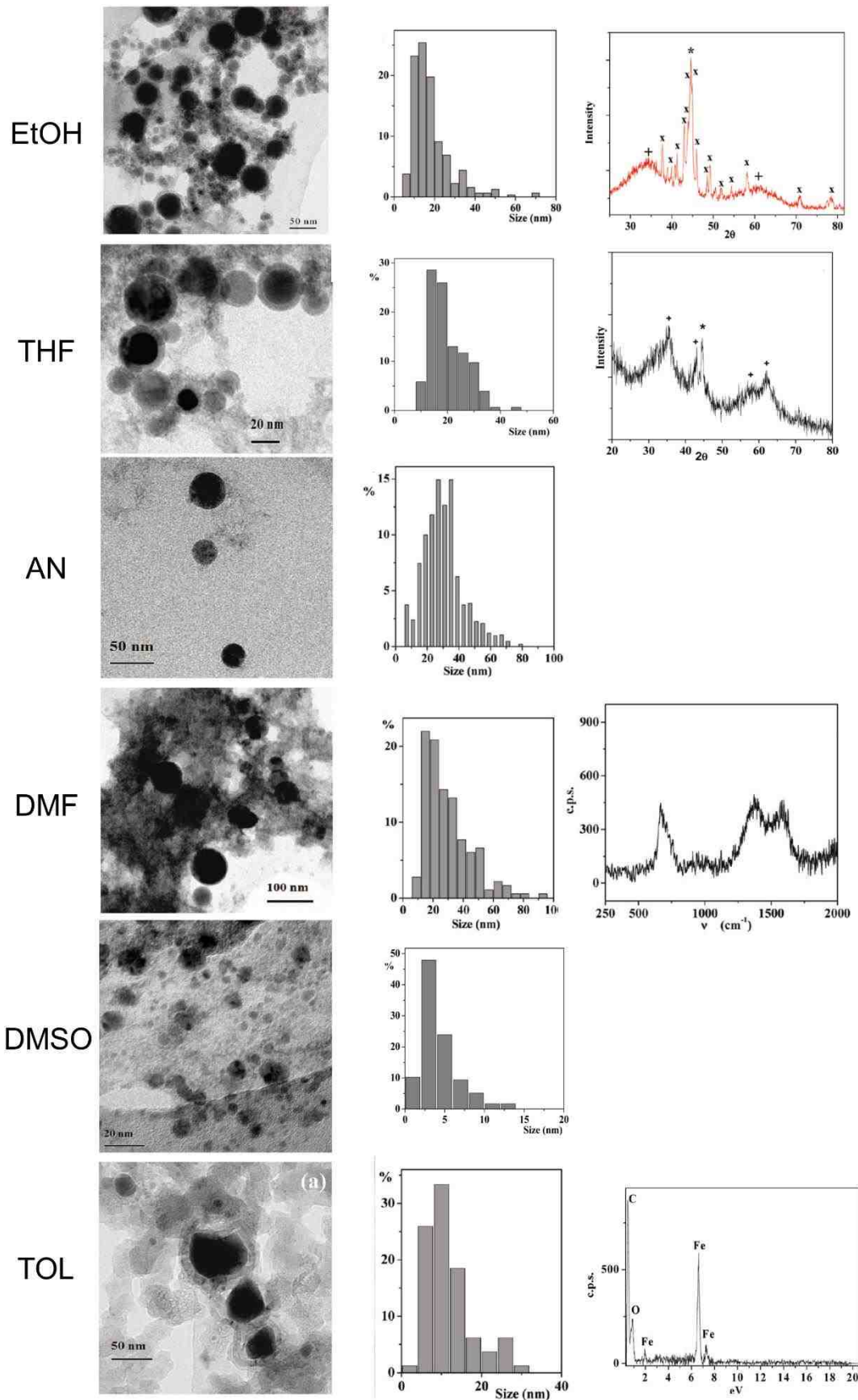


Figure 3.2 Nanoparticles synthesized with various solvents using laser ablation techniques. **(Top to bottom)** The solvents implemented were ethanol (EtOH), tetrahydrofuran (THF), acetonitrile (AN), dimethylformamide (DMF), dimethylsulfoxide (DMSO) and toluene (TOL). **(Left to right)** TEM micrographs obtained, histograms displaying size distribution, and X-ray diffraction data for some samples. Reproduced with permission from Ref²⁶.

Using DMSO as solvent could be further researched for applications which need superparamagnetic zero-valent iron nanoparticles. It can be noted that mostly all other solvents produced particles with a wide range of sizes (5-80 nm). Furthermore, the magnetic properties of these materials are yet to be known as magnetization was tested by observing their physical attraction to a neodymium magnet. There remains a substantial amount of room for improvement and optimization to achieve using this synthetic method, yet this research provided excellent insight to solvent contribution to nanoparticle formation.

Wang *et al.* have also synthesized iron nanoparticles by ablation of a 0.5 mm diameter iron wire with a laser source at low pressures²⁷. Nanoparticle sizes ranged from 1-3 nm and consisted of an iron core with γ -Fe₂O₃ shell. Crystallization of the iron nanoparticles through annealing and an increased particle size confirmed their amorphous nature.

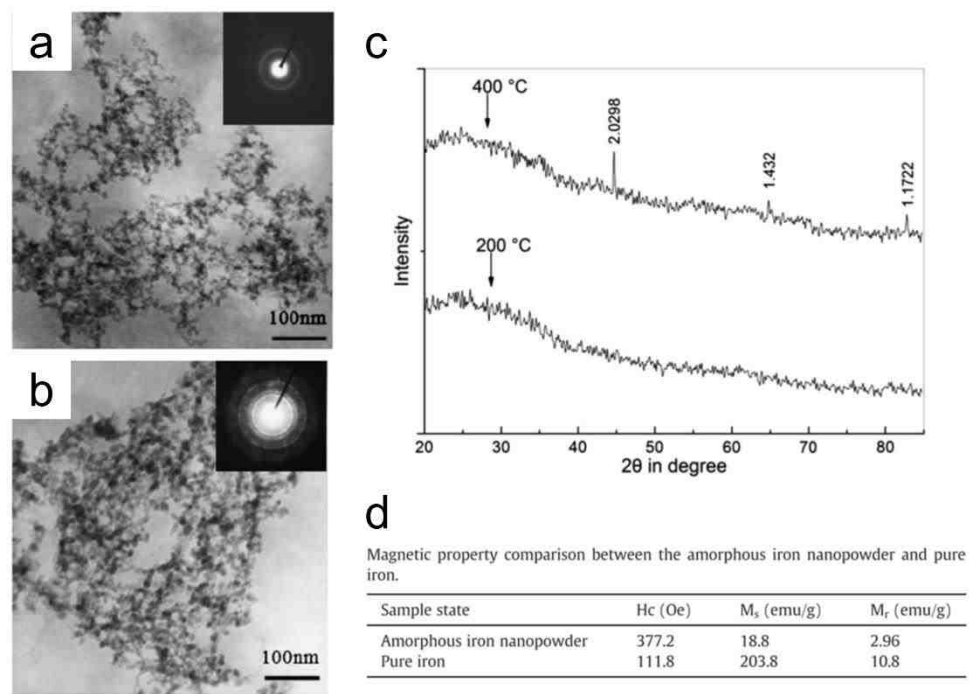


Figure 3.3 (a,b) TEM images and their corresponding electron diffraction patterns of the amorphous Fe nanoparticles annealed at (a) 200°C and (b) 400°C. (c) XRD patterns of the amorphous Fe nanoparticles annealed at temperatures of 200 and 400°C. (d) Magnetic property comparison between the amorphous iron nanopowder and pure iron. Reproduced with permission from Ref²⁷.

Control over nanoparticle properties still remained a challenging task, as coercivity remained somewhat high at 377 Oe (30,000 A/m) and the saturation magnetization of the iron nanoparticles was 18.8 emu/g (18.8 Am²/kg), which is just ~8.5% of the value for bulk iron.

3.2. Bottom-Up Approaches to Nanoparticle Synthesis

3.2.1. Introduction

Early methods of producing iron nanoparticles in the 1940s and 1950s were through a mercury-based synthesis³⁶. The work by Luborsky involved iron particle formation through electrodeposition in mercury, and the particles could be utilized in further kinetic studies³⁷. These early methods were used to produce particles which were confirmed to be single-domain. Yet over time these methods were slowly replaced by organic solvent-based syntheses and other techniques, due to the rising concerns of mercury toxicity. This section outlines the more conventional techniques which are commonplace today.

3.2.2. Reduction of Iron Salts

Possibly the most common bottom up approach in literature for the formation of zero-valent iron nanoparticles is through the chemical reduction of iron salts³⁸. This is the main synthetic route to producing large scale zero-valent iron nanoparticles used to remove contaminants such as arsenic, heavy metals, and even uranium from groundwater³⁹⁻⁴⁰. For the majority of these syntheses, ferrous (Fe(II)) or ferric (Fe(III)) salts are reduced with sodium borohydride; however, hydrazine or lithium borohydride have also been proven to be effective reducing agents⁴¹⁻⁴².



An advantage of this method is its simplicity. The process can be performed in air, contain inexpensive and simple chemical reagents, and progress at relatively low temperatures. However, it is also known for producing particles with large size dispersities. Sun *et al.* utilizes this method which produces nanoparticles ranging from 25 nm to 300+ nm in size, which covers a large range of magnetic properties⁴³. TEM micrographs and respective size analysis for these samples are shown in Figure 3.4 below; the micrographs display their tendency to form large aggregates.

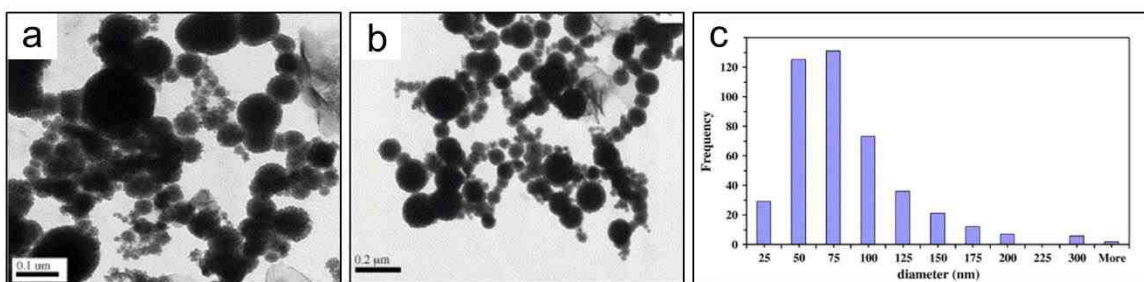


Figure 3.4 (a) and (b) TEM micrographs of aggregates of iron particles. Nanoparticles formed through the reduction of iron salts with sodium borohydride. (c) Particle size distribution (PSD) of nanoparticle product. Median diameter is located at 60.2 nm. Reproduced with permission from Ref⁴³.

Sun and coworkers further refined this method by implementing a polyvinyl alcohol-co-vinyl acetate co-itaconic acid (PV3A) dispersant which can reduce particle size while retaining surface activity. However, because this method uses water as the solvent, nanoparticles tend to form oxide layers or iron hydroxides⁴⁴. Although the formation of zero-valent iron can occur in the presence of water, even iron in oxygen-free water will oxidize over time. Depending on the oxide formed, these layers could end up acting as

magnetically dead layers which will decrease the overall magnetization of the nanoparticle⁴⁵. Even if strict size control using this method could be implemented to produce nanoparticle sizes ranging from 2-20 nm, an oxide shell of 1-2 nm present due to the solvent would have a much larger impact on magnetic properties due to their very high surface area to volume ratio. While this method presents a cheap and effective route for scalable synthesis of zero-valent iron nanoparticles, those who seek to display effective control over small nanoparticle sizes while retaining desired magnetic properties might search further for alternative synthetic routes.

3.2.3. Reduction of Iron Oxides

An alternative method for the formation of zero-valent iron nanoparticles is through the reduction of iron oxide particles with reducing gases such as hydrogen⁴⁶. Through this method, particles that have low size dispersity are annealed in a hydrogen gas, reducing the iron oxide such as goethite or hematite to zero-valent iron. Although one advantage of this method is that it provides robust control over crystalline phases formed compared to sodium borohydride reductions, it was also noted that this reduction technique leads to more angular-shaped particles with strong surface faceting⁴⁷⁻⁴⁸. They also tend to form linear or fractal aggregates due to chemical and magnetic interaction⁴⁹⁻⁵⁰.

Another approach involves the precipitation, dehydration, and reduction of iron hydroxide needles (hematite, α -Fe₂O₃)⁴⁶. The evolution of iron oxide phases was studied in detail during the high temperature reduction by coating the hematite needles with alumina, preventing particle coalescence⁵¹. During hydrogen reduction, particles passed through magnetite (Fe₃O₄) and wüstite (FeO) before reaching a final zero-valent iron phase.

Post reduction, particles were passivated with an ethanol vapor gas. This was essential for preventing rapid oxidation which would cause harm to their magnetic properties. The magnetization saturation slightly suffered from the alumina and iron oxide coating, producing M_{Sat} values of 165 Am²/kg. Even though a main advantage to this method is its scalability for industrial purposes, it remains a very complicated process that would require a great deal of effort for improvement and optimization.

3.2.4. Sonochemical Decomposition (Sonolysis)

Sonochemical synthesis is based upon acoustic cavitation, where the formation, growth, and collapse of bubbles in a liquid lead to nucleation and particle growth. Organometallic complexes within these bubbles decompose when they collapse and create local short-lived hot spots with temperatures up to ~5000K⁵². Suslick *et al.* was one of the first to utilize this method by sonochemically decomposing iron carbonyl in decane to produce nanoscopic amorphous iron powders⁵³. Following this initial work, he performed ultrasonic irradiation of iron carbonyl in octanol with polyvinylpyrrolidone (PVP) and octadec-9-ene-1-carboxylic acid (oleic acid) as surfactant to form superparamagnetic iron nanoparticles⁵⁴.

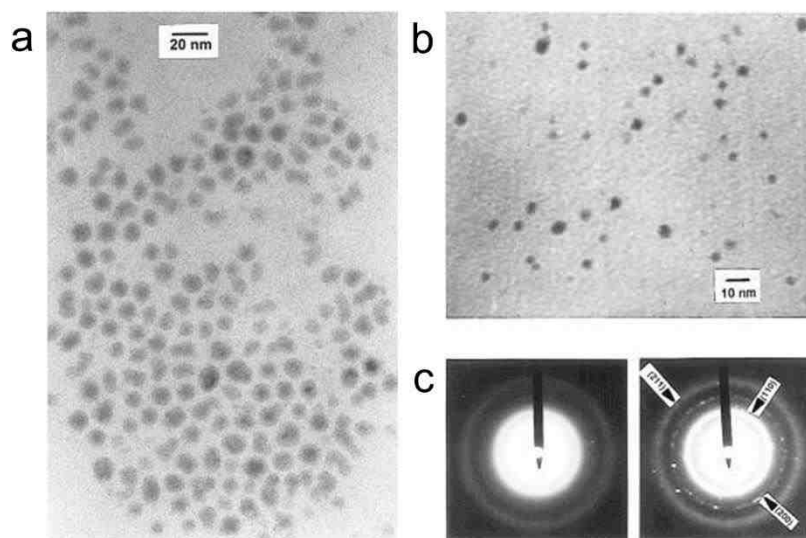


Figure 3.5 (a) TEM showing amorphous iron nanoparticles stabilized by oleic acid as surfactant, produced through the sonochemical decomposition of iron carbonyl. Scale bar represents 20 nm. (b) TEM showing as-synthesized amorphous iron nanoparticles stabilized by PVP. (c) Electron diffraction pattern of the as-synthesized iron nanoparticles showing its amorphous nature (left), and heating from the beam induces crystallization in situ (right), forming a weak FeO phase. Reproduced with permission from Ref⁵⁴.

Particles obtained from this method range from 3-8 nm (Figure 3.5). Shape control with this method is seemingly difficult, most likely due to particle aggregation and coalescence. Particles produced by this method reached saturation magnetizations of 101 Am²/kg, roughly 45% of the saturation magnetization of bulk iron. Despite the presented complications of difficult shape control and low saturation magnetization, an enormous advantage of this method is that it allows particles to be synthesized with or without stabilizing surfactants. This opened the possibility to develop a fundamental understanding

of how stabilizing surfactants interact with and alter the properties of the as-synthesized magnetic particles which is detailed later in this chapter.

3.2.5. Thermal Decomposition

3.2.5.1. Introduction

Thermal decomposition is the chemical decomposition of an organometallic compound driven by heat. Common compounds for forming iron nanoparticles through this method include iron pentacarbonyl ($\text{Fe}(\text{CO})_5$), triiron dodecacarbonyl ($\text{Fe}_3(\text{CO})_{12}$), and ferrocene (*bis*(cyclopentadienyl)iron, $(\text{C}_5\text{H}_5)_2\text{Fe}$)⁵⁵⁻⁶⁰. One of the most commonly used precursors out of these compounds is iron pentacarbonyl. This is due to it being extremely cost efficient, commercially available and highly pure, and its willingness to dissociate⁶¹. Since very little energy is needed for iron pentacarbonyl to decompose, it is an excellent precursor for thermal decomposition synthesis. The real obstacle lies in its decomposition pathway. The decomposition kinetics are very complicated, as it is shown below that reaction rates and even order can change over time^{59, 62}.

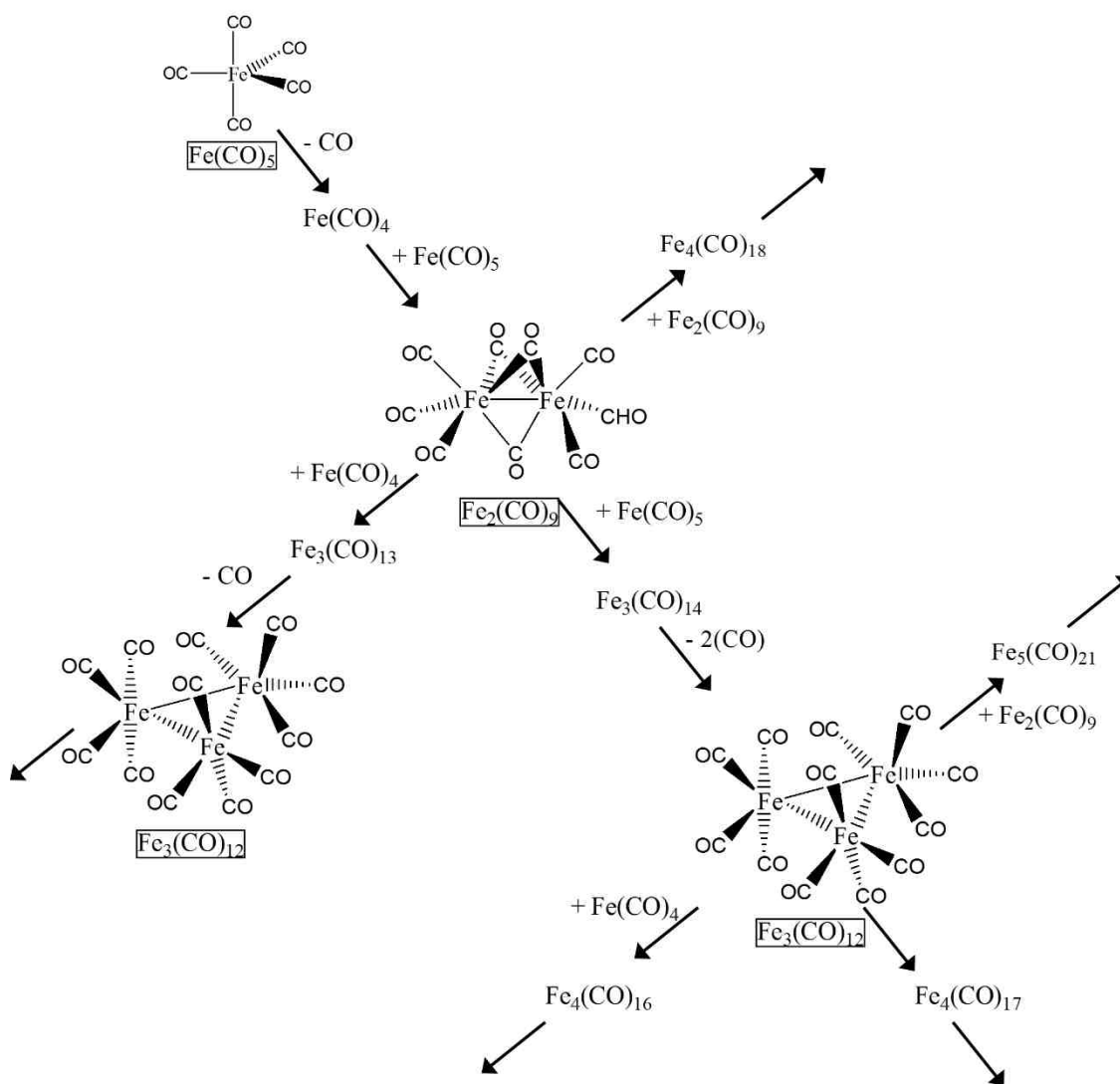


Figure 3.6 Pathways showing the early stages of decomposition for iron pentacarbonyl. This is an exceptional visual representation which displays the complexity involved in decomposition, and why reaction kinetics are difficult to control. Structures shown are drawn for well-known, metastable, isolable compounds. Reproduced with permission from Ref³.

The difficulty is increased with these reactions, as it complicates size and shape control significantly. Nevertheless, it is still a widely-used precursor due to its ease of use and lack of byproducts. Also, the one main by-product, carbon monoxide (CO), has proven to be advantageous for the formation of zero-valent iron nanoparticles. Mørup and van Wonterghem *et al.* demonstrated that it can provide a reducing atmosphere, lowering the opportunities for iron oxidation. They proved this by showing the reduction of an intermediate iron complex formed in their reaction containing Fe^{2+} was being caused by CO molecules⁶³. Overall, the advantages with this method overcome the complications presented. If reaction kinetics are controlled/avoided and a scale-up technique is implemented, this system becomes extremely effective for the industrial production of highly magnetic zero-valent iron nanoparticles.

3.2.5.2. Literature Review

Early work surrounding iron pentacarbonyl decomposition began with Smith and Wychick, who performed this research for Xerox Corporation in the 1970s^{59, 64}. They decomposed iron pentacarbonyl at 140-160°C with the aid of polymer surfactants in a decalin solvent to form nanoparticles with sizes ranging from 6-20 nm. Yields were normally in the range of 50% and saturation magnetizations ranged from 82 Am^2/kg for 8 nm particles to 172 Am^2/kg for similarly sized particles, depending on the polymer surfactant used.

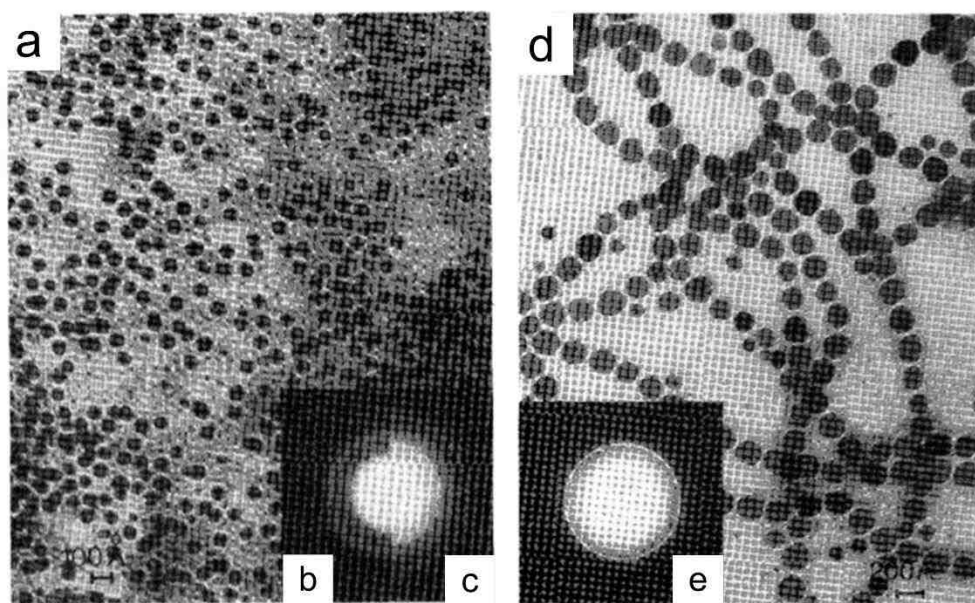


Figure 3.7 (a) Dispersion of ~6 nm particles prepared in poly(4-vinylpyridine-styrene)/dichlorobenzene. Diffraction patterns below of the (b) as prepared particles and (c) after standing for 1 year. (d) Dispersion of ~16 nm particles prepared in poly(4-vinylpyridine-styrene)/dichlorobenzene which spontaneously form magnetic chains and (e) the diffraction pattern inset. Reproduced with permission from Ref⁶⁴.

An exceptional result from this research was that particles formed chains spontaneously when prepared for TEM analysis, a feat which requires very delicate balance between magnetic forces and particle size. It also provided fundamental insight into surfactant interactions and their impact on iron nanoparticle properties, which is discussed in detail in the following section.

Herman *et al.* went a separate route of synthesizing nanoparticles through decomposition of an alternative organometallic iron compound similar to ferrocene, *bis*(η^5 -1,3,5-*exo*-6-tetramethylcyclohexadienyl) iron(II), $[\text{Fe}(\eta^5\text{-C}_6\text{H}_3\text{Me}_4)_2]$ ⁶⁵. The iron precursor

is decomposed thermally through an instant hot injection method at 300°C in 1-octadecene with an oleylamine (OLAm) surfactant. The particles were cooled, cleaned, and dimercaptosuccinic acid (DMSA) was exchanged with OLAm to render the particles water soluble. Although a water stable particle was their goal, this exchange lead to an oxide layer present at the surface which reduced magnetic interactions and resulted in a saturation magnetization of 148 Am²/kg. This method also displays a slight lack of shape control, possibly due to the iron precursor decomposition. The iron precursor used is not available commercially and must be custom synthesized, which also complicates industrial scale-up syntheses. Nevertheless, this work displays a promising pathway for future research to study the decomposition of iron sandwich compounds as an alternative to iron pentacarbonyl.

Another method utilized a platinum catalyst core to seed iron nanoparticles in the presence of small molecule surfactants in a dioctyl-ether solvent⁶⁶. This was modeled after a reaction used for the synthesis of iron-platinum alloy particles⁸. Particles produced by this method possess magnetic properties that are equivalent to and in a few cases better than what is achieved with polymeric surfactants. The platinum cores are formed *in situ* which then catalyze iron pentacarbonyl decomposition with the presence of a small molecule surfactant (oleic acid and oleylamine) at 287°C. After this first stage, a subsequent addition of iron precursor is added along with lower heating at 260°C. Synthesized particles ranged from 7 to 9 nm and produced saturation magnetizations of 175 and 200 Am²/kg, respectively. However, the presence of a 0.5 nm oxide layer was noted by the author. The most likely sources of oxidation are impurities in the reagents or

incorporation through decomposition of the intermediate iron-oleate precursor which forms. Another cause could be the possible liberation of water from heating up an amide which is known to form during room temperature between oleic acid and oleylamine³.

Iron pentacarbonyl decomposition can occur in the absence of a catalyst, as shown in recent work performed at Sandia National Laboratories⁶⁷. This simple technique involves only three species; iron pentacarbonyl, solvent, and a single surfactant. The goal of the Sandia work was to have particles that are coated and stable but have minimal surfactant interaction, thus maximizing magnetic interactions between particles and achieving as little deterioration as possible to the system's magnetic properties. Highly magnetic nanoparticles were obtained by creating very little steric bulk using 2,4-pentanedione as surfactant.

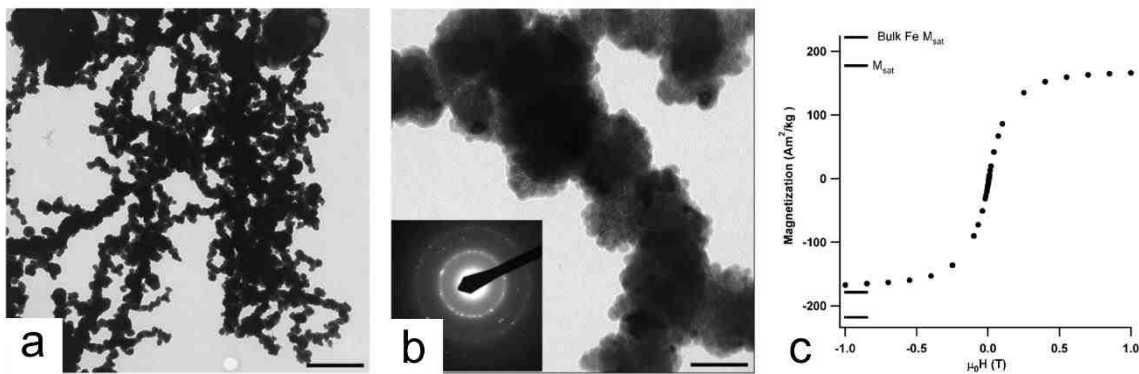


Figure 3.8 (a) TEM micrographs of iron nanoparticles at low magnification, showing their formation of chain-like aggregates form in the absence of an external applied field. The scale bar represents 600 nm. (b) Higher magnification images show that these aggregates are made up of individual nanoparticles in the range of 6 nm in diameter. The scale bar represents 60 nm. Inset diffraction pattern verifies that this sample is pure bcc Fe with diffraction rings at 0.8, 0.9, 2.0, 1.2,

1.4 and 2.0 Å. (c) Magnetization vs field for the same nanoparticle sample at 150K. The sample is below the blocking temperature and therefore shows a weak, but detectible coercivity (5.6 mT). Saturation magnetization is determined by extrapolating to infinite field, and is 178 Am²/kg. Reproduced with permission from Ref⁶⁷.

The nanoparticles formed were 6 nm in size, which magnetically agglomerated readily in solution. These agglomerates could be disrupted temporarily through aggressive mixing, redispersing for about a minute before crashing out of solution. Saturation magnetizations for this size reach as high as 178 Am²/kg. When this surfactant underwent further studies by Monson *et al.*, saturation magnetizations improved to 209 Am²/kg, greater than 90% of the value of bulk iron⁶⁸. Also, size control using this technique is extremely convenient which is achieved by modifying the surfactant to iron precursor mole ratio.

3.3. Surfactant Stabilization and Passivation

3.3.1. Introduction

Two key issues dominate the magnetic properties of nanoparticles - finite-size effects and surface effects. Therefore, understanding the fundamental interactions that lead to intrinsic particle stability and surface passivation of highly reactive particles on the nanoscale is of great importance. Because a correlation between the surfactant-particle interaction and saturation magnetizations has been established, choosing the correct surfactant for a particular system is an important undertaking. Owing to iron's highly reactive surface, a majority of syntheses produce iron with an outer oxide or magnetically dead layer. This proves that surface passivation remains a challenging task, particularly on

the nanoscale. Developing an understanding of this relationship between the iron surface and stabilizing surfactants is imperative for interpreting their magnetic behaviors and future selection of surfactants.

Due to the greater reactivity of zero-valent iron nanoparticles compared to that of their oxide constituents, surface stabilization is known to be more difficult and even more critical. An ideal surfactant would protect the iron nanoparticle surface from oxidation and agglomeration while retaining all desired magnetic properties mentioned. A weakly binding surfactant will not fully stabilize the surface and can lead to oxidation or magnetic agglomeration; whereas a strongly binding surfactant can lead to decreased magnetization saturations and/or more disperse particle sizes. Therefore, the production of ideal and high quality zero-valent iron nanoparticles begins with choosing the correct surfactant.

3.3.2. Literature Review

As mentioned in the previous section, Smith and Wychick studied polymeric surfactant effects on their nanoparticle properties. They implemented a polybutadiene homopolymer, butadiene-styrene copolymer, and styrene-4-vinylpyridine copolymer, which produced saturation magnetization values of 172, 125, and 82 Am²/kg, respectively. This work was fundamental because it showed that as polarity of the surfactant increased, a decrease in overall particle magnetization was observed.

Gedanken *et al.* also provided an extremely useful fundamental understanding of nanoparticle-ligand interactions by reporting how particle magnetization changes as a function of increasing ligand reactivity. This was shown by taking a nanoparticle sample

with known properties, dividing it into aliquots, and functionalizing those aliquots with numerous surfactants to determine their effect on the sample's magnetic properties. The surfactants used included a variety of alcohols and acids with a fairly broad range in reactivity. Decreasing in reactivity, a phosphonic acid, sulfonic acid, carboxylic acid, and an alcohol produced M_{sat} values of 5, 10, 55, and 85 Am²/kg, respectively⁶⁹⁻⁷⁰. One can conclude from this research that to maintain high saturation magnetizations, a weakly reactive but still coordinative ligand must be used for surface passivation.

Through previous research it can be summarized that ligands, polymers, or surfactants used in surface stabilization largely affect the magnetic characteristics of a system. For example, the decomposition of iron pentacarbonyl can be catalyzed by amines, nitrogen nucleophiles or even its own iron products⁷¹. Particularly in a thermal decomposition synthesis iron pentacarbonyl is known to undergo facile valence disproportionation reactions with nitrogen nucleophiles, leading to changes in reaction kinetics⁷². Because reproducibility and particle sizes depend on the decomposition of iron carbonyl in reaction, understanding and minimizing the decomposition effects a surfactant has on the iron forming reaction is vital. Our group arrived on 2,4-pentanedione because it is a well-known and lightly coordinating organic surfactant⁶⁷. 2,4-Pentanedione is able to chelate with iron but is not known to readily oxidize iron surfaces like alcohols or carboxylic acids, which can lead to a magnetically suppressive or dead layer. In the later sections, it is detailed that with minimal structural modification to this surfactant, one can systematically control nanoparticle size, magnetic properties, and the reaction kinetics we face in these reactions.

3.4. Mechanisms of Nanoparticle Formation

For many years, the process of nanoparticle nucleation and growth has been described through what is known as the LaMer mechanism⁷³. Introduced by Victor LaMer in 1950, this mechanism was used to explain how sulfur colloids form and grow in solution. Aside from sulfur compounds, it is highly applicable to particulate systems. It conceptually divides the particle formation process into three stages, pre-nucleation, nucleation, and growth:

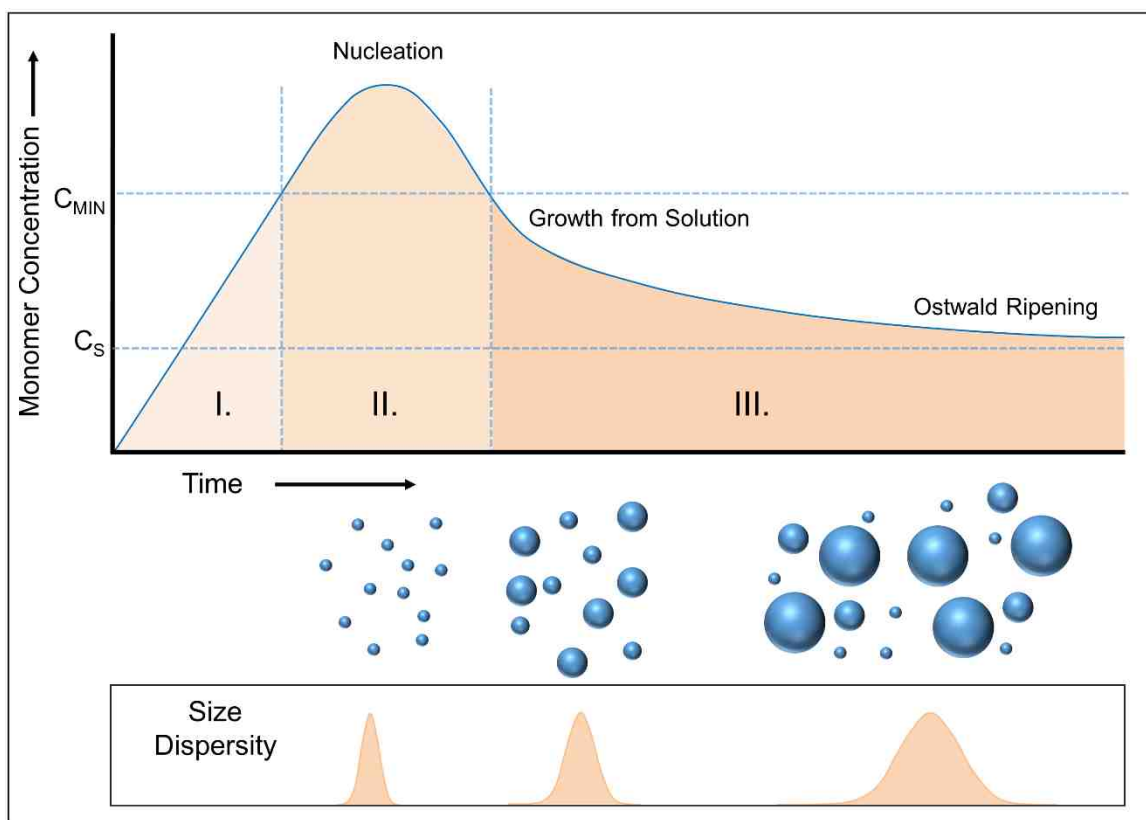


Figure 3.9 The classic LaMer mechanism to nanoparticle synthesis. In stage I, the concentration of monomer increases until it reaches a critical supersaturated state (C_{MIN}). In stage II, burst nucleation partially relieves this supersaturation and the monomer concentration drops below the

critical nucleation concentration. In stage III, growth of nuclei occurs by diffusion of the monomer to the particle surface, and the monomer concentration slowly approaches the lower solubility limit (C_S). Being a closed system, additional growth of the nanoparticles occurs through ripening due to the change in nanoparticle solubility as a function of size. This ripening leads to increased particle dispersity, thus affecting particle properties.

Stage I begins with the addition of a precursor. The monomer is the reacted precursor species that is dissolved in solution, but is unstable and able to form or attach to a particle. The monomer concentration slowly increases, passes a solubility limit (C_S), and becomes a supersaturated solution. It continues to increase until it reaches a critical level of supersaturation (C_{MIN}). In stage II, a burst nucleation event occurs to partially relieve the critical supersaturation of the monomer in solution, thus effectively reducing its concentration. After this point, being a closed system with no monomer addition to increase the concentration, there is no further nucleation occurring due to the lowered monomer concentration. Stage III follows, where growth occurs under the control of diffusion of the monomer in solution. The significance of this mechanism is that it divided nanoparticle formation into stages which could be understood and manipulated to produce nanoparticles of desired size and shape. By modifying a given system to produce a short-lived nucleation event, nuclei would be of a similar size and would grow at the same rate, leading to low-size dispersity. However, it was noticed that this was not always the case. In the final stage III, it was observed that over time smaller particles would dissolve and redeposit onto larger ones, a phenomenon which is known as “Ostwald ripening⁷⁴.” This occurred due to the change in nanoparticle solubility as a function of particle size. Smaller particles, having a

high solubility and surface area in solution, would redissolve and allow the larger particles to grow at their expense. This leads to increased size dispersity, thus affecting nanoparticle properties.

Recent work performed by researchers at Sandia National Laboratories showed that this ripening effect can be avoided to create spherical iron oxide nanoparticles with low-size dispersity. Vreeland *et al.* did this effectively by the slow and constant addition of monomer (iron precursor) over time, avoiding the complications that arise in a closed system.

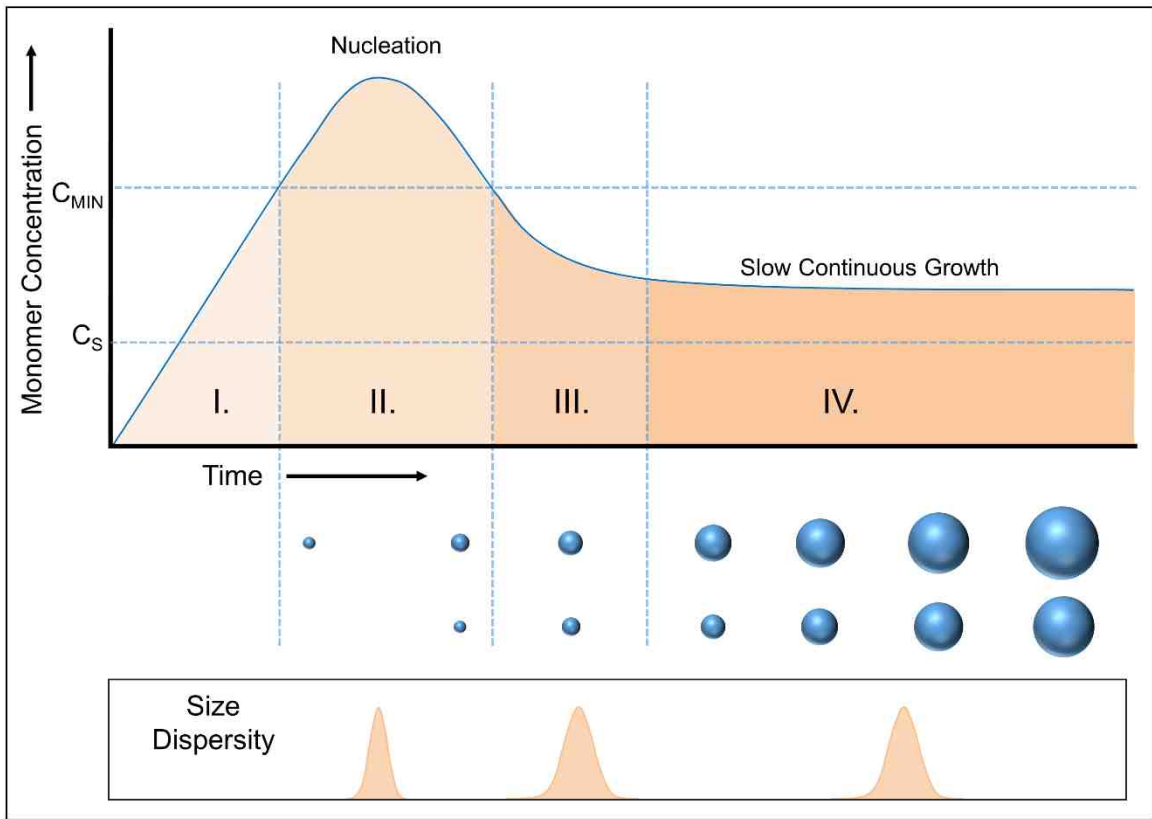


Figure 3.10 The extended LaMer mechanism for nanoparticle formation. The beginning stages mirror the classic LaMer mechanism. However, the continuous addition of monomer in the

extended LaMer introduces a new stage, stage IV. With the continuous addition of precursor to solution, there is no observable ripening effects that occur. This method leads to a slow but steady particle growth and low size dispersity.

With the continuous addition of iron precursor to the system, the concentration essentially remains unchanged, leading to a slow and even growth stage, stage IV. With this method iron oxide nanoparticles were synthesized with exquisite size control. Nanoparticles ranging from 10 to 25 nm in size were obtained with size dispersities as low as 5.4%.

Chapter 4. Characterization

This section details the various techniques used for nanoparticle characterization and analysis. Complementary techniques were utilized when possible to provide a complete understanding of physical and chemical nanoparticle properties. The synthesized ligands used for nanoparticle stabilization were analyzed and their composition confirmed with NMR. Post synthesis analysis of particle size, shape, and dispersity was carried out by TEM and SAXS. Particle structure was characterized with XRD and TEM. The magnetic characterization of samples was completed on a SQUID magnetometer and quantitative analysis of iron for SQUID samples was performed on a UV-Vis spectrometer.

4.1. Transmission Electron Microscopy (TEM)

Transmission electron microscopy (TEM) has been found to be a vital tool for directly imaging nanoparticles to obtain quantitative measures of particle size, particle size distribution, and morphology. Because TEMs utilize electrons instead of light to illuminate the sample, TEM imaging has significantly higher resolution than light-based imaging techniques. This high resolution allows for individual particle imaging and provides quantitative measurement of particle sizes unattainable through other techniques.

Nanoparticle samples to be analyzed by TEM were prepared by deposition of a diluted nanoparticle solution onto a 200 mesh holey carbon coated copper TEM grid (Structure Probe, Inc.; West Chester, PA). Nanoparticle samples were cleaned before deposition due to the high concentration of organic substances in the reaction. A 200 μ L aliquot of a given sample was added to a microcentrifuge tube containing hexanes in

isopropyl alcohol (25% v/v) and vortexed to mix. The heterogeneous mixture was then centrifuged at 1.32×10^5 rpm for 10 minutes. After centrifugation, the liquid was decanted and the previous process was repeated 3 times. After the third decantation, the nanoparticles were redispersed in pure hexanes and were vigorously vortexed. A 2.5 μ L aliquot was quickly drawn after being vortexed and added to the TEM grid surface. A Kimwipe was strategically placed under the grid to aid in solvent removal and to disperse the nanoparticles evenly across the holey carbon surface.

Bright field TEM images of iron nanoparticles were acquired at an accelerating voltage of 120 kV with a JEOL 1200 EX instrument (Tokyo, Japan). The instrument has a point to point resolution around 9 Å. Micrographs selected for analysis were collected on a Gatan slow scan CCD camera with magnification between 30000 and 50000x. At these magnifications one nanometer in length is equal to 3.28 and 5.80 pixels across, respectively. ImageJ (public domain software, National Institutes of Health; Bethesda, MD, USA) was used for TEM image analysis to determine nanoparticle size and size distribution. The particle diameters were calculated from the nanoparticle area measured, assuming morphology is that of a spherical particle. A minimum of 400 particles were selected for analysis, excluding those which touched the edge of the image and particles that were overlapping.

4.2. SQUID Magnetometry

A SQUID (Superconducting Quantum Interference Device) is a sensitive type of magnetometer which measures extremely low magnetic fields and properties effectively.

However, the SQUID does not directly detect magnetic fields in samples. Rather, it acts as a sensor that is connected to a system of superconducting detection coils by superconducting wires. This combination of detection coils, wires, and SQUID input coil form a closed superconducting loop. Therefore, when samples are passed through the superconducting detection coils, an electric current is induced in the detection coils from the magnetic moment of the sample which changes the persistent current in the detection circuit. The SQUID acts as a linear current-to-voltage converter and converts this variation in current to a voltage signal, which is directly proportional to the magnetic moment of the sample⁷⁵.

The magnetic measurements of individual samples were recorded with a SQUID Magnetic Property Measurement System (MPMS) manufactured by Quantum Design (San Diego, CA). The MPMS allows for the measurement of samples with subtle magnetic fields or low moments and is capable of detecting magnetic moments as low as 10^{-10} Am² for DC measurements⁷⁶. The measurements of low moments with such precision owes to the combination of multiple features within the MPMS system:

- Superconducting magnet – capable of generating fields up to 7T
- SQUID detector and amplifier
- Superconducting magnetic shield surrounding the SQUID
- Sample handling mechanism – controls the movement of the sample through the pick-up coils

- Temperature control unit – allowing temperature of the sample to adjust between 2 to 400K
- Integrated computer for operation and analysis

The as-synthesized nanoparticles were carefully pipetted into a 5 mm high-throughput standard NMR tube in glove box under inert atmosphere. The tube was sealed securely and transferred to a Schlenk line also under inert atmosphere. After purging for 5 minutes with nitrogen, negative pressure was applied to the tube (<100 mbar) for 20 minutes for degassing, then it was flame sealed for analysis. For analysis, the nanoparticle sample was cooled to 5K with no applied field, then zero-field cooled (ZFC) magnetization curves were obtained recording the magnetization of the sample while heating from 5K to 250K under a weak 10 Oe (0.8 kA/m) magnetic field. Field-cooled (FC) magnetization curves were obtained by then cooling the sample from 250K to 5K with the weak 10 Oe (0.8 kA/m) field still applied. Magnetization versus applied magnetic field (MvH) curves were obtained by cooling the sample to 5K and measuring magnetization utilizing a field sweep from 5T to -5T.

4.3. X-ray Diffraction (XRD)

X-ray powder diffraction (XRD) measurements provided useful information on the crystalline structure formed after synthesis and post-processing techniques. A general figure of how an X-ray functions is shown below.

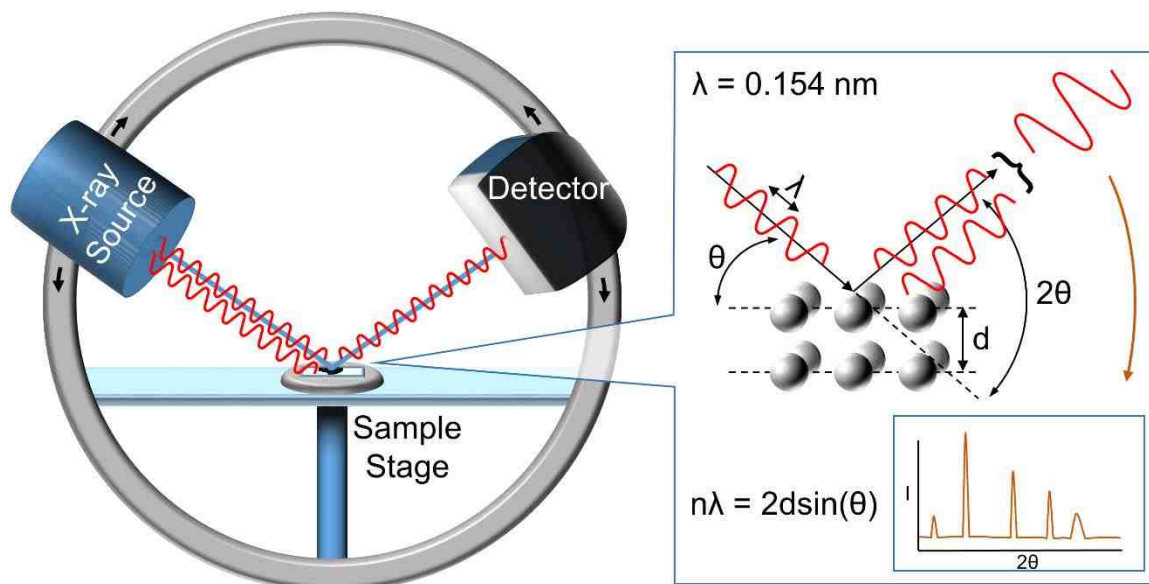


Figure 4.1 Schematic of an X-ray diffractometer. X-rays are generated by striking a pure anode of a particular metal with high energy electrons in a sealed vacuum tube and are directed toward the sample. The sample diffracts the X-ray beam differently, depending on its orientation and structure. An area detector then collects the diffracted X-rays. The crystal structure is then determined from the diffraction pattern which consists of reflections of various intensities.

For a simplistic explanation, X-rays of wavelength λ are generated by striking a pure anode of a particular metal, usually Copper (Cu, $\lambda = 0.154$ nm), with high-energy electrons in a sealed vacuum tube. These generated X-rays produce a “beam” which is directed toward a powdered sample. The incident X-ray beam interacts with the sample’s crystalline lattice with a lattice spacing of distance d , and produces a diffracted beam of X-rays related to the interplanar spacings in the crystalline powder. This mathematical relationship is known as “Bragg’s Law”⁷⁷:

$$n\lambda = 2d \sin\theta \quad (\text{Eq. 4.1})$$

The diffraction pattern obtained of intensity versus angle of 2θ (degrees) allows for the identification of crystalline or lack of crystalline phases.

Powder X-ray measurements were obtained using a Rigaku SmartLab diffractometer with SmartLab Guidance system control software (Rigaku, The Woodlands, TX). Measurements were collected at 44 kV and 40 mA using a Cu $K\alpha$ radiation source ($\lambda = 0.154$ nm) along with a scintillation detector and diffracted beam monochromator at a scanning rate between 0.1 and 5°/min. Analysis and phase identification of the diffraction spectra obtained was performed with Rigaku PDXL analytical software with ICDD (International Center for Diffraction Data) PDF2 database.

Nanoparticle samples were cleaned before deposition onto a glass slide due to the high concentration of organic substances in the reaction. A 500 μL aliquot of a given sample was added to a microcentrifuge tube containing hexanes in isopropyl alcohol (25% v/v) and vortexed to mix. The heterogeneous mixture was then centrifuged at 10000 rpm between 10 and 15 minutes. After centrifugation, the liquid was decanted, the hexanes and isopropyl solution was re-added and the previous process was repeated 3 times. After the third decantation, the particles were redispersed in a pure hexane solution and vortexed vigorously to mix. Particles were dropcast every ~15 seconds onto a silicon substrate, allowing enough time for the particles to deposit and solvent to evaporate. The thin film on silicon substrate was complete and ready for analysis after ~30-45 droplets were cast.

4.4. Small Angle X-ray Scattering (SAXS)

Size analysis was performed with SAXS as a complementary technique to TEM. Although fundamentally very similar to XRD, SAXS is considered a complementary method which provides the ability to analyze particle size and size distribution of an ensemble of particles in solution. An advantage of this method in our particular case is that a crystalline sample is not needed. Small-angle specifically refers to the measurement occurring at scattering angles typically between 0.1 and $10^\circ 2\theta$. The X-ray scattering signal is derived from the difference in the average electron density between particles and their surrounding environment ($\sim 0.33 \text{ e}^-/\text{\AA}^3$ for hexanes)⁷⁸. Because electron density contrast is affected by changes in solvent composition and particle concentration, sample consistency is important. The figure below provides a simplified schematic of how a SAXS spectrum is obtained.

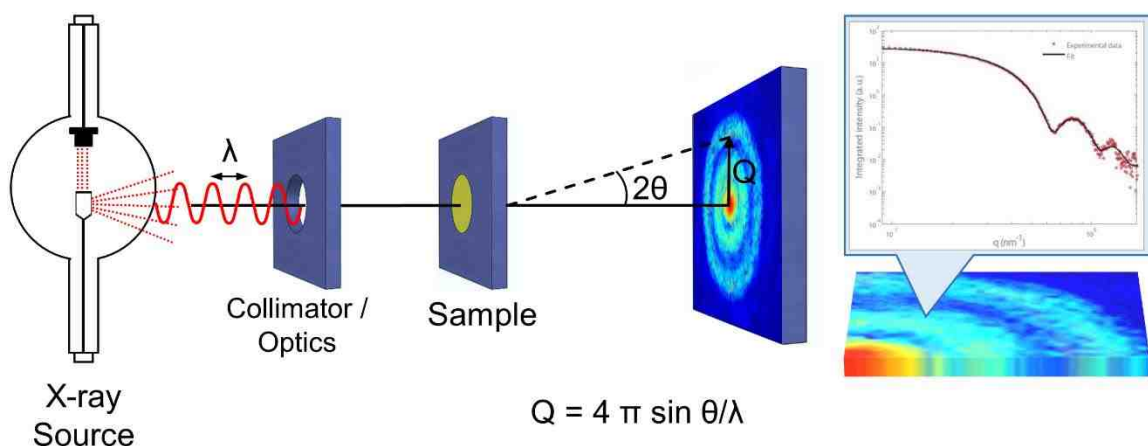


Figure 4.2 Simplified schematic of how a SAXS spectrum is obtained. A sample is illuminated by a collimated monochromatic X-ray beam, and the intensity of the scattered X-rays is recorded by

an X-ray detector. The resulting scattering pattern is related to the overall shape and size of the particles in the sample.

SAXS measurements were performed on a Rigaku SmartLab X-ray diffractometer with the SmartLab Guidance system control software. Measurements were collected at 44 kV and 40 mA using a Cu K α radiation source ($\lambda = 0.154$ nm) in transmission geometry with a scintillation detector. Nano-solver v. 3.5 was the software chosen for fitting the scattering profile. To obtain information on nanoparticle size and size distribution, a spherical model fit confirmed by TEM was utilized and the data was fit using a least-squares fitting method.

Samples were prepared by taking an aliquot of particles from each synthesis and dispersing in either hexanes or 1-octadecene. To redisperse heavily agglomerated samples, two methods were used. Samples were first heated up with stirring in air to create a small oxide layer, reducing the strong magnetic interactions between particles. Samples with some agglomeration remaining went through a ligand exchange procedure by heating up nanoparticles in 1-octadecene with ~100-200 μ L oleylamine to 75°C while stirring. It can be seen through TEM images taken before and after the atmosphere heating procedure that the oxide layer created by heating up samples in air is modest and can be assumed to only reduce magnetic interactions, and not lead to a drastic change in nanoparticle size.

4.5. UV-Visible Spectroscopy (UV-Vis)

Ultraviolet and visible (UV-Vis) absorption spectroscopy is an exceptionally useful characterization technique for quantitative and qualitative analysis, as well as detecting

functional groups and impurities in a given sample⁷⁹. A UV-Vis absorbance spectrum is obtained by exposing a given sample to a range of wavelengths provided by a light source. This light source strikes a diffraction grating which works like a prism and separates the light into its component wavelengths. The grating is rotated, so only a specific wavelength of light reaches the exit slit. These wavelengths lie between 190-380 nm for ultraviolet and 380-750 nm for visible light. When the light energy the sample is exposed to matches the energy difference between an electronic ground and excited state, the sample will absorb a fraction of that light of frequency (ν) and promote electrons to the higher energy state orbital as seen in Figure 4.3. This change in electronic states leads to a change in the absorbance or transmittance of the sample which is measured by a detector.

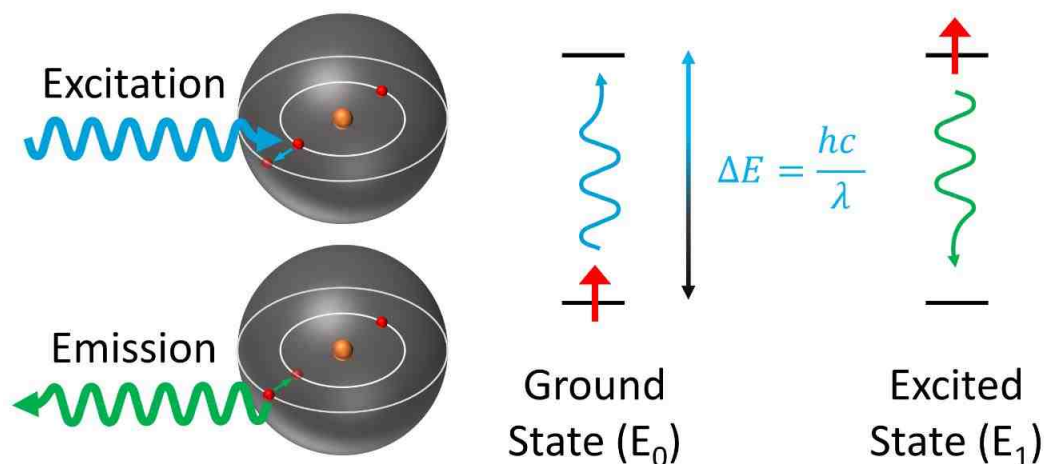


Figure 4.3 Schematic of UV-Vis excitation and emission. When the light energy the sample is exposed to matches the energy difference between an electronic ground and excited state, the sample will absorb a fraction of that light of frequency (ν) and promote electrons to the higher energy state orbital.

This transition can be calculated by the equation below, where the energy difference (ΔE) of the ground (E_0) and excited (E_1) states is equal to the product of the frequency of light exposure and Planck's constant ($h = 6.626 \times 10^{-34} \text{ m}^2 \text{ kg/s}$).

$$E_1 - E_0 = h\nu \quad (\text{Eq. 4.2})$$

UV-Vis spectroscopy was the most viable method used for quickly determining iron concentrations in samples run on SQUID magnetometry and iron used for catalytic experiments. A total destructive method was chosen to determine the iron concentration. A 15 mL borosilicate glass scintillation vial was charged with 2-5 mL of water and 0.2-0.5 mL of the iron nanoparticle sample containing iron nanoparticles with surfactant in organic solution. Water was used as an additive because it was discovered that annealing the solution in its absence lead to the formation of iron carbide phases or carbonaceous residue, which was insoluble in the hydrochloric acid used for sample preparation⁸⁰⁻⁸¹. It has been noted that while the chemical properties of iron-carbon alloys and steels have been reported in literature, there has been an extremely scarce amount of studies reporting the properties of the individual carbide phases⁸². The water and nanoparticle mixture was heated to 130°C for 30 minutes to allow the water to slowly boil off and react with the iron nanoparticles, preventing the formation of carbide phases. The temperature was then increased to 300°C for 1 hour and finally 600°C for 3 hours to ensure all organics were decomposed. The red iron powder that remained was then dissolved in 6 mL of 1 M HCl solution and stirred with light heat to fully dissolve. The resulting yellow solution was then carefully transferred to

volumetric flasks ranging from 10 to 500 mL in size depending on the expected iron concentration. The scintillation vial was rinsed with DI water 3-5 times to ensure all iron was removed. The volumetric flask containing iron solution was then diluted to the calibration mark, capped, and inverted 3-4 times to ensure proper mixing. Aliquots from this final stock solution were prepared accordingly to the ASTM standard test method for iron using a 1,10-phenanthroline method. This method produces a phenanthroline/Fe²⁺ complex which can be spectrophotometrically quantified⁸³.

4.6. Nuclear Magnetic Resonance (NMR)

Nuclear magnetic resonance (NMR) is a highly versatile method which delivers valuable structural information and in many cases, can determine a complete and distinct organic structure. NMR does this by analyzing the response of multiple atomic nuclei's spin (I) within a compound to an applied external magnetic field. When applying a weak external magnetic field, an atomic nuclei's spin will orient itself either with the applied field (α , $I = +1/2$, lower energy) or against the applied field (β , $I = -1/2$, higher energy). When irradiating the nucleus with electromagnetic radiation of the correct energy, a nucleus in a low energetic orientation α , can be excited to the higher energetic state, β . This absorption of energy during this transition is the basis of NMR and can be summarized in the following figure:

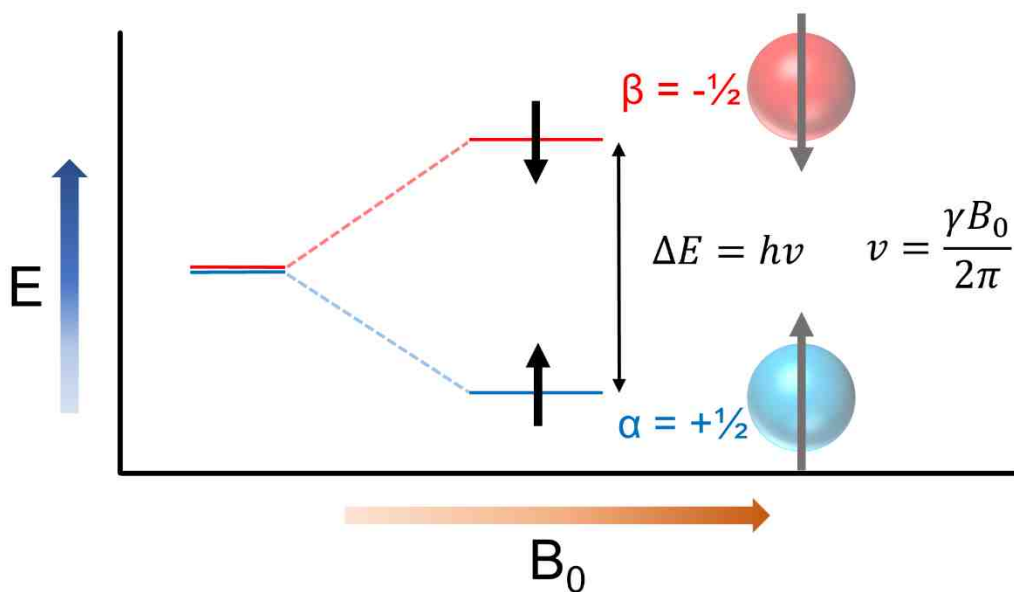


Figure 4.4 NMR analyzes the response of multiple atomic nuclei's spin within a compound to an applied external magnetic field. Applying a weak external magnetic field causes the atomic nuclei's spin to orient with the applied field (α , $I = +1/2$, lower energy) or against the applied field (β , $I = -1/2$, higher energy). When irradiating the nucleus with electromagnetic radiation of the correct energy (ΔE), a nucleus in a low energetic orientation α , can be excited to the higher energetic state, β .

Similar to (Eq. 4.2) seen in the fundamentals of UV-Vis spectroscopy, the energy difference between two nuclear spin states ΔE is equal to the frequency of absorbed electromagnetic radiation ν and Planck's constant ($h = 6.626 \times 10^{-34}$ J/s). In turn, the frequency is related to the applied magnetic field B_0 through a proportionality constant known as the gyromagnetic ratio γ shown in the following equation:

$$v = \frac{\gamma B_0}{2\pi} \quad (\text{Eq. 4.3})$$

This constant between the magnetic dipole moment and the angular momentum is specific to each nucleus. For example, a field strength of $B_0 = 1.0 \text{ T}$, ^1H absorbs radiation with a frequency around 42.6 MHz and ^{13}C absorbs radiation with a frequency around 10.7 MHz. Since the frequency of absorbed electromagnetic radiation depends on the molecular environment of a nucleus which is different for various elements and is different for isotopes of the same element, this is an extremely useful technique for determining structural configuration.

NMR was used for structural confirmation of the synthesized surfactant products (3-octadecyl-2,4-pentanedione and 3-decyl-2,4-pentanedione) obtained. Purified surfactants were thoroughly dried and resuspended in 500-700 μL of CDCl_3 , and this solution was placed into a 5 mm high-throughput standard NMR tube for analysis. ^1H NMR spectra were recorded at 90 MHz on an Anasazi EFT-90 spectrometer (Anasazi Instruments, Inc., Indianapolis, IN). Chemical shifts for ^1H NMR spectra are reported (in parts per million) relative to internal tetramethylsilane (Me_4Si , $\delta = 0.00$) with CDCl_3 as solvent. ^{13}C NMR spectra were recorded at 90 MHz on the Anasazi EFT-90, and chemical shifts are reported (in parts per million) relative to the CDCl_3 solvent ($\delta = 77.0$). Collected NMR spectra were analyzed using the NUTS NMR spectral analysis program (Acorn NMR, Fremont, CA).

Chapter 5. Nanoparticle Size Control Through Reversible Magnetic Agglomeration

5.1. Introduction

Here, we propose a reversible magnetic agglomeration mechanism to escape complex reaction kinetics and achieve true thermodynamic reaction control for the synthesis of zero-valent iron nanoparticles with narrow size distribution and high magnetic saturation. Magnetic agglomeration occurs when the dipole-dipole interaction of the particles becomes strong enough to overcome the electrostatic and steric stabilization provided by the surfactant, leading to precipitation. This reduces the magnetostatic energy of the entire ensemble, leading to a local energy minimum for the system. We then show that with continuous addition of iron precursor, the cycle of nanoparticle growth and magnetic agglomeration can be repeated indefinitely, leading to gram scale synthesis of highly magnetic zero-valent iron nanoparticles with tight size distribution.

Since the strength of the magnetic dipole is directly related to nanoparticle size, agglomeration occurs within a very narrow size range, thus leading to nanoparticles with a tight size distribution. The reversible part of the agglomeration mechanism is introduced post-synthesis for completed reactions which have proceeded through at least one agglomeration event.

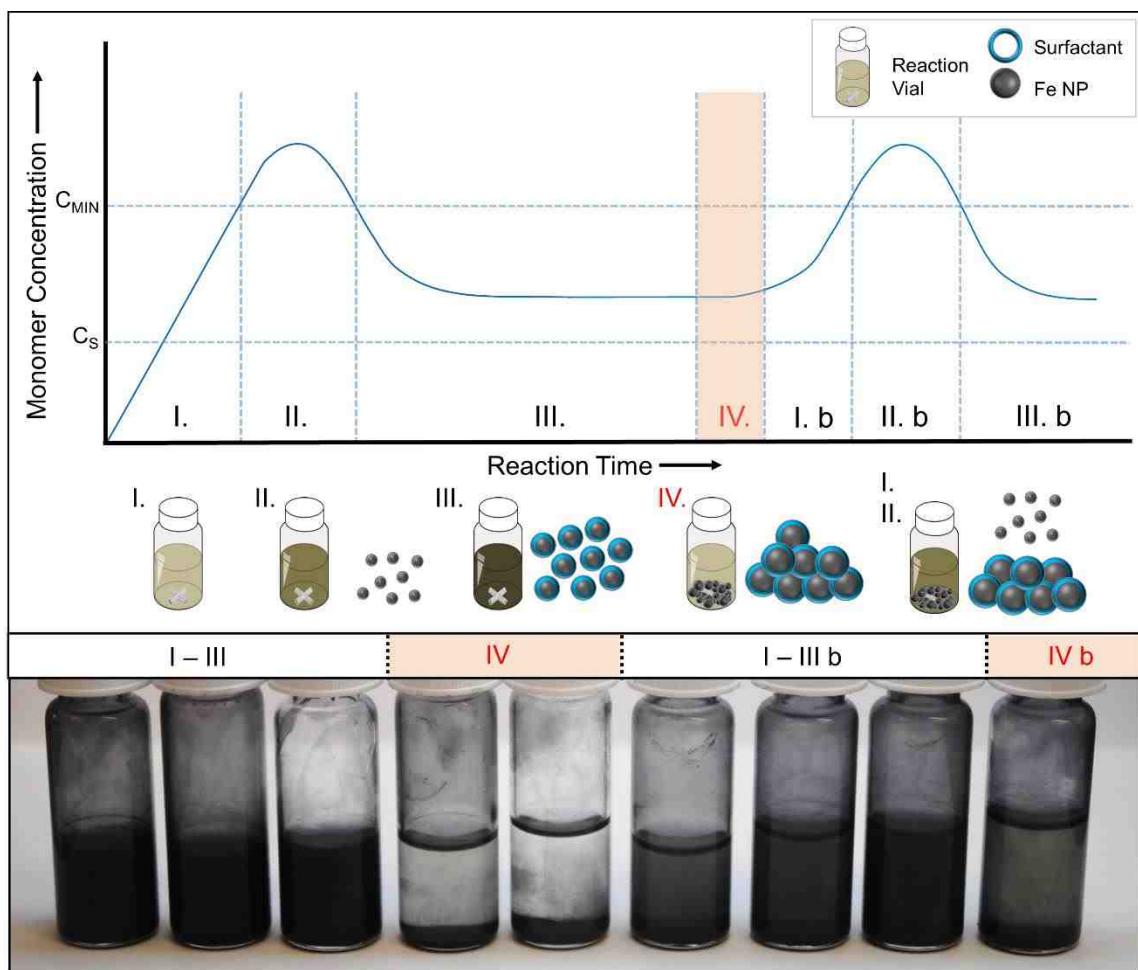


Figure 5.1 (a) The reversible magnetic agglomeration mechanism can be explained through the following stages: Stage I, monomer concentration increases to a critical supersaturated level (C_{MIN}) which is then partially relieved by a nucleation event (Stage II). In Stage III, monomer concentration drops below the level required for nucleation and particle growth occurs. Then, due to a continuous addition of monomer, the reaction enters steady state growth conditions. In Stage IV, particles grow to a critical size before their magnetic dipole interactions become strong enough to overcome steric stabilization leading to a magnetic agglomeration event. Once particles agglomerate and precipitate out of solution, their reactivity is drastically decreased. Monomer concentration again begins to increase to a critical supersaturated level (I b), and a second

nucleation event takes place (II b). These newly formed nanoparticles then grow until magnetic agglomeration occurs, and the cycle repeats (III b – IV b). (b) A visual representation of reversible magnetic agglomeration taken from an experiment using unsubstituted 2,4-pentanedione as surfactant.

The reversible magnetic agglomeration mechanism is shown schematically in Figure 5.1. It occurs in a system in which an iron precursor solution containing $\text{Fe}(\text{CO})_5$, an alkylated 2,4-pentanedione surfactant and 1-octadecene (1-ODE) is continuously added via syringe to a solution of surfactant and 1-ODE, heated under an inert atmosphere. The initial stages of the mechanism are in agreement with the classic LaMer mechanism⁷³. As iron precursor solution is added, iron monomer concentration increases (Stage I) reaching a critical level of supersaturation where nucleation is thermodynamically favorable (Stage II). The nuclei grow and due to the continuous addition of iron precursor, steady state growth conditions emerge (Stage III). This type of steady-state growth has recently been shown to lead to tight size distributions in iron oxide nanoparticles grown in an extended LaMer mechanism⁸⁴. As the nanoparticles grow, their magnetic moment increases⁸⁵. Eventually, the magnetic dipole interaction between particles becomes strong enough to overcome the steric stabilization provided by the surfactant. At this point (Stage IV), particles magnetically agglomerate and precipitate out of solution. Once particles precipitate their reactivity is drastically decreased and any further growth is negligible. However, the continuous addition of iron precursor solution quickly reestablishes an increasing iron monomer concentration. This leads to the reemergence of a critical supersaturated state (Stage I b), a subsequent nucleation event (Stage II b), and particle

growth (Stage III b). Continued addition of iron precursor then leads to a second magnetic agglomeration event (Stage IV b), and the mechanism begins again. As iron addition rate is constant and particle size is determined by the interplay between steric stabilization and magnetic dipole interaction, each agglomeration event occurs within a very narrow size range, leading to a tight nanoparticle size distribution.

The reversible magnetic agglomeration mechanism can be observed visually with nanoparticles synthesized using 2,4-pentanedione as surfactant (Figure 1b). A black solution (I-III) indicates particles are well dispersed and have not yet reached the maximum size. The observation of a clear supernatant (IV) indicates a magnetic agglomeration event has occurred. As we continue to introduce monomer, we observe a reemergence of a black colored solution which increases in opacity. This is consistent with a renucleation event and subsequent further growth of the newly nucleated particles (I-III b). A second magnetic agglomeration event is then observed (IV b), confirming the cyclability of the mechanism. Agglomerated nanoparticles could be resuspended post-synthesis in most common organic solvents with some energy input, *e.g.*, heat or sonication, confirming the reversibility of the agglomeration.

5.2. Experimental

Chemicals

All chemicals used in syntheses underwent very rigorous drying, degassing, and purification procedures. All performed procedures occurred on a Schlenk line adapted with a large purifier tube containing copper catalyst and molecular sieves (MBRAUN USA,

Stratham, NH). This set up was under the constant flow of highly pure in-house nitrogen to ensure the exclusion of oxygen and moisture. Once samples were prepared they were transferred under reduced pressure to an MBRAUN Unilab glovebox (<0.1 ppm H₂O and <0.1 ppm O₂).

All reagents in the following are purchased from Sigma Aldrich (St. Louis, MO) unless stated otherwise. 1-Octadecene (1-ODE, technical grade 90%, CAS 204-012-9) was dried over sodium lump ($\geq 99.8\%$ in kerosene) in a 1 liter round bottom flask under inert atmosphere for a minimum of 24 hours. It was then distilled under reduced pressure into a flame-dried Schlenk flask. This flask was transferred to the Schlenk line where it was degassed using a freeze-pump-thaw technique. It was sealed and immediately transferred under reduced pressure to an inert atmosphere glove box for storage and stock preparation. Iron pentacarbonyl (Fe(CO)₅, >99.99%, CAS 236-670-8) was degassed and sublimed into a flame-dried Schlenk flask which was immediately sealed and pumped into an inert atmosphere glovebox for stock preparation. 2,4-Pentanedione (Acac, 99% Alfa Aesar, CAS 204-634-0) and 1-iodooctadecane (95%, CAS 629-93-6) were distilled and degassed using the same preparation as 1-octadecene. Sodium hydride (60% disp. in mineral oil) was used for surfactant synthesis and when not in use was permanently stored in a dry box with desiccant. Anhydrous N,N-dimethylformamide (DMF, 99.8%, CAS 200-679-5) and anhydrous tetrahydrofuran (THF, $\geq 99.9\%$ inhibitor-free, CAS 109-99-9) were both used as solvents in surfactant syntheses. They were both used as is and transferred using air-free techniques via cannula. Diethyl ether ($\geq 99.0\%$ anhydrous, CAS 60-29-7) was purchased from Acros and used for surfactant purification.

5.2.1. Surfactant Synthesis

3-Octadecyl-2,4-Pentanedione

3-Octadecyl-2,4-pentanedione is not commercially available and had to be custom synthesized. An oven-dried 250 mL three-necked round bottom flask was charged with 0.737 g (18.4 mmol) of NaH (60% disp. in oil). Under nitrogen, 150 mL of anhydrous DMF was transferred into the round bottom flask. Next, 1.54 g (15.4 mmol) of 2,4-pentanedione was added dropwise through a syringe. Additional 2,4-pentanedione was added dropwise (0.15 g, 1.5 mmol) until all NaH was dissolved. Once deprotonation of 2,4-pentanedione was complete, 7.0 g (18.4 mmol) of 1-iodooctadecane was added quickly under high nitrogen flow. The reaction was then heated at 90°C for 4 days. An orange tint can be seen in solution as reaction nears completion, the tint becomes much stronger as the reaction progresses. Once reaction was complete, the reaction solution was cooled to room temperature and neutralized with a 1M hydrochloric (HCl) solution. In a separatory funnel, the neutralized solution was extracted into ether 3 times. The combined ether layers were washed 3 times with 1M HCl. After washing, the ether was lightly heated to dissolve any residual solids and was set in a freezer overnight (-18°C) to recrystallize. After recrystallization was complete, the solid product was filtered via vacuum filtration. Filtration must occur immediately after removal from the freezer, as the solid product will redissolve if left at room temperature. The solid product was then washed twice with ether stored at 18°C. Do not wash the solid filtered product with ether at room temperature, this will dissolve product and decrease yield. The solid product was collected and spread onto a large weigh paper, finely crushed to evaporate residual ether, and set into a vacuum oven

with no heating for 30 minutes. This was then transferred immediately into a scintillation vial and stored in a dry box with desiccant. The product yield was 2.50 g, which is 42.0% of the theoretical yield of 5.95 g.

5.2.2. Surfactant Characterization

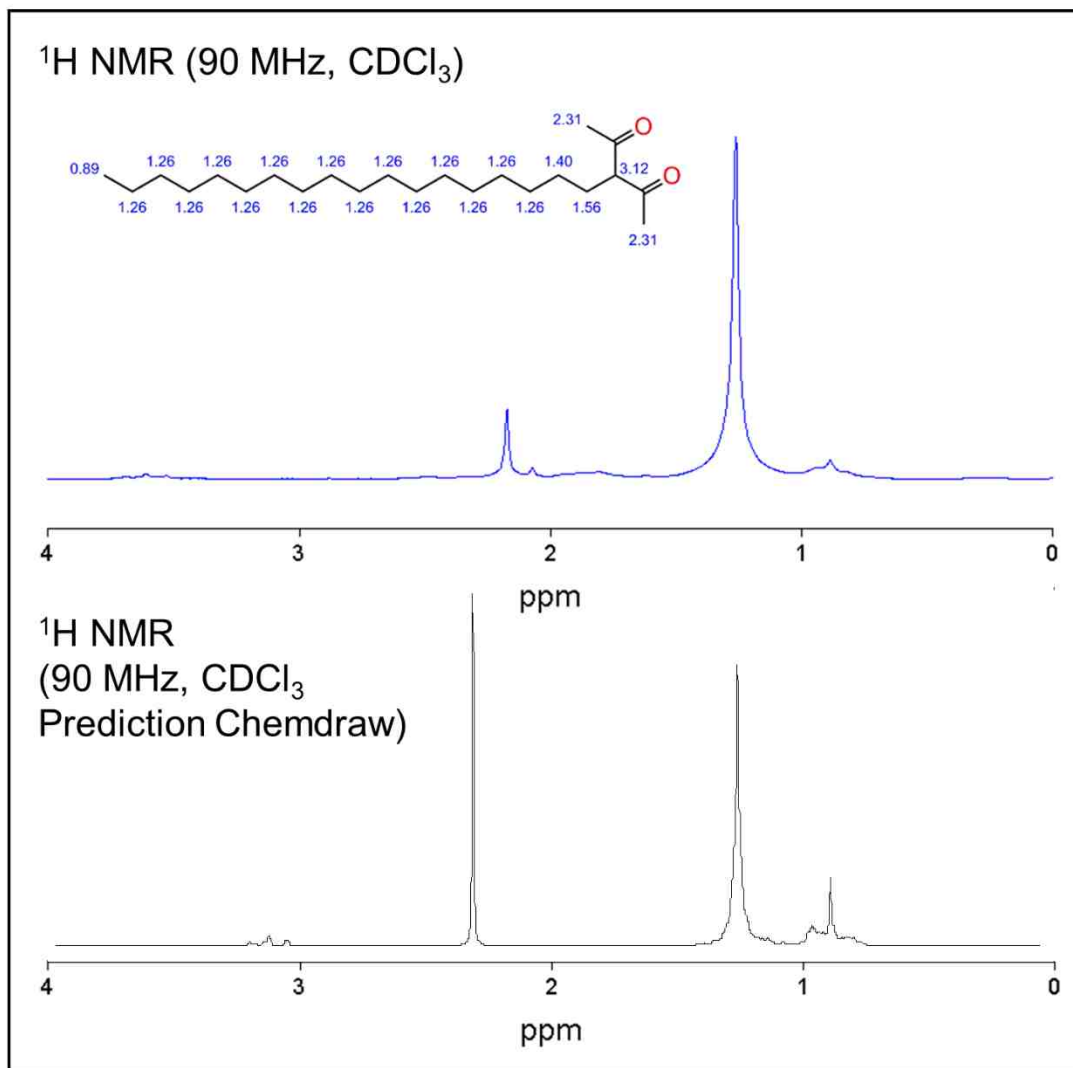


Figure 5.2 (a) Processed ^1H NMR spectra (90 MHz, CDCl_3) of the 3-octadecyl-2,4-pentanedione product after purification (normalizing 3.4 ppm triplet to 1.0 H): δ 3.61 (t, 1.00H), 2.17 (s, 6.44H),

1.81 (m, 3.65H), 1.26 (s, 39.34H), 0.89 (t, 4.66H). **(b)** Predicted ^1H NMR spectra of 3-octadecyl-2,4-pentanedione: δ 3.12 (t, 1H), 2.31 (s, 6H), 1.56 (m, 2H), 1.40 (m, 2H), 1.26 (s, 30H), 0.89 (t, 3H).

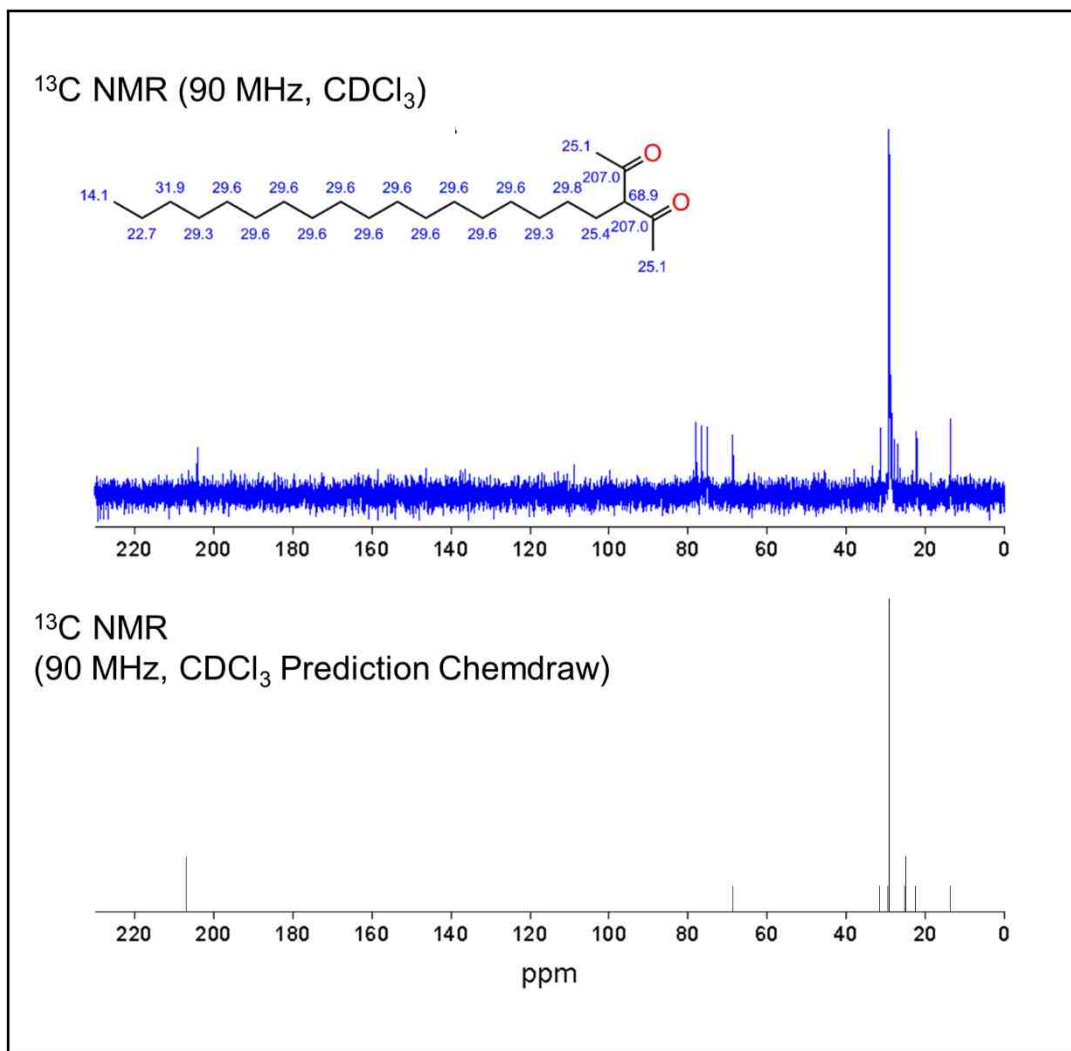


Figure 5.3 (a) Processed ^{13}C NMR spectra (90 MHz, CDCl_3) of the 3-octadecyl-2,4-pentanedione product after purification (excluding 3 CDCl_3 peaks at 75.0, 76.0 and 78.0): δ 204.2, 68.7, 31.5,

29.2, 28.9, 28.6, 27.9, 27.1, 22.3, 13.7. **(b)** Predicted ^{13}C NMR spectra of 3-octadecyl-2,4-pentanedione: δ 207.0, 68.9, 31.9, 29.8, 29.6, 29.3, 25.4, 25.1, 22.7, 14.1.

5.2.3. Synthesis of Nanoparticles

All chemicals were vigorously dried and degassed prior to use as mentioned previously. All chemicals and materials were prepared in a glove box and transferred to a Schlenk line under inert atmosphere unless stated otherwise. An oven-dried Minum-Ware[®] round bottom flask was charged with 20 mg ($5.67\text{E-}2$ mmol) 3-octadecyl-2,4-pentanedione and 5 mL (15.6 mmol) 1-octadecene under a nitrogen atmosphere with controlled flow. The solution was heated to 220°C under a condenser. A syringe loaded with 48 mg (0.136 mmol) 3-octadecyl-2,4-pentanedione dissolved in 9.0 mL (28.1 mmol) 1-octadecene and 4.0 mL (29.7 mmol) iron pentacarbonyl was slowly added dropwise to the reaction flask at a rate of 1.6 mL/hr. Amounts added ranged from 0.8 to 11.2 mL (9.1 mmol to 25.5 mmol Fe). Once the drip was completed, the reaction was allowed to proceed under a flow of nitrogen with continued heating for a minimum of one additional hour. Meticulous care was taken during sample transfer to ensure nanoparticle oxidation and exposure to atmosphere was minimized.

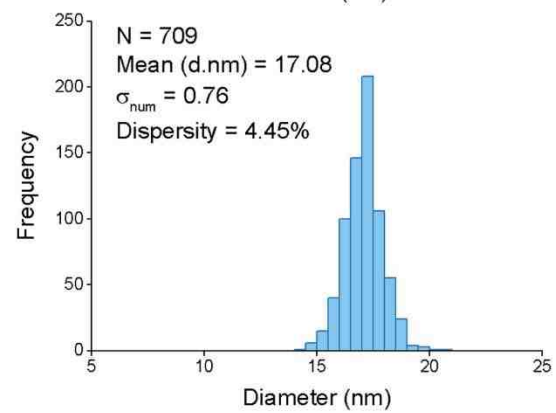
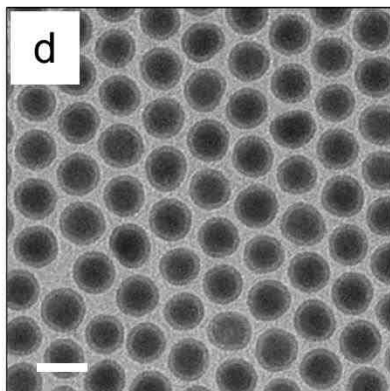
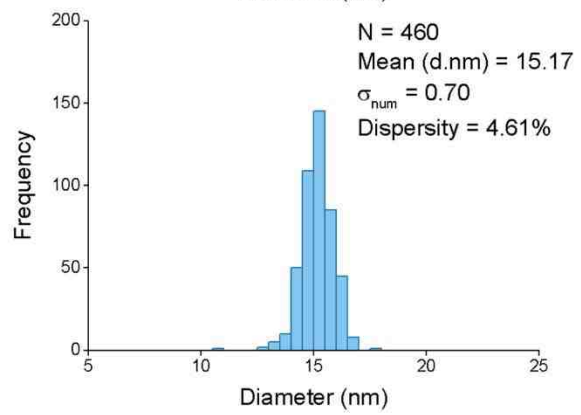
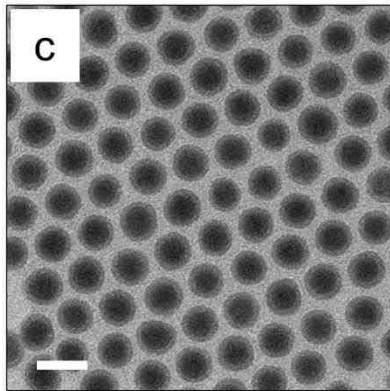
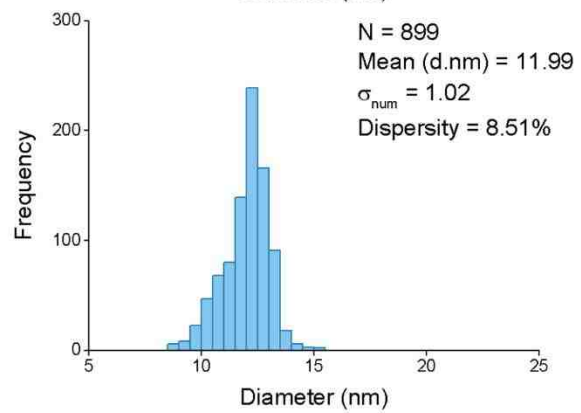
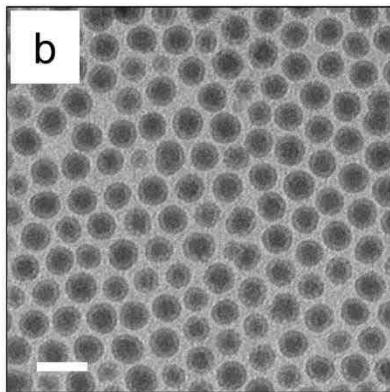
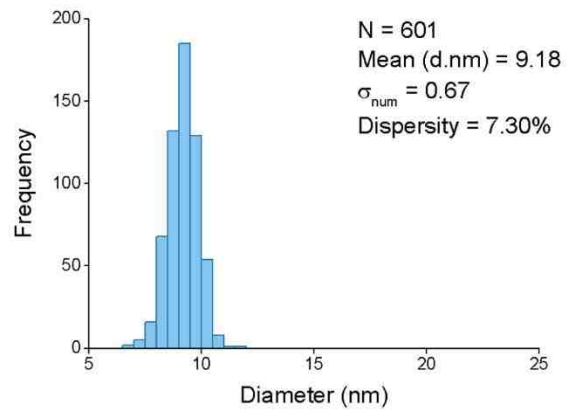
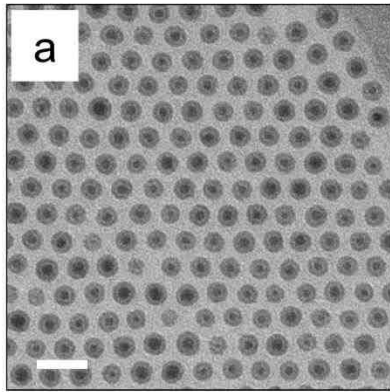
5.3. Results and Discussion

To further confirm the reversible agglomeration mechanism reactions were performed using the 3-octadecyl-2,4-pentanedione as surfactant. The longer alkyl chain length delayed magnetic agglomeration due to increased steric stabilization, leading to larger nanoparticle sizes that were more suitable for characterization. Particles that were synthesized with smaller molecule surfactants nucleate, grow, and agglomerate on a much

faster scale for similar concentrations. Therefore, it is best to analyze the largest surfactant which produces a slower rate of growth and a large range of sizes, thus lengthening the mechanism.

5.3.1. Transmission Electron Microscopy

Transmission electron micrographs were obtained for as-synthesized particles using 3-octadecyl-2,4-pentanedione as the stabilizing surfactant. These images and their corresponding histograms produced from size analysis is shown below.



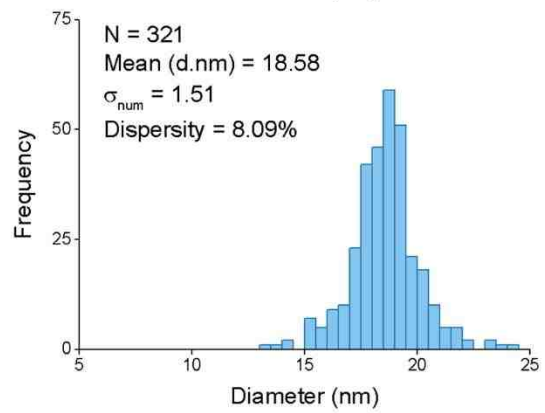
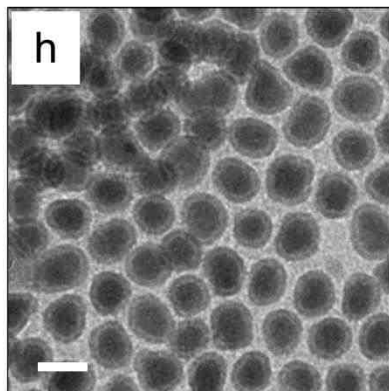
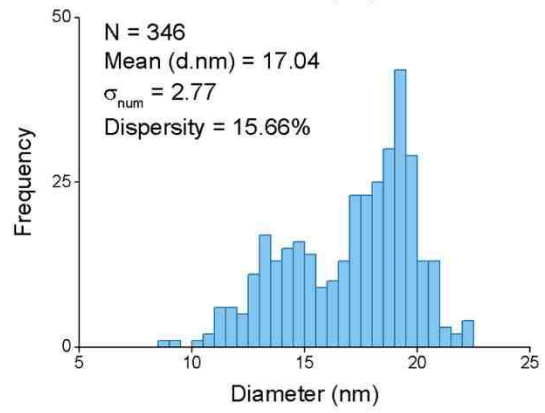
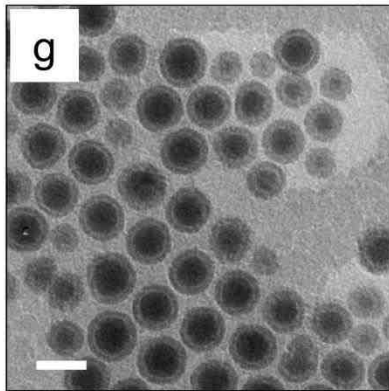
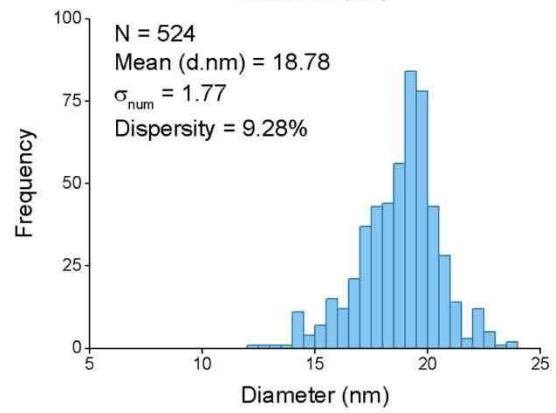
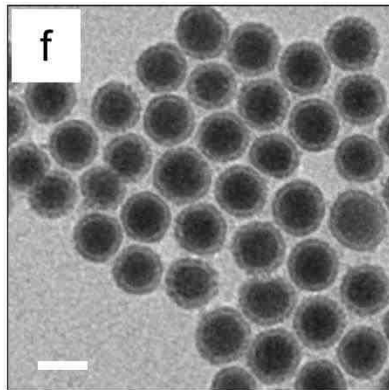
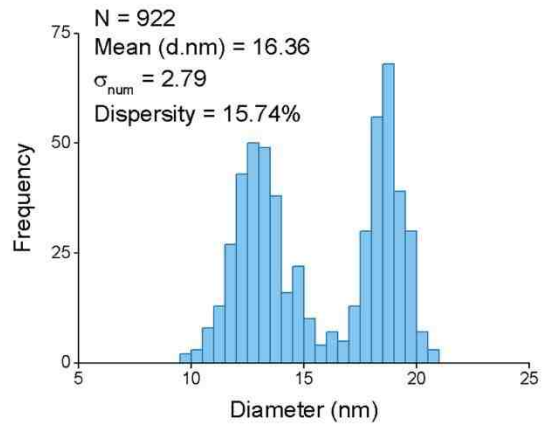
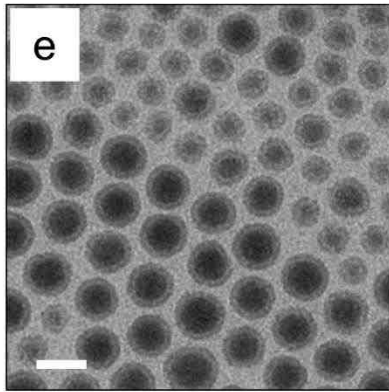


Figure 5.4 (a-h) Transmission electron microscopy (TEM) images and their corresponding histograms produced from size analysis of iron nanoparticles synthesized using 3-octadecyl-2,4-pentanedione as the stabilizing surfactant. All scale bars are equal to 20 nm. Average nanoparticle sizes are 9.2 ± 0.7 nm, 12.0 ± 1.0 nm, 15.2 ± 0.7 nm, 17.1 ± 0.8 nm, 16.4 ± 2.6 nm, 18.8 ± 1.7 nm, 16.8 ± 2.7 nm, and 18.6 ± 1.5 nm for images (a-h), respectively.

Figure 5.4 shows TEM analysis of iron nanoparticles synthesized in a reversible magnetic agglomeration mechanism using 3-octadecyl-2,4-pentanedione as surfactant. Figure 5.4a-h correspond to nanoparticles synthesized by adding 1.8, 3.6, 7.3, 9.1, 10.9, 14.6, 18.2 and 25.5 mmol of iron precursor, respectively. A series of histograms (right a-h) gives size distribution analysis taken from the corresponding TEM images. Figure 5.4a-d show growing nanoparticles, with mean sizes of 9.2 ± 0.7 nm, 12.0 ± 1.0 nm, 15.2 ± 0.7 nm, respectively. In Figure 5.4e we observe a bimodal size distribution with populations of nanoparticles 13.0 ± 1.2 nm and 18.4 ± 0.8 nm in size. This indicates a magnetic agglomeration event has occurred, causing the larger particles to precipitate out of solution, followed by a renucleation event and subsequent growth. In Figure 5.4f we observe that the second population of nanoparticles has grown to reach a maximum mean size of 18.8 ± 1.7 nm. After 18.2 mmol of iron precursor has been added (Figure 5.4g) we observe a second magnetic agglomeration-nucleation event, yielding a bimodal distribution of nanoparticles 13.9 ± 1.6 nm and 18.9 ± 1.2 nm in size. Finally, after 25.5 mmol of Fe is added the entire population of nanoparticles possess a mean maximum diameter of 18.6 ± 1.5 nm. Through three observed magnetic agglomeration and renucleation events, the mean particle diameter does not exceed 18.8 ± 1.7 nm; confirming nanoparticle diameter

is directly dependent on steric stabilization provided by the surfactant. A summary of TEM size analysis is shown in Table 5.1.

Table 5.1 Summary of nanoparticle size analysis obtained from transmission electron micrographs.

| Amount Drip (mL) | Total Fe mmol | TEM Diameter (nm) | Size Dispersity |
|-------------------------|----------------------|--------------------------|------------------------|
| 0.8 | 1.8 | 9.2 | 7.3% |
| 1.6 | 3.6 | 12.0 | 8.3% |
| 3.2 | 7.3 | 15.2 | 4.6% |
| 4.0 | 9.1 | 17.1 | 4.5% |
| 4.8 | 10.9 | 16.4 | 15.7% |
| 6.4 | 14.6 | 18.8 | 9.3% |
| 8.0 | 18.2 | 17.0 | 15.7% |
| 11.2 | 25.5 | 18.6 | 8.1% |

Further look into transmission electron micrographs of samples before and after magnetic agglomeration helps to provide visual aid which displays how particle size and size distribution change throughout this event.

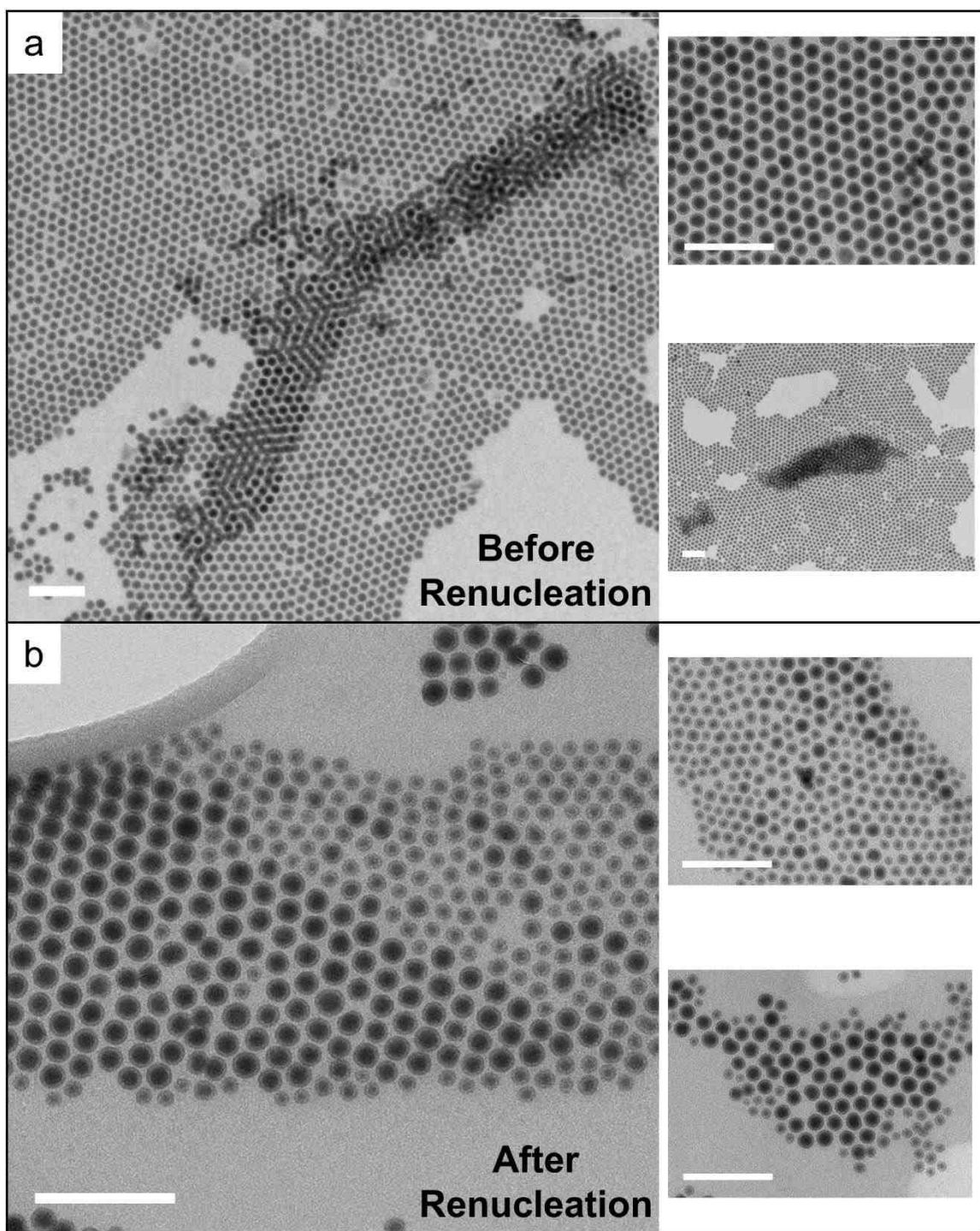


Figure 5.5. Transmission electron micrographs of iron nanoparticles synthesized using 3-octadecyl-2,4-pentanedione as the stabilizing surfactant before and after a renucleation event. All

scale bars are equal to 100 nm. **(a)** Iron nanoparticles before the renucleation event, synthesized with 9.1 mmol iron addition. Average nanoparticle size is 17.1 ± 0.8 nm (4.5% dispersity). **(b)** Iron nanoparticles after the renucleation event, synthesized with 10.9 mmol iron addition. Average nanoparticle size is 16.4 ± 0.8 nm (15.7% dispersity).

Figure 5.5 shows the renucleation event that occurs between (a) 9.1 mmol and (b) 10.9 mmol iron addition. At the point of 9.1 mmol addition of iron, the mean particle size is 17.08 nm with an extremely low size dispersity of only 4.5%. This is the lowest size dispersity achieved with all of the nanoparticles synthesized with 3-octadecyl-2,4-pentanedione. At this point it can be speculated that the low-size dispersity is a direct product of the proven constant addition slow-growth mechanism (Extended LaMer) achieved by Vreeland *et al.*⁸⁴. Analysis of the 10.9 mmol addition of iron shows that a renucleation event occurs somewhere after 9.1 mmol iron addition but before this point. The mean particle size for the 10.9 mmol addition decreases to 16.4 nm with the dispersity reaching a high of 15.7%.

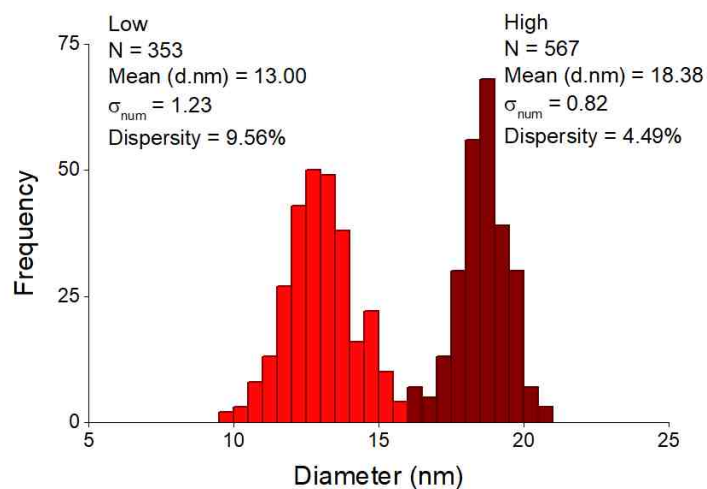


Figure 5.6 Histogram produced from size analysis of TEM images from 10.9 mmol iron addition. The bimodal distribution shows a distinct renucleation event that has occurred. Analysis can be broken into a high and low distribution of sizes. The low distribution shows a mean size of 13.0 ± 1.2 nm (9.6% dispersity). The high distribution shows a mean size of 18.4 ± 0.8 nm (4.5% dispersity).

Breaking down the bimodal size distribution into a high and low analysis helped gather further information on their respective mean sizes and dispersities. The low distribution of the bimodal for 10.9 mmol iron shows a mean size of 13.0 nm with a dispersity of 9.6%. The high distribution for the bimodal shows a mean size of 18.4 nm, slightly higher than the 17.1 nm seen in the 9.1 mmol addition, and a low dispersity of 4.5%. This is extremely similar to the dispersity seen in the 9.1 mmol addition, so it can be concluded that these particles grew to a slightly larger mean size by a difference of 1.3 nm, then agglomerated which drastically decreases their reactivity. A plot which includes the

average size, along with the high and low distribution for the 2 renucleation events is shown in Figure 5.7.

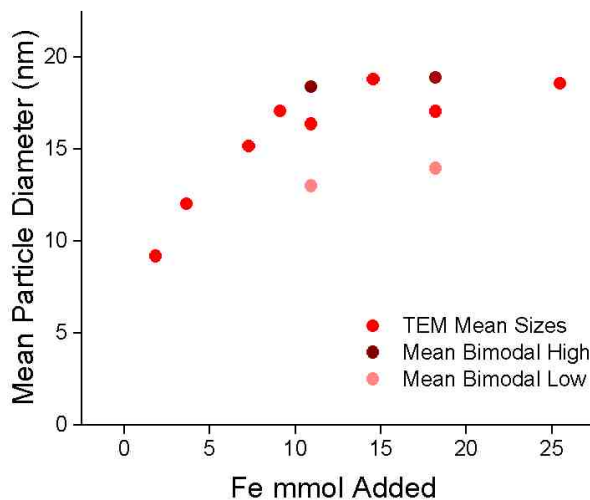


Figure 5.7 Summary of nanoparticle size analysis through TEM. The mean bimodal high and low are included to show where the maximum particle size is achieved before agglomeration.

Plotting the bimodal high distribution helps display where nanoparticle size maxes out with this surfactant. The mean maximum size range estimate for the 3-octadecyl-2,4-pentanedione surfactant is around 18.4 – 18.8 nm.

5.3.2. Small Angle X-ray Scattering

Small angle x-ray scattering (SAXS) experiments were performed as a complementary technique to TEM in order to provide further size analysis. The advantage of SAXS over TEM for these samples is that it provides size analysis over a global distribution or entire ensemble of nanoparticles. However, it is complementary because it relies on TEM to provide clues about the nanoparticle morphology for use in data analysis.

Figure 5.8 shows a typical SAXS measurement where the raw data was modelled assuming a spherical shape and Gaussian size distribution, as confirmed with TEM.

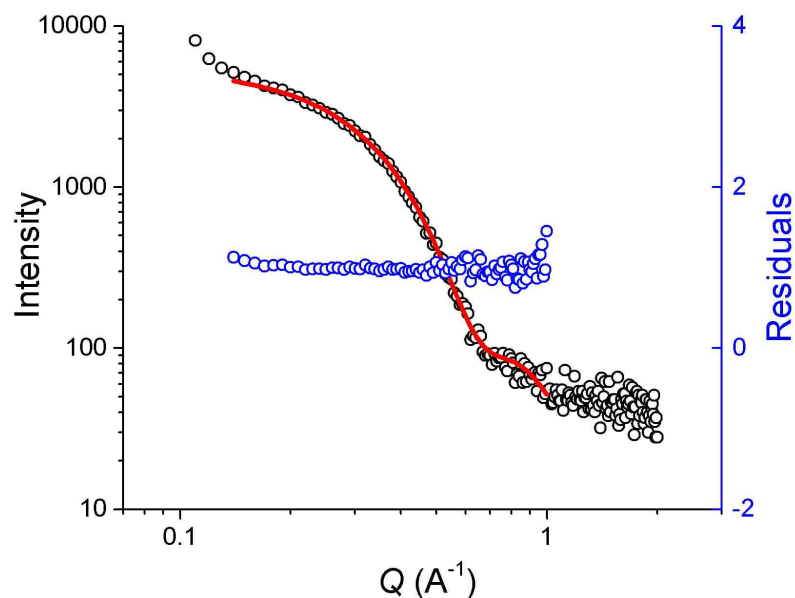


Figure 5.8 A typical SAXS measurement of as-synthesized nanoparticles showing the experimental raw data, the simulated fit (red), and the simulation residuals.

On average, experimental raw data was obtained between 0.06 and 4.0 degrees 2θ . A simulated spherical model (red line) was fit to the raw data, using iron (Fe) as the elemental core (density = 7.87 g/cm^3) and 1-octadecene as the solvent (density = 0.789 g/cm^3). The blue data points represent the residuals between the raw data and the simulated fit. These points can be summarized as a plot of deviation from linearity.

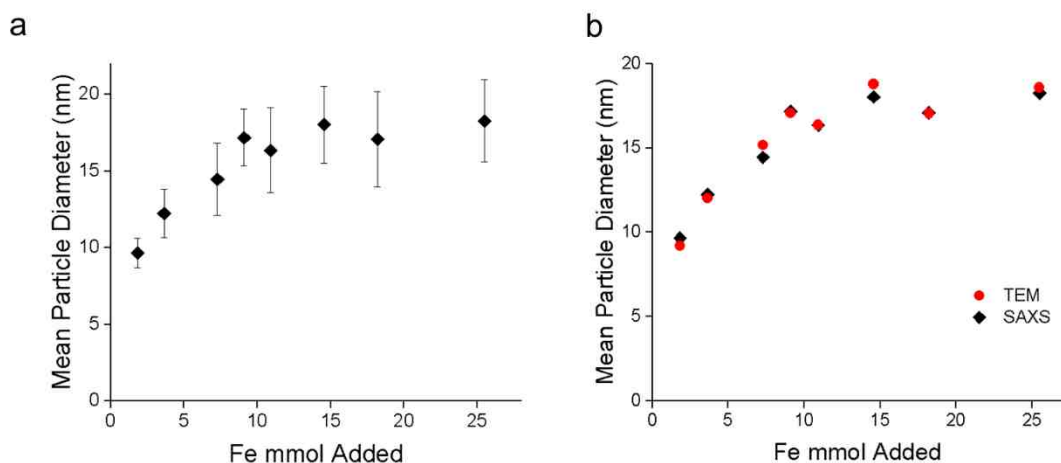


Figure 5.9 (a) Nanoparticle sizes obtained with small angle X-ray scattering (SAXS) experiments. Renucleation events can be observed in SAXS by a decrease in particle size accompanied by an increase in size dispersity, a characteristic of a bimodal size distribution. Average nanoparticle sizes are 9.2 ± 0.7 nm, 12.0 ± 1.0 nm, 15.2 ± 0.7 nm, 17.1 ± 0.8 nm, 16.4 ± 2.6 nm, 18.8 ± 1.7 nm, 16.8 ± 2.7 nm, and 18.6 ± 1.5 . (b) Comparison of mean particle sizes obtained through SAXS and TEM analytical techniques.

SAXS analysis shows a slow and steady increase in nanoparticle size until 17.2 nm, in good agreement with TEM size analysis (Figure 5.9a). A decrease in total mean nanoparticle size is observed at 10.9 mmol Fe, along with an increase in the size distribution. This is characteristic of a bimodal distribution and can be attributed to a renucleation event. This occurs again after the addition of 18.2 mmol Fe, in good agreement with the second renucleation event observed in TEM. Finally, the mean nanoparticle size increases to 18.2 nm, indicating all nanoparticles have grown to the maximum mean size. A comparison between the two analytical methods is shown in Figure 5.9b. The raw experimental data obtained on all samples is collectively displayed in Figure 5.10. The

intensity has been normalized here due to intensity fluctuations between samples. The unnormalized raw experimental SAXS data for all samples is shown in Figure 5.11 and a summary of the sizes obtained is shown in Table 5.2.

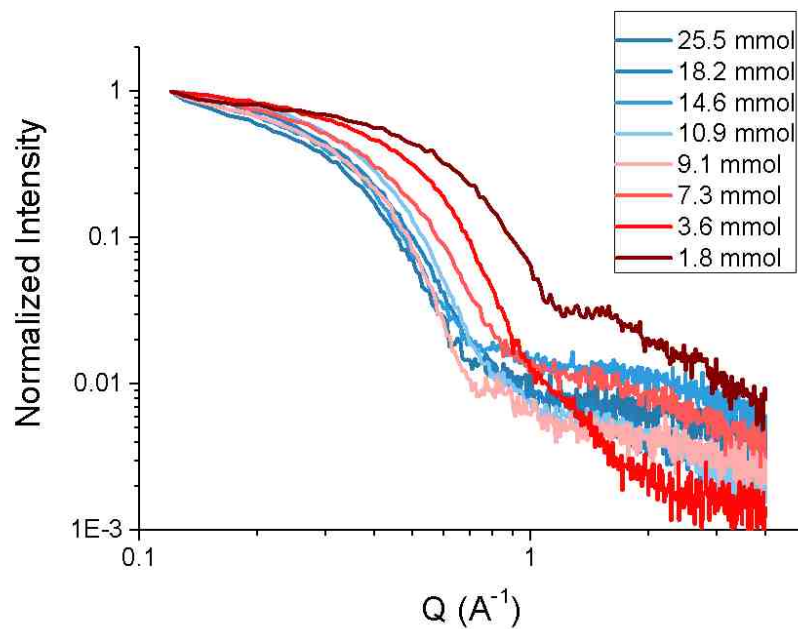


Figure 5.10 All raw experimental SAXS measurements of as-synthesized nanoparticles with 3-octadecyl-2,4-pentanedione surfactant. Intensity has been normalized to allow for comparison.

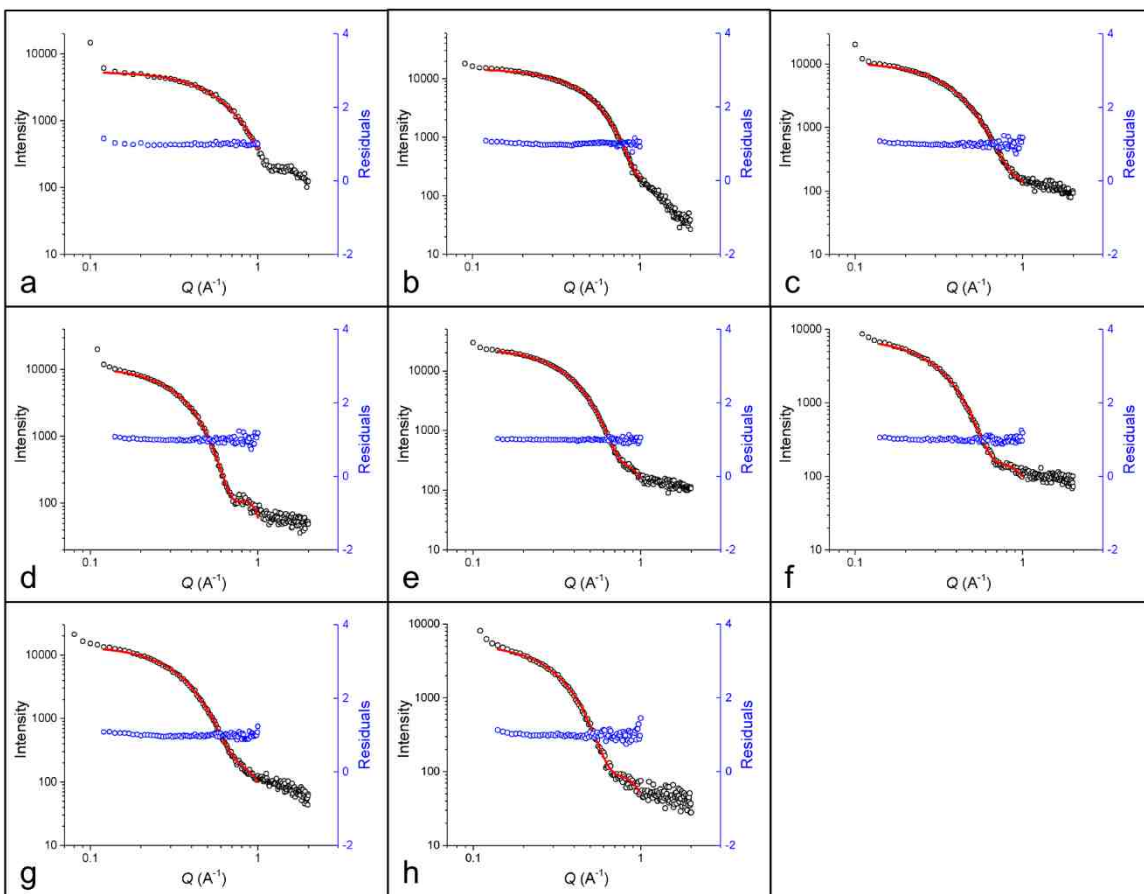


Figure 5.11 Experimental raw data, the simulated fit (red), and the simulation residuals for nanoparticles samples composed of 1.8, 3.6, 7.3, 9.1, 10.9, 14.6, 18.2, and 25.5 mmol Fe for samples (a-h), respectively.

Table 5.2 Summary of nanoparticle size analysis obtained from small angle X-ray scattering (SAXS) for particles synthesized with 3-octadecyl-2,4-pentanedione.

| Amount Drip (mL) | Total Fe mmol | SAXS Diameter (nm) | Size Dispersity |
|-------------------------|----------------------|---------------------------|------------------------|
| 0.8 | 1.8 | 9.7 | 9.8% |
| 1.6 | 3.6 | 12.2 | 12.7% |
| 3.2 | 7.3 | 14.5 | 16.4% |
| 4.0 | 9.1 | 17.2 | 10.8% |
| 4.8 | 10.9 | 16.3 | 17.0% |
| 6.4 | 14.6 | 18.0 | 13.9% |
| 8.0 | 18.2 | 17.1 | 18.2% |
| 11.2 | 25.5 | 18.3 | 14.7% |

5.3.3. SQUID Magnetometry

The magnetic properties of the nanoparticles with the 3-octadecyl-2,4-pentanedione surfactant were measured using SQUID magnetometry. The magnetic response of each sample was obtained while an external field was applied ranging from -5T to 5T. For the 3-octadecyl-2,4-pentanedione surfactant, hysteresis loops were obtained at 5 and 250K. The values reported for the magnetization saturations are at 5K.

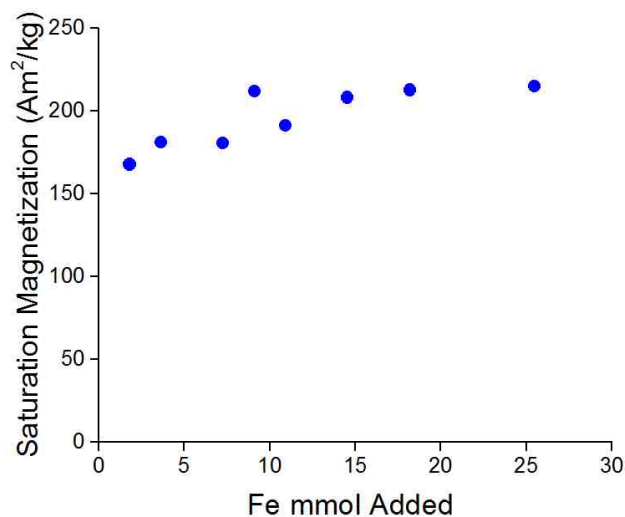


Figure 5.12 Plot displaying saturation magnetization values obtained for all samples synthesized with 3-octadecyl-2,4-pentanedione surfactant.

The particles display a net increase in saturation magnetization as a function of size. A value of 211.9 Am²/kg was obtained for the sample with 9.1 mmol Fe addition, which is the point right before renucleation. After renucleation, the magnetization saturation slightly decreased to 191 Am²/kg. This decrease is somewhat expected, and can be explained through the introduction of a small volume of smaller, less magnetic nanoparticles into a solution containing particles near the maximum size with a high magnetic moment. As you continue to increase the quantity of maximum-sized nanoparticles (around 18 d.nm), the saturation magnetization slowly increases past this point. A high value is reached for the 25.5 mmol Fe addition of 214.7 Am²/kg. This trend was also anticipated, as the quantity of larger particles is slowly increasing throughout the reaction.

5.3.4. Effects of Ligand Concentration

A series of experiments was performed to determine what concentration was best to view the agglomeration mechanism. An ideal synthesis would have a short and fast

nucleation event, so that a narrow size dispersity is achieved. Higher surfactant concentrations have been known to lead to a wider range of sizes, and not enough surfactant in solution can lead to the particle surface not being completely coated, leading to agglomeration or coalescence. While the reversible magnetic agglomeration mechanism is ideal for producing zero-valent iron nanoparticles of a certain size for scale-up reactions, another goal was to also study a range of sizes that are still well dispersed in solution with strict size control. However, achieving this is a very delicate balance between iron, solvent, and surfactant concentrations along with many other factors which in turn affect nucleation. To achieve this, the effects of ligand concentration were studied in the 3-octadecyl-2,4-pentanedione reactions while keeping all other factors (i.e. heat, drip rate, total drip amount, syringe concentrations, and solvent concentration) constant.

In these reactions, nucleation is largely affected by the varying ligand concentration. For this reason, it was monitored and documented so that changes in particle sizes and dispersity can be paralleled to observations in nucleation events. Nucleation can be seen visually as iron is added to the reaction solution. The reaction mixture begins as an orange solution, then progresses to a deep orange, then to reddish-brown, and finally to a brown-black solution containing iron nuclei. A visual of these color changes and when nucleation is believed to occur is shown in Figure 5.13. For all of these reactions, nucleation was recorded at this same point. Since color changes can be perceived differently depending on the individual, the observer remained constant.

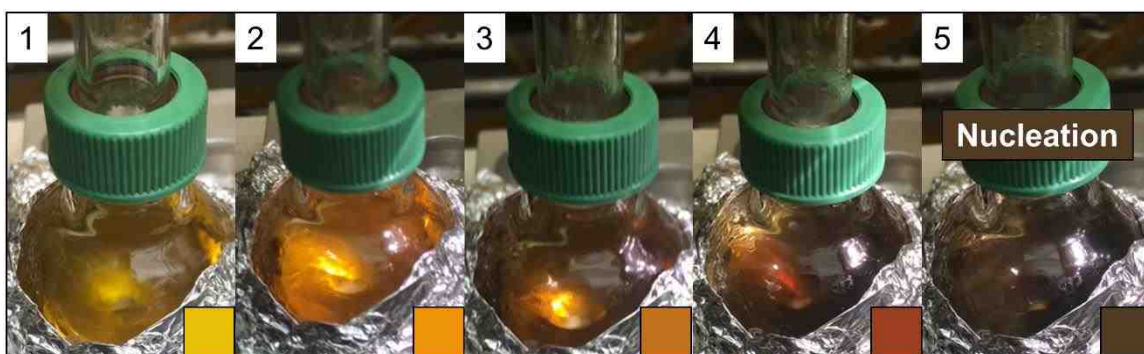


Figure 5.13 (1-5) Stages of iron precursor addition. When the iron precursor is added through the syringe the initial solution is a light-yellow color. As iron carbonyl heats up and slowly decomposes, this solution progresses to a light orange and reddish orange color. Nucleation occurs during the transition from a reddish-brown solution to a brown-black solution.

The concentration of 20 mg for the flask was chosen as it satisfied the ideal criteria previously mentioned. It produced a single nucleation event which lead to very narrow size distribution and also gave us a wider window of size control. As one can imagine, it is preferred to have a slow growth of 1.0 nm over the period of 0.5 mL iron addition versus a growth of 1.0 nm over 0.05 mL addition, where smaller errors in the concentration can have large effects on the reaction. Transmission electron micrographs and size analysis of samples prepared with varying concentrations of 5mg, 10mg, 20mg, and 40mg are shown in Figure 5.14.

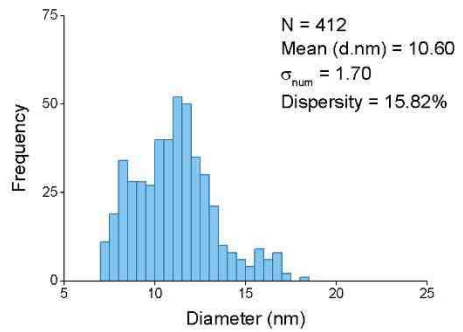
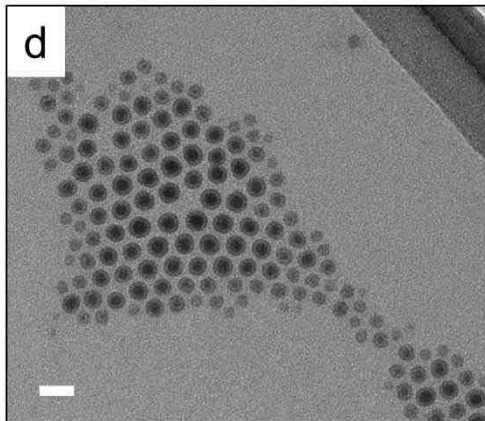
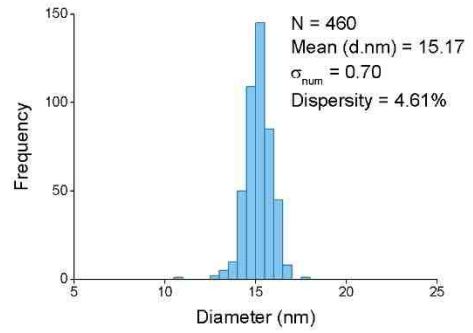
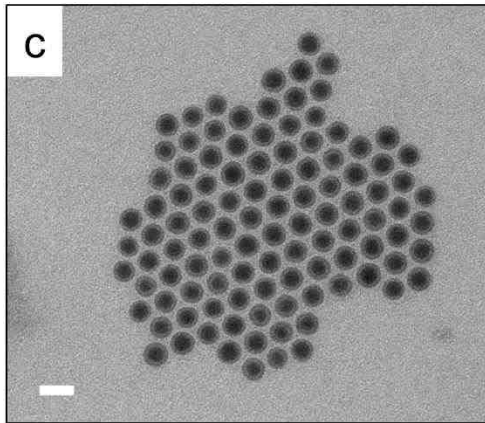
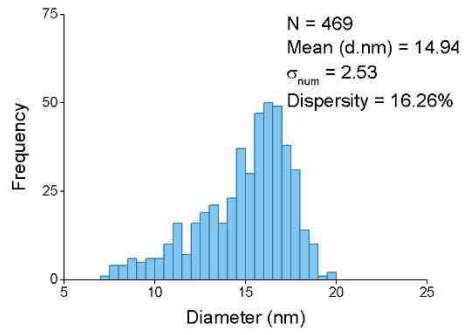
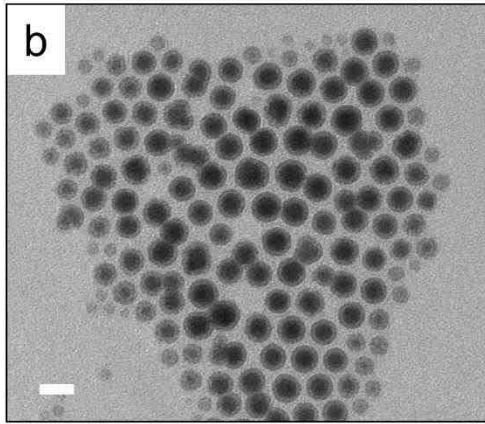
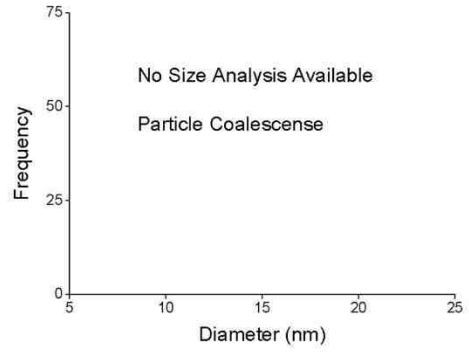
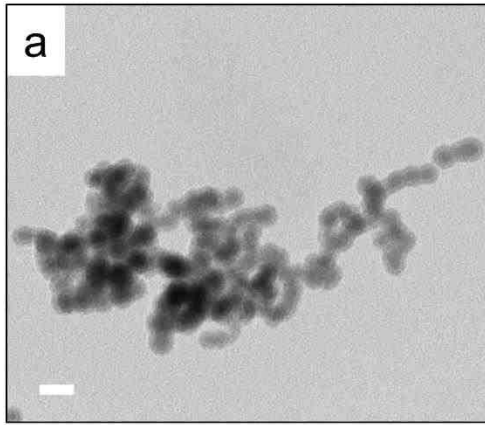


Figure 5.14 Transmission electron micrographs of iron nanoparticles synthesized using 3-octadecyl-2,4-pentanedione as the stabilizing surfactant with varying concentrations. All scale bars are equal to 20 nm. Particles synthesized with **(a)** 5 mg, **(b)** 10 mg, **(c)** 20 mg, and **(d)** 40 mg 3-octadecyl-2,4-pentanedione surfactant in starting flask.

In these reactions, it was observed that the lowest ligand concentration lead to agglomeration and particle coalescence. This is due to the combination of the particle surface not being fully passivated, the high reactivity of an unprotected iron surface, and particle magnetization. If the surfactant binding rate occurs quickly and the concentration of surfactant in solution is low, the nanoparticle surface is exposed for a longer period of time and has a higher probability of reacting with another particle. This leads to the coalescence effect seen here. For the 10 mg reaction, it can be speculated that a renucleation event has already occurred at this point which led to a larger size dispersity. As mentioned previously, it is undesirable for this reaction to have such rapid growth and agglomeration, since a main goal is to achieve a slow growth with a wide range of control. This amount produced a mean diameter of 14.9 nm with a high dispersity of 16.3%. The 20 mg reaction was the most efficient, producing a short, single nucleation event with extremely narrow size dispersity with good control. The average size for this reaction was 12.0 nm with size dispersity as low as 8.5%. For the 40 mg reaction, it was determined that a high ligand concentration in solution allows for a prolonged nucleation event, ultimately leading to a widened size distribution.

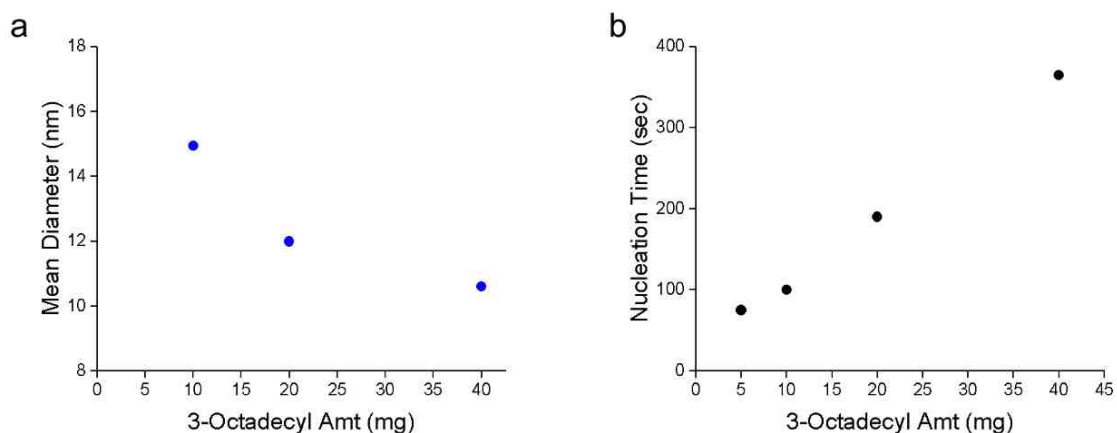


Figure 5.15 (a) Average nanoparticle sizes for reactions synthesized with 3-octadecyl-2,4-pentanedione. Amounts shown are from 10 mg, 20 mg, and 40 mg. Due to nanoparticle coalescence observed in the 5 mg reaction, it is excluded from this data. (b) Nucleation time (seconds) as a function of 3-octadecyl-2,4-pentanedione amounts. The nucleation timer is started once the first drip of the iron precursor solution is added to the solvent and surfactant.

The highest ligand concentration (40 mg) reaction allows more iron to be added to the reaction solution, which suppresses the occurrence of nucleation (Figure 5.15). Therefore, when nucleation finally occurs, a much larger number of nuclei form and due to the overwhelming amount of ligand in solution, growth is slow and more sporadic. This theory is supported through the 40 mg 3-octadecyl reaction. This reaction produced a wide range of sizes with the mean size being 10.6 nm in diameter with a dispersity of 15.8%. This is not the case with the 10 mg 3-octadecyl reaction, where the nucleation time is a fraction of the 40 mg reaction. A summary of these experiments is shown below in Table 5.3.

Table 5.3 Summary of reactions performed with increasing the amount of 3-octadecyl-2,4-pentanedione surfactant.

| Flask 3-OD (mg) | 3-OD Amt (mmol) | Mean Diameter (nm) | Size Dispersity | Nucleation Time (secs) |
|------------------------|------------------------|---------------------------|------------------------|-------------------------------|
| 5 | 1.42E-2 | - | - | 75 |
| 10 | 2.84E-2 | 14.9 | 16.3% | 100 |
| 20 | 5.67E-2 | 12.0 | 8.5% | 190 |
| 40 | 1.13E-1 | 10.6 | 15.8% | 365 |

5.3.5. Post Processing Techniques

Another goal of this research was to utilize post synthesis processing techniques of the nanoparticles, so that desired magnetic properties can be achieved post synthesis if they are not achieved initially. One approach proposed is to take an aliquot of nanoparticles and reduce them under a hydrogen-rich atmosphere (or other gases) with added thermal energy. This is the method our research utilized to discover that nanoparticle properties could in fact be altered and ultimately tailored. The results here do not go in great detail, rather summarize a few experiments which demonstrate the concept and show promising results for future research.

For these experiments, we used a stock solution of as-synthesized zero-valent iron nanoparticles with 3-octadecyl-2,4-pentanedione surfactant in 1-octadecene solvent. The hydrogenation reduction procedure is as follows:

- 1) **Parr Reactor Reduction** - This reduction method was performed in a 300 mL pressurized Parr reactor. The stock solution was transferred to a 250 mL glass

liner that fits inside the Parr reactor and it was pressurized to 250 psi with pure hydrogen gas. This solution was heated to 200°C for 24 hours with stirring to prevent particle aggregation and coalescence.

After reactions were performed, samples were transferred to an inert atmosphere glove box for further preparation and examination.

Reduction techniques schematic (Figure 5.16):



Figure 5.16 Schematic of the Parr reactor reduction set up. This set up involves a hot plate with a bored-out aluminum block which heats the reactor, producing even heating with improved heat transfer.

5.3.5.1. Results and Discussion

DC SQUID magnetometry was used to analyze the magnetic characteristics of the post processed nanoparticles. A fundamental goal of this research was to improve the saturation magnetization of the nanoparticles that might not be achievable through particle synthesis. This achievement could be confirmed through field (MvH) sweeps performed

on the SQUID magnetometer. Temperature sweeps were also performed to see how blocking temperature would be affected using this method. TEM analysis was implemented to confirm that no coalescence or agglomeration occurred with these two techniques. Detailed analysis of the reduction method is shown below.

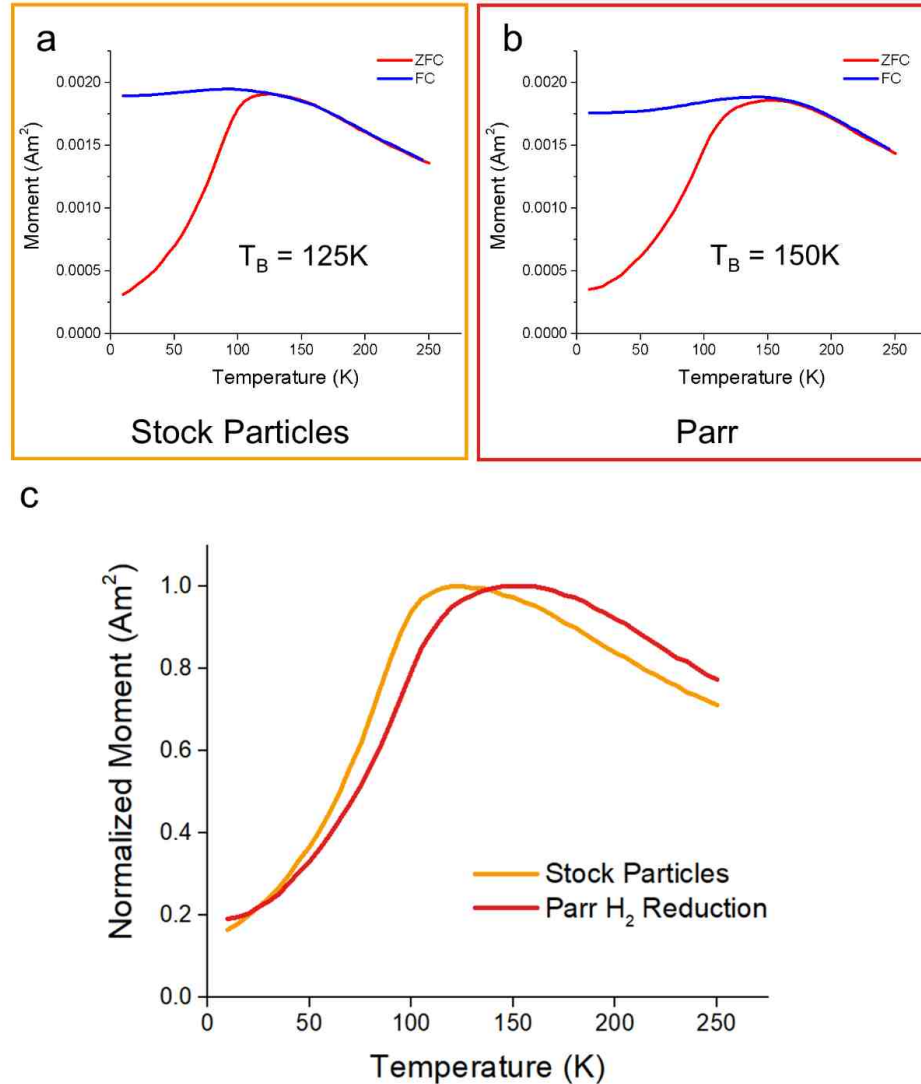


Figure 5.17 All temperature sweeps (MvT) were performed with the same sequence. For zero-field cooled measurements, sample moments were measured 5K to 250K with no applied field. For

field-cooled measurements, a weak 10 Oe field was applied and sample moments were measured from 250K down to 5K. Temperature sweeps are shown for **(a)** stock nanoparticle solution, $T_B = 125\text{K}$, and **(b)** Parr reduction product, $T_B = 150\text{K}$. **(c)** Comparison of blocking temperatures before and after Parr reduction method.

First, the blocking temperature was analyzed to see if any noticeable changes were observed. The stock nanoparticle solution originally had a blocking temperature of 125K. For the Parr reactor reduction, the blocking temperature had become slightly more widened and shifted to 150K. These results can be seen in Figure 5.17. For simplification, the Parr reactor reduction technique is labeled “Parr.”

Field sweeps were performed to determine if the reduction method was successful in improving the magnetization saturation of the samples. These measurements are shown in Figure 5.18 and the acquired information is summarized in Table 5.4.

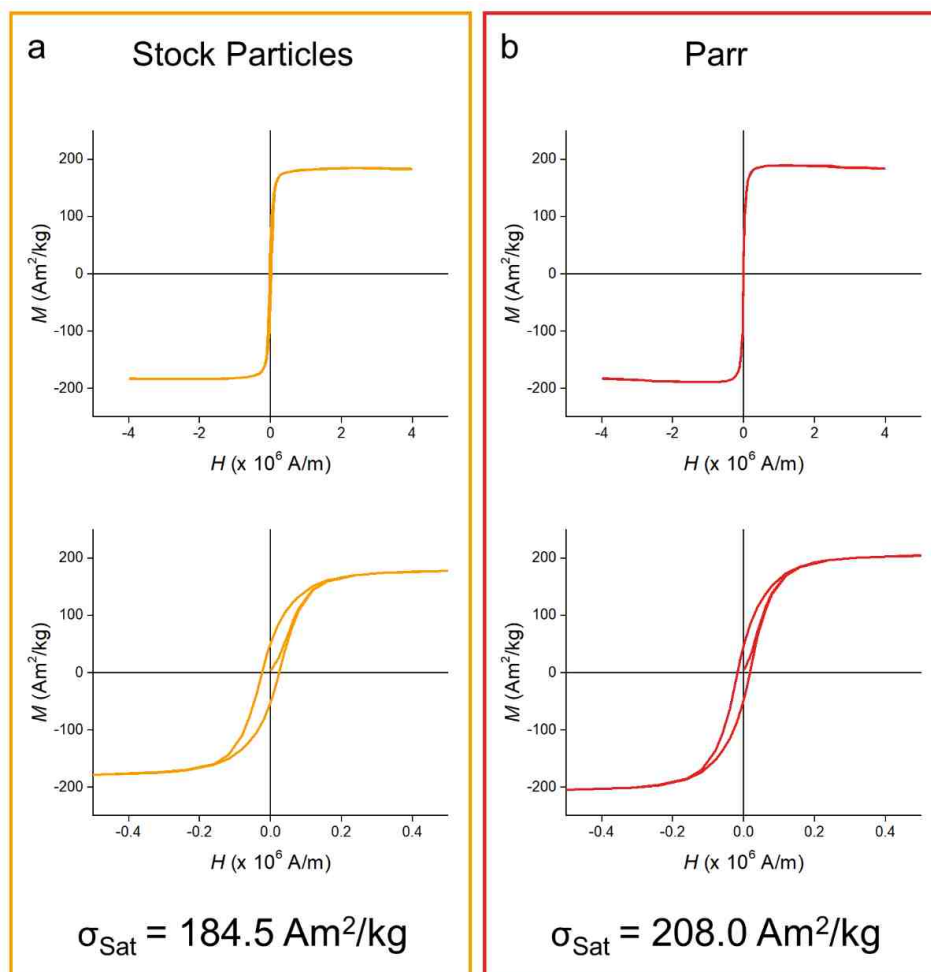


Figure 5.18 Field sweeps were performed on both samples from -5 to 5 T at 5K and 250K. Field sweeps are shown for **(a)** stock nanoparticle solution, $M_{\text{Sat}} = 184.5 \text{ Am}^2/\text{kg}$, and **(b)** Parr reduction product, $M_{\text{Sat}} = 208.0 \text{ Am}^2/\text{kg}$.

Table 5.4 Summary of properties obtained from the reduction techniques performed. The data listed is at the temperature of 5K.

| Sample | T _B (K) | M _{Sat} | M _{Sat} Difference | Remanent Field / Field at Saturation (M _R /M _S) |
|-----------------|--------------------|------------------|-----------------------------|--|
| Stock Particles | 125 | 184.5 | - | 27.9% |
| Parr | 150 | 208.0 | +12.5% | 22.7% |

It was observed that the Parr reduction method was successful in our attempt to improve the overall magnetization of these particles. The Parr reduction improved the overall magnetization saturation of the nanoparticles from 184.5 to 208.0 Am²/kg, an increase of 12.5%. Because the samples produced varied saturation values, the coercivity was calculated as a function of the highest moment obtained. This is done by taking the sample moment remaining when the applied field is 0 A/m and dividing by the highest moment obtained (saturation value). The Parr reduction method decreases the coercivity of the stock sample, reducing it from 27.9% to 22.7%.

TEM was used to observe structural changes that might have occurred following these reductions, such as full particle oxidation of a nanoparticle or particle coalescence. It was determined that the nanoparticles were visually unaltered. A slightly larger oxide shell or other artifacts were not recognized with thorough review and particles appeared to be identical from image to image, maintaining their spherical morphology and size (Figure 5.19).

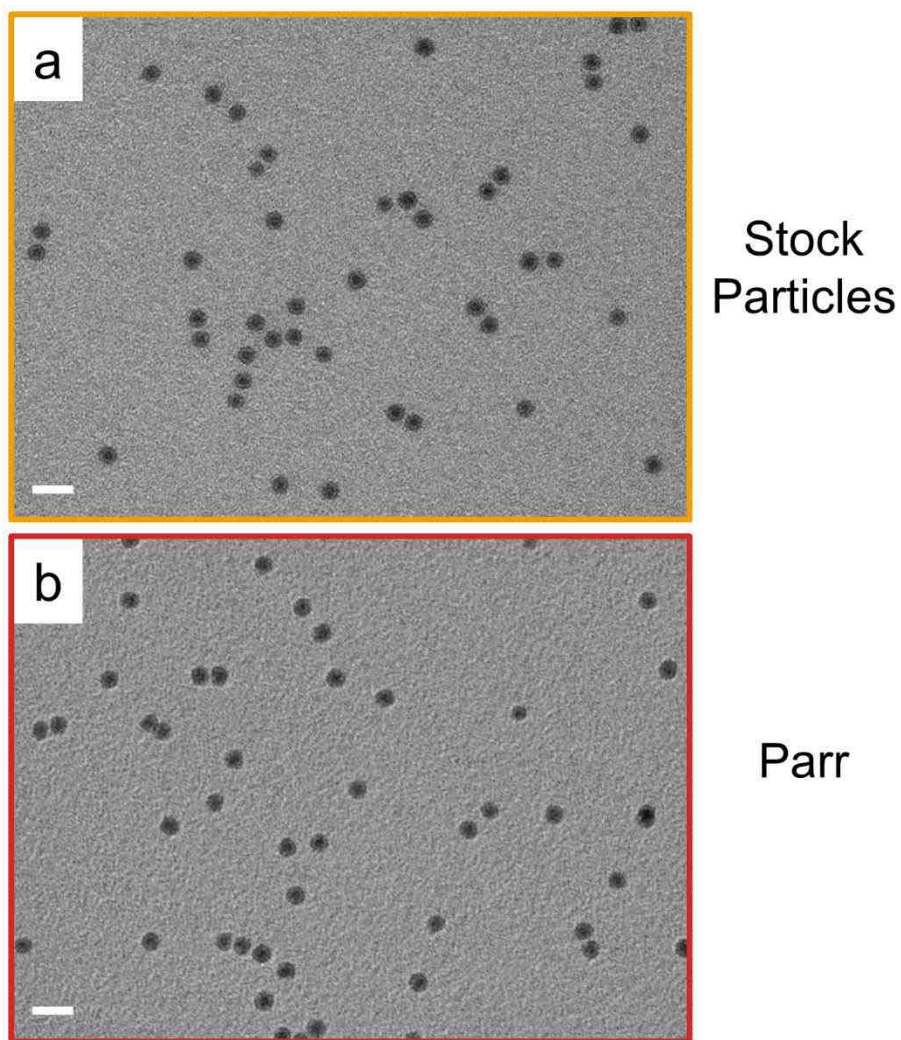


Figure 5.19 Transmission electron micrographs of (a) the stock nanoparticle sample before undergoing reduction, and (b) reduced nanoparticles using the Parr reactor technique. All scale bars represent 20 nm.

It can be concluded that both the Parr reduction techniques was successful in introducing another route to customize nanoparticle properties. This method presents a simple one-step process to achieving higher magnetic saturations while lowering coercivity, introducing an ideal post-processing technique for improving the magnetic

properties of soft magnetic nanoparticles. While the extent of the experiments and characterization accomplished was brief, it familiarizes a method which displays extremely promising results that can be researched in greater detail in the near future. While work in this specific area was brief, our goal with future experimentation is to observe how magnetic nanoparticle properties alter with varying carrier gases.

5.4. Conclusions

Highly magnetic nanoparticles with low size dispersity have been synthesized with 3-octadecyl-2,4-pentanedione surfactant using the proposed mechanism. Sizes ranged from around 8 to 20 nm with a mean maximum size of 18.6 nm in diameter. SAXS confirms this behavior by measuring the ensemble of particles to be smaller sizes at renucleation points and larger sizes when renucleated particles grow and near the mean maximum size. SQUID magnetometry confirms the superparamagnetic state of these particles and their ability to produce magnetization values nearing 96.7% of that of the value for bulk iron (222 Am²/kg). We have also shown that the ligand has pronounced effects on nanoparticle nucleation, growth, and stabilization in this system. Understanding this relationship was key to producing nanoparticles with tight shape and size control. Post-processing techniques of the as-synthesized particles allowed us to improve and alter desired nanoparticle properties, introducing customization into this system.

Chapter 6. Size Control through Modification of the Stabilizing Surfactant

6.1. Introduction

The reversible agglomeration mechanism suggests that increasing the alkyl chain length of the surfactant can delay magnetic agglomeration due to a higher level of steric stabilization. Therefore, further control over the size where nanoparticles agglomerate can be implemented simply by modifying the stabilizing surfactant used in these reactions. The introduction and variation of an alkyl chain to the 3 position on 2,4-pentanedione increases the steric stabilization, allowing the nanoparticles to grow to larger sizes before the magnetic attraction between nanoparticles overcomes this provided steric bulk. A schematic which shows the proposed agglomeration mechanism with varying surfactants is shown in Figure 6.2. To achieve this, we designed and prepared a few custom surfactants. Substitution was carried out at the 3-position with alkyl chains composed of 4 (butyl), 10 (decyl), and 18 (octadecyl) carbons to yield several different length surfactants (Figure 6.1)

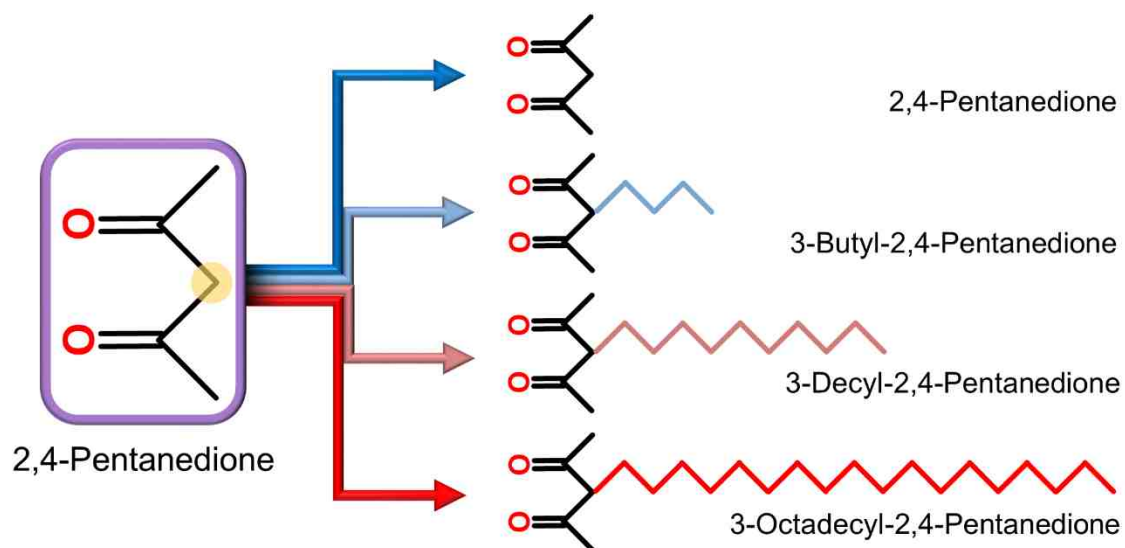


Figure 6.1 Substitution was carried out at the 3-position of 2,4-pentanedione with alkyl chains composed of 4 (butyl), 10 (decyl), and 18 (octadecyl) carbons to yield several different length surfactants.

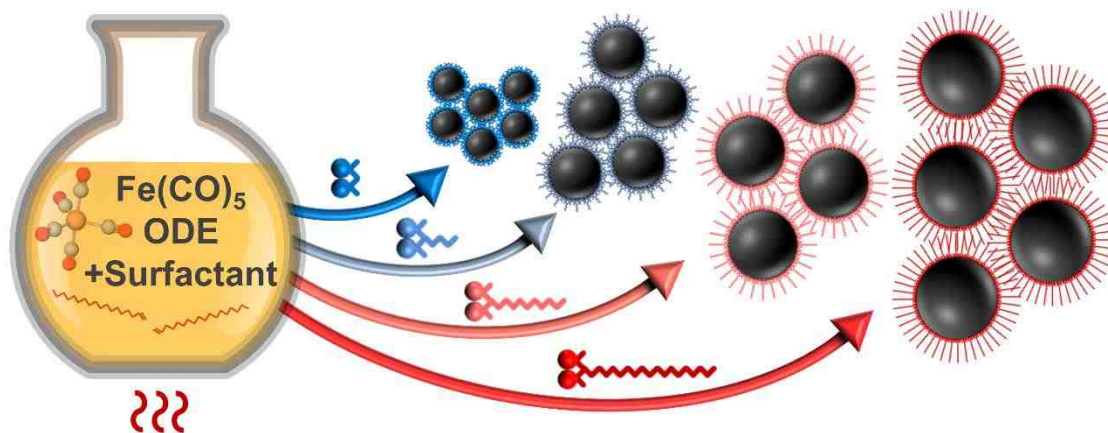


Figure 6.2 Schematic showing the proposed agglomeration mechanism with varying surfactants. The larger steric bulk provided by the surfactant allows for larger nanoparticles to be synthesized before magnetic agglomeration occurs.

6.2. Experimental

6.2.1. Materials

In addition to all the materials previously mentioned in chapter 4, 3-butyl-2,4-pentanedione (98% Alfa Aesar, CAS 216-274-1) was distilled and degassed using the same preparation as 1-octadecene.

6.2.2. Synthesis of Stabilizing Surfactants

3-Octadecyl-2,4-Pentanedione

3-Octadecyl-2,4-pentanedione was synthesized as detailed in the previous chapter (4).

3-Decyl-2,4-Pentanedione

An oven-dried 250 mL three-necked round bottom flask equipped with a condenser was charged with 1.48 g (37 mmol) of NaH (60% disp. in oil). Under a nitrogen atmosphere, 150 mL of anhydrous THF was transferred into the round bottom flask. Next, 3.33 g (33.3 mmol) of 2,4-pentanedione was added dropwise to the NaH slurry with constant stirring. The reaction was stirred for 1 hour at room temperature to ensure complete deprotonation of the 2,4-pentanedione. Additional 2,4-pentanedione was added dropwise until all NaH was dissolved. 4.96 g (19.4 mmol) of 1-iododecane was added via syringe. The mixture was then heated at 60°C for 3 days.

Once reaction was complete, the reaction solution was cooled to room temperature and neutralized with a 1M HCl solution. In a separatory funnel, the neutralized solution was extracted into ether three times. The combined ether layers were washed 3 times with

1M HCl. The final collected ether layer was then dried over magnesium sulfate. The ether solution was then gravity filtered and the product was evaporated via rotary evaporator. The product was then purified via column chromatography using 9:1 v/v hexane:ethyl acetate. After column purification, yield was 2.90g (65.2%).

6.2.3. Surfactant Characterization

^1H and ^{13}C NMR confirmed that the desired 3-substituted product was obtained as shown in the figures below.

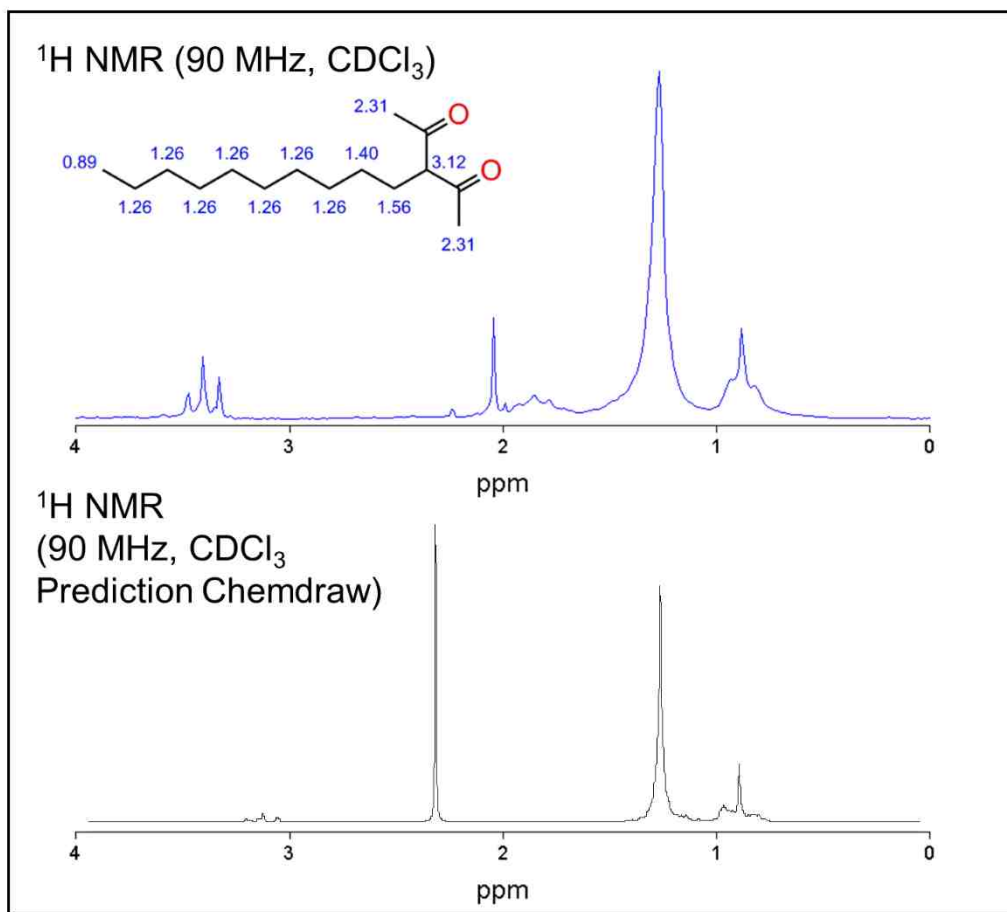


Figure 6.3 (a) Processed ^1H NMR spectra (90 MHz, CDCl_3) of the 3-decyl-2,4-pentanedione product after purification: δ 3.40 (t, 1H), 2.05 (s, 6H), 1.86 (m, 2H), 1.26 (s, 14H), 0.89 (t, 3H) (b) Predicted ^1H NMR spectra of 3-decyl-2,4-pentanedione: δ 3.12 (t, 1H), 2.31 (s, 6H), 1.56 (m, 1H), 1.40 (m, 1H), 1.26 (s, 14H), 0.89 (t, 3H).

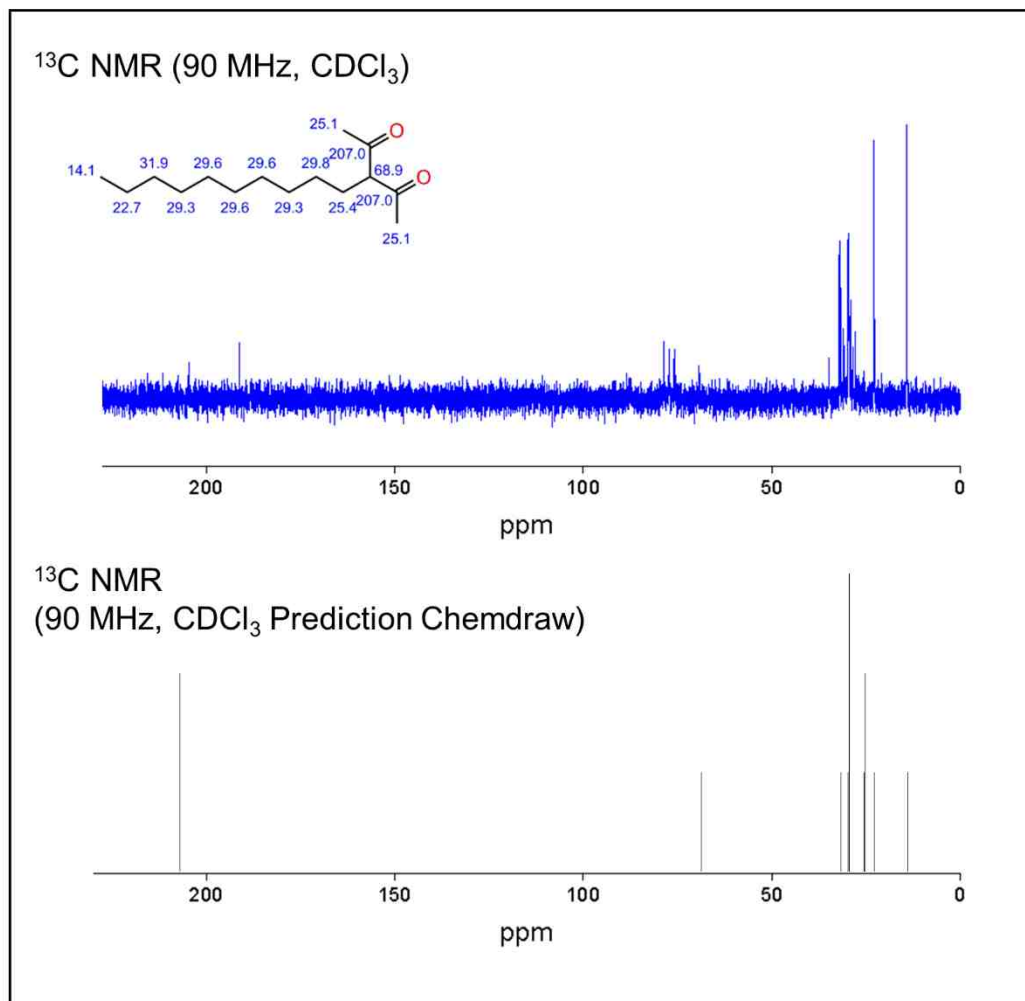


Figure 6.4 (a) Processed ^{13}C NMR spectra (90 MHz, CDCl_3) of the 3-decyl-2,4-pentanedione product after purification: δ 204.7, 191.1 69.3, 34.9, 31.8, 31.0, 29.8, 29.7, 29.6, 29.2, 27.8, 22.8,

14.2. (b) Predicted ^{13}C NMR spectra of 3-decyl-2,4-pentanedione: δ 207.0, 68.9, 31.9, 29.8, 29.6, 29.3, 25.4, 25.1, 22.7, 14.1.

6.2.4. Synthesis of Nanoparticles

Nanoparticle Synthesis Using 2,4-Pentanedione (Acac)

All chemicals were vigorously dried and degassed prior to use. All chemicals and materials were prepared in a glove box and transferred to a Schlenk line under inert atmosphere unless stated otherwise. An oven-dried Minum-Ware[®] round bottom flask was charged with 7.99 μL ($7.78\text{E-}2$ mmol) 2,4-pentanedione and 2.0 mL (6.25 mmol) 1-octadecene under a nitrogen atmosphere with controlled flow. The solution is heated to 200°C under a condenser. A syringe loaded with 59.9 μL (0.583 mmol) 2,4-pentanedione, 15 mL (4.69 mmol) 1-octadecene, and 6.0 mL (4.45 mmol) iron pentacarbonyl was slowly added dropwise to the reaction flask at a rate of 1.6 mL/hr. Amounts added ranged from 0.1 to 0.5 mL. Once the drip was completed, the reaction was allowed to proceed under a flow of nitrogen for a minimum of one additional hour. Meticulous care was taken during sample transfer to ensure nanoparticle oxidation and exposure to atmosphere was minimized.

Nanoparticle Synthesis Using 3-Butyl-2,4-Pentanedione

All chemicals were vigorously dried and degassed prior to use. All chemicals and materials were prepared in a glove box and transferred to a Schlenk line under inert atmosphere unless stated otherwise. An oven-dried Minum-Ware[®] round bottom flask was charged with 3.28 μL ($1.95\text{E-}2$ mmol) 3-butyl-2,4-pentanedione and 2.0 mL (6.25 mmol)

1-octadecene under a nitrogen atmosphere with controlled flow. The solution is heated to 200°C under a condenser. A syringe loaded with 2.36 μL ($1.40\text{E-}2$ mmol) 3-butyl-2,4-pentanedione, 1.44 mL (4.50 mmol) 1-octadecene, and 158.4 μL (1.20 mmol) iron pentacarbonyl was slowly added dropwise to the reaction flask at a rate of 1.6 mL/hr. Amounts added ranged from 0.2 to 1.4 mL (0.151 to 1.05 mmol Fe total). Once the drip was completed, the reaction was allowed to proceed under a flow of nitrogen for a minimum of one additional hour. Meticulous care was taken during sample transfer to ensure nanoparticle oxidation and exposure to atmosphere was minimized.

Nanoparticle Synthesis Using 3-Decyl-2,4-Pentanedione

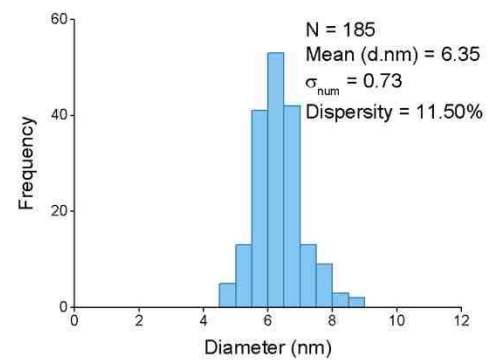
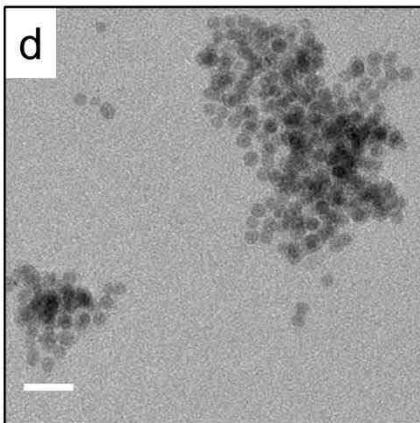
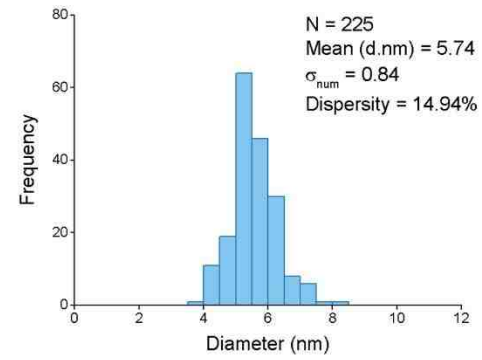
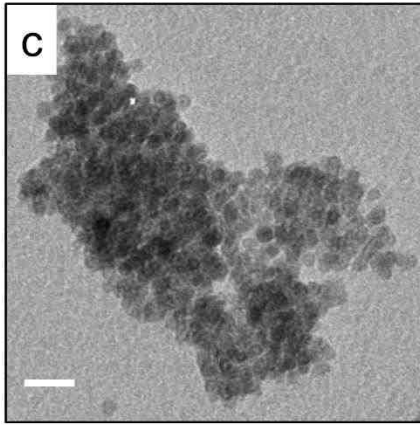
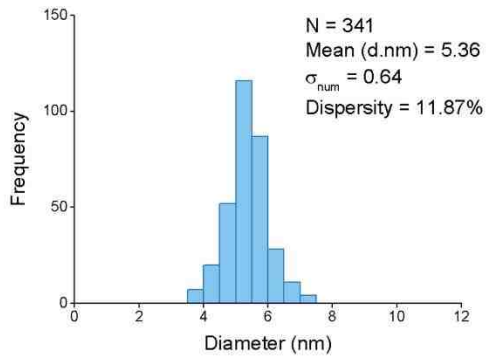
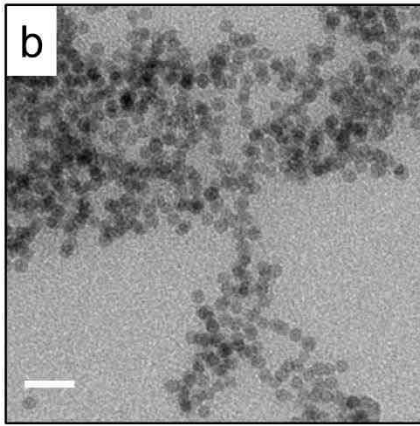
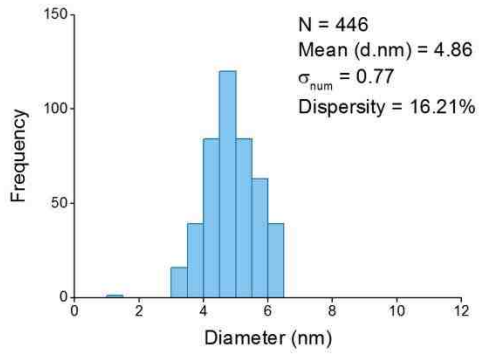
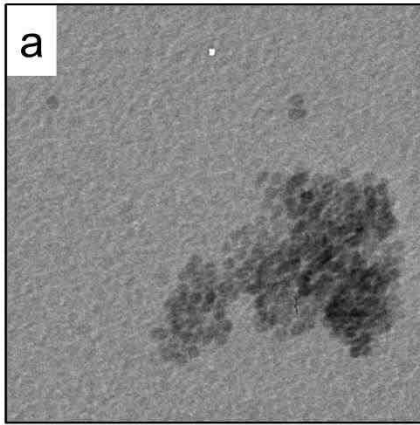
All chemicals were vigorously dried and degassed prior to use. All chemicals and materials were prepared in a glove box and transferred to a Schlenk line under inert atmosphere unless stated otherwise. An oven-dried Minum-Ware[®] round bottom flask was charged with 10.4 μL ($3.89\text{E-}2$ mmol) 3-decyl-2,4-pentanedione and 2.0 mL (6.25 mmol) 1-octadecene under a nitrogen atmosphere with controlled flow. The solution is heated to 200°C under a condenser. A syringe loaded with 78 μL (0.292 mmol) 3-decyl-2,4-pentanedione, 15 mL (4.69 mmol) 1-octadecene, and 1.5 mL (11.1 mmol) iron pentacarbonyl was slowly added dropwise to the reaction flask at a rate of 1.6 mL/hr. Amounts added ranged from 0.5 to 8.0 mL. Once the drip was completed, the reaction was allowed to proceed under a flow of nitrogen for a minimum of one additional hour. Meticulous care was taken during sample transfer to ensure nanoparticle oxidation and exposure to atmosphere was minimized.

6.3. Results and Discussion

6.3.1. 2,4-Pentanedione Surfactant

Transmission Electron Microscopy

As mentioned previously, particles synthesized with 2,4-pentanedione tend to nucleate, grow, and agglomerate on a much faster scale. This could be due to the higher surface area of these small particles, leading to greater reactivity. Slowing the growth and agglomeration of these particles was not a main focus of this work, due to the fact that a limited range of sizes are manufactured using this surfactant. TEM analysis is fairly difficult, as these particles tend to aggregate while drying for grid preparation. The smaller size also leads to a lower contrast, making particle edges difficult to distinguish. For total area size analysis in Image J, a bandpass filter was applied to enhance the edges of the particles against the carbon coated copper background. Particles were also measured manually from edge to edge to verify the validity of the measurements obtained through this method. All samples were found to be in good agreement. Transmission electron micrographs for samples prepared with 2,4-pentanedione can be seen in Figure 6.5.



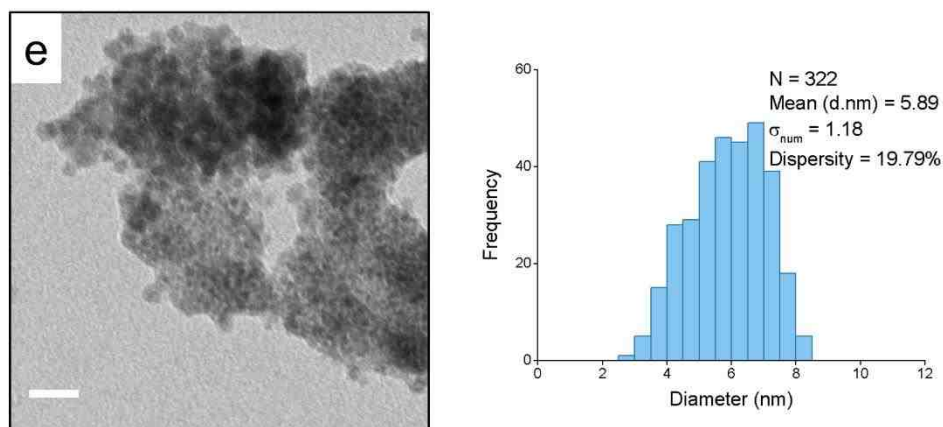


Figure 6.5 Transmission electron micrographs and their corresponding histograms produced from size analysis of iron nanoparticles synthesized using 2,4-pentanedione as the stabilizing surfactant. All scale bars are equal to 20 nm. Average nanoparticle sizes are 4.9 ± 0.8 , 5.4 ± 0.6 , 5.7 ± 0.8 , 6.4 ± 0.7 , and 5.9 ± 1.2 nm for images (a-e), respectively.

Nanoparticles were synthesized with this surfactant using total Fe additions of 0.067, 0.135, 0.202, 0.269, and 0.337 mmol for samples (a-e). Average particle sizes for these samples were 4.9 ± 0.8 , 5.4 ± 0.6 , 5.7 ± 0.8 , 6.4 ± 0.7 , and 5.9 ± 1.2 nm, respectively. Figure 6.7 below displays the average particle diameters obtained and their standard deviations (size dispersity) as a function of total iron added for the 2,4-pentanedione surfactant.

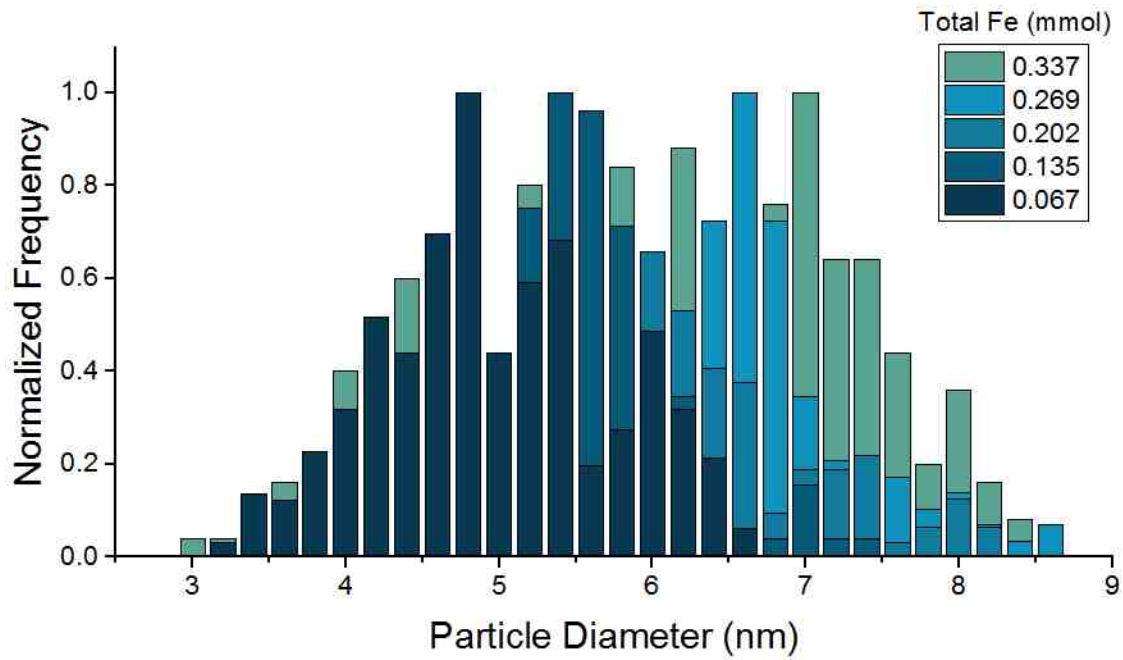


Figure 6.6 Combined histograms obtained from size analysis of transmission electron micrographs for all samples synthesized with 2,4-pentanedione surfactant.

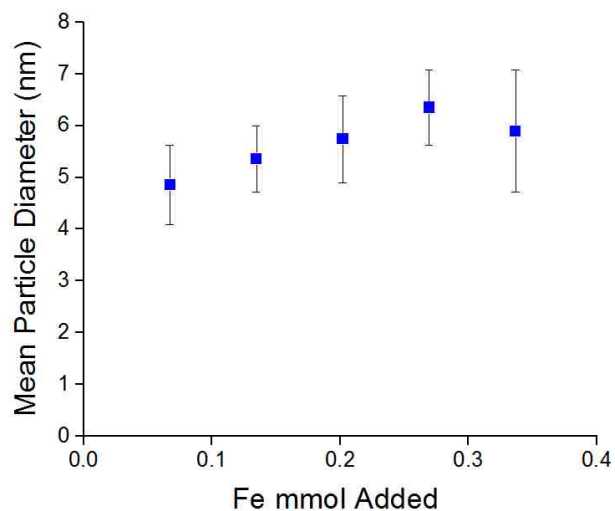


Figure 6.7 Graph of mean particle diameter (nm) vs Fe mmol addition for iron nanoparticles synthesized using 2,4-pentanedione as the stabilizing surfactant. Particle sizes for the 0.067, 0.135, 0.202, 0.269, and 0.337 Fe mmol additions were 4.9 ± 0.8 , 5.4 ± 0.6 , 5.7 ± 0.8 , 6.4 ± 0.7 , and 5.9 ± 1.2 nm, respectively. The mean maximum size obtained with this surfactant was determined to be 6.4 nm, as renucleation can be observed in the 0.337 mmol Fe addition, leading to a lower average particle size with increased size dispersity.

Table 6.1 Summary of nanoparticle size analysis obtained from transmission electron micrographs for 2,4-pentanedione surfactant.

| Amount Drip (mL) | Total Fe mmol | TEM Diameter (nm) | Size Dispersity |
|-------------------------|----------------------|--------------------------|------------------------|
| 0.1 | 0.067 | 4.9 | 16.2% |
| 0.2 | 0.135 | 5.4 | 11.9% |
| 0.3 | 0.202 | 5.7 | 14.9% |
| 0.4 | 0.269 | 6.4 | 11.5% |
| 0.5 | 0.337 | 5.9 | 19.8% |

It was noted that these particles nucleate and grow to 5 nm in diameter very quickly, then continue to grow slowly to a mean maximum size of around 6.4 nm in diameter before magnetically agglomerating and inducing renucleation. At the renucleation point there is a decrease in the mean particle diameter from 6.4 nm to 5.9 nm, along with increased dispersity 11.5% to 19.6% due to the incorporation of newly nucleated particles. Renucleation can be observed visually even within magnetic agglomerates. Both small and large particles had the propensity to agglomerate with similarly sized particles on the TEM grid during preparation and drying. Transmission electron micrographs display this behavior Figure 6.8b below.

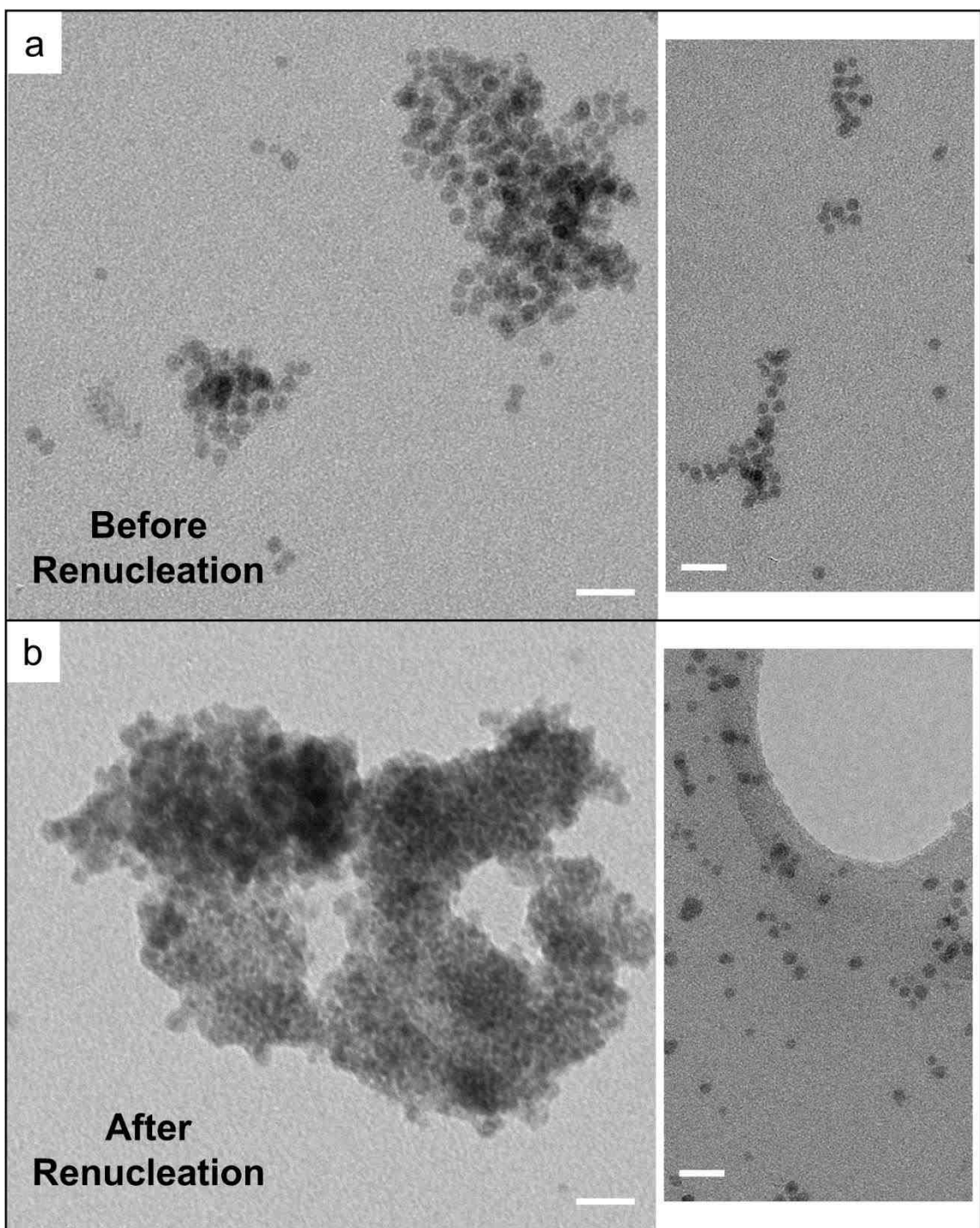


Figure 6.8 Transmission electron micrographs of iron nanoparticles synthesized using 2,4-pentanedione as the stabilizing surfactant before and after a renucleation event. All scale bars are

equal to 20 nm. **(a)** Iron nanoparticles before the renucleation event, synthesized with 0.269 mmol iron addition. Average nanoparticle size is 6.4 ± 0.7 nm (11.5% dispersity). **(b)** Iron nanoparticles after the renucleation event, synthesized with 0.337 mmol iron addition. Average nanoparticle size is 5.9 ± 1.2 nm (19.8% dispersity). A near bimodal distribution can be observed visually within magnetic agglomerates, where small and large particles had the tendency to agglomerate with similar sizes.

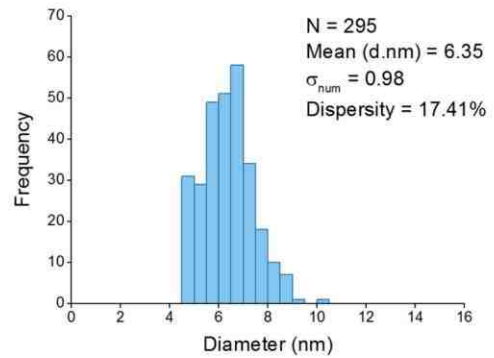
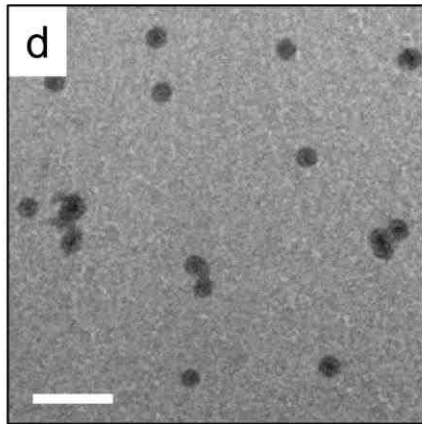
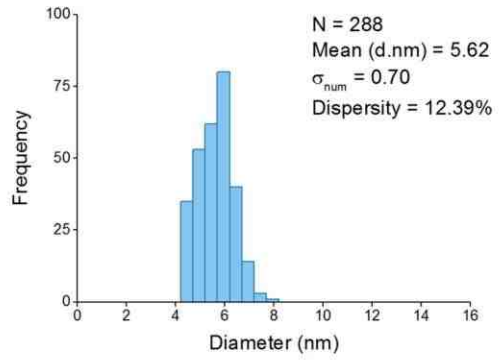
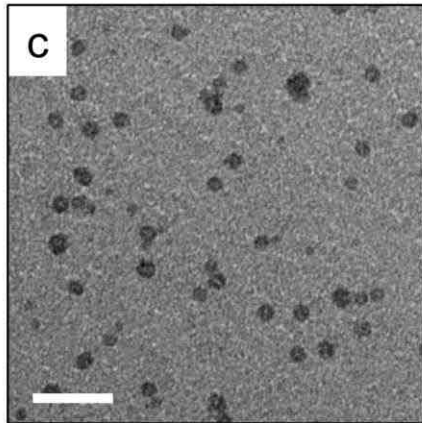
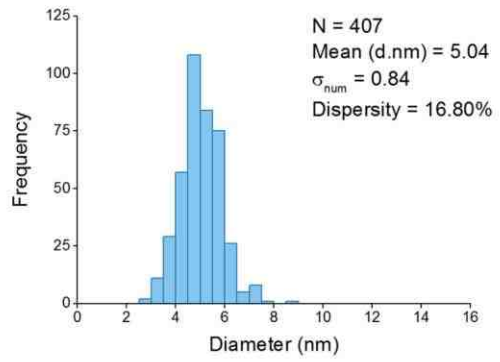
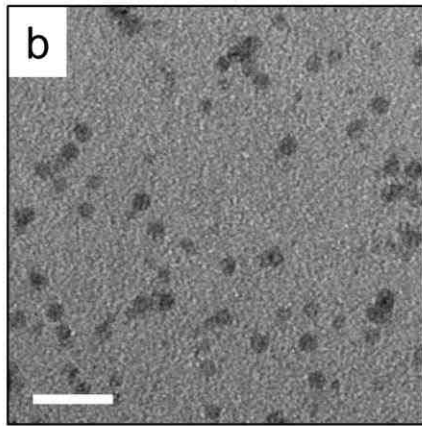
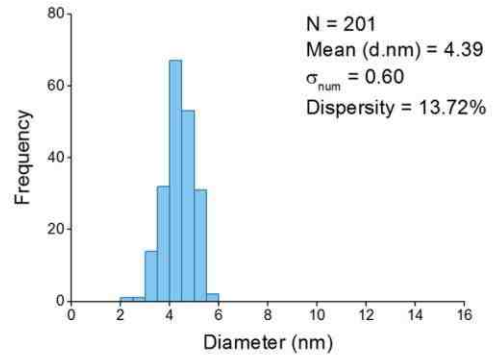
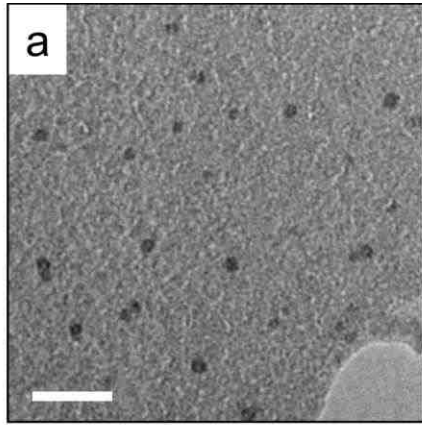
The renucleation event that occurs with 2,4-pentanedione is not easily discernible in the histograms constructed from size analysis, which is normally introduced as a bimodal size distribution. This is presumably owed to more than just a couple factors, but a few that are the most likely contenders are outlined here. First, there is a limited size range of nanoparticles that can be manufactured with this surfactant. A smaller size range increases the likelihood that the low end of a bimodal size distribution produced from a renucleation event would overlap with that of high end distribution from maximum-sized nanoparticles. Another effect is the lack of extreme size control. Although size dispersities of less than 12.0% are considered to be respectable for nanoparticles of this size, a lower-size dispersion increases the probability that a distinct bimodal distribution will emerge.

The range of nanoparticle sizes obtainable with this surfactant was determined easily through TEM size analysis. The smallest particles detected in the sample with the lowest total amount of iron (0.067 mmol) were around 3.2 nm in diameter. When renucleation occurs, the smallest particles measured that were dispersed on the grid were around 3.0 – 3.6 nm in diameter, which is in good agreement with smallest particles measured in the first sample. Therefore, it is concluded that nanoparticles utilizing 2,4-

pentanedione as the surfactant can be synthesized with sizes ranging from 3.0 to 8.6 nm in diameter.

6.3.2. 3-Butyl-2,4-Pentanedione Surfactant

Nanoparticles synthesized with 3-butyl-2,4-pentanedione grow and agglomerate on a slower scale than those employing the unalkylated 2,4-pentanedione surfactant. Thus, a larger size range was achieved and particles reached a marginally higher maximum size than that of the unalkylated surfactant before agglomeration, due to the introduced steric bulk. Beneficially, larger particle sizes in turn lead to better contrast in transmission electron micrographs, so a bandpass filter was not used for micrograph processing and nanoparticle size analysis. Transmission electron micrographs and their corresponding size analyses for nanoparticles with this surfactant are shown below.



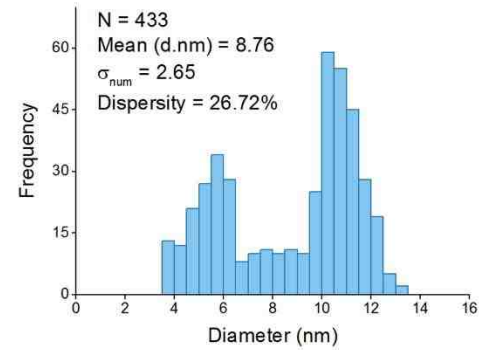
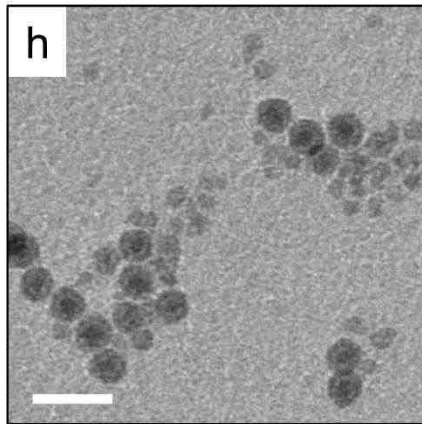
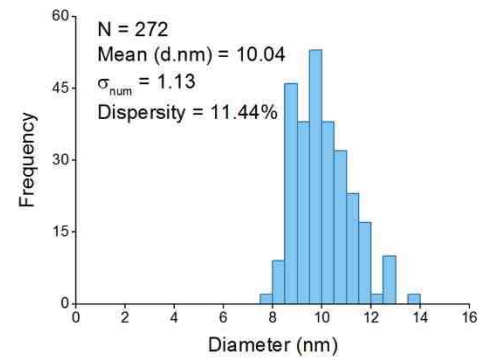
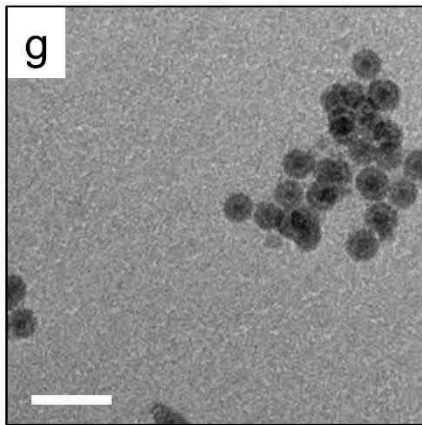
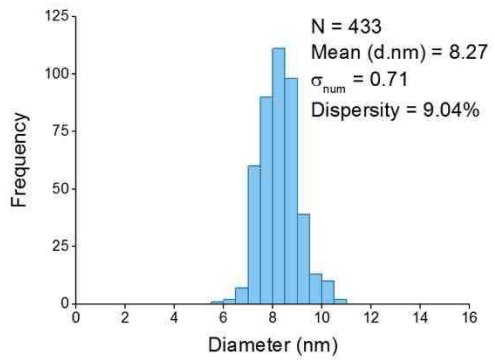
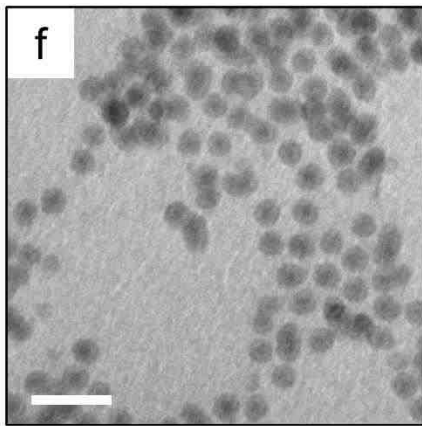
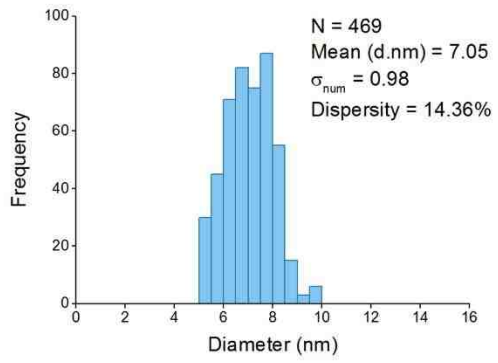
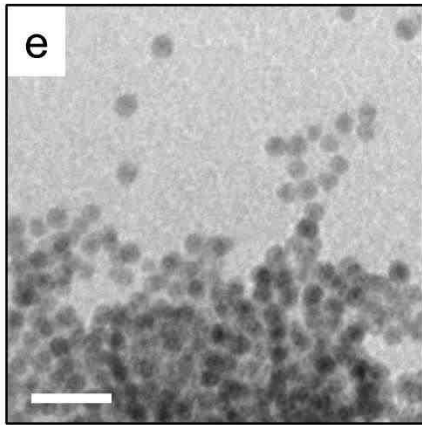


Figure 6.9 Transmission electron micrographs and their corresponding histograms produced from size analysis of iron nanoparticles synthesized using 3-butyl-2,4-pentanedione as the stabilizing surfactant. Average nanoparticle sizes are 4.4 ± 0.6 , 5.0 ± 0.8 , 5.6 ± 0.7 , 6.4 ± 1.1 , 7.1 ± 1.0 , 8.3 ± 0.7 , 10.0 ± 1.1 , and 8.8 ± 2.7 nm for images (a-h), respectively. All scale bars are equal to 20 nm.

Nanoparticles were synthesized with a 3-butyl-2,4-pentanedione surfactant using total Fe additions of 0.151, 0.226, 0.301, 0.452, 0.602, 0.753, 0.903, and 1.05 mmol for samples (a-h). Average particle sizes for these samples were 4.4 ± 0.6 , 5.0 ± 0.8 , 5.6 ± 0.7 , 6.4 ± 1.1 , 7.1 ± 1.0 , 8.3 ± 0.7 , 10.0 ± 1.1 , and 8.8 ± 2.7 nm, respectively. The average particle diameters obtained and their standard deviations (size dispersity) as a function of total iron added for the 3-decyl-2,4-pentanedione surfactant is displayed in Figure 6.10a. Similar data is plotted along with the integrated mean bimodal high and low sizes, which is shown in Figure 6.10b.

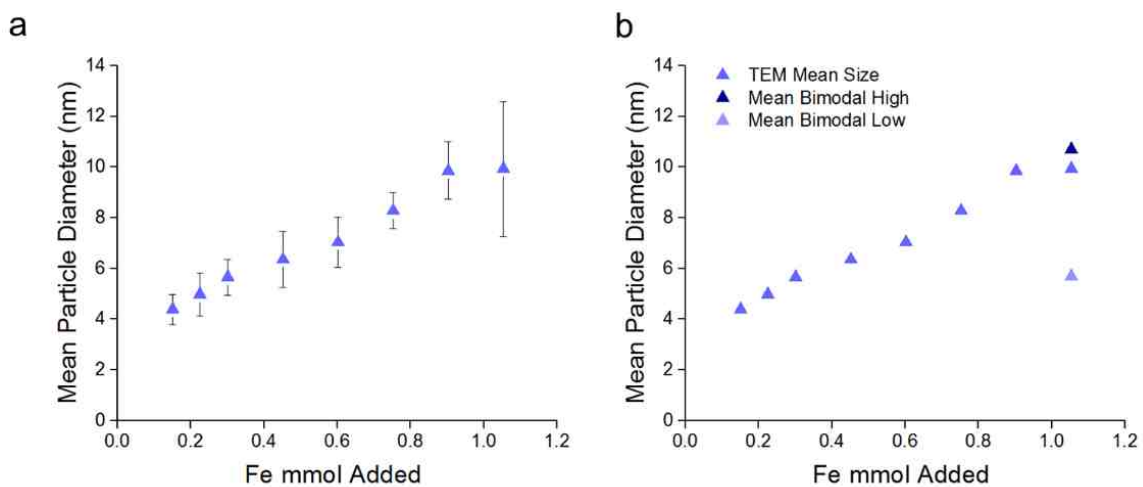


Figure 6.10 (a) Mean particle diameter (nm) vs Fe mmol addition for iron nanoparticles synthesized using 3-butyl-2,4-pentanedione as the stabilizing surfactant. Particle sizes for the

0.151, 0.226, 0.301, 0.452, 0.602, 0.753, 0.903, and 1.05 mmol Fe additions were 4.4 ± 0.6 , 5.0 ± 0.8 , 5.6 ± 0.7 , 6.4 ± 1.1 , 7.1 ± 1.0 , 8.3 ± 0.7 , 10.0 ± 1.1 , and 8.8 ± 2.7 nm, respectively. **(b)** Graph including the average high and low sizes from the bimodal distribution for the 1.05 Fe mmol reaction. The mean size for the low and high segments are 5.7 ± 1.1 nm (19.4% dispersity), and 10.7 ± 1.0 nm (9.2% dispersity), respectively.

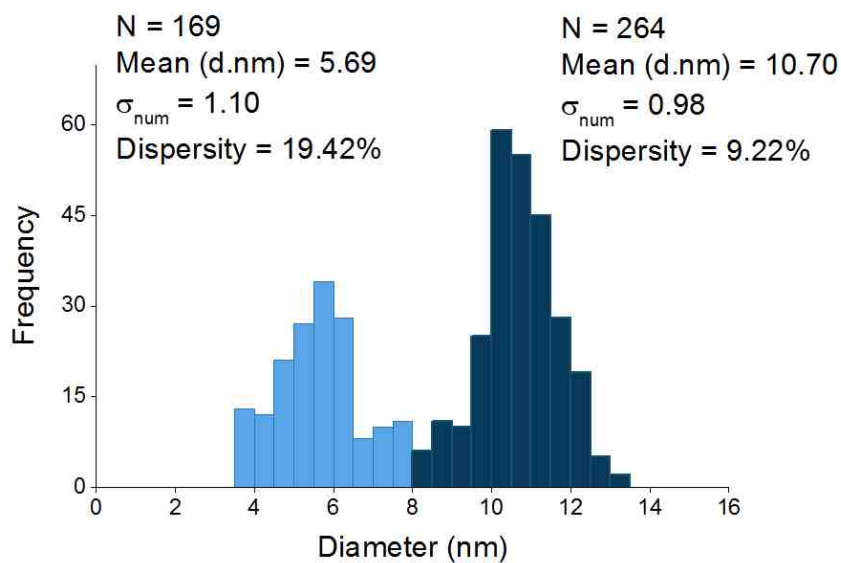


Figure 6.11 Histogram size analysis for the 1.05 Fe mmol addition which shows renucleation has occurred through a bimodal size distribution.

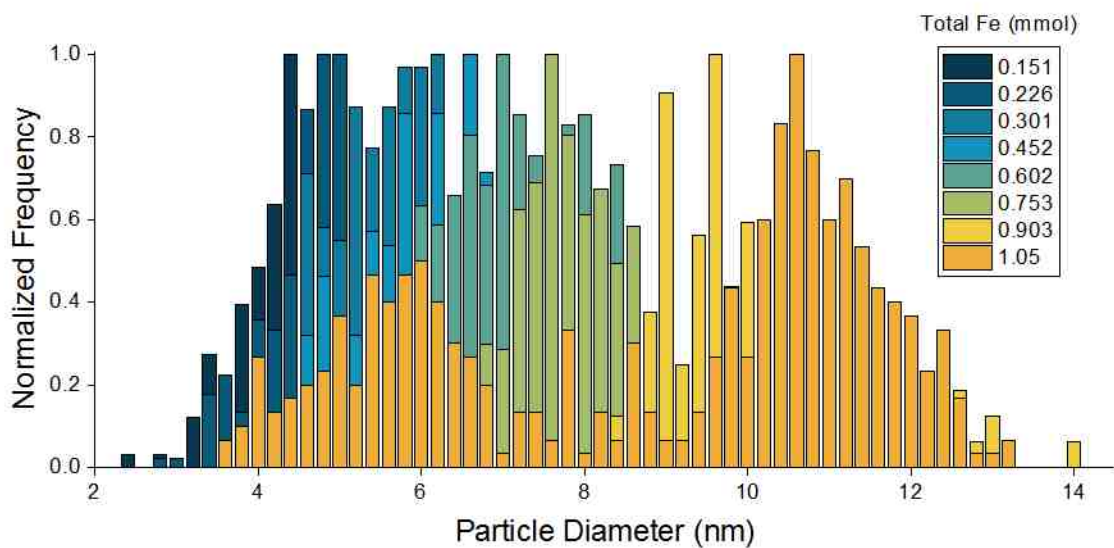


Figure 6.12 Combined histograms obtained from size analysis of transmission electron micrographs for all samples synthesized with 3-butyl-2,4-pentanedione surfactant.

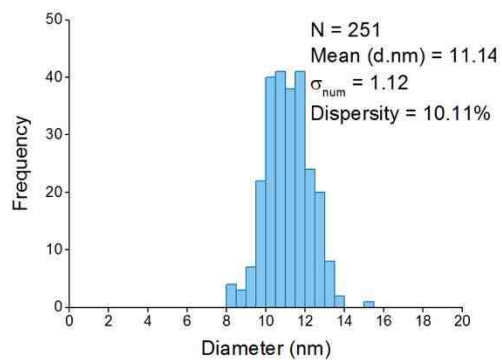
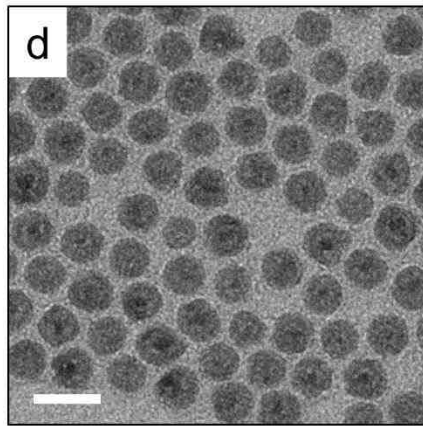
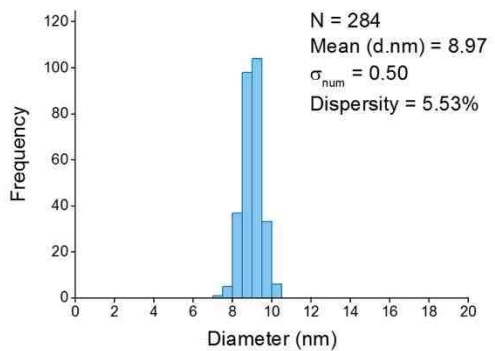
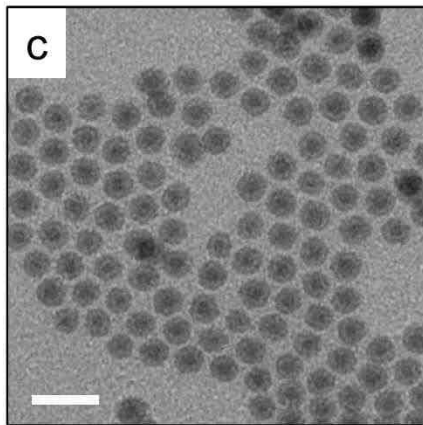
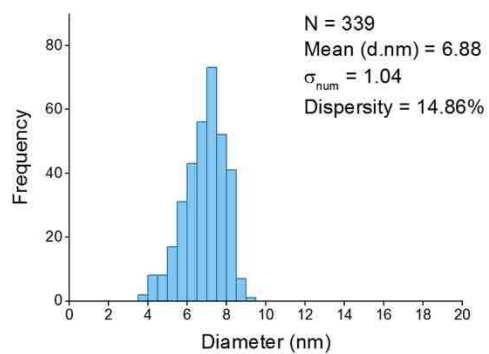
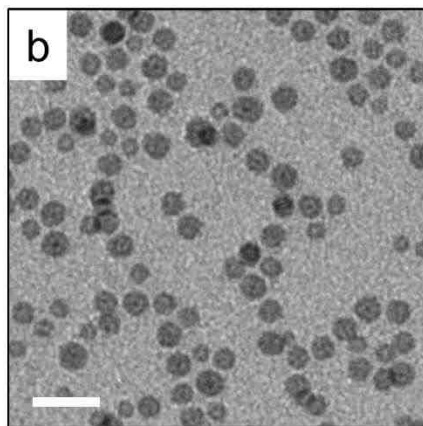
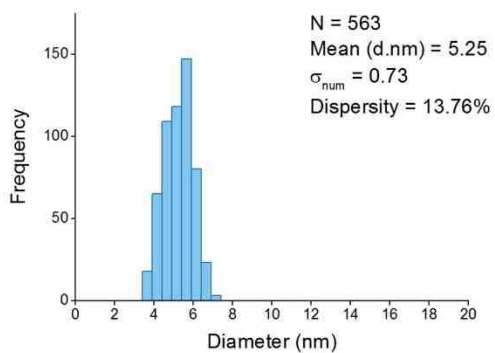
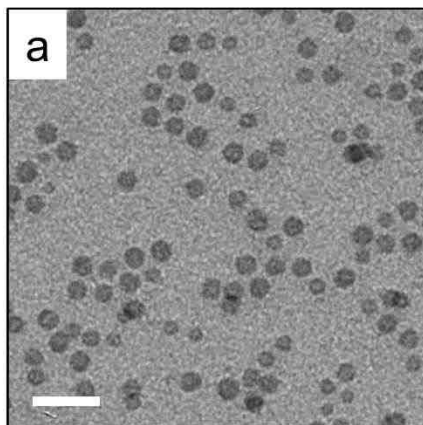
Table 6.2 Summary of nanoparticle size analysis obtained from transmission electron micrographs for 3-butyl-2,4-pentanedione surfactant.

| Amount Drip (mL) | Total Fe mmol | TEM Diameter (nm) | Size Dispersity |
|------------------|---------------|-------------------|-----------------|
| 0.2 | 0.151 | 4.4 | 13.7% |
| 0.3 | 0.226 | 5.0 | 16.8% |
| 0.4 | 0.301 | 5.6 | 12.4% |
| 0.6 | 0.452 | 6.4 | 17.4% |
| 0.8 | 0.602 | 7.1 | 14.4% |
| 1.0 | 0.753 | 8.3 | 9.0% |
| 1.2 | 0.903 | 10.0 | 11.4% |
| 1.4 | 1.05 | 8.8 | 26.7% |

Renucleation becomes more evident in reactions implementing a physically larger surfactant. This is clear through TEM size analysis with the emergence of a bimodal distribution composed of low and high segments. Similar to 3-octadecyl-2,4-pentanedione, a slightly decreased average particle size (10.0 to 8.8 nm) accompanied with a drastically larger size dispersity (11.4 to 26.7%) are genuine characteristics of the occurrence of a renucleation event. The mean maximum size attainable with this surfactant was determined to be 10.7 ± 1.0 nm. This is the mean particle size of the high component in the bimodal size distribution. Size analysis confirms that the range of sizes possible with this surfactant is around 3.0 to 13.0 nm in diameter.

6.3.3. 3-Decyl-2,4-Pentanedione Surfactant

Nanoparticles synthesized with the 3-decyl-2,4-pentanedione surfactant displayed many similarities to particles with 3-octadecyl-2,4-pentanedione surfactant with the main difference being the maximum size obtainable. Also, a lower size range was possible with this surfactant, whereas the lowest size observed with all 3-octadecyl-2,4-pentanedione reactions was around 7.0 to 8.0 nm in diameter. These particles have very narrow size dispersion, display strong magnetic attraction and possess a slow and stable growth. Transmission electron micrographs and their corresponding size analyses for nanoparticles with this surfactant are shown below.



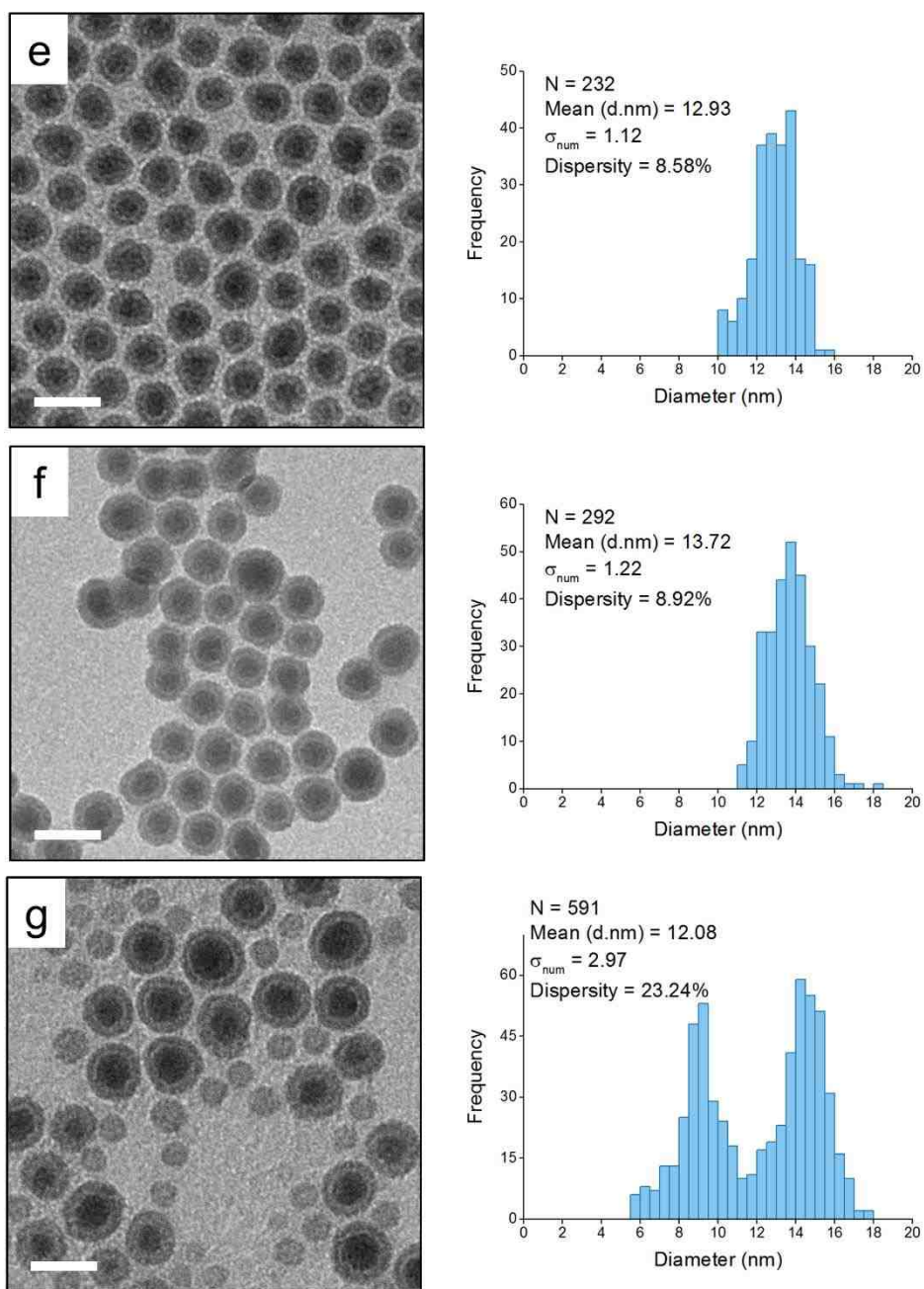


Figure 6.13 Transmission electron micrographs and their corresponding histograms produced from size analysis of iron nanoparticles synthesized using 3-decyl-2,4-pentanedione as the stabilizing surfactant. Average nanoparticle sizes are 5.3 ± 0.7 , 6.9 ± 1.0 , 9.0 ± 0.5 , 11.1 ± 1.1 , 12.9

± 1.1 , 13.7 ± 1.2 , and 12.1 ± 3.0 nm for images (a-g), respectively. All scale bars are equal to 20 nm.

Nanoparticles were synthesized with a 3-decyl-2,4-pentanedione surfactant using total Fe additions of 0.336, 0.671, 1.34, 2.01, 2.68, 3.36, and 5.37 mmol for samples (a-g). Average particle sizes for these samples were 5.3 ± 0.7 , 6.9 ± 1.0 , 9.0 ± 0.5 , 11.1 ± 1.1 , 12.9 ± 1.1 , 13.7 ± 1.2 , and 12.1 ± 3.0 nm, respectively. The average particle diameters obtained and their standard deviations (size dispersity) as a function of total iron added for the 3-decyl-2,4-pentanedione surfactant is displayed in Figure 6.14a. Similar data is plotted along with the integrated mean bimodal high and low sizes, which is shown in Figure 6.14b.

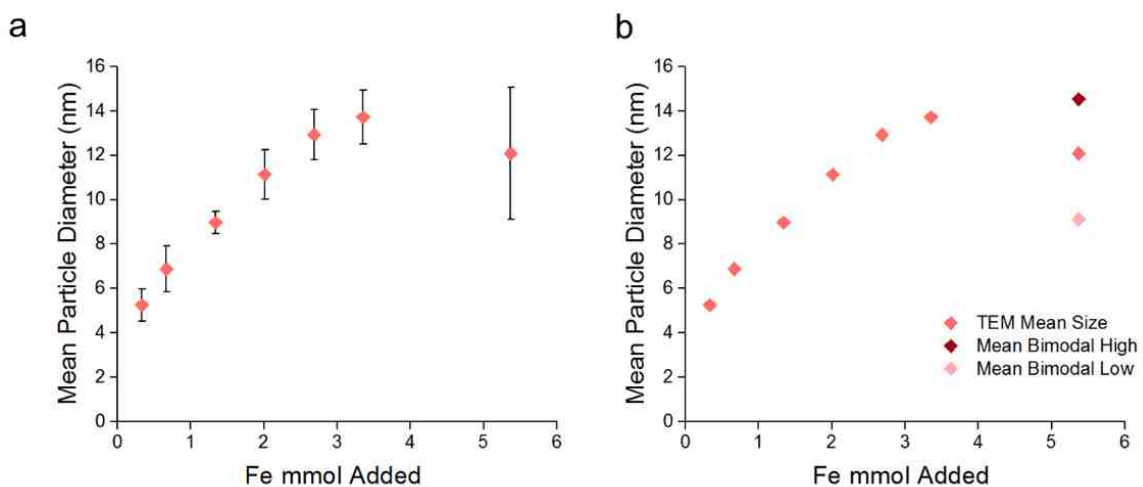


Figure 6.14 (a) Mean particle diameter (nm) vs Fe mmol addition for iron nanoparticles synthesized using 3-decyl-2,4-pentanedione as the stabilizing surfactant. Particle sizes obtained were 5.3 ± 0.7 , 6.9 ± 1.0 , 9.0 ± 0.5 , 11.1 ± 1.1 , 12.9 ± 1.1 , 13.7 ± 1.2 , and 12.1 ± 3.0 nm for the 0.336, 0.671, 1.34, 2.01, 2.68, 3.36, and 5.37 mmol Fe additions, respectively. (b) Graph including the average low and high sizes from the bimodal distribution for the 5.37 Fe mmol reaction. The

mean size for the low and high segments are 9.1 ± 1.4 nm (14.9% dispersity) and 14.5 ± 1.1 nm (7.7% dispersity), respectively.

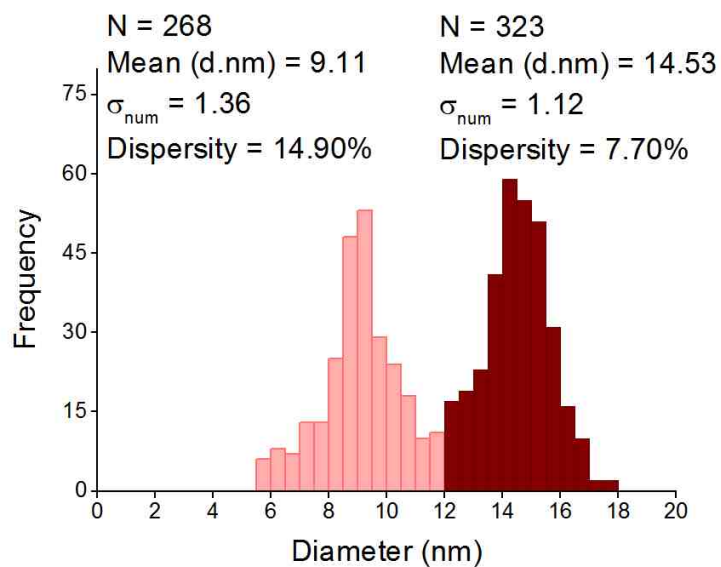


Figure 6.15 Histogram size analysis for the 5.37 Fe mmol addition which shows renucleation has occurred through a bimodal size distribution.

Table 6.3 Summary of nanoparticle size analysis obtained from transmission electron micrographs for 3-decyl-2,4-pentanedione surfactant.

| Amount Drip (mL) | Total Fe mmol | TEM Diameter (nm) | Size Dispersity |
|-------------------------|----------------------|--------------------------|------------------------|
| 0.5 | 0.336 | 5.3 | 13.8% |
| 1.0 | 0.671 | 6.9 | 14.9% |
| 2.0 | 1.34 | 9.0 | 5.5% |
| 3.0 | 2.01 | 11.1 | 10.1% |
| 4.0 | 2.68 | 12.9 | 8.6% |
| 5.0 | 3.36 | 13.7 | 8.9% |
| 8.0 | 5.37 | 12.1 | 23.2% |

Small Angle X-ray Scattering

Small angle x-ray scattering (SAXS) experiments were performed as a complementary technique to TEM which provided further size analysis. The 3-decyl-2,4-pentanedione surfactant provided enough particle stability in solution to obtain small angle x-ray scattering information. Particles synthesized with 2,4-pentanedione and 3-butyl-2,4-pentanedione aggregated and precipitated out of solution in SAXS capillary tubes. The normal surfactant exchange procedure was unsuccessful with nanoparticles capped with small surfactants, as oleic acid and oleylamine exchanges lead to dissolution of the nanoparticles leaving behind an orange-brown tinted solvent.

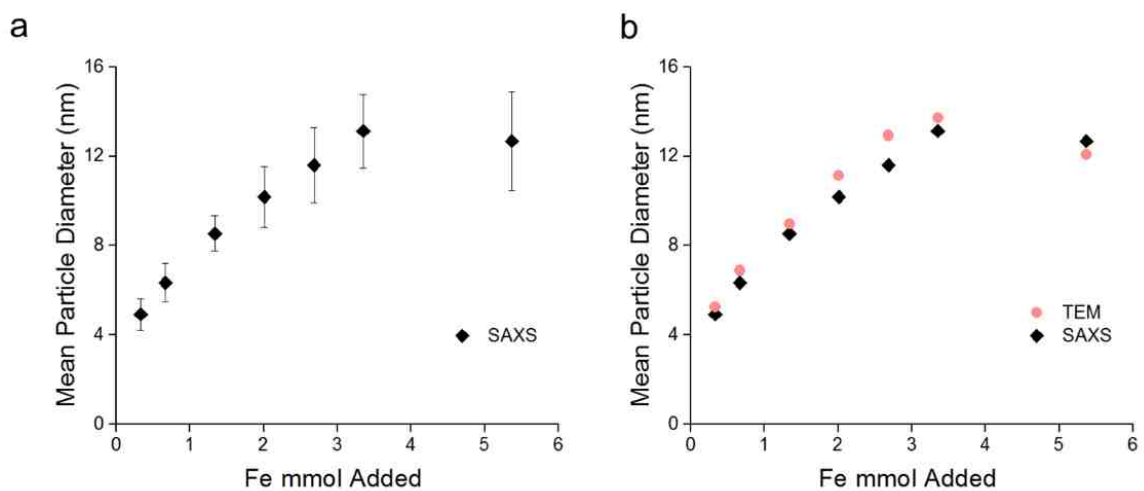


Figure 6.16 (a) Nanoparticle sizes obtained with small angle X-ray scattering (SAXS) experiments. Average nanoparticle sizes are 4.9 ± 0.7 nm, 6.3 ± 0.9 nm, 8.5 ± 0.8 nm, 10.2 ± 1.4 nm, 11.6 ± 1.7 nm, 13.1 ± 1.7 nm, and 12.7 ± 2.2 for the samples synthesized with 0.336, 0.671, 1.34, 2.01, 2.68, 3.36 and 5.37 mmol Fe additions, respectively. (b) Comparison of mean particle sizes obtained through SAXS and TEM analytical techniques.

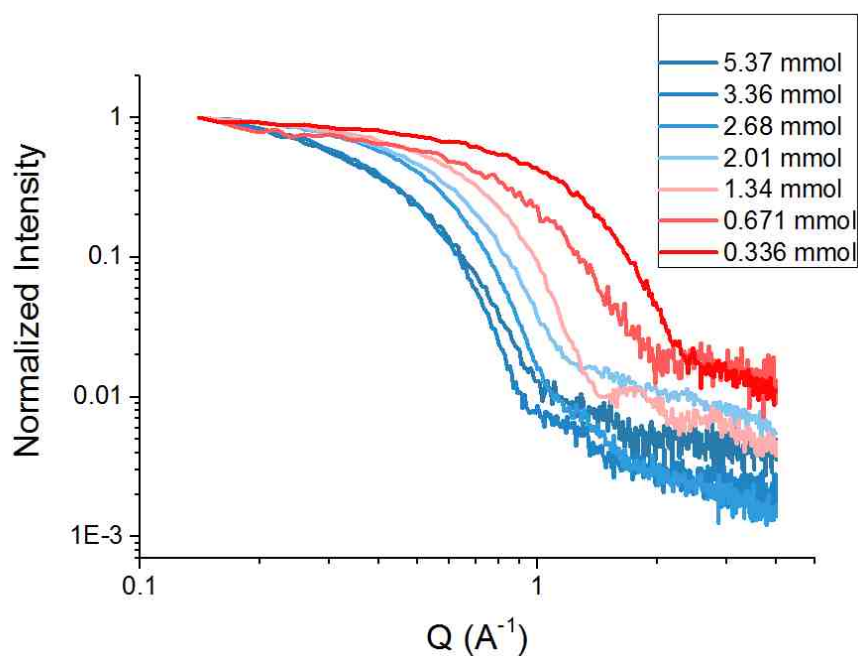


Figure 6.17 All raw experimental SAXS measurements of as-synthesized nanoparticles with 3-decyl-2,4-pentanedione surfactant. Intensity has been normalized to allow for comparison.

Table 6.4 Summary of nanoparticle size analysis obtained from small angle X-ray scattering (SAXS) for particles synthesized with 3-decyl-2,4-pentanedione surfactant.

| Amount Drip (mL) | Total Fe mmol | SAXS Diameter (nm) | Size Dispersity |
|------------------|---------------|--------------------|-----------------|
| 0.5 | 0.336 | 4.9 | 14.4% |
| 1.0 | 0.671 | 6.3 | 13.5% |
| 2.0 | 1.34 | 8.5 | 9.4% |
| 3.0 | 2.01 | 10.2 | 13.4% |
| 4.0 | 2.68 | 11.6 | 14.5% |
| 5.0 | 3.36 | 13.1 | 12.6% |
| 8.0 | 5.37 | 12.7 | 17.5% |

6.3.4. Further Characterization

X-ray diffraction was used to examine the phase of iron formed throughout these reactions. Since iron oxide phases can readily form when zero-valent iron nanoparticles are exposed to air, an air-free holder was used to maintain an oxygen-free environment. The sample holder (2392B101, shown below) was purchased directly from Rigaku.

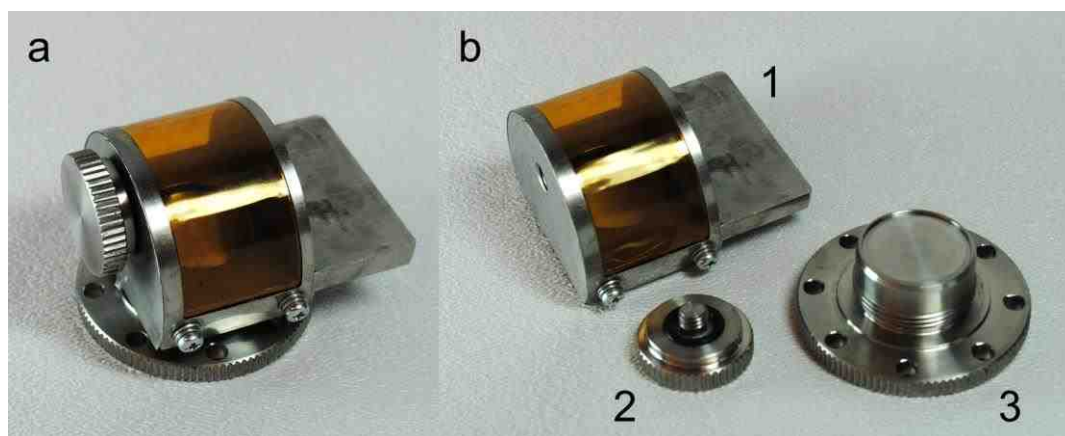


Figure 6.18 (a) Assembled air-free holder purchased from Rigaku (Part #2392B101). (b) Disassembled air-free holder, showing the sample enclosure (1), the venting plug with an O-ring seal (2), and the sample stage (3).

The sample holder was pumped into an inert atmosphere glove box, where sample preparation took place. Nanoparticles were deposited onto a glass substrate which was subsequently placed onto the sample stage. The enclosure lid was then attached to the sample stage and the venting plug was screwed in tightly to the enclosure lid. The obtained X-ray diffraction spectrum is shown in Figure 6.19.

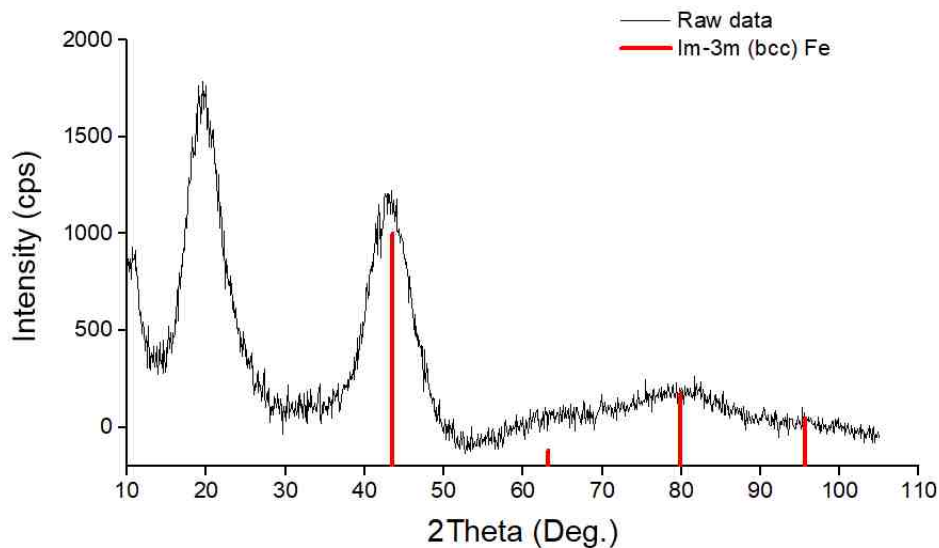


Figure 6.19 X-ray diffraction spectra obtained for the as-synthesized iron nanoparticles with 2,4-pentanedione surfactant. The red lines correspond to bcc Fe peak positions (ICSD #01-085-1410).

It can be concluded that the crystalline phase of the nanoparticles was determined to be Im-3m (bcc) through a best fit analysis. The broad peak observed at 20° 2θ is most likely from the glass substrate or organic surfactant, as it does not correspond to any crystal structure included in the ICSD database composed of Fe, Fe-C, or Fe-O. The observation of very broad peaks in the spectrum is due to the small crystallite size of the nanoparticles. These peaks were analyzed using the Scherrer equation to determine the crystallite size. Using our main peak at 43.2° 2θ and the FWHM value of 6.37° 2θ (0.111 rad, calculated using Origin software), the crystallite size is calculated to be 1.34 nm. Being that this value is smaller than what is expected from TEM size analysis (5.9 ± 1.2 nm), these particles are most likely polycrystalline. This work exhibits a strong correlation to previous work performed in our laboratory using similar methods and air-free analysis, which produced

crystalline iron nanoparticles⁶⁸. Therefore, it is strongly suggested that the as-synthesized nanoparticles are polycrystalline bcc iron nanoparticles. Although no conclusive determination could be made, this work warrants further research to be performed in the future to gain a full understanding into the crystalline nature of these particles.

Furthermore, a stronger explanation is provided through the magnetic nature observed in these samples. Amorphous iron is known to have a lower saturation magnetization than that of its crystalline counterpart. Grinstaff and Suslick *et al.* studied the magnetic properties of amorphous and crystalline Fe formed through sonochemical synthesis. They found that amorphous iron particles had a saturation magnetization of 173 Am²/kg, while the crystalline Fe particles had a corresponding value of 217 Am²/kg⁸⁶. Lacroix and Sun *et al.* also discovered similar results when producing amorphous particles in the thermal decomposition of iron pentacarbonyl. By varying the surfactant in this system, they could produce crystalline and amorphous Fe nanoparticles. The net magnetization of the crystalline particles (102 Am²/kg) was improved by a factor of 45% over the amorphous nanoparticles (70 Am²/kg)⁵⁸. Because the saturation magnetization of nanoparticles formed in our system is 97% of the value for bulk iron (222 Am²/kg), it strongly supports this theory.

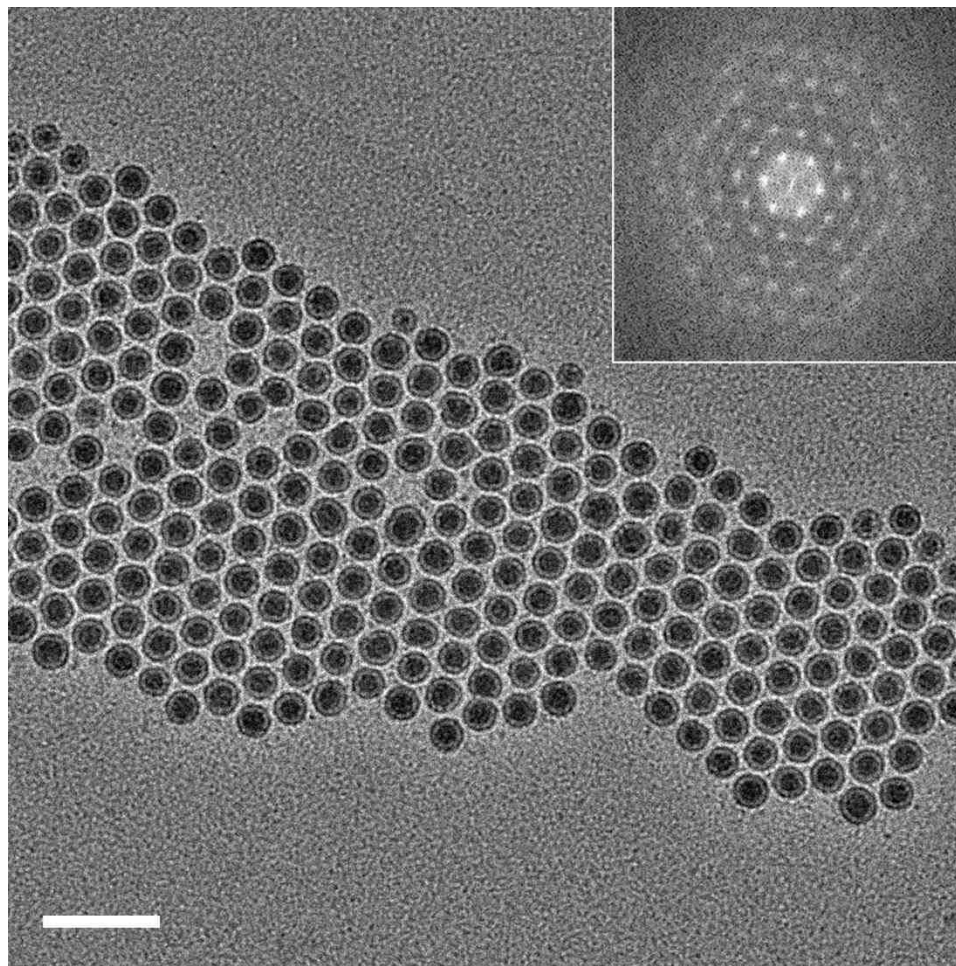


Figure 6.20 High resolution TEM image of a cluster of iron nanoparticles. Scale bar represents 50 nm. (**Inset**) FFT pattern obtained showing the hexagonal close packing of the nanoparticles.

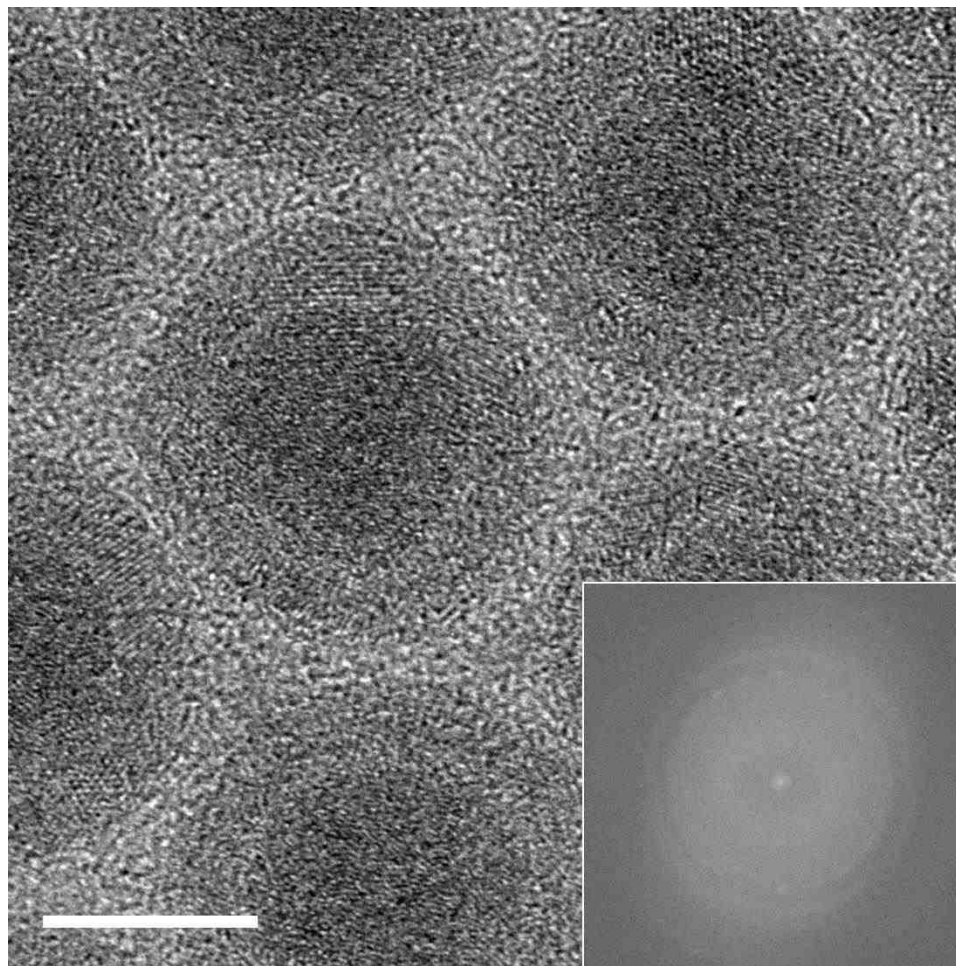


Figure 6.21 High resolution TEM of a single zero-valent iron nanoparticle. Scale bar represents 5 nm. **(Inset)** Selected area electron diffraction (SAED) of particles shown in transmission electron micrograph.

High-resolution TEM (HRTEM) was used to further analyze the composition of the nanoparticles as seen with X-ray diffraction. Because the TEM used was not equipped with air-free sample transfer capabilities, the oxide shell present is most likely due to sample preparation in an open atmosphere. Crystalline nature can be observed in the oxide shell,

but no structural determinations could be made from the nanoparticle core. Although there appears to be the lack of crystallinity, its appearance could be due to the oxide shell.

6.3.5. Summary of All Surfactants

A variety of surfactants varying in length were implemented to ultimately control the size at which nanoparticles agglomerate by increasing steric bulk at the surface. Estimated surfactant lengths were calculated using Chemdraw to be 2.6 Å, 7.9 Å, 14.5 Å, and 24.7 Å for 2,4-pentanedione, 3-butyl, 3-decyl, and 3-octadecyl, respectively. Estimated lengths were obtained by measuring in a head to toe fashion, from the ketone head to the furthestmost hydrogen on the fully elongated alkyl chain.

Initial calculations were performed to estimate the size at which particles will magnetically agglomerate in the presence of different surfactants. Calculations used these surfactant lengths to account for the magnetic reduction from the surfactant. The size at which particles will agglomerate in a given system is dependent on the magnetic susceptibility of the nanoparticle. The susceptibility of the nanoparticle core can be represented by χ_c . To account for the steric stabilization provided by the surfactant which is considered a non-magnetic layer, the magnetic susceptibility of the nanoparticle and surfactant ensemble (χ_e) is represented by (Eq. 6.1).

Here, the overall magnetic susceptibility of the nanoparticle and surfactant shell is the product of the magnetic susceptibility of the nanoparticle core and the volume ratio of the nanoparticle to nanoparticle with surfactant. This ratio is calculated using the radius of the nanoparticle core radius (r_c), and the surfactant length (r_s).

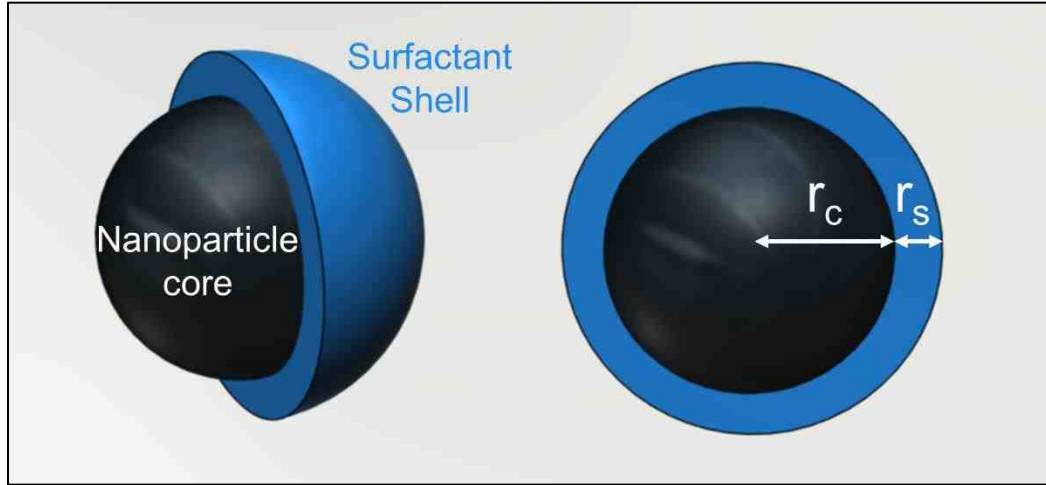


Figure 6.22 Image showing the radius of the nanoparticle core (r_c) and shell (r_s).

$$\chi_e = \chi_c \left(\frac{\frac{4}{3}\pi r_c^3}{\frac{4}{3}\pi (r_c + r_s)^3} \right) \quad (\text{Eq. 6.1})$$

Which can be simplified to:

$$\chi_e = \chi_c \left(\frac{r_c^3}{(r_c + r_s)^3} \right) \quad (\text{Eq. 6.2})$$

This equation accounts for the non-magnetic layer provided by the surfactant, treating the susceptibility of the nanoparticle with surfactant as a whole. Simulated experiments performed by Martin and Huber *et al.* demonstrate that collective particle interactions can be separated into three regimes. The “weak collective interaction” regime occurs when $\chi_e < 3$, where magnetic interactions are smaller than multi-domain particles.

This arises most likely due to a nanoparticle with low-spin density or is capped with a thick non-magnetic layer or oxide. The “strong collective interaction” regime occurs when χ_e lies between 3 and 5. Stronger collective magnetism is expected here, yet the possibility for particles to remain dispersed still exists. The last regime is for χ_e values greater than 5, which is called the “domain formation” regime. This is where the magnetic interactions between particles can cause significant clustering and agglomeration. For this reason, it is expected that magnetic susceptibility should be in the proximity of or slightly greater than this value depending on reaction conditions.

Theoretical Calculations of Nanoparticle Core Susceptibility (χ_c)

To calculate the overall susceptibility of the nanoparticle core and shell ensemble we must first calculate the susceptibility of the nanoparticle core, χ_c . We use the Langevin function to account for the reduction in overall magnetic moment attributed to the steric bulk provided from all surfactants, as well as the reduced M_{sat} due to the high reaction temperature. Experimental data shows that magnetization can be approximated as linear in the low magnetic field range of -1.0×10^5 A/m to 1.0×10^5 A/m (-0.1 to 0.1 T), as seen in Figure 6.23. Therefore, we can calculate particle susceptibility at low fields, which becomes a good approximation for initial susceptibility.

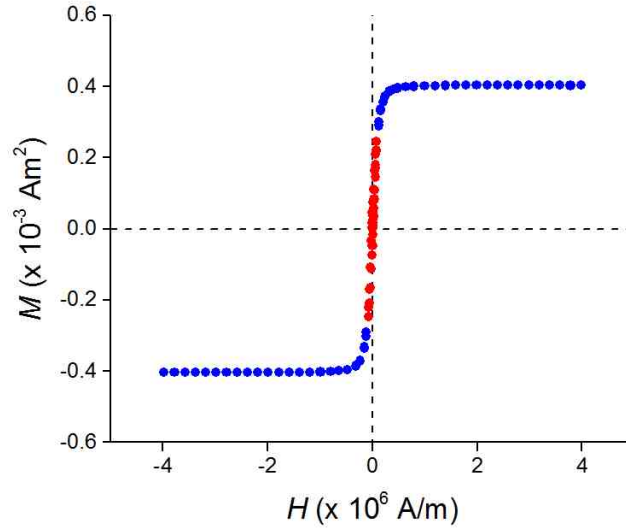


Figure 6.23 Hysteresis curve displaying the low magnetic field range utilized in calculations where susceptibility remains constant.

We began by calculating the dynamics for an ensemble of particles in low fields and high temperature by using the Langevin function.

$$L(x) = \coth(x) - \left(\frac{1}{x}\right) \quad (\text{Eq. 6.3})$$

$$x = \frac{\mu_0 M_{Sat} V \rho H_0}{k_B T} \quad (\text{Eq. 6.4})$$

Where μ_0 is the vacuum permeability of free space ($1.257 \times 10^{-6} \text{ m kg/s}^2 \text{ A}^2$), M_{Sat} is the magnetization saturation at reaction temperature, V is the nanoparticle volume, ρ is the density of iron (7870 kg/m^3), H_0 is the magnetic field ($1.0 \times 10^5 \text{ A/m}$), k_B is Boltzmann's

constant ($1.38 \times 10^{-23} \text{ kg m}^2/\text{s}^2 \text{ K}$), and T is the reaction temperature. We then calculate the nanoparticle moment by:

$$m_p = S\mu_B L(x) \quad (\text{Eq. 6.5})$$

Where S is the total number of spins per particle and μ_B is the value for a Bohr magneton (9.27×10^{-24} units). The moment is then used to calculate the magnetic susceptibility of the nanoparticle, χ_c , at low field. Here, χ_c represents the magnetic susceptibility of the “core”, not accounting for the surfactant.

$$\chi_c = \frac{m_p}{VH_0} \quad (\text{Eq. 6.6})$$

Using the values obtained from (Eq. 6.6) for the range of nanoparticle sizes, we can calculate the magnetic susceptibility for the nanoparticle ensemble, χ_e , to account for the magnetic reduction provided by the surfactant. The maximum nanoparticle size can be tailored through surfactant length modification as seen in the plotted calculations below (Figure 6.24).

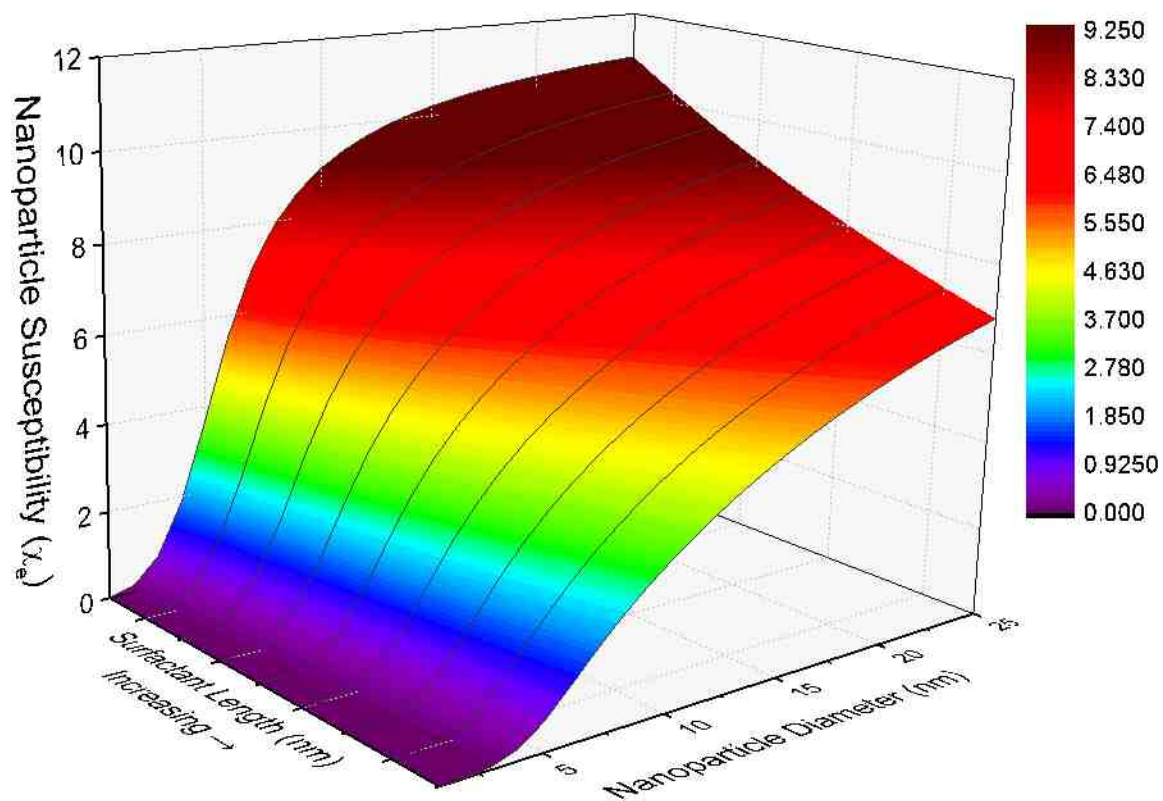


Figure 6.24 3D color map constructed from theoretical calculations for nanoparticle susceptibility with increasing size and surfactant length (nm).

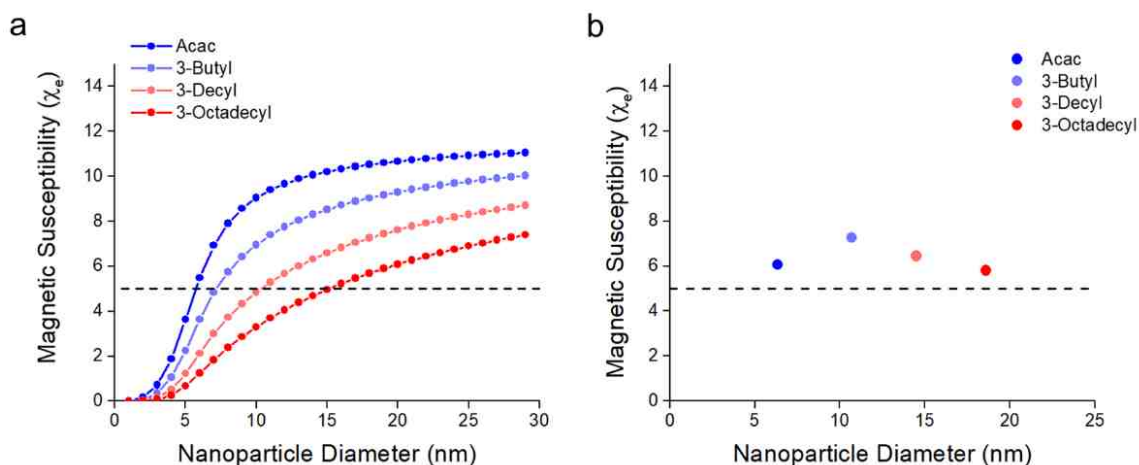


Figure 6.25 (a) Theoretical calculations for the magnetic susceptibility (χ_e) of zero-valent iron nanoparticles synthesized with surfactants varying in length. The magnetic susceptibility for the “domain formation” regime is plotted linearly at $y = 5$. For any given surfactant, nanoparticle sizes in close proximity to this line can provide an expected range for the maximum nanoparticle size obtainable before agglomeration and precipitation occurs. (b) Calculated susceptibilities for the obtained experimental sizes were 6.05, 7.27, 6.44, and 5.80 for nanoparticle diameters of 6.4, 10.7, 14.5, and 18.6 nm, respectively.

Our experimental data displays results that are very similar to what was predicted through theoretical calculations. In Figure 6.25a it is observed that at the low field susceptibility value where magnetic agglomeration occurs, nanoparticles with a larger surfactant should agglomerate at a much larger size than those with shorter alkyl chain surfactants. Experimentally agglomerated sizes were 6.4, 10.7, 14.5 and 18.6 nm, which corresponds to calculated susceptibilities of 6.05, 7.27, 6.45, and 5.80, respectively (Figure 6.25b). A value of $\chi_e = 5$, defined as the onset of agglomeration, is also depicted in Figure 6.25b. The calculated values for susceptibility were somewhat higher, although a value of

5 is considered the point of initial interparticle interaction. In a real system, this value might be slightly higher due to incomplete collision before the full onset of agglomeration, allowing for further nanoparticle growth.

Displayed below are the mean nanoparticle sizes obtained for reactions with varying surfactant sizes under the same conditions applied for theoretical calculations (Figure 6.26). Similar to what is seen in theoretical calculations, nanoparticles with increasing surfactants lengths are allowed to grow to larger sizes due to the increased steric stabilization at the surface and magnetic suppression provided by the surfactant.

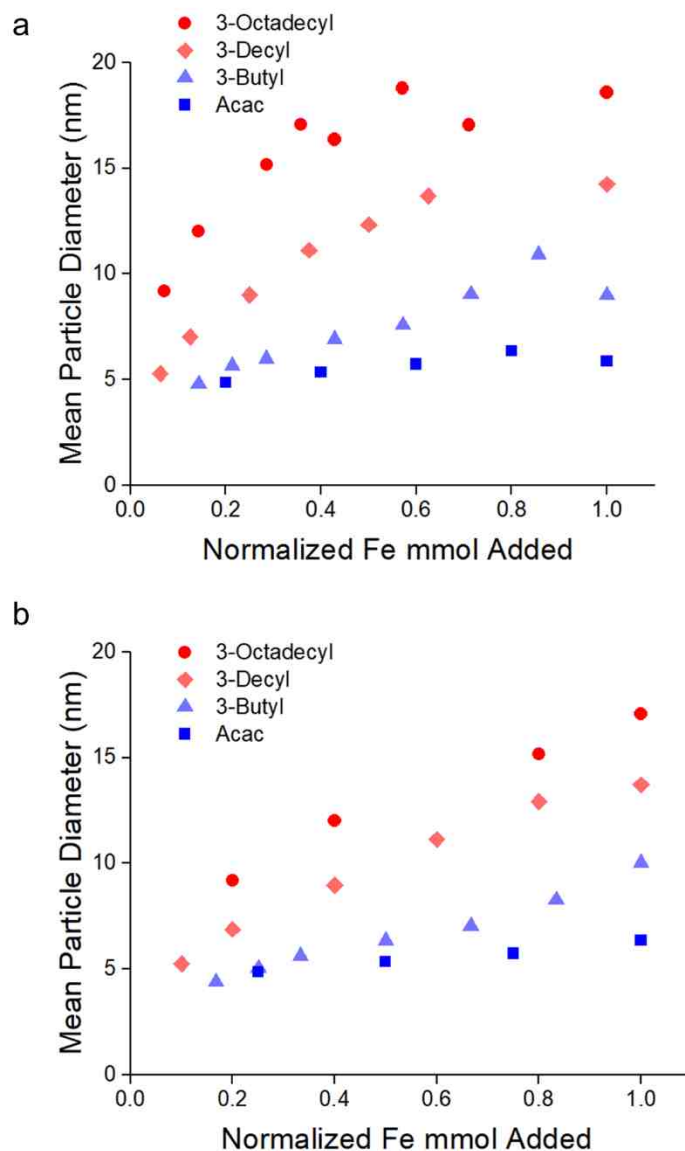


Figure 6.26 (a) Graph of mean particle diameters (nm) vs normalized Fe mmol addition for iron nanoparticles synthesized using 3-octadecyl-2,4-pentanedione, 3-decyl-2,4-pentanedione, 3-butyl-2,4-pentanedione and 2,4-pentanedione as the stabilizing surfactants. The amount of Fe is normalized due to the total Fe amount added (mmol) varying slightly between reactions. Because larger nanoparticles require more precursor, growing the particles to larger sizes required more Fe to be added. (b) Same information in 6.22a, except plot is normalized to the first observed

agglomeration event. This plot displays the maximum or near-maximum size obtained for each surfactant.

The general trend of increasing size as a function of increasing surfactant length emerges through these experiments. The maximum nanoparticle size obtained is strongly dependent on the steric stabilization provided by the surfactant. In this research, strongly magnetic nanoparticles were successfully synthesized with maximum sizes of 6.4, 10.7, 14.5, and 18.6 nm for 0, 4, 10, and 18 carbon chains, respectively. Figure 6.27 shows the experimental data for the maximum nanoparticle diameter obtained for the various surfactants.

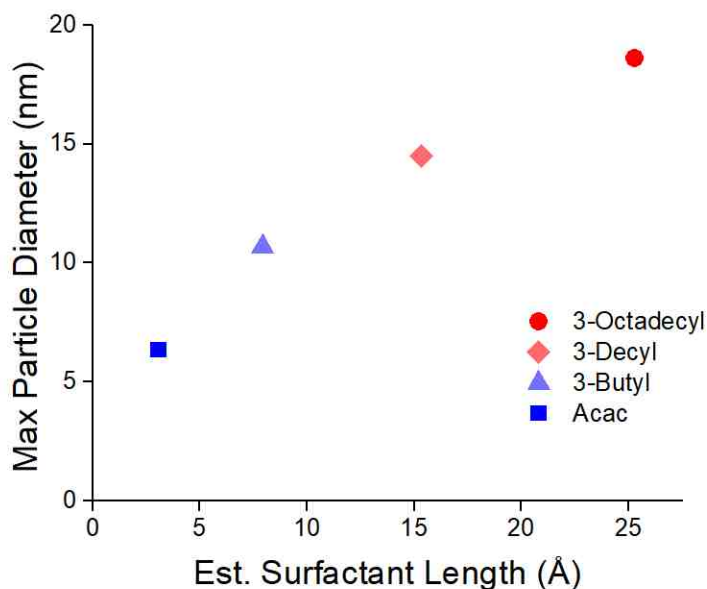


Figure 6.27 Graph of the mean maximum particle diameter (nm) vs the estimated surfactant length (Å) for iron nanoparticles synthesized using 2,4-pentanedione, 3-butyl-2,4-pentanedione, 3-decyl-2,4-pentanedione and 3-octadecyl-2,4-pentanedione. Particle sizes max out at 6.4, 10.7, 14.5, and

18.6 nm for the 0, 4, 10, and 18 carbon chain, respectively. Here it can be visualized how the maximum particle size varies with respect to increasing steric bulk provided by the surfactant.

6.3.6. Scale-Up Synthesis

A few reactions have been performed with results that are extremely promising for the fabrication of these nanoparticles on a larger scale. Decylamine was chosen as the surfactant because it is commercially available and has been used in previous iron nanoparticle syntheses. When designing a system scaled for larger volumes, using a custom synthesized surfactant increases the difficulty surrounding reaction design and execution. The scale-up reaction adds roughly 30 times the total amount of Fe (mmol) than that of the typical 2,4-pentanedione or 3-butyl-2,4-pentanedione synthesis mentioned previously in this chapter. Synthetic conditions and characterization are detailed below.

All chemicals were vigorously dried and degassed prior to use as mentioned previously. All chemicals and materials were prepared in a glove box and transferred to a Schlenk line under inert atmosphere unless stated otherwise. An oven-dried 100 mL 3-neck round bottom flask was charged with 0.51 g (3.2 mmol) decylamine and 30 mL (93.6 mmol) 1-octadecene under a nitrogen atmosphere with controlled flow. The solution was heated to 200°C under a condenser. A syringe loaded with 0.18 g (1.1 mmol) decylamine dissolved in 10.5 mL (32.8 mmol) 1-octadecene and 4.0 mL (33.4 mmol) iron pentacarbonyl was added dropwise to the reaction flask at a rate of 5.0 mL/hr. Total addition was 15 mL of syringe solution. Once the drip was completed, the reaction was allowed to proceed under a flow of nitrogen with continued heating for a minimum of one

additional hour. Meticulous care was taken during sample transfer to ensure nanoparticle oxidation and exposure to atmosphere was minimized.

6.3.6.1. Scale-Up Nanoparticle Synthesis Using Decylamine

To further confirm our agglomeration mechanism, we performed a scale-up synthesis with an inexpensive and commercially available surfactant, decylamine. With this surfactant, nanoparticle nucleation occurs almost immediately when the syringe solution enters the reaction flask solution. Although the nucleation event occurs differently to that of the pentanedione based surfactants, the mechanism remains the same. This method produced a very wide range of nanoparticle sizes, with the magnetically agglomerated particles containing a mean size of 14.1 nm in diameter. TEM images of the as-synthesized nanoparticles are seen in Figure 6.28.

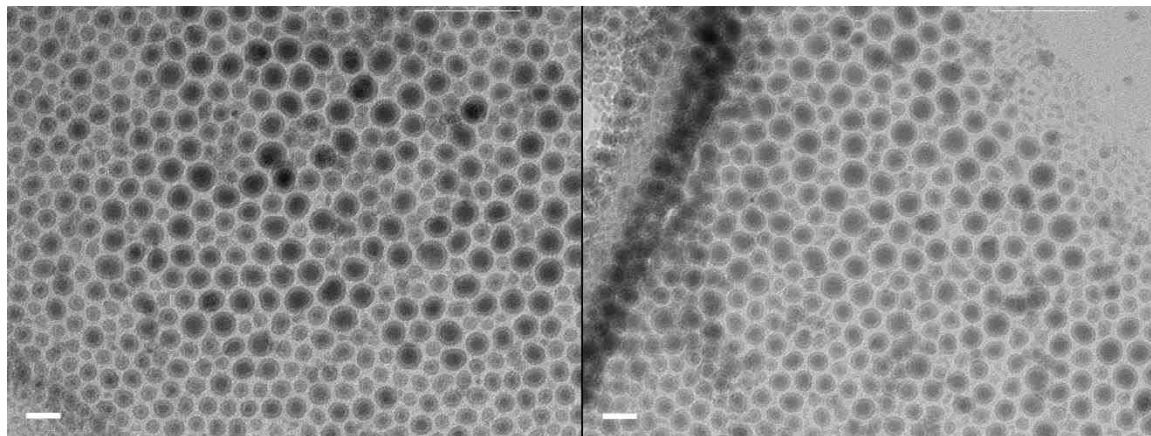


Figure 6.28 TEM images for as-synthesized nanoparticles from the scale-up reaction using the decylamine surfactant. All scale bars represent 20 nm.

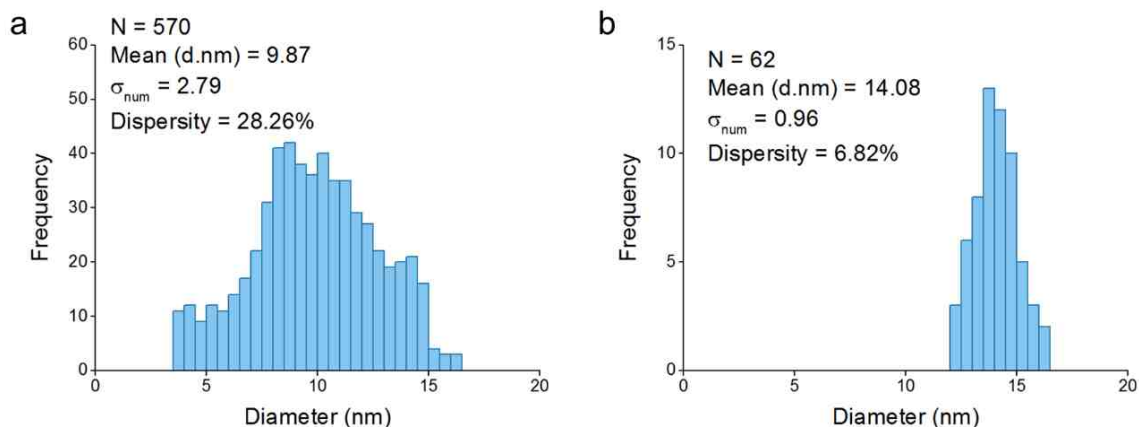


Figure 6.29 (a) Histogram produced from size analysis of all visible particles in TEM images. (b) Histogram produced from size analysis of particles in the range of the max size observed. The mean size at which particles agglomerate is around 14.1 nm in diameter.

Figure 6.29 shows the histograms from the size analysis of this sample. The mean particle size for this sample is 9.9 nm with a high dispersity of 28.3%. A number of maximum-sized and near max size particles were chosen in the TEM images for further analysis. These are the particles that appear in the center of the TEM images shown in Figure 6.28. Analysis of these particles confirms the mean maximum size at which these particles agglomerate, which is around 14.1 nm in diameter.

Due to this being a large volume reaction with a fast injection rate, this wide size range is most likely due to the continuous nucleation. To grow the nucleated particles to their peak size without inducing more nucleation, one could simply slow down the precursor addition rate after the fast addition (5 mL/hr) which produces a high number of nuclei. This will allow the nucleated particles to slowly grow in solution without creating more local “hot spots” with high iron concentration that could possibly induce more

nucleation. Due to time constraints in this reaction, we did not perform the slow addition required as it is expected that it could take a long period of time to complete.

Another way to obtain the maximum sized particles produced by the scale-up reactions could be through magnetic separation. As the smaller particles do not magnetically agglomerate and precipitate out of solution readily, the larger particles could be magnetically separated through multiple iterations, allowing for the larger more magnetic particles to be obtained and also achieving a lower size dispersity. This reaction shows extremely promising results for the scale up using commercial surfactants.

6.4. Conclusions

The variation of surfactant length was effective in proving that the steric stabilization from the surfactant can ultimately control the size at which the nanoparticles magnetically agglomerate and precipitate out of solution. Increasing the surfactant length from the bare surfactant 2,4-pentanedione, to 4, 10, and 18 carbon chains increased the nanoparticle size as expected. Through this method, producing a large volume of nanoparticles with desired size and properties is achievable. We have also successfully utilized this method to scale up production of zero-valent iron nanoparticles using a commercially available surfactant.

Chapter 7. Size Dependent Catalytic Activity of Magnetically Recoverable Heterogeneous Zero-Valent Iron Nanoparticle Catalysts

7.1. Introduction

Aside from serving a vital role in magnetic materials, iron has been proclaimed to be a highly effective catalyst for a wide range of reactions⁸⁷. Recent developments show that iron-catalyzed reactions cover almost the full scope of transformations presented in modern day organic textbooks. These span from the Haber process where iron combines nitrogen and hydrogen gases to form ammonia to the Fischer-Tropsch process of converting a mixture of carbon monoxide and hydrogen gases into liquid hydrocarbons. While bulk iron can also act as a catalyst, it has been established that unique properties materialize on the nanoscale. This phenomenon can be observed in the case of gold, which is well known as one of the least reactive metals and is commonly referred to as chemically inert. However, nanoparticles of gold supported on inert materials are remarkably robust catalysts, e.g., for the selective oxidation of styrene in the presence of oxygen⁸⁸. Nanomaterial catalysts are generally heterogeneous catalysts broken up into metal nanoparticles in order to speed up the catalytic process. In most cases, the increased catalytic activity achieved through these materials is due to the higher exposed surface area, thus allowing a higher frequency of reactions to occur at the same time. Recent advances in catalytic nanomaterials present an intensely promising future for this research area with little to no sign of slowing down.

Through further research, it was discovered that iron nanoparticles manufactured with our technique are active heterogeneous catalysts for the hydrogenation of alkenes,

with high potential for use with structurally similar substrates. Furthermore, their high magnetic susceptibility provides an easy, efficient route to magnetic separation and recovery. Because this method of synthesizing iron nanoparticles allows for the production of highly magnetic iron nanoparticles with a very low-size dispersity, the opportunity to study the catalytic activity of these nanoparticles as a function of particle size was possible. The goal of this section is to present the findings for catalytic performance as a function of nanoparticle size for nanoparticles synthesized with this method, as well as contribute to a fundamental understanding to what factors affect this system.

The nanoparticles used for these studies were those synthesized with 3-octadecyl-2,4-pentanedione. This was due to the narrow size dispersity achieved in these reactions, and the wider range of sizes produced with this surfactant allows a respectable size range to be studied. Particles chosen for analysis were those synthesized with 1.8, 7.3, and 10.9 mmol of iron, leading to the average particle sizes of 9.2 ± 0.7 , 14.6 ± 1.1 , and 18.4 ± 0.8 nm, respectively.

7.2. Experimental

7.2.1. Synthesis of Stabilizing Surfactants

3-Octadecyl-2,4-Pentanedione Synthesis

3-Octadecyl-2,4-pentanedione was synthesized as detailed in the previous chapter (4).

7.2.2. Nanoparticle Stock (Catalyst) Preparation

Nanoparticles were synthesized as previously reported and immediately pumped into an inert atmosphere glove box. The total iron amounts used for these reactions were

1.81, 5.45, and 10.9 mmol which produce the low, medium, and high ends of the size spectrum seen with particles synthesized with 3-octadecyl-2,4-pentanedione. The nanoparticles synthesized with 10.9 mmol of iron occurred after a renucleation event, thus a strong neodymium magnet was used to magnetically separate the larger particles of the bimodal distribution from those of smaller particles. Because the smaller particles tend to stay dispersed in solution and do not readily separate with a magnet, magnetic separation was a straightforward process. Particles were pulled down with the neodymium magnet in the reaction flask for ~5 minutes. The supernatant was then decanted into a separate vial. A mixture of surfactant and toluene was then added to the reaction flask, and this mixture was vortexed vigorously to redisperse. Once particles were redispersed and no magnetic agglomerates could be seen, the neodymium magnet was set under the reaction flask and this magnetic filtration procedure was repeated 3-4 times until a clear supernatant was observed. This was a sign that no smaller particles were dispersed. After the final magnetic filtration step, the resultant particles were added to a toluene and surfactant solution, ready to be prepared for reactions. These stock particle solutions were analyzed by SAXS and TEM to confirm their size and size dispersity.

Determining the amount of nanoparticles to be used in a reaction was a multi-step process. Larger nanoparticles formed magnetic precipitates over time, and even after vortexing and dispersing, aliquots of the stock lead to various amounts of iron per reaction. The most efficient way of determining the iron concentration per aliquot, thus determining the amount of substrate to add, was through a weighing, annealing, and a destructive iron analysis procedure. The ultimate goal here was to graph the actual amount of iron (the

catalytically active species) in mg versus the aliquot amount (stock particles). The aliquot amount weighs more than the actual amount of iron due to organics in the solution such as the solvent and surfactant.

Five to ten small aliquots (generally 3-10 mg) were added to a 20 mL scintillation vial. These aliquots were capped and put onto a weighing scale. The scale was allowed to stabilize for 30 minutes until the aliquot weight was no longer adjusting (due to toluene evaporation). The final weight of this aliquot was recorded. This was then annealed to remove organics which can interfere in the iron determination procedure. For annealing, 2-3 mL of deionized water was added to the scintillation vial. This was to ensure that the fully oxidized iron oxide phase forms instead of an iron carbide phase which is insoluble in the hydrochloric acid solution used for iron determinations. The sample was heated to 130°C for 30 minutes, ramped up to 300°C for 1 hour, and then finally to 600°C for 3 hours. Once complete, a red powder of pure iron oxide with no organics was observed. This was then dissolved in a dilute hydrochloric acid solution and prepared for UV-Visible spectroscopy analysis.

From this procedure the total quantity of iron was obtained, which was then used to calculate the amount of substrate to add per aliquot. Generally, this amount was 70-80% of the aliquot weight taken in the first steps of this procedure. Because the amount of residual organics and toluene varies slightly between stock solutions, this same procedure was repeated for every stock. Two examples of stock solution iron determinations are shown below for the 18.4 and 14.6 nm stocks.

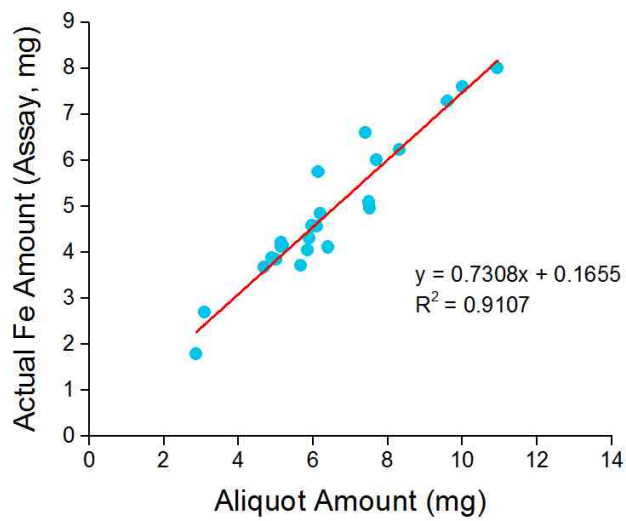


Figure 7.1 Actual amount of iron per aliquot (mg) against the aliquot amount (scale weight, mg) for the 18.4 nm stock. The aliquot amount is the weight of the stock particles with organics such as surfactant and solvent. The actual amount of iron is obtained through annealing followed by assessment performed on a UV-Visible spectrometer.

For the 18.4 nm stock, it was found that the average iron amount per aliquot was 73.1%. This suggests that on average, residual organics account for 26.9% of the aliquot amount. The plotted data is displayed below (Table 7.1).

Table 7.1 A summary of the aliquot amounts (scale weight, mg), actual amount of iron per aliquot (assay, mg), the percent difference between the scale weight and assay, and the percent weight, which is the actual amount of iron over the scale weight for the 18.4 nm stock.

| 18.4 nm Stock Solution Fe Determination | | | |
|--|---|---------------------|-----------------|
| Scale Weight (Aliquot, mg) | Actual Fe Amount (Assay, mg) | % Difference | % Weight |
| 2.9 | 1.8 | 38.1% | 61.9% |
| 3.1 | 2.7 | 12.9% | 87.1% |
| 4.7 | 3.7 | 21.8% | 78.2% |
| 4.9 | 3.9 | 20.9% | 79.1% |
| 5.0 | 3.8 | 23.3% | 76.7% |
| 5.1 | 4.2 | 18.0% | 82.0% |
| 5.2 | 4.1 | 20.0% | 80.0% |
| 5.2 | 4.1 | 20.4% | 79.6% |
| 5.7 | 3.7 | 34.4% | 65.6% |
| 5.9 | 4.1 | 30.8% | 69.2% |
| 5.9 | 4.3 | 27.2% | 72.8% |
| 6.0 | 4.6 | 23.3% | 76.7% |
| 6.1 | 4.6 | 25.2% | 74.8% |
| 6.2 | 4.8 | 22.0% | 78.0% |
| 6.4 | 4.1 | 35.7% | 64.3% |
| 7.4 | 6.6 | 11.0% | 89.0% |
| 7.5 | 5.1 | 32.2% | 67.8% |
| 7.5 | 5.0 | 33.9% | 66.1% |
| 7.7 | 6.0 | 22.1% | 77.9% |
| 8.3 | 6.2 | 25.1% | 74.9% |
| 9.6 | 7.3 | 24.2% | 75.8% |
| 10.0 | 7.6 | 24.0% | 76.0% |
| 10.9 | 8.0 | 26.9% | 73.1% |

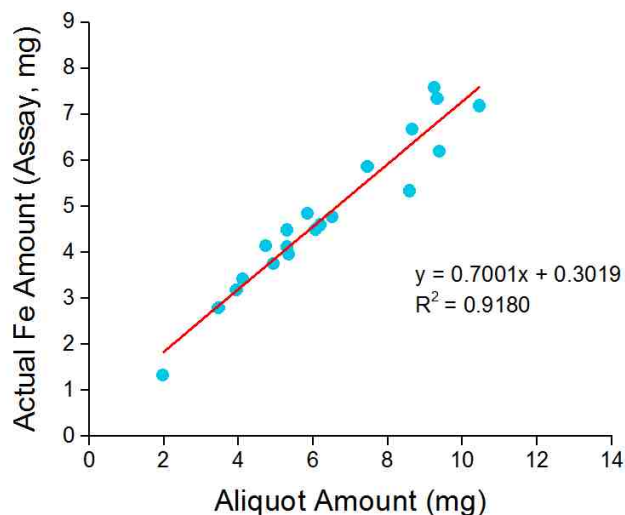


Figure 7.2 Actual amount of iron per aliquot (mg) against the aliquot amount (scale weight, mg) for the 14.6 nm stock. The aliquot amount is the weight of the stock particles with organics such as surfactant and solvent. The actual amount of iron is obtained through annealing followed by assessment performed on a UV-Visible spectrometer.

For the 14.6 nm stock, it was found that the average iron amount per aliquot was 70.0%. For this stock, the average amount of residual organics account for 30.0% of the aliquot amount. This is exactly what is expected for smaller particles with a higher surface area. A higher surface area would translate to a greater number of residual organics, assuming most of the residual organics originate from bound ligand on the iron nanoparticle surface. This stock on average has 3.1% more organics per aliquot than 18.4 nm particle stock. The plotted data is displayed below (Table 7.2).

Table 7.2 A summary of the aliquot amounts (scale weight), actual amount of iron per aliquot (assay, mg), the percent difference between the scale weight and assay, and the percent weight, which is the actual amount of iron over the scale weight for the 14.6 nm stock.

| 14.6 nm Stock Solution Fe Determination | | | |
|--|-------------------------------------|---------------------|-----------------|
| Scale Weight (Aliquot, mg) | Actual Fe Amount (Assay, mg) | % Difference | % Weight |
| 2.0 | 1.3 | 33.2% | 66.8% |
| 3.5 | 2.8 | 19.7% | 80.3% |
| 4.0 | 3.2 | 19.7% | 80.3% |
| 4.1 | 3.4 | 17.3% | 82.7% |
| 4.4 | 2.4 | 45.8% | 54.2% |
| 4.7 | 4.1 | 13.0% | 87.0% |
| 4.9 | 3.8 | 24.2% | 75.8% |
| 5.3 | 4.1 | 22.7% | 77.3% |
| 5.3 | 4.5 | 15.6% | 84.4% |
| 5.4 | 4.0 | 26.2% | 73.8% |
| 5.9 | 4.8 | 17.5% | 82.6% |
| 6.1 | 4.5 | 26.1% | 73.9% |
| 6.2 | 4.6 | 26.1% | 73.9% |
| 6.5 | 4.8 | 27.0% | 73.0% |
| 7.5 | 5.9 | 21.5% | 78.6% |
| 8.6 | 5.3 | 38.0% | 62.0% |
| 8.7 | 6.7 | 22.9% | 77.1% |
| 9.3 | 7.6 | 18.2% | 81.8% |
| 9.3 | 7.3 | 21.3% | 78.7% |
| 9.4 | 6.2 | 34.1% | 65.9% |
| 10.5 | 7.2 | 31.3% | 68.7% |

This procedure was used on the stock particle solutions that were 18.4 and 14.6 nm in size, however the 9.2 nm particles are exceptionally stable and do not magnetically precipitate out of solution. Two methods were investigated to prepare these stable particles.

The first method was to centrifuge down the particles, decant the supernatant, and resuspend them in toluene in the glove box under inert atmosphere. The second method was to use as-synthesized nanoparticles in 1-octadecene. The reasons both of these methods were used for the smaller 9.2 nm particles is mentioned later in this section. However, for both of these methods the smaller particles resuspended without future agglomeration or precipitation. This allowed us to take aliquots in the amounts of 50, 100, and 150 mL, anneal to remove the organics, and analyze using UV-visible spectroscopy to obtain a calibration curve. As mentioned previously, this method was unsuccessful with larger particles that would slowly agglomerate or precipitate, as the amount of iron varied considerably between aliquots.

7.2.3. Materials

Parr Pressure Reactor Vessel

All reactions were performed in a 300 mL non-stirred pressure vessel (Model 4760, Parr Instrument Company, Moline, IL). The general-purpose pressure vessel has a maximum temperature of 350°C and a maximum pressure of 3000 psi (200 bar).



Figure 7.3 Picture of the Parr 300 mL non-stirred pressure vessel (model 4760) used in these reactions. This general-purpose pressure vessel has a maximum temperature of 350°C and a maximum pressure of 3000 psi (200 bar).

Chemicals

All chemicals underwent very rigorous drying, degassing, and purification procedures. All performed procedures occurred on a Schlenk line adapted with a large purifier tube containing copper catalyst and molecular sieves (MBRAUN USA, Stratham, NH). This set up was under the constant flow of highly pure in-house nitrogen to ensure the exclusion of oxygen and moisture. Once samples were prepared they were transferred

under reduced pressure to an MBRAUN Unilab glovebox (<0.1 ppm H₂O and <0.1 ppm O₂).

1,1'-(Ethane-1,2-diyl)dibenzene (99%, bibenzyl, 103-29-7), 1,1'-[(1E)-Ethene-1,2-diyl]dibenzene (*trans*-stilbene, 96%, 103-30-0) were purchased from Acros Organics. The solvent used for these reactions, toluene (≥99.5%, 108-88-3), was purchased from Thermo Fisher Scientific (Waltham, MA). Sodium lump (≥99.8% in kerosene) which is used for chemical drying and chloroform-d (99.5 atom % D, contains 0.03 % (v/v) TMS, 865-49-6) used for NMR analysis were purchased from Sigma Aldrich (St. Louis, MO). Toluene was dried over sodium lump in a 1 liter round bottom flask under inert atmosphere for a minimum of 24 hours. It was then distilled into a flame-dried Schlenk flask. This flask was transferred to the Schlenk line where it was degassed using a freeze-pump-thaw technique. It was sealed and immediately transferred under reduced pressure to an inert atmosphere glove box for storage and stock preparation. The *trans*-stilbene stock solution was made in the glovebox by dissolving 0.75 mg (4.2 mmol) of *trans*-stilbene in 16 mL (151 mmol) of toluene with light stirring for 10 minutes at room temperature to fully dissolve. This solution was then sealed tightly and stored for future use. The compressed hydrogen gas (99.99%, 1333-74-0) used for these hydrogenations was purchased from Matheson Tri-Gas (Montgomeryville, PA).

Hydrogenation Reaction Setup

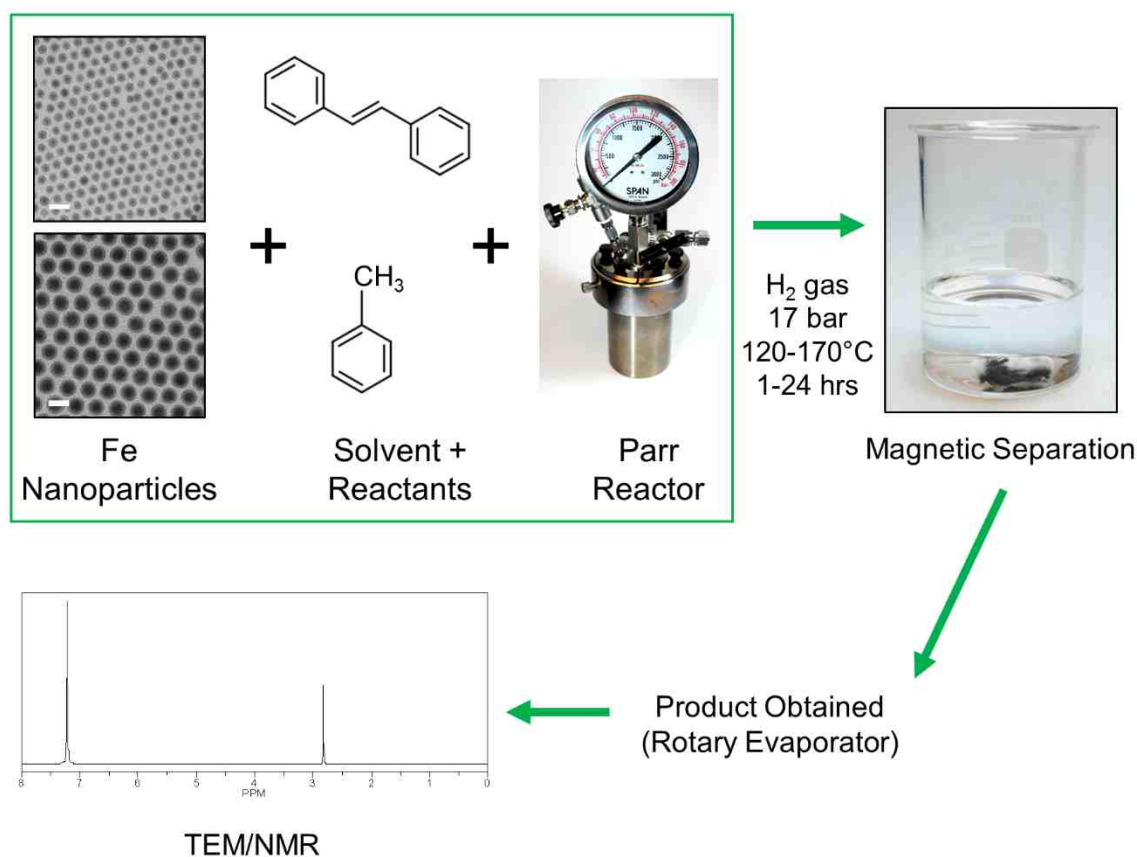


Figure 7.4 General steps performed during the hydrogenation reactions. First, nanoparticles are weighed and combined with solvent, substrate, and a Teflon stir bar in the general-purpose reaction vessel under inert atmosphere. The vessel is pressurized with H₂ gas and set at a given temperature for a known period of time. Post reaction, the particles are then magnetically separated from the solvent and substrate. The solvent and substrate mixture is put on a rotary evaporator for product separation, and the dried product is suspended in deuterated chloroform for ¹H NMR analysis.

An aliquot of nanoparticles was obtained according to the previous procedures. A 300 mL Parr custom glass cup was charged with the iron nanoparticle catalyst, the

appropriate amount of stilbene stock, a stir bar, and was diluted with toluene to a total volume of 60 mL. The reactor was then sealed and transferred to a fume hood where it was pressurized to 250 psi (17.2 bar) with H₂ gas. The Parr vessel was then heated to temperatures of 100 – 170°C on a hot plate with vigorous stirring for 1 – 48 hours. The reaction timer officially started once the reaction reached temperature. The average time it took to reach temperature was about 1 hour. As we are unable to get up to the full reaction temperature instantaneously, we have observed in separate experiments that there was essentially no reaction during this period. Once the time was complete, the heat source was turned off and the vessel was immediately removed and allowed to cool down to room temperature. Then the nanoparticles were magnetically separated and collected. They were annealed to remove all organics and analyzed using UV-visible spectroscopy to determine the total iron content. The solution containing product and toluene was put on a rotary evaporator to remove the toluene, leaving behind the obtained product. This was then prepared for nuclear magnetic resonance by dispersing a small amount of the collected product in a 5 mm capillary tube and diluting with 1-2 mL of deuterated chloroform.

7.2.4. Characterization Techniques

Nuclear Magnetic Resonance (NMR) Analysis

¹H NMR was the most efficient and readily available method of determining the starting reagent and product concentrations in these reactions. What differentiates the starting material and product on ¹H NMR is the emerging peak at 2.8 ppm after fully saturating the bridging alkenyl group (to –CH₂–CH₂–) for bibenzyl. A slight challenge to

utilizing this method however is due to the fact that both bibenzyl and stilbene contain peaks in the 7-8 ppm region. These peaks overlap, meaning it is more difficult to use for quantitative analysis. However, by consistently integrating the emerging 2.8 ppm bibenzyl peak to what is known to be four hydrogens and using this to obtain a ratio of the 2.8 ppm peak to the peaks in the 7-8 ppm region, the amount of starting material and product in each reaction can be determined. The predicted ^1H NMR spectra for (E)-stilbene and bibenzyl are shown in Figure 7.5.

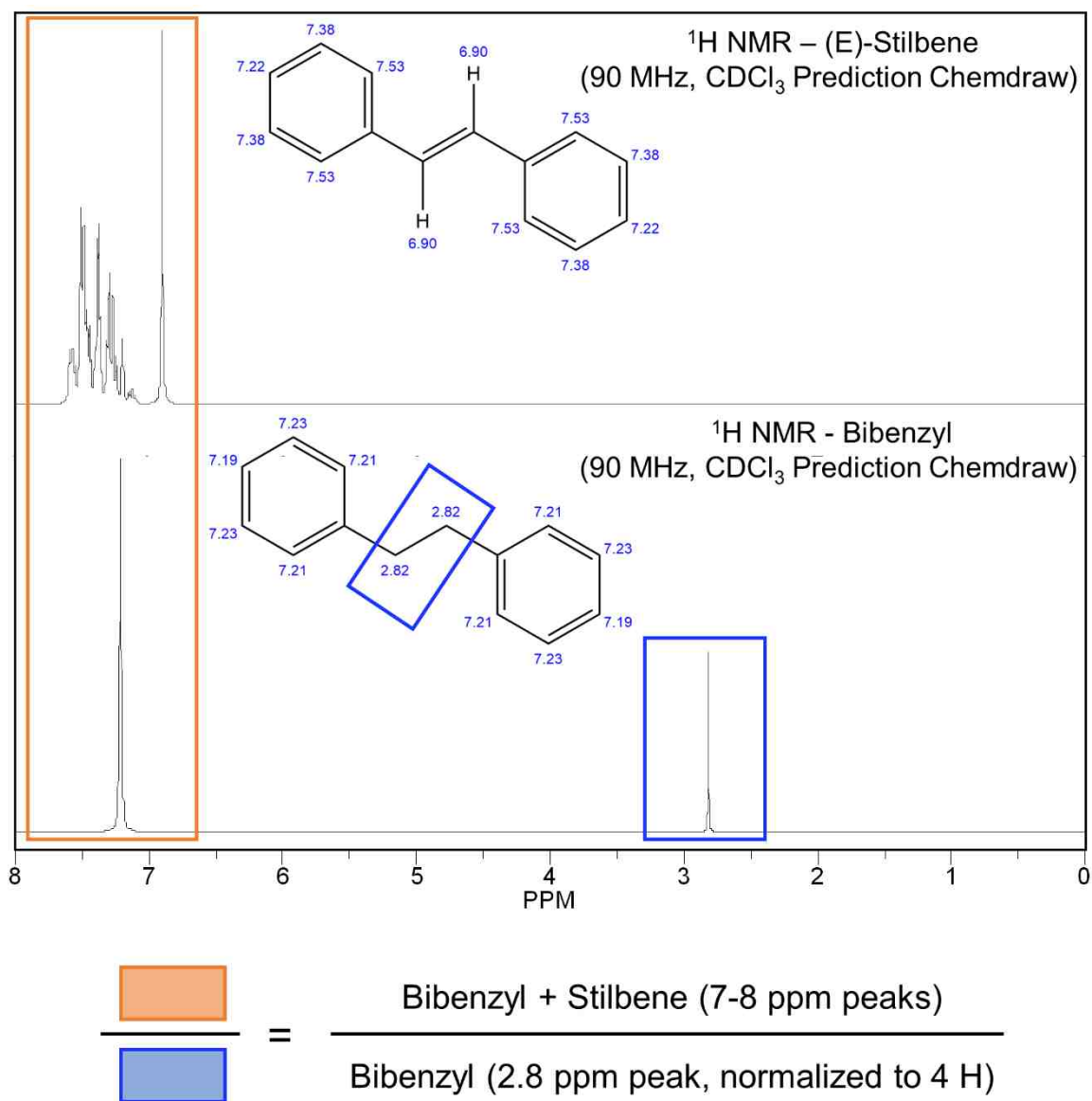


Figure 7.5 Predicted ¹H NMR spectra for E-stilbene (*trans*-stilbene) and bibenzyl. Spectra were calculated in ChemDraw using a 90 MHz source and deuterated chloroform (CDCl₃) solvent. For products obtained experimentally, the ratio of the integral peak value for the 7-8 ppm peaks over the normalized 2.8 ppm peak helped to determine the amount of substrate that was successfully hydrogenated.

A very large 7-8:2.8 ppm ratio suggests that the product is almost all *trans*-stilbene, or unsaturated starting material. A much lower ratio suggests that conversion is successful and the saturated product obtained is majority bibenzyl.

To create an accurate and reliable calibration curve which provided the amount of starting material that was successfully converted to product, several mixtures of commercially available *trans*-stilbene and bibenzyl were produced and analyzed. A total of 10 stocks were prepared with the known amount of bibenzyl ranging from 100 to 6.25 (mol %). An outline of these stocks is shown in Table 7.3. A summary of all raw ¹H NMR spectra for the stock solutions, showing the reaction progression for the full conversion of *trans*-stilbene to bibenzyl, is seen in Figure 7.6. The 2.8 ppm peaks for bibenzyl have been normalized to four hydrogens.

Table 7.3 Stock solutions containing various mixtures (mol %) of starting material (*trans*-stilbene) and hydrogenated product (bibenzyl). Ten stocks varying from 100 to 6.25 mol % bibenzyl were formulated. These stocks were analyzed using ¹H NMR.

| Stock | Bibenzyl (mol %) | Stilbene (mol %) | Integrated 7-8 ppm Peak Value | 2.8 ppm peak | Ratio (7-8:2.8) ppm |
|-------|------------------|------------------|-------------------------------|--------------|---------------------|
| 1 | 6.3 | 93.7 | 217.9 | 4 | 54.5 |
| 2 | 12.5 | 87.5 | 98.6 | 4 | 24.7 |
| 3 | 25.0 | 75.0 | 49.2 | 4 | 12.3 |
| 4 | 37.5 | 62.5 | 30.7 | 4 | 7.7 |
| 5 | 50.0 | 50.0 | 22.2 | 4 | 5.6 |
| 6 | 62.5 | 37.5 | 17.7 | 4 | 4.4 |
| 7 | 75.0 | 25.0 | 14.0 | 4 | 3.5 |
| 8 | 87.5 | 12.5 | 12.2 | 4 | 3.1 |
| 9 | 93.8 | 6.2 | 11.3 | 4 | 2.8 |
| 10 | 100.0 | 0.0 | 10.5 | 4 | 2.6 |

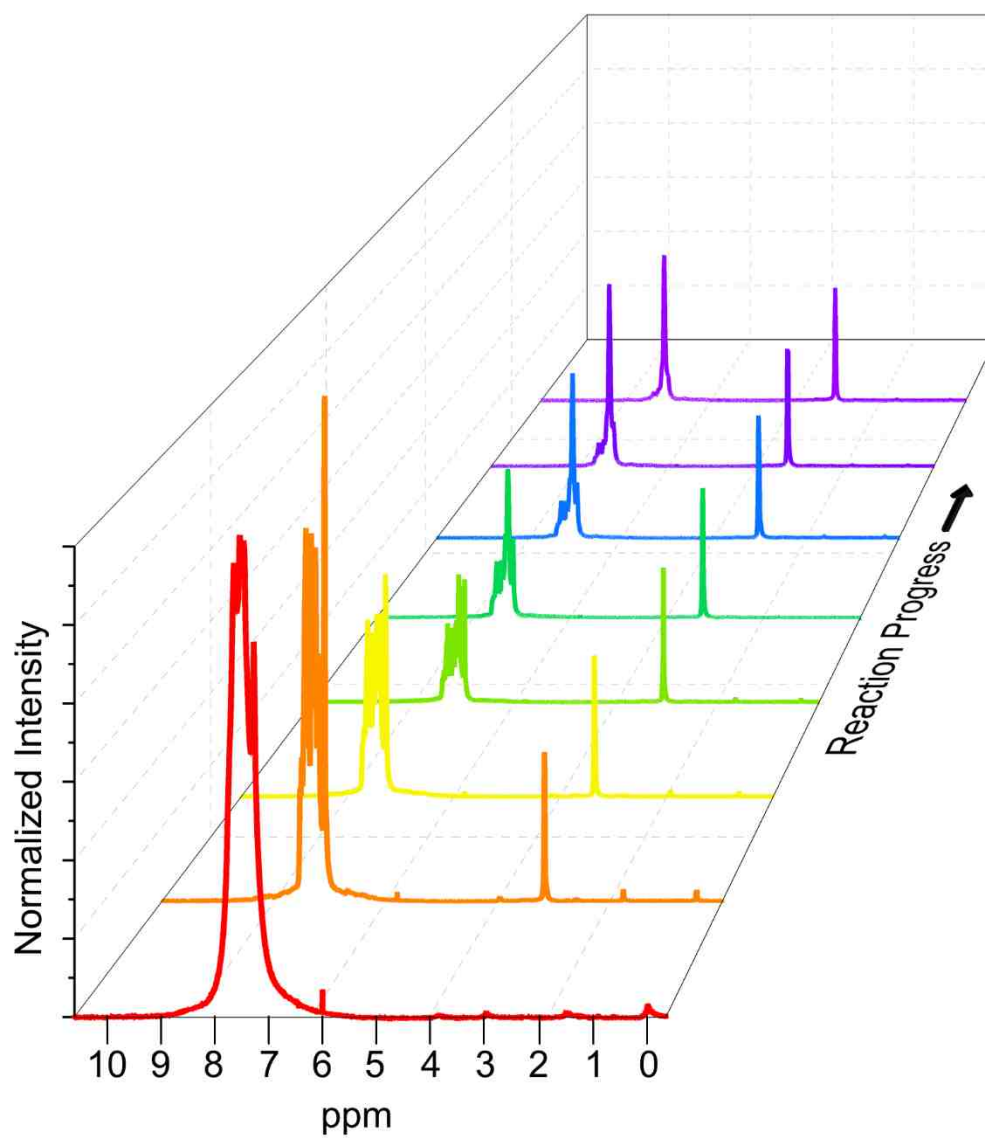


Figure 7.6 Experimental ^1H NMR spectra for the stock solutions containing various mixtures of *trans*-stilbene and bibenzyl. The forefront red spectrum is that of pure *trans*-stilbene (substrate), and as the spectra shift upward, the bibenzyl (product) concentration increases. This model displays ^1H NMR spectra progression as the reaction nears full conversion.

These stocks were then plotted to display the bibenzyl amount (mol %) against the integrated peak value (stilbene and bibenzyl). The forefront red spectrum is that of pure *trans*-stilbene (substrate), and as the reaction advances upward the bibenzyl (product) concentration increases. This model displays ¹H NMR spectra progression as the reaction nears full conversion.

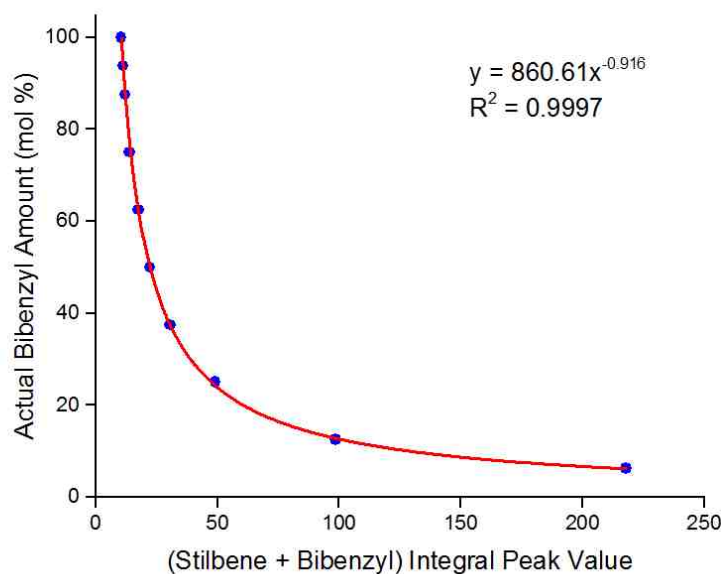


Figure 7.7 Plot of the actual bibenzyl amount (mol %) against the integrated peak value of the 7-8 ppm peaks on ¹H NMR. The plot uses the (S+B) integrated peak value for the x-axis for simplicity. When the integrated peak value is obtained after product analysis, it can simply be plugged into the equation above, producing the degree of conversion.

Product conversion was determined by plugging in the integral peak value for the combined 7-8 ppm peaks obtained through ¹H NMR spectrum analysis. This is the value obtained after normalizing the 2.8 ppm peak to four hydrogens, as is expected for pure

bibenzyl starting material. After the conversion amount (mol %) was acquired and an iron determination was performed, the conversion rate used for a heterogeneous catalyst ($\text{mol}/\text{m}^2\text{s}$) was calculated and used for further data analysis.

7.3. Results and Discussion

7.3.1. Nanoparticle Catalytic Activity

7.3.1.1. 18.4 (d.nm) Nanoparticle Catalyst

First, nanoparticles containing an average diameter of 18.4 nm were investigated, which falls on the larger end of our size spectrum. These particles were found to be successful in the catalytic conversion of *trans*-stilbene to bibenzyl. The temperatures implemented ranged from 100 to 170°C. The average amount of catalyst (mol %) used for

these reactions was 4.0%. A summary of the 170, 155, 140, and 100°C reactions are shown below.

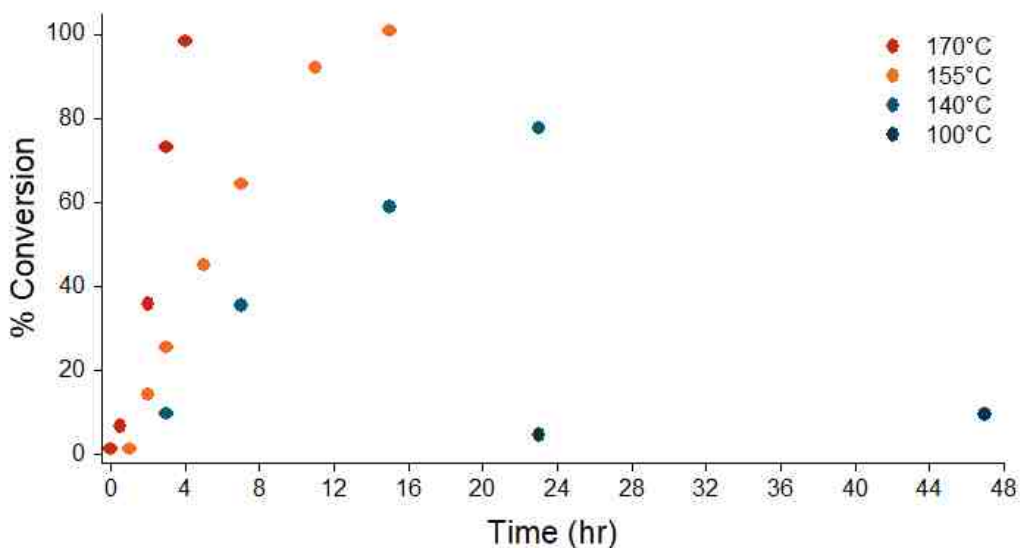


Figure 7.8 Compiled experimental data for the hydrogenation of *trans*-stilbene to bibenzyl for the 18.4 nm particles at 100, 140, 155, and 170°C.

The experimental reaction rates were 24.9, 9.0, 3.2, and 0.2 mol %/hr for the temperatures of 170, 155, 140, and 100°C, respectively. Due to the low catalytic activity for the 100°C reactions and also due to time constraints, only two of these were performed. These experiments were inputted solely to provide supplemental information to the reaction kinetics being studied in this system. A detailed view of each of these reactions is shown below.

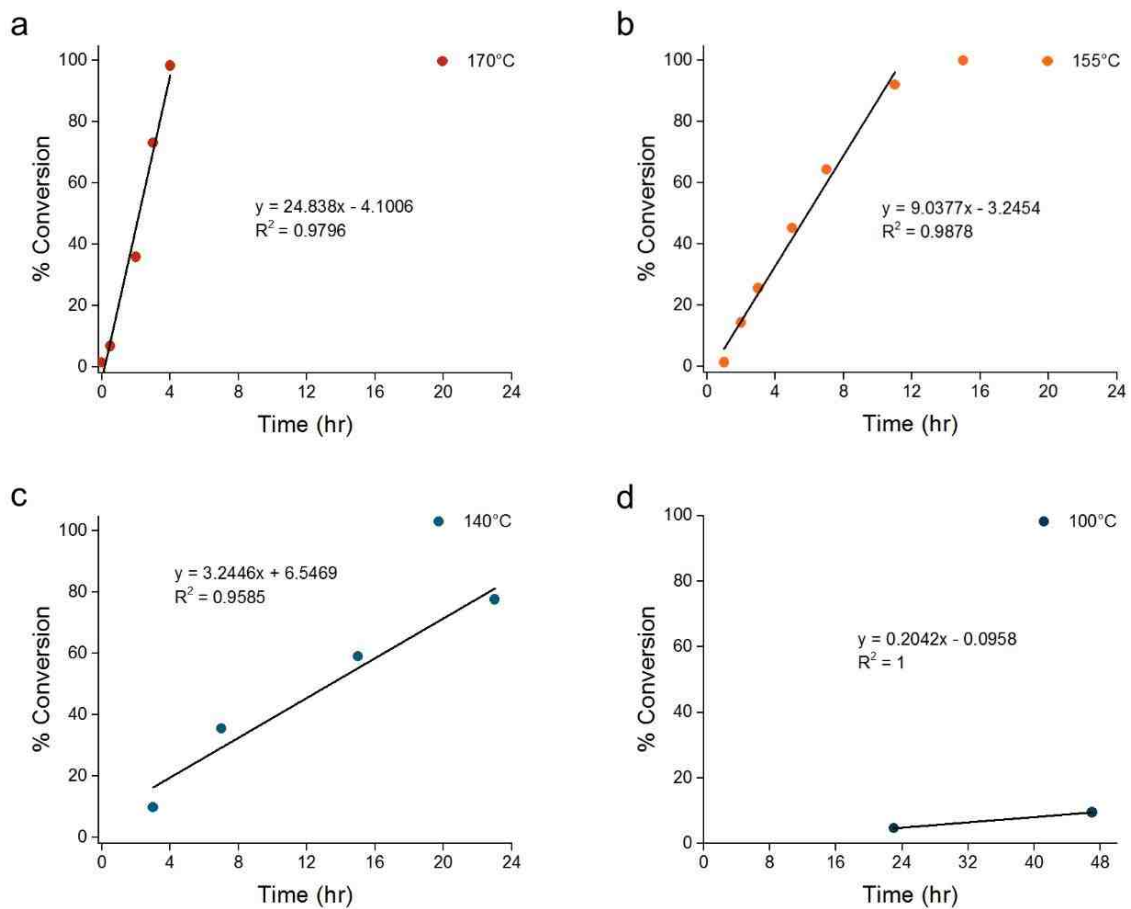


Figure 7.9 Conversion and conversion rates (mol %/hr) at **(a)** 170°C **(b)** 155°C **(c)** 140°C and **(d)** 100°C for the 18.4 nm particles. The rate is equal to the slope of the line (m) in the linear formula $y = mx + b$. Conversion rates were 24.8, 9.0, 3.2, and 0.2 mol %/hr, respectively.

Table 7.4 Summary of experimental data for the 18.4 nm hydrogenation reactions. Conversion rates are displayed in mol %/hr.

| Temp (°C) | Temp (K) | Pressure (psi) | Conversion Rate (mol%/hr) |
|------------------|-----------------|-----------------------|----------------------------------|
| 170 | 443.15 | 250 | 24.8 |
| 155 | 428.15 | 250 | 9.0 |
| 140 | 413.15 | 250 | 3.2 |
| 100 | 373.15 | 250 | 0.2 |

Foremost, it was observed that the catalytic activity of the nanoparticles increased as a function of reaction temperature. This is precisely what is expected to happen, and it can be explained through conventional reasoning. The rise in temperature increases the reaction rate most likely for two reasons. First is the increase in the collision frequency. Particles react when they collide, and heating a substance leads to faster particle movement and therefore the frequency of collisions is greater. Second is the more frequent high-energy collisions. Collisions between particles result in a reaction if the particles collide with enough energy to start a reaction. This minimum amount of energy is known as the activation energy. Typically, the majority of particles do not have enough energy and will simply bounce apart. However, a fraction of these particles considered to be highly energetic particles will collide with enough energy (equal or greater than the activation energy) to react. Higher temperatures increase the amount of these highly energetic particles, leading to an increased reaction rate.

The Parr reactor was heated using an aluminum block controlled by the hot plate and the reaction temperature was monitored through a connection on the Parr reactor. For

this reason, temperatures slightly varied between reactions and temperatures were recorded through these reactions to ensure they were within a close range. It was noticed that small variations in reaction temperatures and catalysts did not have significant impacts on the yields. To explain anomalous or outlying data, a plot of the reaction temperature, amount of catalyst, and percent conversion was developed. An example of this is shown below in Figure 7.10. In some cases, this helps clarify why a reaction yield would be slightly lower than expected. An example might be a reaction that had a combination of a lower than average catalyst amount and a lower than average reaction temperature. However, significant variations from the average values were treated as outliers and these reactions were repeated.

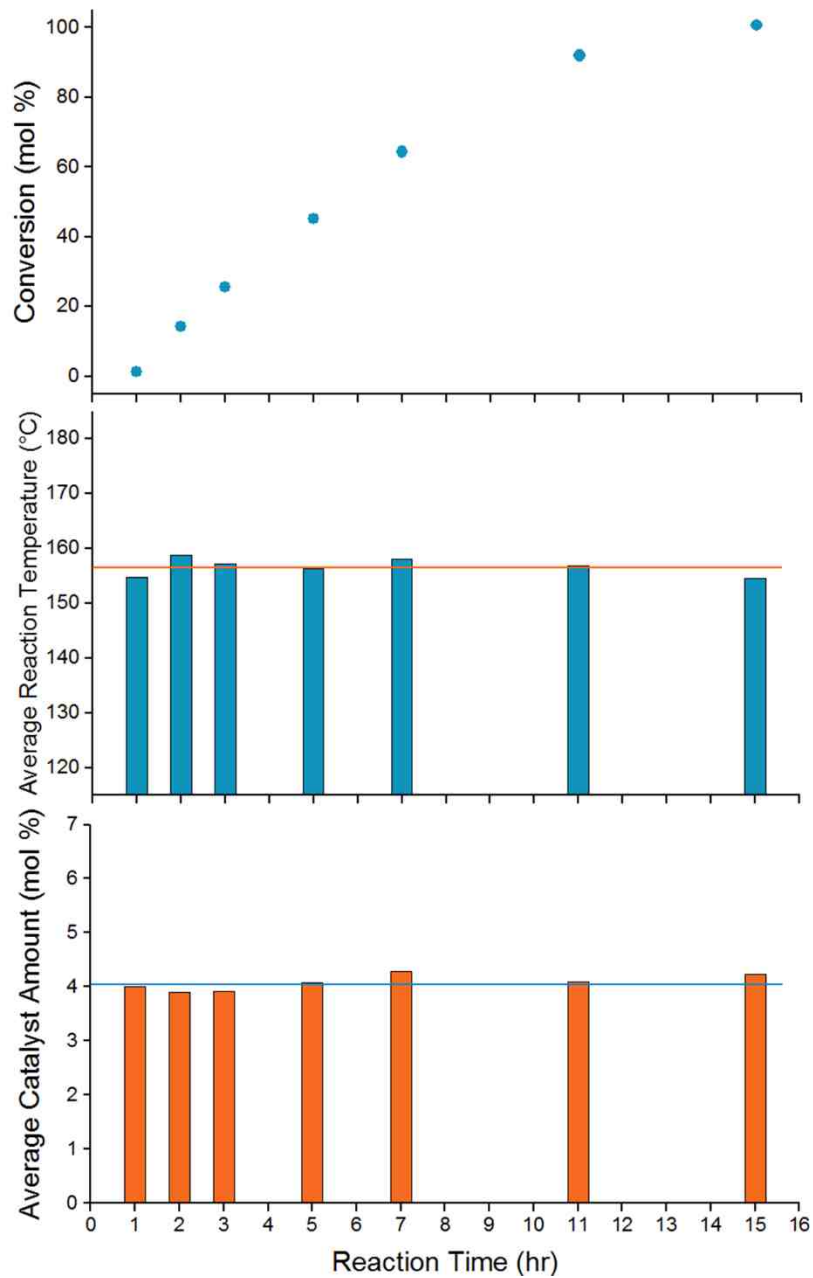


Figure 7.10 (Top) Conversion amount (mol %) for the 155°C reaction using 18.4 nm particles. **(Middle)** Average reaction temperature as a function of reaction time. **(Bottom)** Average amount

of catalyst (mol %) as a function of reaction time. These plots aided in the better understanding of why catalytic activity was higher or lower than expected.

All of the reactions included in our reported experimental data did not deviate significantly from the average temperatures or catalyst loading amounts. For the 155°C reactions plotted above, the average temperature was 156.6 ± 1.6 °C with an average catalyst amount of 4.1 ± 0.1 mg.

7.3.1.2. 18.4 (d.nm) Nanoparticle Catalyst Reaction Kinetics

The reaction kinetics were examined to help further develop a fundamental understanding of this system. The reaction rate of a heterogeneous process is normally a function of surface area, translating to a higher number of active sites as surface area increases quickly with decreasing particle size. Sponza *et al.* reported that the reduction rates of zero-valent iron were first order with respect to surface area⁸⁹. Furthermore, Lin *et al.* showed that the decomposition of hydrogen peroxide with iron oxide nanoparticles is a first order process with respect to iron, and the reaction rate is independent of the initial hydrogen peroxide concentration⁹⁰. Although many other factors influence these reactions, it can be noted that surface area is one of the most important elements in this system.

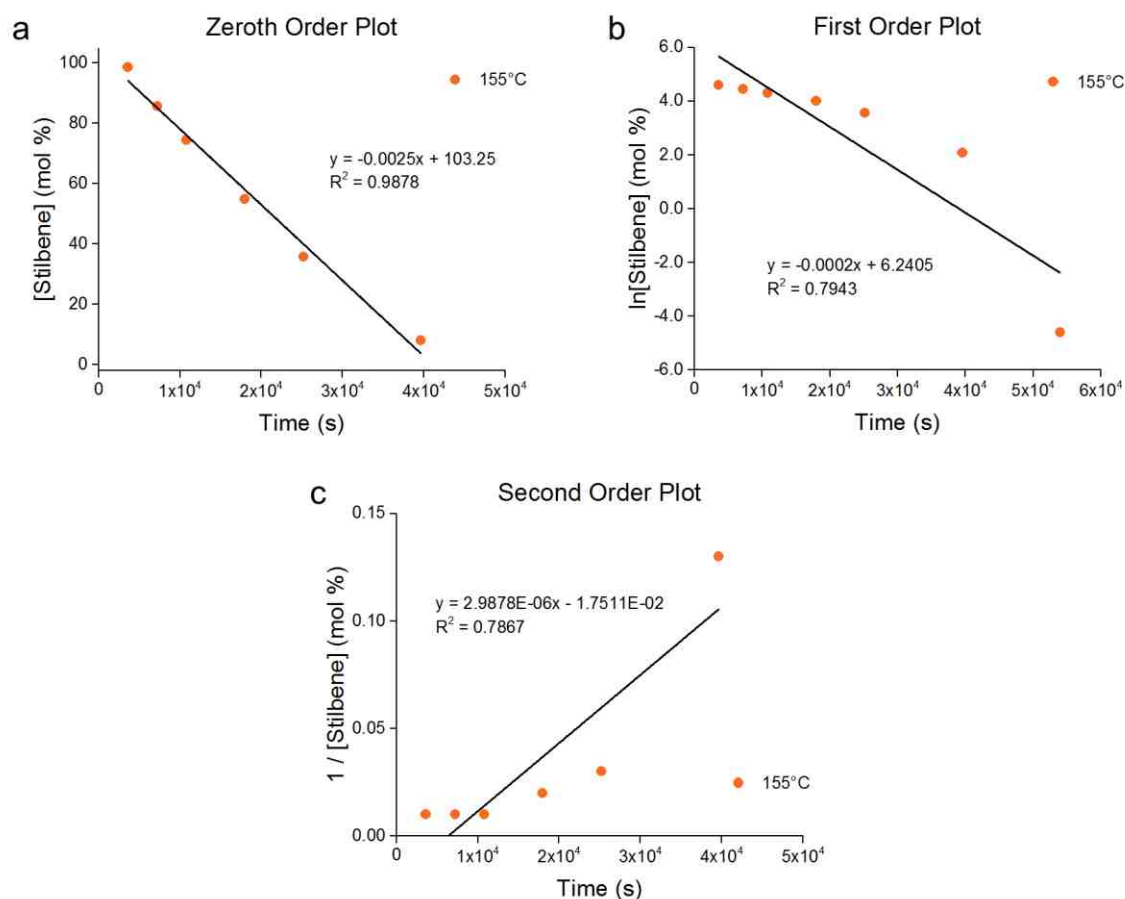


Figure 7.11 Graphs of the conversion of the substrate (*trans*-stilbene, mol %) as a function of reaction time. **(a)** A zeroth order reaction is linear with respect to the substrate concentration versus reaction time. A linear regression to our experimental data produces a coefficient of determination (R^2) value of 0.9878, displaying a strong correlation to zeroth order kinetics with respect to the substrate. **(b)** A first order plot is linear for the natural log of the concentration as a function of reaction time. This model shows significant deviation from our data with an R^2 of 0.7943. **(c)** A second order plot is linear for the inverse of the concentration as a function of time. Again, this model shows significant deviation from what would be a linear plot, with an R^2 of 0.7867.

In Figure 7.11a, the substrate concentration can be seen decreasing linearly over time, obeying zero-order kinetics (coefficient of determination $R^2 > 0.98$). It was further noted that when the *trans*-stilbene concentration was doubled, the conversion rate was essentially unchanged. Since the reaction is independent of its concentration, this reaction is zeroth-order with respect to *trans*-stilbene. On the other hand, increasing the iron concentration two-fold also doubled the reaction rate, showing that this reaction is first order with respect to iron. This follows a similar trend to what was reported with the findings of Sponza *et al.* and Lin *et al.*⁸⁹⁻⁹⁰. This would indicate that the reaction is largely influenced by the *trans*-stilbene adsorption onto the iron nanoparticle surface and the surface availability and reactivity.

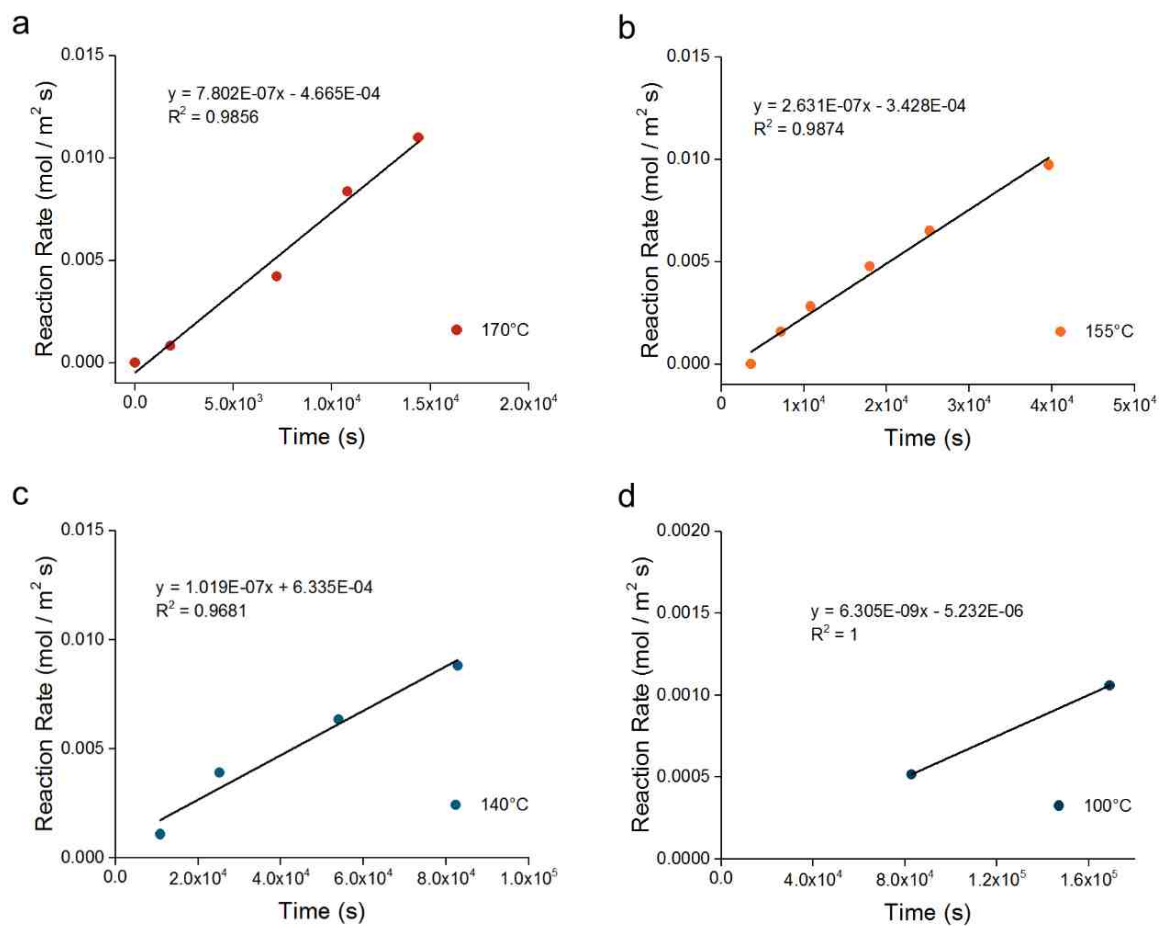


Figure 7.12 Conversion rates (mol/m²s) for temperatures at (a) 170°C (b) 155°C (c) 140°C and (d) 100°C for the 18.4 nm particles. The rate is equal to the slope of the line (m) in the linear formula $y = mx + b$. Conversion rates were 7.8E-07, 2.6E-07, 1.0E-07, and 6.3E-09 mol/m²s, respectively.

Table 7.5 Summary of experimental data for the 18.4 nm hydrogenation reactions. Conversion rates are displayed in mol/m²s.

| Temp (°C) | Temp (K) | 10 ³ /T (K ⁻¹) | Reaction Rate (k = mol/m ² s) | ln (k) |
|-----------|----------|---------------------------------------|---|--------|
| 170 | 443.15 | 2.257 | 7.8E-07 | -14.1 |
| 155 | 428.15 | 2.336 | 2.6E-07 | -15.2 |
| 140 | 413.15 | 2.420 | 1.0E-07 | -16.1 |
| 100 | 373.15 | 2.680 | 6.3E-09 | -18.9 |

Researching the particulars of the reaction rates in this mechanism for processes such as adsorption, surface reaction, and desorption would be fairly time consuming. This is true especially since our reaction mechanism is not fully understood. However, initial calculations into the activation energy and collision frequency were calculated since the reaction rates as a function of temperature were studied. This can be done by completing the Arrhenius equation, proposed by Svante Arrhenius in 1889:

$$k = Ae^{-E_a/(RT)} \quad (\text{Eq. 7.1})$$

In this equation, the reaction rate constant k is dependent on the absolute temperature T (in kelvins), the pre-exponential factor A that defines the rate due to the frequency of collisions, the activation energy E_a , and the universal gas constant R (8.3145 J/mol K). Solving this by taking the natural logarithm yields (Eq. 7.2).

$$\ln(k) = \ln(A) - \frac{E_a}{R} \frac{1}{T} \quad (\text{Eq. 7.2})$$

And rearrangement gives:

$$\ln(k) = -\left(\frac{E_a}{R}\right)\frac{1}{T} + \ln(A) \quad (\text{Eq. 7.3})$$

Which has the same form as the equation for a straight line:

$$y = mx + b \quad (\text{Eq. 7.4})$$

Where x is the reciprocal of T , the slope m is the activation energy over the universal gas constant ($-E_a/R$), y is the natural logarithm of the reaction rate, and b is the (x,y) intercept which can be used to calculate the collision frequency.

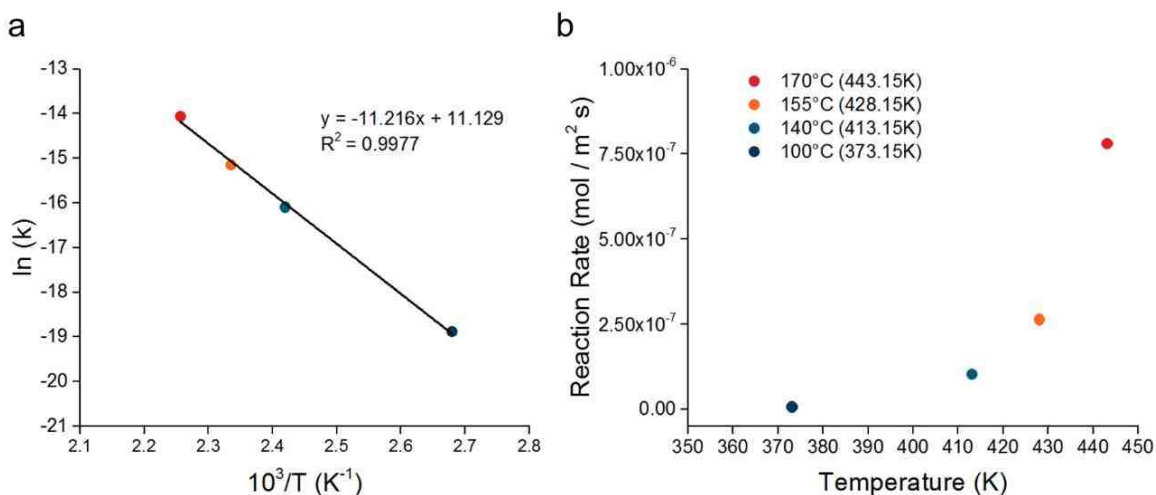


Figure 7.13 (a) Arrhenius plot displaying the logarithm of the reaction rate constants ($\ln(k)$) against inverse temperature (K^{-1}). Arrhenius plots are used to analyze the effect of temperature on the rates of chemical reactions. From the Arrhenius equation, an activation energy and collision frequency for the 18.4 nm reactions were obtained. (b) Reaction rate constants ($\text{mol}/\text{m}^2\text{s}$) for reactions executed at 100 (373.15K), 140 (413.15K), 155 (428.15K), and 170°C (443.15K).

From these equations and the plot above, the activation energy for this system can be obtained using (Eq. 7.5).

$$E_a = -mRK \quad (\text{Eq. 7.5})$$

$$E_a = -(-11216) \left(8.3145 \frac{J}{\text{mol K}} \right) (K) \quad (\text{Eq. 7.6})$$

$$E_a = 93.3 \frac{kJ}{\text{mol}} \quad (\text{Eq. 7.7})$$

And the collision frequency can be obtained through the equation

$$A = e^b \text{ sec}^{-1} \quad (\text{Eq. 7.8})$$

Where b is the intercept from the linear equation (Eq. 7.4).

$$A = e^{(11.129)} \text{ sec}^{-1} \quad (\text{Eq. 7.9})$$

$$A = 6.8E04 \text{ sec}^{-1} \quad (\text{Eq. 7.10})$$

From this information, it could be summarized that for the 18.4 nm reactions, the activation energy is calculated to be 93.3 kJ/mol with a collision frequency of 6.8E04 sec⁻¹ (6.8E04 collisions per second).

A classically useful generalization supported by the Arrhenius equation is that the reaction rate doubles for every 10°C increase in temperature⁹¹. Utilizing the initial rate of 6.3E-09 mol/m²s at 100°C (373.15 K), it is observed that the reaction rate constants

obtained through experimental data display a strong correlation to this hypothesis, coinciding with the generalization provided by Arrhenius.

7.3.1.3. 14.6 (d.nm) Nanoparticle Catalyst

Subsequently moving down in size from the 18.4 nm nanoparticles, particles with an average diameter of 14.6 nm were studied. These particles were also found to be successful in the catalytic conversion of *trans*-stilbene to bibenzyl. The temperatures implemented ranged from 140 to 170°C. The average amount of catalyst (mol %) used for these reactions was 4.1%. A summary of the 170, 155, and 140°C reactions are shown below. Due to time constraints and three temperatures providing sufficient information on the reaction rate, the 100°C reactions were not performed with this size.

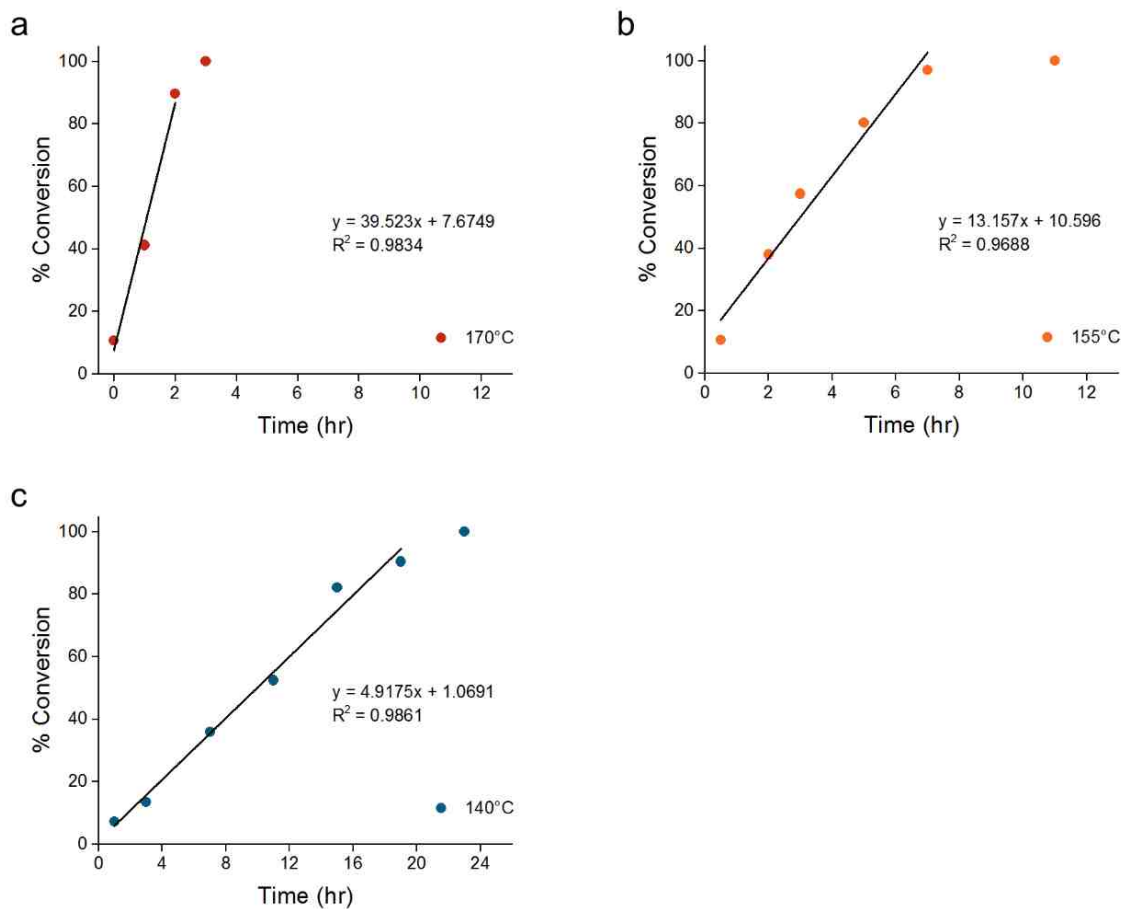


Figure 7.14 Graphs showing the conversion and conversion rates (mol %/hr) at (a) 170°C (b) 155°C and (c) 140°C for the 14.6 nm particles. The rate is equal to the slope of the line (m) in the linear formula $y = mx + b$. Conversion rates were 39.5, 13.2, and 4.9 mol %/hr, respectively.

Table 7.6 Summary of experimental data for the 14.6 nm hydrogenation reactions. Conversion rates are displayed in mol %/hr.

| Temp (°C) | Temp (K) | Pressure (psi) | Conversion Rate (mol % / hr) |
|-----------|----------|----------------|------------------------------|
| 170 | 443.15 | 250 | 39.5 |
| 155 | 428.15 | 250 | 13.2 |
| 140 | 413.15 | 250 | 4.9 |

A summary of all three temperature experiments is shown in Figure 7.15.

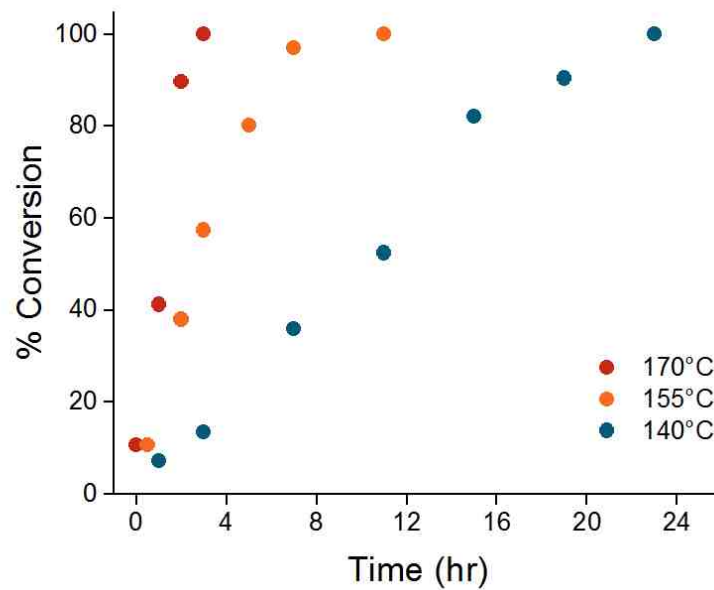


Figure 7.15 Compiled experimental data for the hydrogenation of *trans*-stilbene to bibenzyl for the 14.6 nm particles at 140, 155, and 170°C.

7.3.1.4. 14.6 (d.nm) Nanoparticle Catalyst Reaction Kinetics

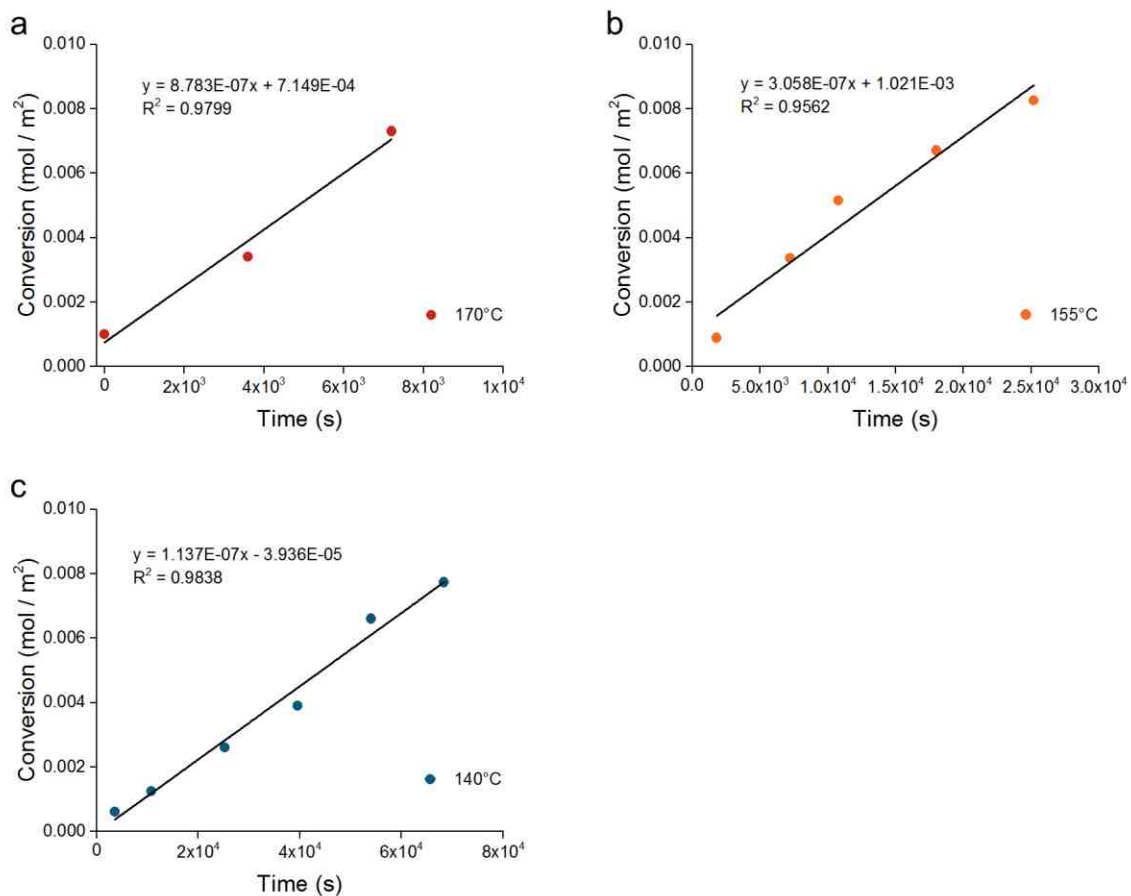


Figure 7.16 Conversion rates (mol/m²s) for temperatures of (a) 170°C (b) 155°C and (c) 140°C for the 14.6 nm particles. The rate is equal to the slope of the line (m) in the linear formula $y = mx + b$. Conversion rates were 8.8E-07, 3.1E-07, and 1.1E-07 mol/m²s, respectively.

Table 7.7 Summary of experimental data for the 14.6 nm hydrogenation reactions. Conversion rates are displayed in mol/m²s.

| Temp (°C) | Temp (K) | 10 ³ /T (K ⁻¹) | Reaction Rate (k = mol/m ² s) | ln (k) |
|-----------|----------|---------------------------------------|--|--------|
| 170 | 443.15 | 2.257 | 8.8E-07 | -13.9 |
| 155 | 428.15 | 2.336 | 3.1E-07 | -15.0 |
| 140 | 413.15 | 2.420 | 1.1E-07 | -16.0 |

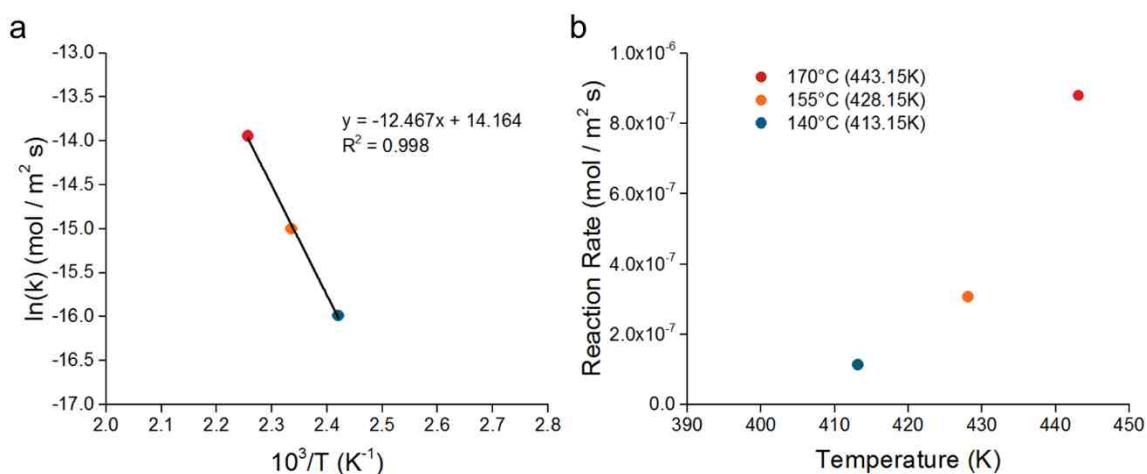


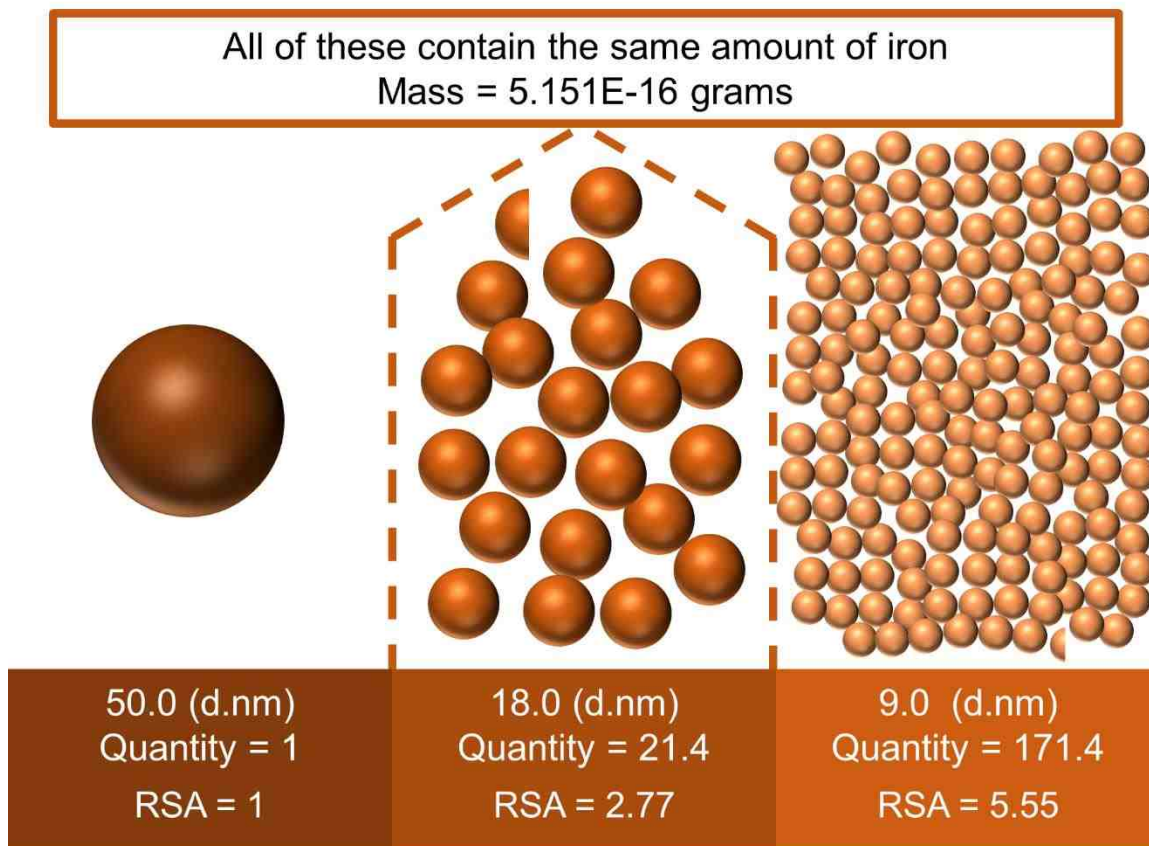
Figure 7.17 (a) Arrhenius plot displaying the logarithm of the reaction rate constants (ln(k)) against inverse temperature (K⁻¹) for the 14.6 nm reactions. (b) Reaction rate constants (mol/m²s) for reactions at 140 (413.15K), 155 (428.15K), and 170°C (443.15K).

From the Arrhenius plot, an activation energy of 103.7 kJ/mol was obtained with a collision frequency of 1.4E06 sec⁻¹ (1.4E06 collisions per second).

7.3.1.5. 9.2 (d.nm) Nanoparticle Catalyst

Finally, nanoparticles containing an average diameter of 9.2 nm were investigated, which falls on the smallest end of our size spectrum. Through conventional reasoning, these

are expected to possess the highest amount of catalytic activity due to the dramatic increase in surface area. The illustration below depicts how surface area is affected by the amount of iron and changes in nanoparticle size.



*RSA = Relative Surface Area

Figure 7.18 This figure depicts the quantity of nanoparticles of various sizes needed to achieve an equal mass of iron. All three segments contain the same amount of iron (mass = 5.151E-16 grams). To achieve this mass, one would need (1) 50.0 d.nm particle, (21.4) 18.0 d.nm particles, or (171.4) 9.0 d.nm particles.

The mass of iron in a 50.0 d.nm nanoparticle is a good starting point to observe how these properties change drastically with small changes in size (mass = 5.151E-16 grams). To achieve the same amount of iron for particles that are 18.0 and 9.0 d.nm in size, one would need 21.4 and 171.4 particles, respectively. Collectively, this amount of 18.0 d.nm particles have a relative surface area that is roughly 2.77 times higher than that of the 50.0 d.nm particle. Further decreasing this to 9.0 d.nm generates a relative surface area that is 5.55 times that of 50.0 d.nm particle for this equal mass of iron. For heterogeneous catalytic reactions relying so heavily on the surface area, it is observed how minute changes in size bring about drastic changes in particle properties.

Despite the advantageous increases in activity that normally arises from decreasing particle size, our studies found that the particles synthesized using our method were unsuccessful in the catalytic conversion of *trans*-stilbene to bibenzyl. Time, temperature, and catalyst loading were all variables investigated in these reactions, as small variations in each of these parameters are known to engender changes in catalytic activity. Our ultimate goal for these studies was to gain a partial or better understanding of what causes this anomalous behavior.

Time

First, the catalytic activity of these particles as a function of time was investigated, similar to the experiments performed with the 14.6 and 18.4 nm particles reported previously. The temperature of 155°C was the starting point for these reactions, being between our high and low temperatures. Throughout these experiments, a constant

temperature and catalyst loading was maintained. The results in Figure 7.19 show that these particles are catalytically inactive at all times investigated at this temperature.

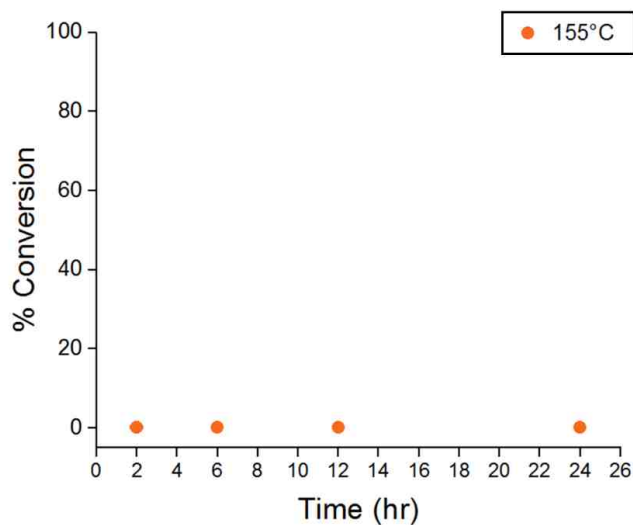


Figure 7.19 Conversion (mol %) versus time at 155°C for the 9.2 nm particles. For these experiments, catalyst loading and temperature remained constant.

Temperature

Based on the initial results from time experiments at a constant temperature of 155°C, it was proposed that perhaps a higher temperature was required to activate the nanoparticles. To either substantiate or reject this claim, the same temperatures previously reported of 170, 155, and 140°C were examined. In this case, catalyst loading again remained constant. At a constant catalyst loading, all of the temperatures studied showed no sign of nanoparticle activity as shown in Figure 7.20.

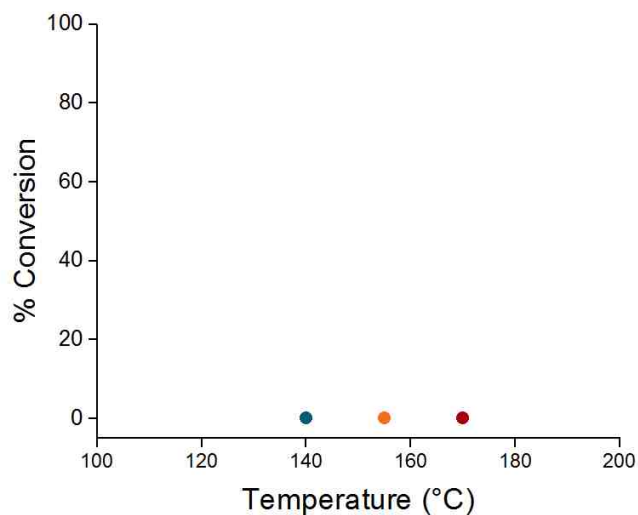


Figure 7.20 Conversion (mol %) versus temperature for increasing temperatures using the 9.2 nm particles.

Due to temperature constraints and uncertainties of nanoparticle coalescence at higher temperatures, the maximum temperature implemented was 170°C. Also, when designing a system that can potentially be implemented for industrial scale hydrogenations, higher temperatures are extremely undesirable as they can translate to elevated manufacturing costs.

Catalyst Loading

Catalyst loading was also studied in detail to ensure that it was not a factor affecting the activity of the nanoparticles. As it was mentioned previously, the rate of this reaction is directly proportional to the available surface area and thus the total iron amount. It can be speculated that increasing the number of particles would also increase the frequency of collisions in solution, giving rise to activity. The catalyst loading was increased two and

three-fold from 5.0 to 10 and 15% (mol %). It was observed through these experiments that increasing the catalyst loading had no effect on catalytic activity as shown in Figure 7.21.

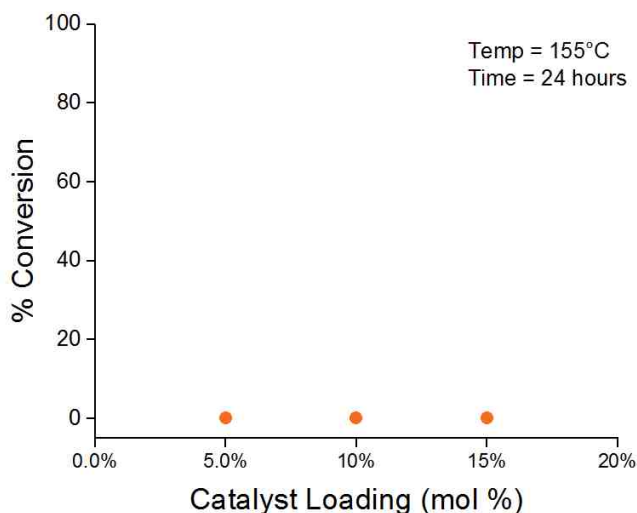


Figure 7.21 Conversion (mol %) as a function of the catalyst loading amount (mol %, iron to stilbene) for the 9.2 nm particles.

Aside from the varying the catalyst load for the 9.2 nm reactions, a hydrogen treatment was performed on all stock solutions in 1-octadecene solvent in the absence of toluene and *trans*-stilbene. At first, this was performed solely to improve the magnetic characteristics of the nanoparticles. However, it was through using this hydrogen treatment where it was discovered that the smaller nanoparticles were catalytically inactive. The two stock solutions containing 14.6 and 18.4 nm particles were successful in converting 1-octadecene to octadecane for the same reaction at 155°C for 24 hours. This was extremely apparent in the case of 1-octadecene, wherein removing the stock solution from the reactor reveals a crystalline solid. 1-Octadecene is a liquid at room temperature; however, there is

a phase change during the formation of the hydrogenated product. Hydrogenation of the double bond allows for a better packing and a higher degree of crystalline order, leading to the white crystalline solid that is octadecane. When the 9.2 nm particles underwent this same procedure, the stock solution removed was still in a liquid solvent, a very clear indication that 1-octadecene was still the dominant solvent. These particles were magnetically removed and ^1H NMR spectra of the obtained solvent displayed no sign of octadecane. In this situation, the molar ratio of iron to 1-octadecene (substrate) is 10.5%, well exceeding the average used throughout the hydrogenation reactions ~4.0-5.0%. Since 1-octadecene is a terminal alkene with a less sterically hindered double bond, one could argue that the less sterically accessible double bond on *trans*-stilbene is not the issue.

The observed phenomenon is not completely unexpected. This size-reactivity correlation has been observed by Iablokov *et al.*, who discovered that when studying cobalt oxide nanoparticles with sizes ranging from roughly 3 to 12 nm in diameter, particles that were 5 to 8 nm in size were most active for the catalytic oxidation of carbon monoxide⁹². Reaction rates decreased for smaller or larger particle sizes that were outside of this range. This group determined that there was a strong correlation between the Co^{3+} trivalent oxidation state and the CO oxidation rate using X-ray photoelectron spectroscopy. While there is certainly no relationship being established between the two systems, it is proof that catalytic activity will not always improve with decreasing particle size. There is still much to be discovered regarding this size-reactivity relationship and what is presented here shows promising initial results which can be explored in the near future.

Further Studies

A question posed after observing that particles increasing in size were still catalytically active was: *to what extent?* Because 18-20 nm is the largest nanoparticle size that could be achieved while maintaining low-size dispersity, it was questioned whether or not particles approaching the micron size regime were also catalytically active. Commercially available micron-sized iron particles (powder, <10 μm , $\geq 99.9\%$, 7439-89-6) were purchased from Sigma Aldrich. These hydrogenation reactions were performed with the same conditions as the previously mentioned setup, using a temperature of 170°C at 250 psi for 24 hours. Two experiments were completed using these micron-sized particles. First, a reaction implementing a similar catalyst loading (mol %), and second, a reaction using an equal surface area to the previously reported reactions were performed. For both reaction calculations, an underlying assumption was that the iron powder contains particles with an average size of 10 μm in diameter. For the first reaction, 7.0 mg (0.125 mmol) of iron powder was added to a solution containing 0.45 g (2.5 mmol) *trans*-stilbene in toluene. The catalyst loading for this reaction is roughly 5.0% (mol %). This is a comparable amount to reactions reported previously that used 5.0-10.0 mg of iron nanoparticles (4.0-5.0 mol % loading) on average. For the second reaction, roughly 3.89 grams of iron powder is needed to achieve the same surface area as 7.0 mg of 18 d.nm particles. Therefore, 3.89 g (69.7 mmol) of iron powder was added to a solution containing 0.45 g (2.5 mmol) *trans*-stilbene in toluene. The catalyst amount was determined to be roughly 2,800% (mol %). Through both of these experiments, it was concluded that the micron-sized particles were not successful in the catalytic hydrogenation of *trans*-stilbene

under the aforementioned reaction conditions. This is to be expected for our system as there exists a fairly generous gap in catalytic activity between the 14.6 and 18.4 nm particles.

7.3.2. Conclusions

Nanoparticles produced through the reversible magnetic agglomeration mechanism that underwent a hydrogenation post-processing technique were found to be successful for the hydrogenation of *trans*-stilbene and 1-octadecene. The activation energies obtained in these experiments warrants the need for further investigation. Classical reasoning would suggest that the smaller particles (14.6 nm) with higher catalytic activity would be easier to activate energetically than the larger particles. Because the lowest temperature (100°C) was not performed with the 14.6 nm particles, omitting this reaction rate from the Arrhenius kinetics calculation for the 18.4 nm particles leads to an activation energy of 102.3 kJ/mol. This is much closer to the value obtained for the 14.6 nm particles of 103.7 kJ/mol. It can be determined that the lower temperature has a significant impact on the Arrhenius calculation. Furthermore, the small difference between these newly obtained values could lie within the standard range of error, leading to alteration of the pre-exponential factor which has a significant effect on the activation energy. Further work will help fully understand these results.

For the investigated substrate, the 14.6 nm diameter particles achieved the highest efficiency while the 18.4 nm diameters followed shortly after. This is to be expected as particles decrease in size leading to a higher surface area to volume ratio. However, the 9.2 nm particles were inactive for all temperatures, reaction times, and catalyst loading

amounts investigated, going against conventional reasoning. Although this size-reactivity behavior was unexpected, it was discovered that this type of behavior has been observed previously⁹². The conversion was determined to be zeroth-order with respect to the substrate and first order with respect to the iron nanoparticle catalyst. This research has proven that the full conversion of these substrates was attainable, and it opens many opportunities for further substrate studies to be performed in the future.

Chapter 8. Conclusions and Outlook

The proposed reversible magnetic agglomeration mechanism has been proven to be an effective synthetic method for the strict size control of highly magnetic nanoparticles. Nanoparticles with a narrow size dispersity were successfully synthesized with sizes ranging from around 8 to 20 nm, ultimately halting growth around a mean size of 18.6 nm in diameter. Magnetically agglomerated particles nearing the peak size were shown to redisperse easily through light heating or sonication. Through these experiments, we were able to provide fundamental insight into how the surfactant influences nanoparticle nucleation, stabilization and growth.

This research has also proven that the maximum size to which the particles can grow using the reversible magnetic agglomeration mechanism is ultimately controlled by the steric bulk provided by the implemented surfactant. Nanoparticles were synthesized through multiple iterations of the mechanism with a range of surfactant sizes, ultimately allowing for a wider range of nanoparticle sizes to be achieved. The scale-up syntheses performed delivers exceptionally promising results, paving the way for the large-scale production of highly magnetic nanoparticles with commercially available and inexpensive surfactants.

Furthermore, post-processing of the as-synthesized nanoparticles allow further customization, opening multiple routes to achieving desired properties for a given system. Through these techniques, we discovered these nanoparticles can serve as inexpensive and

magnetically recoverable catalysts for the hydrogenation of alkenes, with promising prospects for a variety of other structurally similar substrates.

Future Outlook

The results presented here show a significant enhancement to the present synthetic methods for the scalable size control of magnetic iron nanoparticles. Using this method, a variety of surfactants can be implemented to see how further control can be implemented over nanoparticle shape, size, and its physical properties. We believe this method of size control not only applies to our system, but also to other highly magnetic systems where strong magnetic interactions can facilitate nanoparticle growth. While the post-processing techniques mentioned here were solely carried out on nanoparticles synthesized with our method, we believe these techniques can be utilized as-synthesized nanoparticles produced by almost any method. Altering the temperature, pressure, or carrier gas used for these techniques can provide insight to the nanoparticle properties that are affected or altered during this process, thus allowing nanoparticle properties to be tailored for a wide array of applications.

Appendix A. Publications

Journal publications:

Bleier, G. C., Watt, J., Simocko, C. K., Lavin, J. M., & Huber, D. L. (2018). Reversible Magnetic Agglomeration – A Mechanism for True Thermodynamic Control of Nanoparticle Size. *Angewandte Chemie. Submitted.*

Watt, J., **Bleier, G. C.**, Romero, Z. W., Hance, B. G., Bierner, J. A., Monson, T. C., & Huber, D. L. (2018). Gram Scale Synthesis of Fe/Fe_xO_y Core-Shell Nanoparticles and their Incorporation into Matrix-Free Superparamagnetic Nanoparticles. *Awaiting Publication in Journal of Materials Research.*

Watt, J., **Bleier, G. C.**, Austin, M. J., Ivanov, S. A., & Huber, D. L. (2017). Non-volatile iron carbonyls as versatile precursors for the synthesis of iron-containing nanoparticles. *Nanoscale*, 9(20), 6632-6637. doi:10.1039/c7nr01028a

Articles in preparation:

Bleier, G. C., Watt, J., & Huber, D. L. (2018). Size Dependent Catalytic Activity of Iron (0) Nanoparticles as Hydrogenation Catalysts. *Manuscript in preparation.*

References

1. Combating climate change. *Nat Nanotechnol* **2007**, 2 (6), 325.
2. Room for improvement. *Nat Nanotechnol* **2007**, 2 (5), 257.
3. Huber, D. L., Synthesis, properties, and applications of iron nanoparticles. *Small* **2005**, 1 (5), 482-501.
4. Logothetidis, S., *Nanostructured Materials and Their Applications*. 2012.
5. Daniel, M. C.; Astruc, D., Gold nanoparticles: assembly, supramolecular chemistry, quantum-size-related properties, and applications toward biology, catalysis, and nanotechnology. *Chem Rev* **2004**, 104 (1), 293-346.
6. Allcock, H. R., *Introduction to materials chemistry*. Wiley: Hoboken, N.J., 2008; p xviii, 432 p., 8 p. of plates.
7. Gubin, S. P., *Magnetic Nanoparticles*. 1 ed.; Wiley-VCH: Berlin, 2009; p 484.
8. Sun, S.; Murray, C. B.; Weller, D.; Folks, L.; Moser, A., Monodisperse FePt nanoparticles and ferromagnetic FePt nanocrystal superlattices. *Science (New York, N.Y.)* **2000**, 287 (5460), 1989-92.
9. Ross, C., Patterned magnetic recording media. *Annual Review of Materials Research* **2001**, 31 (1), 203-235.
10. Andreas, M.; Kentaro, T.; David, T. M.; Manfred, A.; Yoshiaki, S.; Yoshihiro, I.; Shouheng, S.; Eric, E. F., Magnetic recording: advancing into the future. *Journal of Physics D: Applied Physics* **2002**, 35 (19), R157.
11. Sun, C.; Lee, J. S.; Zhang, M., Magnetic nanoparticles in MR imaging and drug delivery. *Adv Drug Deliv Rev* **2008**, 60 (11), 1252-65.

12. Chertok, B.; Moffat, B. A.; David, A. E.; Yu, F.; Bergemann, C.; Ross, B. D.; Yang, V. C., Iron oxide nanoparticles as a drug delivery vehicle for MRI monitored magnetic targeting of brain tumors. *Biomaterials* **2008**, *29* (4), 487-96.
13. Dobson, J., Magnetic nanoparticles for drug delivery. *Drug Development Research* **2006**, *67* (1), 55-60.
14. Laurent, S.; Forge, D.; Port, M.; Roch, A.; Robic, C.; Vander Elst, L.; Muller, R. N., Magnetic iron oxide nanoparticles: synthesis, stabilization, vectorization, physicochemical characterizations, and biological applications. *Chem Rev* **2008**, *108* (6), 2064-110.
15. Alivisatos, P., The use of nanocrystals in biological detection. *Nat Biotechnol* **2004**, *22* (1), 47-52.
16. Torres Galvis, H. M.; Bitter, J. H.; Khare, C. B.; Ruitenbeek, M.; Dugulan, A. I.; de Jong, K. P., Supported iron nanoparticles as catalysts for sustainable production of lower olefins. *Science (New York, N.Y.)* **2012**, *335* (6070), 835-8.
17. Lu, A. H.; Salabas, E. L.; Schuth, F., Magnetic nanoparticles: synthesis, protection, functionalization, and application. *Angewandte Chemie* **2007**, *46* (8), 1222-44.
18. Cullity, B. D.; Graham, C. D., *Intro to Mag Mater*. 2nd ed.; IEEE/Wiley: Hoboken, N.J., 2009; p xvii, 544 p.
19. Pal, M.; De, A., Polymer–Iron Oxide Based Magnetic Nanocomposites. In *Hybrid Nanocomposites for Nanotechnology*, Merhari, L., Ed. Springer US: Boston, MA, 2009; pp 455-506.
20. Abraham, H.; Langevin, P., *Les quantités élémentaires d'électricité: ions, électrons, corpuscules*. Gauthier-Villars: Paris., 1905; p xvi, 1138 p.
21. Thornton, S. T.; Rex, A., *Modern Physics for Scientists and Engineers*. Cengage Learning: 2012.

22. Ali, K.; Javed, Y.; Jamil, Y., Size and Shape Control Synthesis of Iron Oxide-Based Nanoparticles: Current Status and Future Possibility. **2017**, 39-81.
23. Kerekes, L.; Hakl, J.; Meszaros, S.; Vad, K.; Gurin, P.; Kis-Varga, I.; Uzonyi, I.; Szabo, S.; Beke, D. L., Study of magnetic relaxation in partially oxidized nanocrystalline iron. *Czechoslovak Journal of Physics* **2002**, 52 (S1), A89-A92.
24. Pardavi-Horvath, M.; Takacs, L., Magnetic nanocomposites by reaction milling. *Scripta Metallurgica et Materialia* **1995**, 33 (10-11), 1731-1740.
25. Cheng, W.; Zhang, W. D.; Hu, L. J.; Ding, W.; Wu, F.; Li, J. J., Etching synthesis of iron oxide nanoparticles for adsorption of arsenic from water. *Rsc Advances* **2016**, 6 (19), 15900-15910.
26. Amendola, V.; Riello, P.; Meneghetti, M., Magnetic Nanoparticles of Iron Carbide, Iron Oxide, Iron@Iron Oxide, and Metal Iron Synthesized by Laser Ablation in Organic Solvents. *J Phys Chem C* **2011**, 115 (12), 5140-5146.
27. Wang, Z. M.; Li, X. Y.; Gao, M.; Zeng, X. Y., One-step preparation of amorphous iron nanoparticles by laser ablation. *Powder Technol* **2012**, 215-16, 147-150.
28. Futko, S. I.; Shulitskii, B. G.; Labunov, V. A.; Ermolaeva, E. M., Simulation of the Kinetics of Growth of Iron Nanoparticles in the Process of Chemical Vapor Deposition of Hydrocarbons with Injection of Ferrocene for the Synthesis of Carbon-Nanotube Arrays. *Journal of Engineering Physics and Thermophysics* **2015**, 88 (6), 1432-1441.
29. Xia, W.; Su, D. S.; Birkner, A.; Ruppel, L.; Wang, Y. M.; Woll, C.; Qian, J.; Liang, C. H.; Marginean, G.; Brandl, W.; Muhler, M., Chemical vapor deposition and synthesis on carbon nanofibers: Sintering of ferrocene-derived supported iron nanoparticles and the catalytic growth of secondary carbon nanofibers. *Chemistry of Materials* **2005**, 17 (23), 5737-5742.
30. Wang, J. N.; Zhang, L.; Yu, F.; Sheng, Z. M., Synthesis of carbon encapsulated magnetic nanoparticles with giant coercivity by a spray pyrolysis approach. *J Phys Chem B* **2007**, 111 (8), 2119-24.

31. Strobel, R.; Pratsinis, S. E., Direct synthesis of maghemite, magnetite and wustite nanoparticles by flame spray pyrolysis. *Advanced Powder Technology* **2009**, *20* (2), 190-194.
32. Banerjee, S.; Roy, S.; Chen, J. W.; Chakravorty, D., Magnetic properties of oxide-coated iron nanoparticles synthesized by electrodeposition. *Journal of Magnetism and Magnetic Materials* **2000**, *219* (1), 45-52.
33. Leslie-Pelecky, D. L.; Rieke, R. D., Magnetic Properties of Nanostructured Materials. *Chemistry of Materials* **1996**, *8* (8), 1770-1783.
34. Huang, X., *Nanotechnology research : new nanostructures, nanotubes and nanofibers*. Nova Science Publishers: New York, 2008; p xii, 370 p.
35. Amendola, V.; Meneghetti, M., Laser ablation synthesis in solution and size manipulation of noble metal nanoparticles. *Physical chemistry chemical physics : PCCP* **2009**, *11* (20), 3805-21.
36. Dean, R. S., Davis, Charles W. Permanent magnet. 1941.
37. Luborsky, F. E., The Kinetics of Growth of Spherical Iron Crystallites in Mercury. *J Phys Chem-Us* **1957**, *61* (10), 1336-1340.
38. Kharisov, B. I.; Dias, H. V. R.; Kharissova, O. V.; Jimenez-Perez, V. M.; Perez, B. O.; Flores, B. M., Iron-containing nanomaterials: synthesis, properties, and environmental applications. *Rsc Advances* **2012**, *2* (25), 9325-9358.
39. Fu, F.; Dionysiou, D. D.; Liu, H., The use of zero-valent iron for groundwater remediation and wastewater treatment: a review. *J Hazard Mater* **2014**, *267*, 194-205.
40. Li, Z. J.; Wang, L.; Yuan, L. Y.; Xiao, C. L.; Mei, L.; Zheng, L. R.; Zhang, J.; Yang, J. H.; Zhao, Y. L.; Zhu, Z. T.; Chai, Z. F.; Shi, W. Q., Efficient removal of uranium from aqueous solution by zero-valent iron nanoparticle and its graphene composite. *J Hazard Mater* **2015**, *290*, 26-33.

41. Druzhinina, T. S.; Herzer, N.; Hoepfner, S.; Schubert, U. S., Formation of iron oxide particles by reduction with hydrazine. *Chemphyschem* **2011**, *12* (4), 781-4.
42. O'Connor, C. J.; Seip, C. T.; Carpenter, E. E.; Li, S. C.; John, V. T., Synthesis and reactivity of nanophase ferrites in reverse micellar solutions. *Nanostructured Materials* **1999**, *12* (1-4), 65-70.
43. Sun, Y. P.; Li, X. Q.; Cao, J.; Zhang, W. X.; Wang, H. P., Characterization of zero-valent iron nanoparticles. *Advances in colloid and interface science* **2006**, *120* (1-3), 47-56.
44. Sun, Y. P.; Li, X. Q.; Zhang, W. X.; Wang, H. P., A method for the preparation of stable dispersion of zero-valent iron nanoparticles. *Colloids and Surfaces a-Physicochemical and Engineering Aspects* **2007**, *308* (1-3), 60-66.
45. Issa, B.; Obaidat, I. M.; Albiss, B. A.; Haik, Y., Magnetic nanoparticles: surface effects and properties related to biomedicine applications. *International journal of molecular sciences* **2013**, *14* (11), 21266-305.
46. Hisano, S.; Saito, K., Research and development of metal powder for magnetic recording. *Journal of Magnetism and Magnetic Materials* **1998**, *190* (3), 371-381.
47. Nurmi, J. T.; Tratnyek, P. G.; Sarathy, V.; Baer, D. R.; Amonette, J. E.; Pecher, K.; Wang, C.; Linehan, J. C.; Matson, D. W.; Penn, R. L.; Driessen, M. D., Characterization and properties of metallic iron nanoparticles: spectroscopy, electrochemistry, and kinetics. *Environ Sci Technol* **2005**, *39* (5), 1221-30.
48. Liu, Y. Q.; Choi, H.; Dionysiou, D.; Lowry, G. V., Trichloroethene hydrodechlorination in water by highly disordered monometallic nanoiron. *Chemistry of Materials* **2005**, *17* (21), 5315-5322.
49. Yan, W.; Lien, H. L.; Koel, B. E.; Zhang, W. X., Iron nanoparticles for environmental clean-up: recent developments and future outlook. *Environ Sci Process Impacts* **2013**, *15* (1), 63-77.
50. Crane, R. A.; Scott, T. B., Nanoscale zero-valent iron: future prospects for an emerging water treatment technology. *J Hazard Mater* **2012**, *211-212*, 112-25.

51. Varanda, L. C.; Jafelicci, M.; Tartaj, P.; O'Grady, K.; Gonzalez-Carreno, T.; Morales, M. P.; Munoz, T.; Serna, C. J., Structural and magnetic transformation of monodispersed iron oxide particles in a reducing atmosphere. *Journal of Applied Physics* **2002**, 92 (4), 2079-2085.
52. Hinman, J. J.; Suslick, K. S., Nanostructured Materials Synthesis Using Ultrasound. *Top Curr Chem (Cham)* **2017**, 375 (1), 12.
53. Suslick, K. S.; Choe, S. B.; Cichowlas, A. A.; Grinstaff, M. W., Sonochemical Synthesis of Amorphous Iron. *Nature* **1991**, 353 (6343), 414-416.
54. Suslick, K. S.; Fang, M. M.; Hyeon, T., Sonochemical synthesis of iron colloids. *Journal of the American Chemical Society* **1996**, 118 (47), 11960-11961.
55. Watt, J.; Bleier, G. C.; Austin, M. J.; Ivanov, S. A.; Huber, D. L., Non-volatile iron carbonyls as versatile precursors for the synthesis of iron-containing nanoparticles. *Nanoscale* **2017**, 9 (20), 6632-6637.
56. Hufschmid, R.; Arami, H.; Ferguson, R. M.; Gonzales, M.; Teeman, E.; Brush, L. N.; Browning, N. D.; Krishnan, K. M., Synthesis of phase-pure and monodisperse iron oxide nanoparticles by thermal decomposition. *Nanoscale* **2015**, 7 (25), 11142-54.
57. Huuppola, M.; Zhu, Z.; Johansson, L. S.; Kontturi, K.; Laasonen, K.; Johans, C., Anomalous dependence of particle size on supersaturation in the preparation of iron nanoparticles from iron pentacarbonyl. *Journal of colloid and interface science* **2012**, 386 (1), 28-33.
58. Lacroix, L. M.; Huls, N. F.; Ho, D.; Sun, X.; Cheng, K.; Sun, S., Stable single-crystalline body centered cubic Fe nanoparticles. *Nano letters* **2011**, 11 (4), 1641-5.
59. Smith, T. W.; Wychick, D., Colloidal Iron Dispersions Prepared Via the Polymer-Catalyzed Decomposition of Iron Pentacarbonyl. *J Phys Chem* **1980**, 84 (12), 1621-1629.
60. Koprinarov, N.; Konstantinova, M.; Marinov, M., Ferromagnetic Nanomaterials Obtained by Thermal Decomposition of Ferrocene. *Sol St Phen* **2010**, 159, 105-+.

61. Patnaik, P., *Handbook of inorganic chemicals*. McGraw-Hill: New York, 2003; p xv, 1086, 1 p.
62. Baev, A. K.; Gaidym, I. L.; Demyanchuk, V. V., Thermal-Decomposition Kinetics of Iron Nonacarbonyl. *Zh Fiz Khim+* **1975**, *49* (10), 2575-2577.
63. Mørup, S.; Bødker, F.; Van Wonterghem, J.; Madsen, M. B.; Bentzon, M. D., Superparamagnetic amorphous Fe_{1-x}C_x alloy particles in a ferrofluid. *Hyperfine Interactions* **1989**, *51* (1-4), 1071-1077.
64. Griffiths, C. H.; O'Horo, M. P.; Smith, T. W., The structure, magnetic characterization, and oxidation of colloidal iron dispersions. *Journal of Applied Physics* **1979**, *50* (11), 7108-7115.
65. Herman, D. A.; Ferguson, P.; Cheong, S.; Hermans, I. F.; Ruck, B. J.; Allan, K. M.; Prabakar, S.; Spencer, J. L.; Lendrum, C. D.; Tilley, R. D., Hot-injection synthesis of iron/iron oxide core/shell nanoparticles for T2 contrast enhancement in magnetic resonance imaging. *Chemical communications* **2011**, *47* (32), 9221-3.
66. Farrell, D.; Majetich, S. A.; Wilcoxon, J. P., Preparation and characterization of monodisperse Fe nanoparticles. *Journal of Physical Chemistry B* **2003**, *107* (40), 11022-11030.
67. Huber, D. L.; Venturini, E. L.; Martin, J. E.; Provencio, P. P.; Patel, R. J., Synthesis of highly magnetic iron nanoparticles suitable for field structuring using a beta-diketone surfactant. *Journal of Magnetism and Magnetic Materials* **2004**, *278* (3), 311-316.
68. Monson, T. C., *Study of Anomalous Behavior in Solution Synthesized Iron Nanoparticles*. University of Texas: 2012.
69. Kataby, G.; Cojocaru, M.; Prozorov, R.; Gedanken, A., Coating carboxylic acids on amorphous iron nanoparticles. *Langmuir* **1999**, *15* (5), 1703-1708.
70. Srivastava, D. N.; Perkas, N.; Gedanken, A.; Felner, I., Sonochemical synthesis of mesoporous iron oxide and accounts of its magnetic and catalytic properties. *Journal of Physical Chemistry B* **2002**, *106* (8), 1878-1883.

71. Smith, T. W.; Wychick, D., Colloidal iron dispersions prepared via the polymer-catalyzed decomposition of iron pentacarbonyl. *The Journal of Physical Chemistry* **1980**, *84* (12), 1621-1629.
72. Nalwa, H. S., *Nanostructured materials and nanotechnology*. Concise ed.; Academic Press: San Diego, 2002; p xxiii, 834 p.
73. Lamer, V. K.; Dinegar, R. H., Theory, Production and Mechanism of Formation of Monodispersed Hydrosols. *Journal of the American Chemical Society* **1950**, *72* (11), 4847-4854.
74. Voorhees, P. W., The Theory of Ostwald Ripening. *Journal of Statistical Physics* **1985**, *38* (1-2), 231-252.
75. McElfresh, M., *Fundamentals of Magnetism and Magnetic Measurements In Quantum Design*. **1994**.
76. Coey, J. M. D., *Magnetism and Magnetic Materials*. Cambridge University Press: 2010.
77. Bragg, W. S.; Bragg, W. L., *X rays and Crystal Structure*. G. Bell and Sons, Ltd.: London, 1915.
78. Sasaki, A., Size Distribution Analysis of Nanoparticles Using Small Angle X-ray Scattering Technique. *The Rigaku Journal* **2005**, *22* (1), 31-38.
79. Tissue, B. M., *Ultraviolet and Visible Absorption Spectroscopy*. **2002**.
80. Iron; Institute, S., *The Journal of the Iron and Steel Institute*. The Institute: 1897.
81. *The Chemical News and Journal of Physical Science*. Griffin, Bohn and Company: 1904.
82. Kosolapova, T. Y., *Carbides: Properties, Production, and Applications*. Springer US: 2012.

83. ASTM, Standard test method for iron in trace quantities using the 1,10-phenanthroline method. In *ASTM Standard*, ASTM Standard: West Conshohocken, PA, 2000; Vol. E394-00
84. Vreeland, E. C.; Watt, J.; Schober, G. B.; Hance, B. G.; Austin, M. J.; Price, A. D.; Fellows, B. D.; Monson, T. C.; Hudak, N. S.; Maldonado-Camargo, L.; Bohorquez, A. C.; Rinaldi, C.; Huber, D. L., Enhanced Nanoparticle Size Control by Extending LaMer's Mechanism. *Chem Mater* **2015**, *27* (17), 6059-6066.
85. Cheon, J.; Lee, J. H., Synergistically integrated nanoparticles as multimodal probes for nanobiotechnology. *Acc Chem Res* **2008**, *41* (12), 1630-40.
86. Grinstaff, M. W.; Salamon, M. B.; Suslick, K. S., Magnetic properties of amorphous iron. *Physical review. B, Condensed matter* **1993**, *48* (1), 269-273.
87. Bauer, I.; Knolker, H. J., Iron catalysis in organic synthesis. *Chem Rev* **2015**, *115* (9), 3170-387.
88. Turner, M.; Golovko, V. B.; Vaughan, O. P.; Abdulkin, P.; Berenguer-Murcia, A.; Tikhov, M. S.; Johnson, B. F.; Lambert, R. M., Selective oxidation with dioxygen by gold nanoparticle catalysts derived from 55-atom clusters. *Nature* **2008**, *454* (7207), 981-3.
89. Sponza, D. T.; Isik, M., Decolorization and azo dye degradation by anaerobic/aerobic sequential process. *Enzyme and Microbial Technology* **2002**, *31* (1-2), 102-110.
90. Lin, S. S.; Gurol, M. D., Catalytic decomposition of hydrogen peroxide on iron oxide: Kinetics, mechanism, and implications. *Environmental Science & Technology* **1998**, *32* (10), 1417-1423.
91. Pauling, L., *General chemistry*. Dover Publications, Inc.: New York, 1988; p xiv, 959 p.
92. Iablokov, V.; Barbosa, R.; Pollefeyt, G.; Van Driessche, I.; Chenakin, S.; Kruse, N., Catalytic CO Oxidation over Well-Defined Cobalt Oxide Nanoparticles: Size-Reactivity Correlation. *Acs Catalysis* **2015**, *5* (10), 5714-5718.